High Performance Electrode and Catalyst Nano-materials for Energy Storage Devices: Supercapacitors, Pseudocapacitors and Zinc-air Batteries Made from Asphaltene Based Carbon Fibers

by

Seyedehzahra Abedi

A thesis submitted in partial fulfillment of the requirements for the degree of

Doctor of Philosophy

in

Materials Engineering

Department of Chemical and Materials Engineering

University of Alberta

Abstract

The demand for grid-scale energy storage has become more and more significant as the world continues to move towards renewable and sustainable energy storage technologies. Capacitors and batteries are the energy storage devices used in almost all electronic devices. Capacitors are capable of delivering high power densities, since their charge/discharge processes are faster compared with batteries. Batteries are able to store significant amounts of energy (high energy density) due to the nature of the electrochemical reactions occurring when charging.

The first study in this work investigated the performance of asphaltene based carbon fibers (CF) as the electrode material for EDLSs. Asphaltene based activated carbon fibers (ACF) were prepared via chemical activation using KOH pellets. The activation ratio (mass(KOH)/mass(CF)) was varied in the range of 1-4. N_2 physisorption was employed to investigate the SSA and porosity of the ACF-R samples (R = activation ratio). The best performing sample (ACF-3) in this work had a Brunauer–Emmett–Teller (BET) SSA of ~2300 $m^2\ g^{-1}$ and a total pore volume of 1.27 $cm^3\ g^{-1}$. The EDLS fabricated with ACF-3 had a specific capacitance of 205 F g^{-1} at 40 mA g^{-1}.

The focus of the second study was to use ACF as a conductive substrate for birnessite type MnO_2 (δ-MnO_2) as the active material for a pseudocapacitor. ACF-3 was chosen due to its high electrical conductivity and superior capacitance reported in the first study. δ-MnO_2 was prepared through a hydrothermal method. Due to the poor performance of the as prepared material, an annealing step was employed in an oxygen-deficient environment to introduce oxygen-deficient defects and porosity into the microstructure. A temperature of 400 ^oC was the optimum annealing temperature (400-δ-MnO_2). Sample 400-δ-MnO_2 was then synthesized as a coating on

ACF-3 (ACF-400-δ-MnO_2). The pseudocapacitive performance of ACF-400-δ-MnO_2 (328 F g^{-1} at 0.4 A g^{-1}) was superior to that of 400-δ-MnO_2 (195 F g^{-1} at 0.4 A g^{-1}), demonstrating the improvement in the performance by using ACF-3 as the substrate.

The third study dealt with ZABs made with asphaltene based CFs. The main issues regarding rechargeable ZABs are low efficiency and unstable cycling behavior. Spinel type $MnCo_2O_4$ nanoparticles were coated on carbon fibers and carbonized at 1500 ^oC (not activated) to fabricate a homemade air electrode with electrocatalyst for ZABs. The cubic spinel phase was identified and confirmed by SEM, TEM and X-ray photoelectron spectroscopy (XPS). This electrode outperformed the benchmark Pt-RuO_2 electrocatalysts with an efficiency of ~64% at 10 mA cm^{-2} and stable cycling behavior for at least 100 h (200 cycles). The electrolytes used in this work for half-cell and full-cell tests were aqueous, O_2 saturated 1 M KOH and aqueous 6 M KOH + 0.25 M ZnO.

The fourth study investigated the performance of the same homemade air electrode, developed in Chapter five of this thesis ($MnCo_2O_4$/CF), in an all solid-state ZAB. Alkaline poly(acrylic acid) (PAA) based gel polymer electrolytes (GPEs), with different crosslinker concentrations, were synthesized and studied. These electrolytes were examined via visual, rheological and electrochemical tests. Visual and rheological tests revealed that a crosslinker concentration of 20 mM did not result in a GPE that qualified as a solid, but was liquid. Electrochemical tests indicated that 30 mM of the crosslinker in the GPE (Hydrogel-30-mM) led to the best performing electrolyte. Full cell battery tests showed that the battery made with $MnCo_2O_4$/CF and Hydrogel-30-mM had very good performance with an initial efficiency of ~63% at 10 mA cm^{-2}, which degraded by only 6.5% after 200 cycles. The maximum power density achieved by this battery was 240 mW cm^{-2}.

The last part of this work studied the low temperature battery performance of an all solid-state ZAB made with $MnCo_2O_4$/CF and PAA based GPE, that was developed in the previous study. The battery performance was studied in terms of charge/discharge voltage and efficiency, cycle life, power output and cell voltage in a temperature range of -45 ^oC to 21 ^oC. This battery successfully completed 200 cycles of charge/discharge at all temperatures, without failure. The current density used for the cycling test was 2 mA cm^{-2}, which is at least twice the value reported in most of the literature. The power outputs at 0 and -45 ^oC were 75 and 12 mW cm^{-2}, respectively.

Preface

This thesis is focused on the development and characterization of homemade electrodes, fabricated from asphaltene derived carbon fibers, for electrochemical double layer supercapacitors (EDLSs), Faradaic pseudocapacitors and Zn-air batteries (ZABs). In addition, the performance of all solid-state ZABs at room temperature and low temperatures was investigated and characterized. The studies in Chapters 3, 4, 5, 6 and 7 are all my original work.

Chapter 3 was conducted in collaboration with Dr. Desirée Leistenschneider. Dr. Leistenschneider developed and synthesized oxidized asphaltene fibers. I carbonized and activated the fibers, prepared electrodes and the electrolyte and assembled the EDLS cells. All characterization and electrochemical tests were performed by me. A version of Chapter 3 has been published.

- **Z. Abedi**, D. Leistenschneider, W. Chen and D.G. Ivey, "Superior Performance of Electrochemical Double Layer Supercapacitor Made with Asphaltene Derived Activated Carbon Fibers," *Energy Technol*., 2020, vol. 2000588, p. 1.

Chapter 4 was also conduced in collaboration with Dr. Leistenschneider who assisted in oxidized asphaltene fiber preparation. A version of Chapter 4 has been published.

- **Z. Abedi**, D. Leistenschneider, W. Chen and D.G. Ivey, "Improved Capacitive Behavior of Birnessite Type Mn Oxide Coated on Activated Carbon Fibers", J. Electrochem. Soc., 2022, vol. 169, p. 010507.

In the work presented in Chapter 5, Dr. Leistenschneider provided the oxidized asphaltene fibers and the rest of the study was conducted by me. A version of Chapter 5 has been published.

- **Z. Abedi**, D. Leistenschneider, W. Chen and D.G. Ivey, “Spinel Type Mn-Co Oxide Coated Carbon Fibers as Efficient Bifunctional Electrocatalysts for Zinc-air Batteries”, Batter. Supercaps, 2022, vol. 5, p. e202100339.

Chapter 6 was conducted in collaboration with Mr. Jiayao Cui. Mr. Cui synthesized and developed hydrogel electrolytes for the all solid-state Zn-air batteries. A version of Chapter 6 has been published.

- **Z. Abedi**, J. Cui, W. Chen and D.G. Ivey, “Zinc-Air Batteries with Efficient and Stable $MnCo_2O_4$/Carbon Fiber Bifunctional Electrocatalyst and Poly(acrylic Acid) (PAA) Based Gel Electrolyte” *ACS Appl. Energy Mater*., 2022.

Chapter 7 was also investigated with the help of Mr. Cui who assisted in gel polymer electrolyte preparation. A version of Chapter 7 has been submitted for publication.

- **Z. Abedi**, J. Cui, W. Cehn and D.G. Ivey, “Efficient Low Temperature Performance of All Solid-State Zinc-air Batteries with $MnCo_2O_4$/Carbon Fiber Bifunctional Electrocatalyst and Poly(acrylic Acid) (PAA) Polymer Electrolyte” *Batteries and Supercaps.*, 2022.

In addition to the above publications, I also contributed to a number of publications for my groups members and other colleagues at University of Alberta:

1. Y. He, **Z. Abedi**, C. Ni, S. Milliken, K.M. O’Connor, D.G. Ivey and J.G.C. Veinot, “CoNi Nanoparticle-Decorated ZIF-67-Derived Hollow Carbon Cubes as a Bifunctional Electrocatalyst for Zn–Air Batteries”, *ACS Appl. Nano Mater.*, 2022, vol. 5, p. 12496.

2. D. Leistenschneider, **Z. Abedi**, W. Chen and D.G. Ivey, "Facile Dip Coating of Asphaltenes-based Carbon Fibers with V_2O_5 for Supercapacitor Application", *Energy Fuels*, 2022, vol. 36, p. 3328.
3. A. McDougal, **Z. Abedi** and D.G. Ivey, "Tri- and Tetra-metallic Oxides Anchored to Nitrogen-doped Carbon Nanotubes as Bifunctional Electrocatalysts for Rechargeable Zinc-air Batteries", *J. Appl. Electrochem.*, 2021, vol 52, p. 437.
4. D. Leistenschneider, P. Zuo, Y. Kim, **Z. Abedi** , D.G. Ivey , A.D. Klerk, X. Zhang and W. Chen, "A Mechanism Study of Acid-assisted Oxidative Stabilization of Asphaltene-derived Carbon Fibers", *Carbon Trends*, 2021, vol. 5, p. 100090.
5. P. Zuo, D. Leistenschneider, Y. Kim, **Z. Abedi**, D.G. Ivey, X. Zhang and W. Chen, "Asphaltene Thermal Treatment and Optimization of Oxidation Conditions of Low-cost Asphaltene-derived Carbon Fibers", *J. Ind. Eng. Chem.*, 2021, vol. 104, p. 427.
6. M. Labbe, M.P. Clark, **Z. Abedi**, A. He, K.C. Cadien and D.G. Ivey, "Atomic Layer Deposition of Iron Oxide on a Porous Carbon Substrate via Ethylferrocene and an Oxygen Plasma', *Surf. Coatings Technol.*, 2021, vol. 421, p. 127390.

My contributions in publication (1) included electrochemical tests and interpretation of the tests results. In addition, all the electrodes and cells in this study were prepared and assembled by me. My contributions to publication (2) were performing characterization, like scanning/transmision electron microscopy (SEM/TEM), and analysis of the data and interpretation of the electrochemical test results. My contribution to paper (3) included performing SEM and TEM in addition to helping with electrochemical tests. My contributions to papers (4), (5) and (6) were very similar. I performed SEM and helped with electrochemical tests/analysis.

Dedication

This Thesis is dedicated to Iran's modern uprising (2022) and the terroristic attack in Sharif University of Technology (October 03, 2022) on the innocent students and professors and those, whose lives were taken in the right path.

In memory of Navid Afkari, Mahsa Amini, Nika Shakarami and many others!

Woman

Life

Freedom

Acknowledgements

I am genuinly grateful to my supervisors, Dr. Douglas G. Ivey and Dr. Weixing Chen for all of their support during my time at University of Alberta and for allowing and guiding me to explore subjects that I was interested in, during my Ph.D. studies.

Dr. Ivey has been supporting me, guiding me and teaching me since the first day we met. He has always been there for me during difficult times. I would not be able to start/complete my Ph.D. studies if he did not believe in me and take me out of my darkest days, 5 years ago. Dr. Ivey has always been a great example for me and many others. His endless knowledge, work ethic, patience and rationality make him a great professor and a role model. I am always trying to apply everything that I have learnt from him, to my own life. I hope one day I can become a similar person to him and inspire and teach those around me. I will always remember you and what I have learnt from you, Dr. Ivey.

I would like to show my appreciation for all the help from Lily Laser, Dr. Vinay Prasad, Nora Lambrecht, FGSR, Umbuds and our department at UoA in 2019, regarding the obstacle in the way of my studies. I want you to know that your help had such a significant effect on my studies.

I am also very thankful to my fellow graduate students and post doctoral fellows at UoA who have helped me, in any ways, throughout my Ph.D. studies. Desirée Leistenschneider, Peiyuan Zuo, Wendy Tran, Yingjie (Jay) He, Alexandra McDougal, Matthew Labbe, Jiayao (Mark) Cui, Qingping (Ken) Hou and Hang Hu: thank you all for all of your help.

Thank you to my fiance' and former colleague, Dr. Michael P. Clark, for all of your endless love, support and patience. Thank you for the guidance that you continuously provided for me based

on your strong knowledge during my studies and all the proof readings. You are one of the greatest engineers I have met. I am excited for our future together.

Thank you Anqiang He, Shihong Xu, Peng Li, Shiraz Merali and Nathan Gerein for your help with sample characterization and all the training.

Mom and dad, thank you for raising me the best way you could. Maman Simin, you are the freeest woman. You have tought me it is never too late to change a bad thing. You can always count on me. Dad, thank you for all your guidance and for working so hard to give me every opportunity I could wish for. Mohammad, I was the happiest 8 years old girl when you were born. I am proud of you as my brother and I hope you grow to be the best version of yourself. Fatemeh, when you were born, I was extremely happy to have a little sister. I have always felt close to you. I am happy to see you grow up and I am very proud when I see you make smart decisions. I love all four of you endlessly.

I also am grateful Patrick, Rita, Chris and Ben Clark, My fiance's parents and brothers. Thank you for being my second family and always being there for us.

I am grateful for research funding provided by the Natural Sciences and Engineering Research Council of Canada (NSERC) and Alberta Innovates. I am also thankful for travel funding provided by the Faculty of Graduate Studies and Research (FGSR) and the Graduate Students Association (GSA).

Table of Contents

List of Figures

List of Tables

Chapter 1: Introduction

The effects of the greenhouse gases from fossil fuels on the earth's climate have become significantly apparent in recent decades. This has necessitated the search for alternative methods of energy generation, conversion and storage. Renewable energy sources like wind and solar technologies have been growing and improving rapidly and have become the one of the lowest cost source of power in most parts of the world. However, the intermittent nature of wind and solar power remains an issue as power on demand cannot be provided by these technologies. Energy storage devices, like batteries and capacitors, are able to store the energy generated by wind and solar during periods of high generation. This energy can then be released when in demand. Cost-effective, safe, efficient and durable grid-scale energy storage devices are crucial for a renewable energy economy. [1,2]

Capacitors are high power energy storage devices. Their versatility, safety and low cost make them an appealing grid-scale energy storage option. The main components of a capacitor are two electrodes and an electrolyte. Supercapacitors are advanced versions of traditional dielectric capacitors that can achieve higher capacitance values. Electrochemical double layer supercapacitors (EDLSs) and Faradaic capacitors (pseudocapacitors) are the two types of supercapacitors. EDLSs store the energy, electrostatically, in their electrodes without any contribution from electrochemical reactions, while pseudocapacitors take advantage of Faradaic reactions (electrochemical) to store energy. The electrode material in pseudocapacitors often benefits from high specific surface areas (SSAs) compared with dielectric capacitors. The charge storage/release reactions in all capacitors benefit from fast reaction rates, which lead to fast charge/discharge. This provides high power outputs for capacitors and supercapacitors. Supercapacitors are often used to store the energy from wind technology. Supercapacitors are

also used in vehicles to respond during power demand spikes, in smartphones to extend battery life, in transportation applications like braking recuperation systems and in computers as internal back-up power. [3,4]

Batteries are another category of energy storage devices that have been used in grid-scale applications due to their versatility. Many types of batteries are commercially available with varying chemistry, energy and power density, safety issues, cycling behavior and cost. Compared to supercapacitors, batteries have higher energy density and lower power density values. This is due to the nature of the charge/discharge reactions and the electrode active material. Similar to pseudocapacitors, batteries use Faradaic reactions in order to store energy. The Faradaic reactions in pseudocapacitors occur at the surface of the electrodes (fast with no need for deep penetration of the electrolyte). However, in batteries, Faradaic reactions take place throughout the whole electrode and not just the surface, since the electrolyte needs to penetrate inside the electrodes. This results in slower charge/discharge reactions (lower power density) and higher energy density (throughout the whole electrode) in batteries compared with supercapacitors. [5,6]

Batteries suffer from lower efficiencies and cycle life compared with supercapacitors. This is due to the chemistry of the reactions taking place in the electrodes that can cause electrode/cell degradation. Table 1.1 compares a few battery and supercapacitor technologies. [1,5–7] For grid-scale applications, the most important design criteria are safety, cost, cycle life and energy density. Table 1.1 also shows that some mature battery technologies, like lead-acid batteries, are not suitable for grid-scale applications as they were developed for use in portable applications. Lead-acid batteries were invented in 1859 but their low energy density, short cycle life and low depth of discharge make them impractical for grid-scale energy storage. [1]

Table 1.1. Comparison of various energy storage devices

Device	**Power density ($W\ kg^{-1}$)**	**Energy density ($Wh\ kg^{-1}$)**	**Cycle life (Cycles)**	**Efficiency (%)**	**Cost ($\$\ kWh^{-1}$)**
Supercapacitors	>4000	1-5	>100,000	90-100	300-20,000
Pb-acid batteries	200-400	30-50	2000-4500	70-90	120-150
Redox-flow batteries	100	30-50	>12000	60-85	150-1000
Li-ion batteries	315	155	>1200	80-90	250-350
Zn-air batteries	105	230	100-300	50-65	90-120

The electrode material in energy storage devices is one of the key factors that affects the device performance in all aspects. High electrical conductivity, good stability (thermally and chemically), ease of handling, safety, cost-effectiveness and good performance are the main requirements for the electrode material. Carbonaceous materials have been investigated for use as the electrode material in energy storage devices due to the appealing properties of carbon. Asphaltene is a by-product of the oil sands industry in Canada, with much higher supply than demand. Current applications of asphaltene include road and roof making and waterproofing. Asphaltene benefits from a high carbon content which makes it a promising precursor for the electrode material in energy storage devices. Approximately, 260,000 m^3 of bitumen are produced in Alberta, Canada, every day. About 20% of this bitumen consists of asphaltene; asphaltene is the heaviest and the most polar fraction of oil sands bitumen. [8] Asphaltene increases the viscosity of bitumen significantly, which makes transport of bitumen via pipelines

difficult. Therefore, asphaltene is removed from bitumen during the bitumen extraction process. [8,9]

Carbonaceous materials like carbon fibers, nanotubes and graphene have been used as the electrode material in EDLSs. Often, chemical treatment of the precursor is required to increase the SSA and introduce porosity into the microstructure (activated carbon). It is believed that the capacitive behavior of EDLSs improves as the SSA and porosity of the electrode material increase. Carbon based materials can also be coupled with other active materials like transition metal oxides (TMOs) for use as the electrode material in pseudocapacitors. For example, birnessite type MnO_2 is an active material that is capable of intercalating the species in the electrolyte and storing energy. However, TMOs suffer from low electrical conductivity due to their insulating nature. Coupling TMOs with carbonaceous materials can improve the electrical conductivity and the capacitive performance. [3,4,9]

Secondary Zn-air batteries (ZABs) are rechargeable versions of primary ZABs with the ability to recharge and reuse. A typical ZAB includes a metallic Zn electrode, an air electrode which is often carbon based and an alkaline electrolyte. Zinc-air batteries benefit from high energy densities (Table 1.1), while their main issues are low battery efficiency and cycle life caused by the sluggish reaction kinetics taking place at the air electrode. The oxygen reduction reaction (ORR) and oxygen evolution reaction (OER) occur during discharge and charge at the air electrode, respectively. The use of an effective electrocatalyst in the air electrode is crucial to improve the kinetics of ORR/OER and battery performance. Precious metals like Pt and Ru, have conventionally been used as the electrocatalyst in ZABs. However, these materials are costly, rare and may suffer from unstable battery performance. TMOs show promising catalytic activity

towards ORR/OER in ZABs. Similar to pseudocapacitors, carbon based materials like carbon nanotubes and fibers can be coupled with TMOs to further improve battery performance. [10]

The purpose of this work was to develop and investigate the use of asphaltene based carbon fibers as the electrode material in EDLSs, pseudocapacitors and Zn-air batteries. Chapter 2 of this work presents a literature review, summarizing the recent literature and background information about EDLSs, pseudocapacitors, ZABs and characterization techniques. Chapters 3-7 include the results of my Ph.D. research that were published as journal articles. Conclusions and recommendations for future work are presented in Chapter 8.

Chapter 2: Literature Review

2.1 Electrochemical Energy Storage Devices

New energy storage technologies are potential solutions to the need to decrease the world's dependence on fossil fuels, due to environmental problems and global warming. Many renewable energy sources like solar or wind do not provide energy on demand; this necessitates the ability to store the energy when available (the wind is blowing or the sun is shining) and utilize this energy when needed. Electrochemical energy storage devices have been proven to be effective options for grid scale energy storage. Based on the type of mechanism used to store energy and the electrode material, energy storage devices can be divided into different categories, i.e., fuel cells, batteries, capacitors and electrochemical supercapacitors. Among the various energy storage devices, batteries and electrochemical supercapacitors (electrochemical double layer supercapacitors and Faradaic supercapacitors) have played important roles in both industry and academia. Also, apart from grid scale storage, electrochemical energy storage development is largely driven by consumer electronics such as mobile phones and hybrid/electric vehicles. [6,11]

2.1.1 Batteries

Batteries store energy due to Faradaic processes and usually exhibit high energy densities. [12] However, the kinetics of the chemical reactions limit the rate at which energy can be provided, which usually leads to low power densities. [13,14] These devices store and release charge throughout the bulk of the electrode material. The resulting thermal and mechanical stresses in the electrodes and electrolyte (liquid, gel, or solid) are principal causes of degradation in batteries and their lower cycle lives compared with supercapacitors. Electrochemical double layer supercapacitors are stable up to thousands and even tens of thousands of cycles. [15,16]

Figure 2.1 shows a Ragone plot that compares different energy storage devices in terms of energy and power outputs. [17] Batteries (bottom-right) can provide high energy densities, although they may suffer from low power densities. On the other hand, capacitors and supercapacitors (top-left) deliver lower energy densities than those for batteries in shorter times that result in higher power densities. [9]

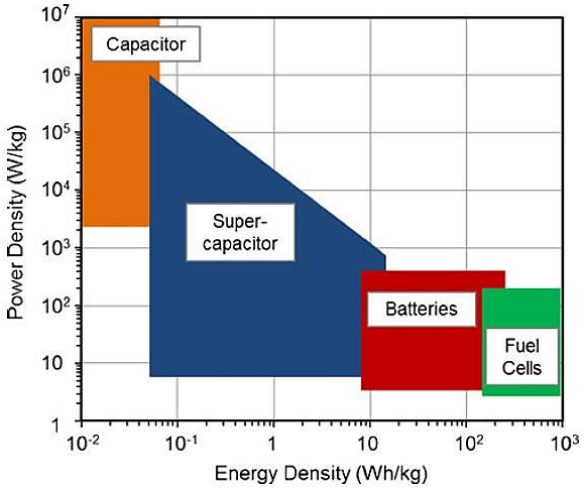

Figure 2.1. Ragone plot showing power density vs. energy density for different energy storage devices. [17]

2.1.1.1 Metal-air Batteries

One important performance metric for many battery applications is specific energy (in Wh kg^{-1}) or energy density (in Wh cm^{-3}). The theoretical energy values for metal-air batteries are exceptional, due to their use of ambient air as the reactant during the discharging process. This eliminates the need for an on-board oxygen source; i.e., in metal-oxygen batteries. Metal-air batteries usually consist of a metallic electrode and an air electrode which is often carbon based. Zn, Li, Al, Mg and Fe are examples of metals used in metal-air batteries. Figure 2.2 represents a comparison of practical and theoretical energy densities for various batteries, H_2-air fuel cells

and gasoline. Comparison of metal-air batteries suggests that Li-, Mg- and Al-air technologies can outperform Zn-air; however, there are many serious issues affecting the development of these batteries. Mg and Al suffer from severe corrosion in aqueous electrolytes, even though it is possible to operate Mg- and Al-air batteries. Li-air batteries need to be operated in non-aqueous electrolytes (e.g., organic); these electrolytes are often costly and unsafe. [12,18]

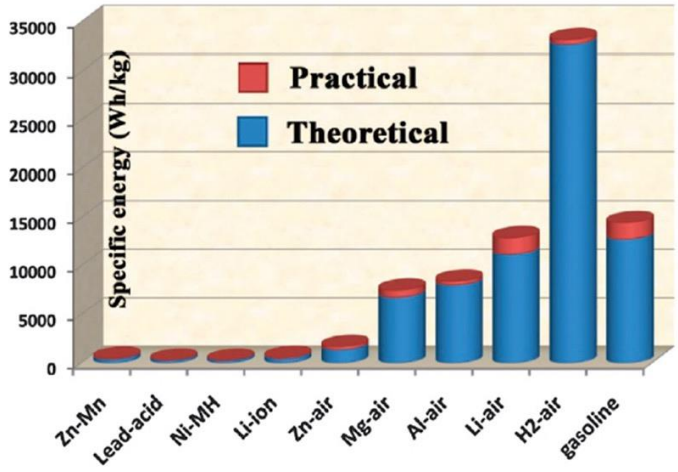

Figure 2.2. Comparison of energy densities of some representative types of batteries alongside gasoline and H_2-air fuel cells. [19]

2.1.1.1.1 Zinc-air Batteries

Zinc-air batteries (ZABs) are attractive electrochemical energy storage devices due to their high specific energy, low cost, safe operation, ease of preparation and handling, abundance of raw materials and environmental compatibility. There are three types of ZABs: 1) primary, 2) secondary (also called rechargeable) and 3) mechanically rechargeable. Primary ZABs have been developed and used for many years as hearing-aid batteries; primary ZABs are non-rechargeable. Rechargeable ZABs are under development to improve the discharge/charge efficiency and cycling behavior. Companies like Fluidic Energy, Eos Energy Enterprises and Revolt have begun

commercialization of rechargeable ZABs. The third type is recharged by physically replacing the used Zn and electrolyte. [1,20–22]

2.1.1.1.1.1 Cell Design and Energy Storage Mechanism for Zinc-air Batteries

A ZAB usually contains three main components: a metallic Zn electrode in the form of a plate, a porous air electrode and an electrolyte. A typical ZAB is schematically shown in Figure 2.3. To prevent hydrogen evolution, which is a parasitic reaction that may occur, and Zn corrosion, electrolytes used in ZABs are highly alkaline. One common electrolyte is 6 M KOH + 0.25 M ZnO. Not all ZABs require a separator; however, a separator may facilitate the transport of hydroxide ions (OH^-). [18,23]

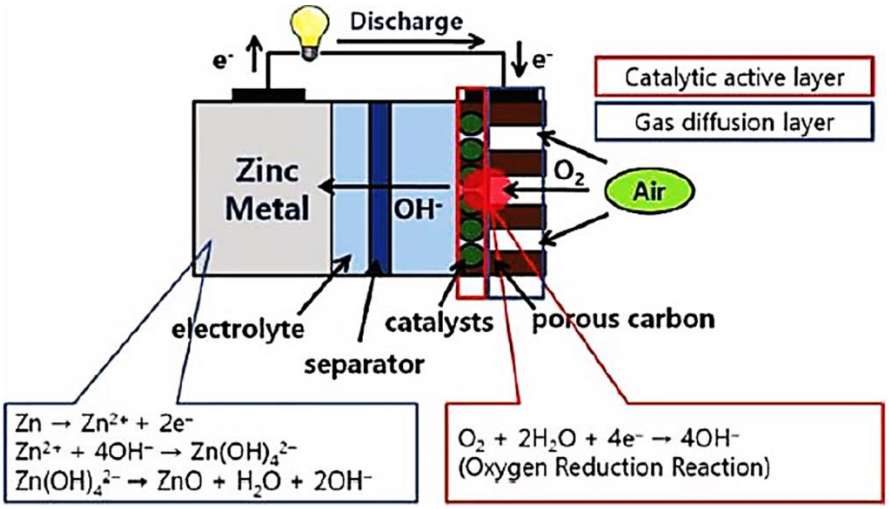

Figure 2.3. Schematic of a typical ZAB cell. [18]

The capacity of a ZAB is entirely determined by the Zn electrode as it utilizes oxygen from ambient air which is available in any amount needed. A simple Zn plate or foil, which is commonly used as the Zn electrode, has a limited surface area. Sponges, powder, fibers and composites can provide higher surface areas; they are alternatives to Zn plates or foils. As the battery discharges, a layer of ZnO starts to form on the surface of the Zn electrode until it

reaches complete passivation; at this point, the battery is fully discharged. Zn dissolves during discharge (Zn^{2+}) and is redeposited during charge. Equations 2.1-2.3 show the reactions that take place at the Zn electrode during discharge. E^0 is the standard potential. [22,24]

$$Zn \rightarrow Zn^{2+} + 2e^- \quad (2.1)$$

$$Zn + 4OH^- \rightarrow Zn(OH)_4^{2-} \quad E^0 = -1.25 \text{ V vs. SHE} \quad (2.2)$$

$$Zn(OH)_4^{2-} \rightarrow ZnO + H_2O + 4OH^- \quad (2.3)$$

The air electrode material is not consumed during charge or discharge. The oxygen reduction reaction (ORR) and oxygen evolution reaction (OER) take place at the surface of the air electrode during discharge and charge, respectively. ORR is presented as Equation 2.4 from left to right and OER is Equation 2.4 from right to left. The overall discharge reaction in a ZAB is given by Equation 2.5. [25,26]

$$O_2 + H_2O + 4e^- \xrightarrow{\text{Discharge}} 4OH^- \quad E^0 = 0.401 \text{ V vs. SHE} \quad (2.4)$$

$$2Zn + 2O_2 \rightarrow 2ZnO \quad E^0 = 1.65 \text{ V} \quad (2.5)$$

ORR and OER suffer from slow kinetics, which necessitates the use of effective electrocatalysts. The electrocatalyst is a major component of the air electrode; it is not consumed during charge/discharge and only enhances the kinetics of ORR/OER. [12]

Figure 2.4 schematically depicts the polarization curves for the Zn (anodic reaction during discharge) and air electrode (cathodic reaction during discharge) reactions. The standard

potential for the anodic and cathodic reactions are -1.25 V and +0.40 V vs. SHE, respectively. This results in a total theoretical cell potential of 1.65 V (discharge). However, the sluggish kinetics of ORR reduces the potential in order to produce sufficient current. ZABs usually operate with a cell voltage < 1.2 V. Kinetic limitations also affect the charge cycle as OER requires a large over potential before reaching appreciable current values. The electrocatalyst is the critical component of the air electrode that reduces the overpotential of the air reactions. Depending on the current density, a ZAB can have a voltage efficiency of 30-60% without electrocatalysts and 50-80% with effective electrocatalysts. Voltage efficiency is defined as $(E_{discharge}\ E_{discharge}^{-1})\times 100$. [12,27]

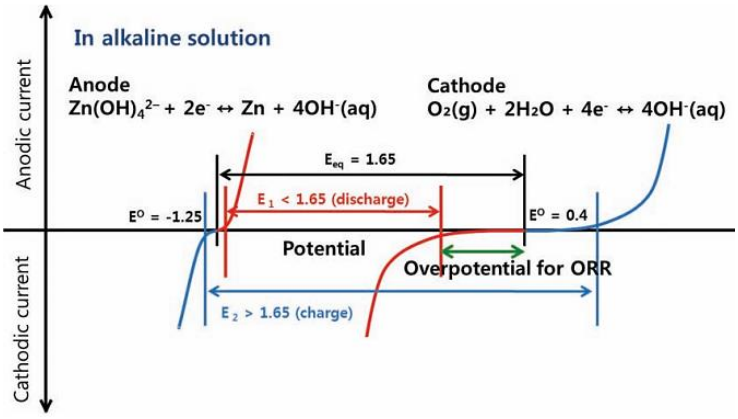

Figure 2.4. Polarization curve for Zn and air electrodes in ZABs. [18]

The performance of a ZAB is significantly affected by the design and structure of the air electrode. The air electrode is sometimes referred to as the gas diffusion layer (GDL) as well. ORR takes place at three phase boundaries amongst air (O_2), electrolyte and electrocatalyst. The air electrode must be highly porous and the electrocatalyst must be well dispersed throughout the air electrode in order to maximize the three phase boundary area and allow gas diffusion. Effective electrocatalyst dispersion is often an issue as most electrocatalyst preparation

techniques like electrodeposition and spray coating can only decorate the surface of the air electrode. Electrical conductivity is another important factor regarding the design of the air electrode. Some electrocatalysts like metal oxides are electrically insulating. Limited electrical conductivity negatively affects the performance of the air electrode and may even cause larger overpotentials. Another important factor in terms of air electrode design is the stability of the air electrode material within the wide potential window of discharge and charge reactions and in the harsh alkaline electrolyte. High surface area carbon is often used in the air electrode and is susceptible to corrosion under these conditions. Carbon corrosion can be reduced or controlled by using graphitic carbon, which is more resistant to corrosion compared with amorphous carbon, or by coating the surface of the carbon with a non-carbonaceous electrocatalyst. The back side of the air electrode that faces ambient air must be completely hydrophobic to prevent electrolyte leakage (also called flooding). Polytetrafluoroethylene (PTFE) can be used for this purpose. [12,28,29]

2.1.1.1.1.2 Materials for the Air Electrode

An effective electrocatalyst for use in ZABs must be sufficiently active towards ORR or OER (or both), cost-effective, stable, safe and abundant. The effectiveness of the electrocatalyst is determined based on the voltage efficiency and performance stability of the battery. Many electrocatalysts do not have stable performance in the harsh alkaline electrolyte and/or the voltage operation window. Performance stability, mostly defined by the electrocatalyst, limits the cycle life of ZABs. Voltage efficiency and performance stability are the main challenges for ZAB development. Rare earth metals and/or their oxides, transition metal oxides (TMOs), carbon based materials and metal organic frameworks (MOFs) are the main electrocatalyst categories. [30–32]

Precious Metals

Precious metals and/or their oxides have traditionally been used as effective electrocatalysts for ORR and OER with reasonable stabilities. For example, Pt and RuO_2 have excellent catalytic activity towards ORR and OER, respectively. However, high cost, scarcity and unstable battery cycling behavior (mostly for Pt) of noble metals make them unrealistic for widespread applications. Other effective electrocatalysts with better or comparable electrocatalytic activities have been developed as alternatives to noble metals. [12,19]

Transition Metal Oxides

Transition metal oxides are promising alternatives to noble metals as ORR/OER electrocatalysts due to their low cost, abundance, catalytic activity, environmental friendliness and ease of handling and preparation. In addition, most TMOs are stable in harsh alkaline environments which makes them attractive for use in ZABs. The main issue regarding the use of TMOs in ZABs is their poor electrical conductivity. Researchers have been trying to address this issue by developing TMO based composite electrocatalysts that take advantage of the benefits of excellent electrical conductivity of carbon based materials or metals. The most common TMOs used in ZABs are MnO_x, CoO_x, NiO_x, FeO_x and transition metal mixed oxides like $MnCo_2O_4$. [2,33]

Carbon Based Materials

Carbon is an attractive material in energy storage devices because of its high electrical conductivity, low-cost, abundance, ease of handling and processing, ability to be operated in wide temperature and voltage ranges and ability to be shaped as desired (e.g., powders, fibers, etc.). The main issue with using carbon in the air electrode of ZABs is carbon corrosion when operated at high voltages (usually charging voltages for OER). If the surface of carbon is covered

with other electrocatalysts like TMOs, corrosion can be reduced significantly. Also, the catalytic performance of carbon based materials can be improved by doping the carbon structure with heteroatoms like S, N, P and B. Doping with heteroatoms alters the electronic structure of C and introduces defects into the microstructure. The defects can provide active sites for O_2 adsorption which facilitates ORR. Nanostructured carbons like carbon nanotubes (CNT) and graphene are the most common types of carbons in ZABs. The electrocatalytic performance of carbon depends on heteroatom doping, porosity and structural defects; these can modify the electronic structure of carbon and improve ORR/OER performance. [11,12,34,35]

Metal Organic Frameworks

Metal organic frameworks (MOFs), also called porous coordination polymers, are composite materials consisting of metal clusters and polymer linkers. The development of MOFs started in early 1990's; since then many different MOF structures have been reported in the literature. MOFs are attractive materials as their structures can be easily modified to achieve desirable properties. For example, in energy storage devices, MOFs are often used as precursors for high surface area materials. One way of preparing a conductive material with a very high surface area is to heat (carbonize) MOFs; this eliminates (carburizes) the organic linkers and leaves behind a porous structure consisting of metal clusters. MOFs have shown superior electrocatalytic activities for use in ZABs. However, MOF-derived electrocatalysts suffer from poor cycling stability especially in harsh alkaline environments due to the dissolution, corrosion and agglomeration of the electrode material. [1,32,36]

2.1.1.1.1.3 Challenges for Rechargeable Zn-air Batteries

Development of rechargeable ZABs faces many challenges like battery efficiency, cycling stability, battery leakage, formation of carbonates on the air electrode and degradation of the Zn and air electrodes during cycling.

The discharge/charge efficiency of a ZAB cell is mostly determined by the structure of the air electrode and the electrocatalyst. The air reactions taking place at the air electrode, i.e., ORR/OER, suffer from poor kinetics and require large overpotentials. An effective electrocatalyst is needed to improve battery efficiency. The electrocatalyst must be cost-effective, have high catalytic activities toward ORR/OER, be safe and have a reasonably simple manufacturing process.[12]

In addition to battery efficiency, the electrocatalyst also plays an important role in determining the cycling life and behavior of the battery. Many electrocatalysts are not stable in harsh alkaline environments and may corrode, dissolve, agglomerate or undergo phase transformations. All of these will negatively affect the battery performance after a few cycles. Therefore, the use of effective and stable electrocatalysts is crucial in terms of ZAB mass production. In some cases, the majority of the air electrode material is the electrocatalyst. If so, degradation of the electrocatalyst changes the structure of the air electrode, negatively affecting battery performance. [10,37]

Battery leakage is an issue for all battery types that involve aqueous electrolytes. In the case of ZABs, since the electrolyte is usually highly alkaline with a pH of 14, electrolyte leakage can cause severe damage of surrounding equipment and cause chemical burns to humans. Furthermore, cell leakage dramatically deteriorates battery performance. Properly sealing the battery can prevent this. Also, the development of gel polymer electrolytes has been very

beneficial to energy storage device technology, including ZABs. Implementing gel polymer electrolytes can prevent battery leakage. [38]

Structural changes to the Zn electrode during cycling is another significant problem facing development of rechargeable ZABs. Zn dissolves during discharge and redeposits during charge. Non-uniform dissolution and deposition of Zn can change the morphology of the Zn electrode. ZnO that forms during discharge can also be deposited on the surface of the Zn electrode and create conductivity inconsistencies on the Zn electrode. The formation of dendrites that occur during electrodeposition of Zn upon charging is another issue. Dendrites can grow large enough to penetrate the separator and cause short circuiting. The use of additives in the electrolyte, separator modifications and AC or pulse charging are potential methods to address the dendrite formation issue. [1]

Atmospheric air contains 0.03 vol% CO_2. Since ZABs utilize atmospheric air as the reactant, CO_2 from the atmosphere can be dissolved in the electrolyte and reduce the electrolyte pH. Dissolved CO_2 can react with the KOH in the electrolyte and form potassium carbonate (K_2CO_3). The formation of carbonate is detrimental to the ZAB performance as it may clog the surface and the porosity of the air electrode. [12,21]

2.1.2 Electrochemical Supercapacitors

Electrochemical supercapacitors (ESs) are interesting energy storage devices because of their high power densities, long life time and wide operating temperatures. [9,39] The power densities that they provide lie between batteries and traditional dielectric capacitors. Traditional dielectric capacitors provide significant power densities. [40] ESs can be employed to improve battery performance in terms of power density and improve dielectric capacitor performance in terms of energy density. [41] The earliest ES patent was filed in 1957. However, not until the 1990s when

it was discovered that ESs can be used to boost batteries or fuel cells in hybrid electric vehicles, did ES technology attract significant investment worldwide. [40]

Figure 2.5 introduces the different components in a typical ES. An ES is composed of two electrodes (usually with high surface area), one separator (to isolate the electrodes and prevent short circuits) and an electrically conductive electrolyte. ESs are similar to batteries in terms of design and manufacturing. [24,40]

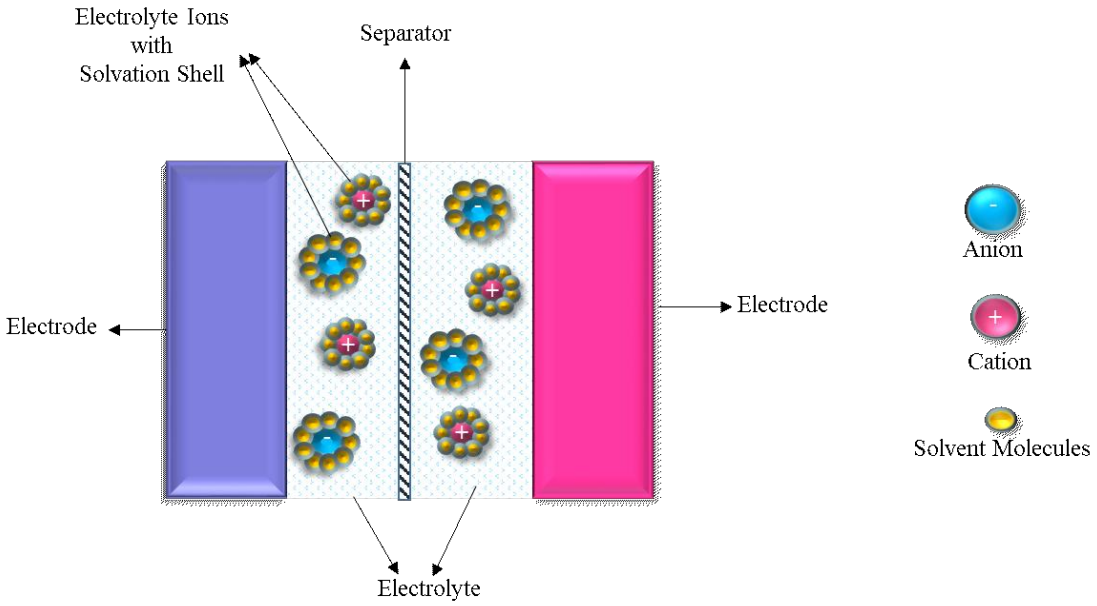

Figure 2.5. Schematic of a typical electrochemical supercapacitor.

There are two main types of ESs, electrochemical double layer supercapacitors (EDLSs or EDLCs) and Faradaic supercapacitors (FSs or pseudocapacitors). The former operates by charging and discharging of the interfacial electrical double layer and charge is physically stored on the surface of the electrodes without any electrochemical reaction. No charge transfer takes place across the interface and the current generated during this process is essentially a displacement current produced by the rearrangement of charges. In the latter, the charge –

discharge mechanism involves Faradaic reactions and there is electrical charge transfer between phases. [42]

2.1.2.1 Electrochemical Double Layer Supercapacitors

Electrochemical double layer supercapacitors (EDLSs) store charge physically on the surface of the electrodes without any contribution from electrochemical reactions. [23] An EDLS uses an electrolyte so there are mobile charge carriers between the electrodes. [15] If a voltage is applied, these charge carriers will be stored at the surface of the positively and negatively charged electrodes, inside the Helmholtz layer, producing current. [43] A schematic of charge carrier species (ions) arrangement on the surface of electrodes in an EDLS is shown in Figure 2.6 (a). Ions in the electrolyte are surrounded by solvent molecules (hydrated). When a negative voltage is applied to the electrode, there is a very thin layer of solvent molecules and adsorbed anions at the surface of electrode, called the inner Helmholtz layer. The region in which the (hydrated) cations are adsorbed is called the outer Helmholtz layer. The inner and outer Helmholtz layers together are called the Helmholtz layer. The region where ions are randomly moving and are not under the force of the negative electrode is called the diffuse layer. Ions are strongly adsorbed on the electrode surface in the Helmholtz layer, whereas in the diffuse layer a homogeneous distribution of the ions exists. [44] Figure 2.6(b) represents the structure of the electrochemical double layer as well as the charge carrier species arrangement under an applied voltage.

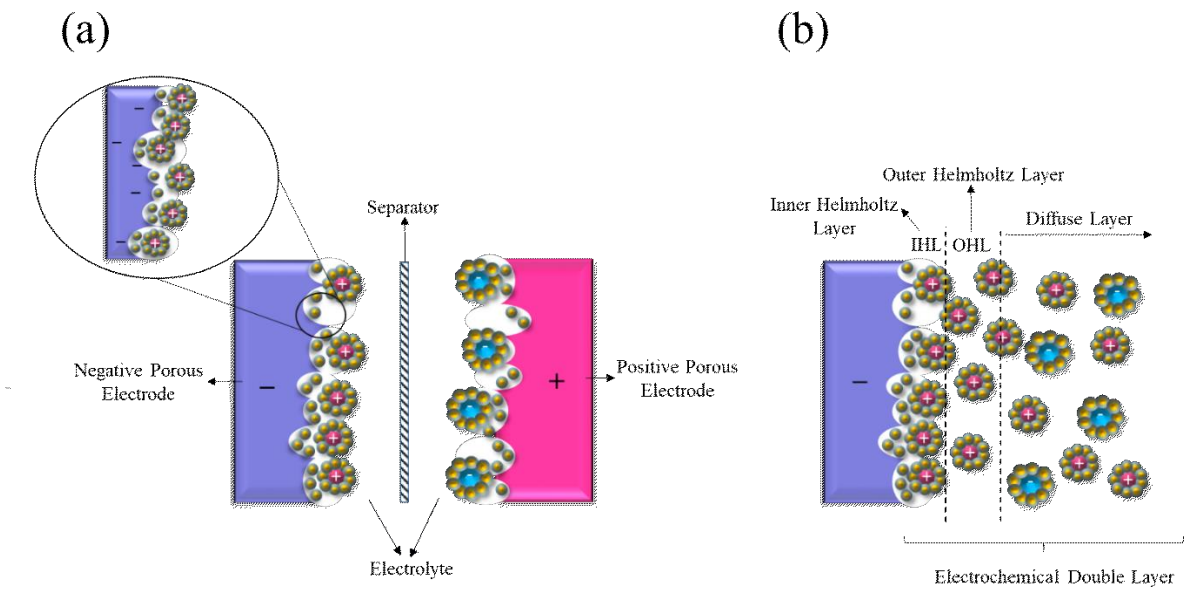

Figure 2.6. Schematic of (a) charge carrier species (ions) arrangement on the surface of electrodes and (b) the structure of the electrochemical double layer and the charge carrier species arrangement when a voltage is applied.

2.1.1.1.1 Energy Storage Mechanism of EDLSs

The electrochemical processes for an EDLS can be written as the following [45]:

Positive electrode:

$$S_{positive} + A^- \xrightarrow{\text{Charge}} S^+ // A^- + e^- \quad (2.6)$$

Negative electrode:

$$S_{negative} + C^+ + e^- \xrightarrow{\text{Charge}} S^- // C^+ \quad (2.7)$$

Overall reaction:

$$S_{positive} + S_{negative} + C^+ + A^- \xrightarrow{\text{Charge}} S^+//A^- + S^-//C^+ \quad (2.8)$$

$S_{positive}$, $S_{negative}$, //, A^- and C^+ represent the positive electrode surface, the negative electrode surface, the double layer, anions and cations, respectively. Discharge processes occur in the opposite direction as written above. [45] According to Equations 2.6-2.8, the charge and discharge processes take place without any contribution from electrochemical reactions. Instead, these processes occur through physical adsorption and desorption of solvated ions at the surface of the electrodes.

The capacitance of a supercapacitor depends on the active sites available for the charge carriers to be stored. Materials with larger specific surface areas and porosities can store more charge carriers on their surfaces, which lead to higher capacitances. [46–48] Highly porous materials that have a pore distribution consisting of micropores (pores less than 2 nm in diameter), mesopores (pore diameter of 2-50 nm) and macropores (pores larger than 50 nm in diameter) exhibit excellent electrochemical properties and are, thus, desirable electrode materials in EDLSs. [3,16,49,50] The average pore size, as well as the interconnectivity of pores, are both important factors in a porous electrode material. Ion transport is much faster in a porous medium with interconnected pores. [50] Also, for a given surface area, a material with an average pore size less than 1 nm exhibits very high capacitance. [51] Figure 2.7 shows the change in the specific capacitance (normalized by the electrode mass) as a function average pore size. Regions I and II correspond to microporous materials with average pore sizes less than 2 nm and region III represents mesoporous materials with an average pore size larger than 2 nm. In region II, the capacitance increases sharply with decreasing average pore size. This is due to distortion of the double layer in the small pores and a decrease in the thickness of the double layer. In region III,

an increase in the specific capacitance is due to better accessibility of the pores. [52] Pores smaller than 0.5 nm affect accessibility of the pores to the electrolyte ions and impact ion transport, decreasing performance. Fabricating large micropores leads to loss of material. For a given total pore volume, a material with smaller average pore size has higher surface area which leads to an increase in the capacitance.

Figure 2.7. Plot of specific capacitance, normalized by the total mass of the electrode material, vs. average pore diameter.

Equation 2.9 shows that at a given voltage (V in volts (V)) the capacitance (C in farads (F)) of a capacitor will increase if the amount of charge (Q in coulombs (C)) stored at the surface of the electrodes increases. The amount of charge stored at the surface of electrodes increases by increasing the specific surface area of the electrode material. [53,54]

$$C = \frac{Q}{V} \tag{2.9}$$

The same equation can be used for EDLSs and FSs or any energy storage device. Similar to EDLSs, FSs and batteries benefit from double layer capacitance and energy in addition to the energy provided by the Faradaic reactions taking place in the system, but to a smaller extent. In reality the capacitance of an EDLS does not necessarily change linearly with surface area (because not all the surface area is accessible to the electrolyte); however, increasing the surface area of the electrode material will still likely increase the capacitance. [55]

2.1.1.1.2 Materials for EDLS Electrodes

Different chemical and physical methods have been studied to develop nanostructured materials with high specific surface area for energy storage applications. [56] The most important material used in energy storage devices is carbon due to its chemical and thermal stability, low cost, high electrical conductivity, stability in harsh electrolytes, non-toxicity, ability to operate in a wide range of temperatures and ease of handling. [9,14,57] Carbon materials are also easy to modify to achieve a desirable active material. [58] Carbon is widely used in making electrodes for EDLSs, so that EDLSs are often referred to as carbon supercapacitors. Among all the carbon based materials that have been used as electrode active materials, e.g., graphene [59], carbon nanotubes [60], carbide – derived carbons and template carbon nanostructures [14], activated carbon (AC) [14] is the most widely used as a high electrochemically available surface area material (the surface area that is available to the electrolyte). [58]

AC is usually derived from carbonaceous materials (natural or waste hydrocarbon precursors) using chemical or physical steps and exhibits large specific surface areas as high as 3000 $m^2\ g^{-1}$. [9,55] The specific capacitance of AC electrodes in EDLSs can reach as high as a few hundreds of F g^{-1}. Additionally, AC is usually in the shape of fibers or powder. [61,62]

2.1.2.2 Faradaic Supercapacitors or Pseudocapacitors

As explained above, an EDLS stores charge electrostatically, while the charge storage mechanism of a Faradaic supercapacitor (FS) is mainly based on Faradaic reactions that take place at the electrolyte/electrode interface. [7,63] Faradaic reactions can be divided into three categories: redox reactions, ion intercalation into the lattice structure and adsorption/desorption of ions. [5,40,64] In FSs, the charge is stored through Faradaic reactions which can be time consuming with slow reaction rates. [3,39] This leads to lower power densities than those of EDLSs. Also in FSs, there may be structural damage to the electrode and concentration changes in the electrolyte due to the Faradaic reactions; this can result in poor cycling stability. [64] However, Faradaic reactions may yield higher specific capacitance and energy values for FSs compared with EDLSs. [6]

2.1.1.1.1 Redox Reactions

Redox reactions are reversible electrochemical reduction (consume electrons) and oxidation (produce electrons) reactions. Consumption or production of electrons and the exchange of protons or cations with the electrolyte, which occurs during redox reactions for many metal oxides and metal hydroxides, is the basic charge storage mechanism of FSs. [65,66] In these reactions, the metal changes its oxidation state, giving high capacitance values to FSs. However, the reactions are typically slow (low power densities) and damaging to the electrodes and the electrolyte (short cycle life). Each redox reaction takes place at a certain voltage and gives rise to the current due to consumption or production of electrons. Equation 2.10 is an example of a redox reaction for manganese oxide, where C^+ is a cation; reduction is from left to right and oxidation is from right to left. [65]

$$MnO_2 + C^+ + e^- \leftrightarrow MnOOC \qquad (2.10)$$

Figure 2.8 represents an example of a cyclic voltammetry (CV) test for a carbon fiber/V_2O_5 pseudocapacitor. CF-V represents the material (carbon fiber-V_2O_5) and 350, 400 and 450 are the heat treatment temperatures. The peaks (change in the current at a certain potential); i.e., E_a (anodic) and E_c (E_1, cathodic), are due to the presence of a redox reaction.

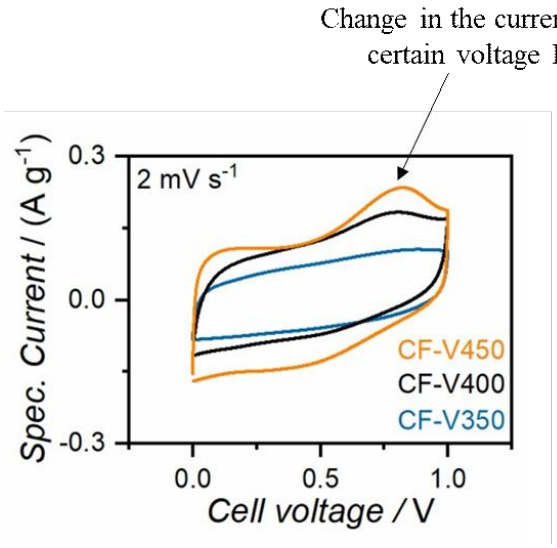

Figure 2.8. Example CV curve of a pseudocapacitor with V_2O_5 as the Faradaic reaction active material. [39]

2.1.1.1.2 Adsorption/desorption

The adsorption/desorption mechanism involves adsorption or desorption of cations onto the surface of the electrodes; e.g., adsorption of H^+ at a Pt or Au surface. This process is called underpotential deposition (UPD). During UPD, a monolayer of an electrochemically active species that can be adsorbed or desorbed quickly is formed on the surface, resulting in capacitive behavior. Due to the absence of diffusion or phase changes, this process is very fast compared with the other forms of Faradaic reactions and does not damage the electrodes. Similar to the charge storage mechanism in EDLSs, the amount of charge stored at the surface depends on the

effective surface area. [1,67] Figure 2.9 schematically represents the adsorption/desorption process on the surface of an electrode in a FS which utilizes MnO_x as the active material.

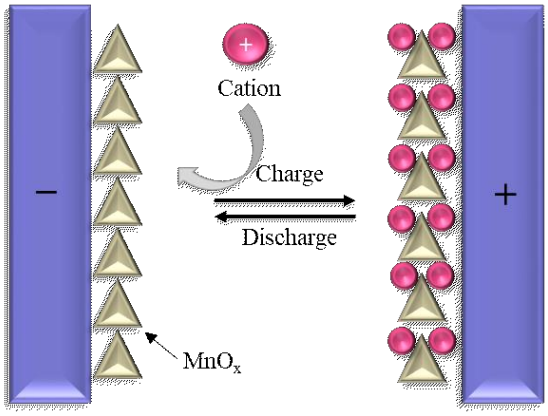

Figure 2.9. Schematic of a pseudocapacitor with MnO_x as the lattice intercalation Faradaic reaction active material.

2.1.1.1.3 Lattice Intercalation

Lattice intercalation of ions is a process similar to UPD with the difference that intercalation occurs in the bulk of the material. [67] As with UPD, intercalation is faster compared with redox reactions. However, intercalation of ions into the crystal structure of the electrode causes strain in the lattice that can lead to mechanical degradation during cycling.

2.1.1.1.4 Materials for FS Electrodes

A material that exhibits one or more of the Faradaic charge storage mechanisms can be employed as the electrode material in a FS. Other factors such as cost, electronic and ionic conductivity and the morphology of the material are also considerations for material selection. Transition metal oxides and conductive polymers are materials that are commonly used in FSs. [40]

Transition Metal Oxides

In addition to storing charge electrostatically in the double layer, transition metal oxides can store charge through Faradaic reactions that introduce high energy densities to FSs. However, due to phase changes and mechanical degradation, these reactions can reduce cycle life. The oxides of many transition metals have been studied; e.g., Mn, Ru, Fe and Co. [5,40]

Mn and Ru oxides are the two most important materials that have been used in FSs. [40] Mn has several oxidation states that allow reversible redox transitions between these states to provide energy storage for Mn oxide pseudocapacitors. [40] The charge storage mechanisms in these pseudocapacitors include electrical double layer, adsorption/desorption of protons and electrolyte cations and mostly redox reactions. An example of a Mn oxide redox reaction is given in Equation 2.11. [68–73]

$$MnO_2 + H^+ + e^- \leftrightarrow MnOOH \quad (2.11)$$

The theoretical capacitance value for MnO_x is ~1300 F g^{-1}. Unfortunately, due to its low electronic conductivity and the slow diffusion rates of protons and cations into the deeper layers of the oxide, practical capacitance values are around 100-300 F g^{-1}. [70] Mn oxide is environmentally friendly, inexpensive and can have a variety of different structures. The structures that are commonly used in electrodes are nanosheets, [74–76], nanowires [77–79] and nanorods. [80,81]

Ru has three stable oxidation states; transitions between these states take place quickly and reversibly. Also, hydrous Ru oxide has good ionic and electronic conductivities. [5,40] Redox transitions in Ru oxide occur according to Equation 2.12. [82]

$$RuO_a(OH)_b + \delta H^+ + \delta e^- \leftrightarrow RuO_{a-\delta}(OH)_{b+\delta} \quad (2.12)$$

The capacitance values of Ru FSs can be as high as 720 F g^{-1}, although the use of Ru in electrochemical applications is limited due to its cost. [41,83] Other examples of electrode materials in electrochemical supercapacitors and their associated capacitance values are illustrated in Figure 2.10.

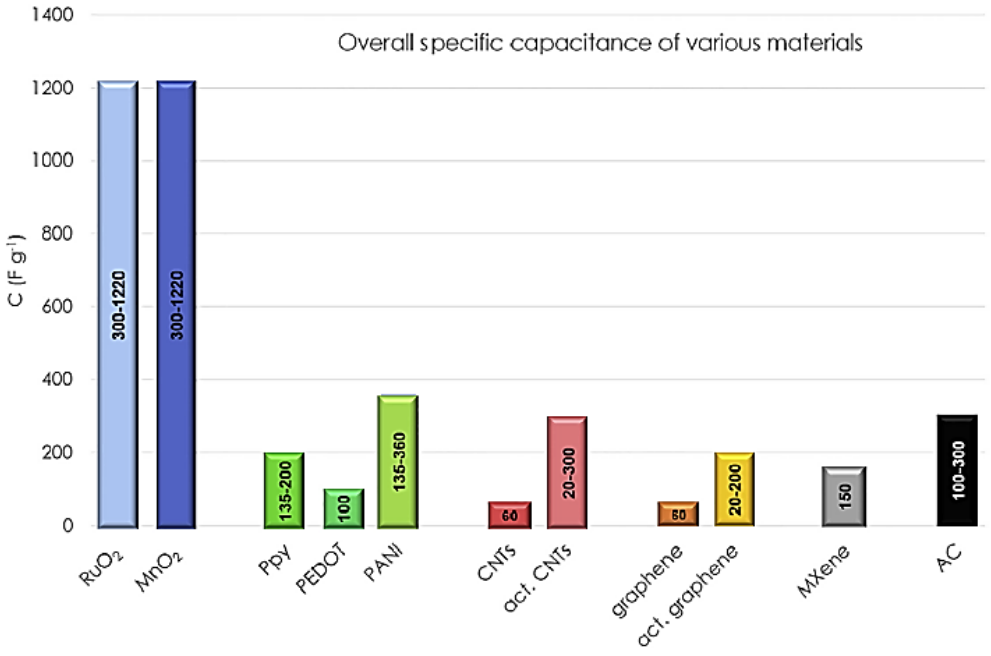

Figure 2.10. Comparison of capacitance values for different electrochemical supercapacitor electrode materials. [58]

EDLSs and FSs can be studied as two dielectric capacitors in series. One capacitor is at the positive electrode surface and electrolyte interface and the other is at the negative electrode surface and electrolyte interface. [84] The actual equivalent electric circuit of a supercapacitor is more complicated than a model consisting of only two dielectric capacitors. A simplified equivalent RC circuit illustration of a single cell supercapacitor (a cell consisting of two electrodes) is shown in Figure 2.11. [85] C_a and C_c represent the capacitance of the anode and

cathode, respectively, R_s is the solution (electrolyte) resistance and R_F is the self-discharge resistance of the electrodes.

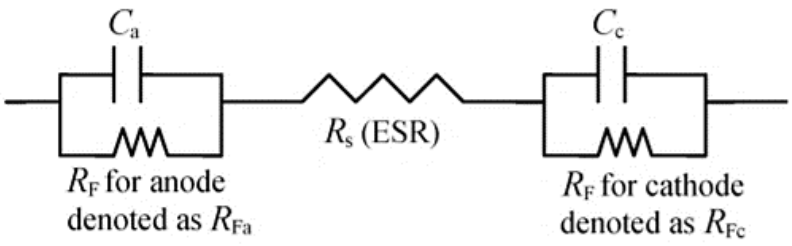

Figure 2.11. A single cell supercapacitor RC equivalent circuit. [85]

Conductive polymers

Conductive polymers (CPs) can be used as electrode materials in pseudocapacitors, where the bulk of the material contributes to the capacitive behavior through fast redox reactions. [86] Their large potential window and conductive nature give them high power capabilities. On the other hand, they suffer from poor cyclability due to swelling during charge and contraction during discharge. [86,87] A few examples of CPs include polyaniline [40,86,88], polypyrole [40,89,90] and PEDOT (poly(3,4-ethylenedioxythiophene)).

2.2 Synthesis of Carbon Fibers for Use in Energy Storage Devices

2.2.1 Oxidation or Stabilization

Carbon fibers can be derived from different melt-spun [91–94] carbonaceous precursors such as asphaltene and pitch. [94,95] After melt spinning the precursor, the fibers are oxidized [96] in an air flow with oxygen to increase the cross-linking of aromatic molecules by removing hydrogen atoms (dehydrogenation). The oxidation temperature range is usually 200-400 ^{o}C. Figure 2.12 shows the possible reactions that peroxyacytyl nitrate (PAN) fibers may go through during oxidation. The side hydrocarbon chains connect with each other via dehydrogenation and form

longer chains. Longer hydrocarbon chains are more stable than the short ones during the next processing steps. [97]

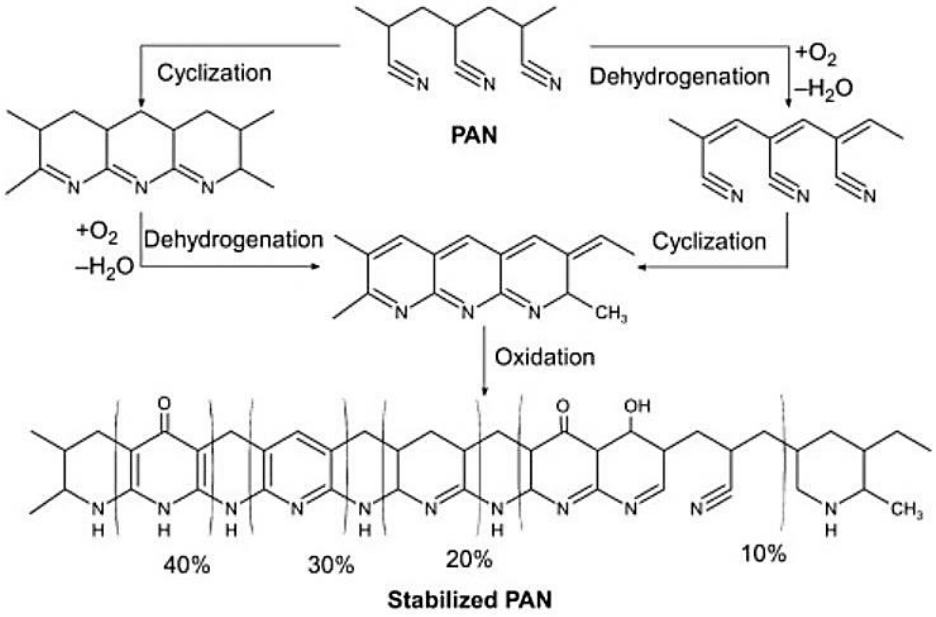

Figure 2.12. Oxidative stablization step for PAN fibers. [98]

2.2.2 Carbonization

At the carbonization temperature, different physiochemical changes such as dehydrogenation, denitrogenation, polymerization and aromatization take place. Carbonization removes inorganic impurities like nitrogen and hydrogen atoms and increases the amount of cross-linking as well as carbon content in the microstructure. Carbonization is done to increase the chemical and thermal stability as well as the conductivity of the fibers. The temperature range in which the carbonization takes place is 500-1000 ^{o}C. Two important reactions that PAN fibers undergo at the carbonization temperature are shown in Figure 2.13. Dehydrogenation and denitrogenation create a more stable carbon structure by removing H_2 and N_2 from the structure and connecting the hydrocarbon chains. [97]

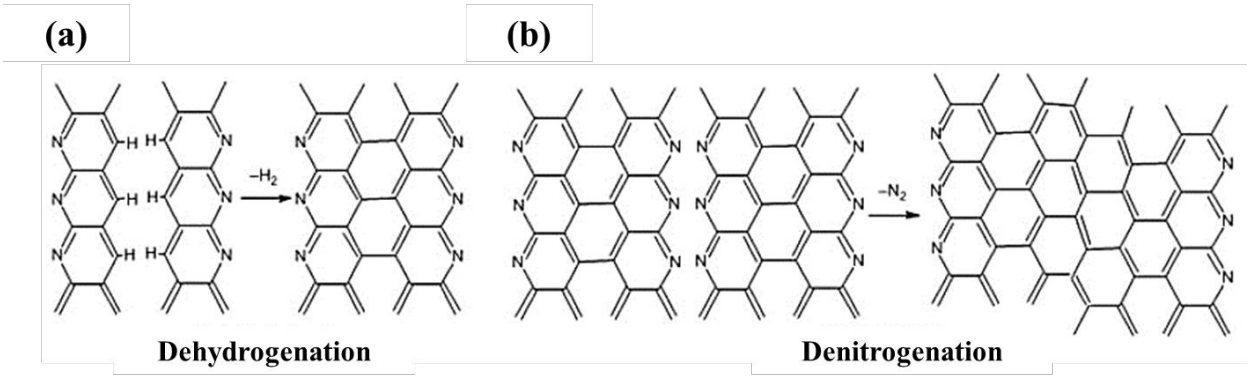

Figure 2.13. (a) Dehydrogenation and (b) denitrogenation during the carbonization process. [98]

2.2.3 Activation Methods

2.2.3.1 Chemical Activation

Chemical activation is a thermal process in which the precursor is exposed to dehydrating (activating) agents such as KOH [99–102], NaOH [103,104] and $ZnCl_2$. [105–107] These activating agents react with fibers at the carbonization temperature, etch carbon atoms and introduce porosity to the carbon fibers. [108,109] If KOH is used for chemical activation, Equations 2.13-2.16 describe the reactions that KOH will go through at the carbonization temperature. [110,111]

$$H_2C + 4KOH \rightarrow K_2CO_3 + K_2O + 3H_2 \quad (2.13)$$

$$2HC + 8KOH \rightarrow 2K_2CO_3 + 2K_2O + 5H_2 \quad (2.14)$$

$$2KOH \rightarrow K_2O + H_2O \quad (2.15)$$

$$K_2CO_3 \rightarrow K_2O + CO_2 \quad (2.16)$$

The reactions that the precursor will experience are shown in Equations 2.17-2.19.

$$H_2O + C \rightarrow H_2 + CO \quad (2.17)$$

$$K_2O + C \rightarrow 2K + CO \quad (2.18)$$

$$K_2CO_3 + 2C \rightarrow 2K + 3CO \quad (2.19)$$

Surface area, porosity and pore size distribution are controlled by the amount of activating agent, carbonization time and carbonization temperature. If a large amount of activating agent is used, the precursor reactions (Equations 2.17-2.19) will be favored; this leads to more etching of carbon atoms, creating higher porosity and a larger surface area. Carbonization time and temperature are two factors that control the pore size distribution and surface area. Longer carbonization times and higher carbonization temperatures will create larger pores that reduce the surface area. At high temperatures (>900 ^{o}C) carbon atoms are highly mobile and their movements create large mesopores. With longer carbonization times, small micropores start to grow and merge with each other, forming larger pores and reducing the surface area. The carbon content, as well as the conductivity, of the final material in the microstructure increase with increasing carbonization temperature.

2.2.3.2 Physical Activation

During physical activation, a reactant gas such as CO_2 or steam is used to selectively burn-off some of the carbon atoms to provide porosity. Reactant gases can be used by themselves, mixed or carried by an inert gas such as N_2. The final porosity of the material is determined by the type of activation gas, the activation temperature and time and flow rate of the gas. Equations 2.20 and 2.21 show two of the possible reactions with carbon. [98]

$$C + H_2O \rightarrow CO + H_2 \quad (2.20)$$

$$C + O_2 \rightarrow 2CO \quad (2.21)$$

Activated carbon fibers (ACFs) that are prepared by chemical activation have higher porosity and surface areas, a higher production yield and a better micropore distribution than those prepared by physical activation. The main advantage of physical activation over chemical activation is the low overall cost due to its straightforward preparation method. [98,112]

2.3 Characterization Techniques

2.3.1 Materials Techniques

Information such as surface area, porosity, morphology, crystal structure and chemical composition are obtained through material characterization techniques.

2.3.1.1 Nitrogen Physisorption

N_2 physisorption is a well-known method for characterizing the structure of porous materials, where N_2 gas is adsorbed on the surface of the material. The specific surface area (SSA) and the pore size distribution are calculated from the amount of the gas adsorbed by the material at 77 K at various pressures smaller than the N_2 saturation pressure. Once adsorption is finished and the relative pressure ($p/p_{saturation}$) of N_2 is close to 1, desorption occurs by removing the N_2 gas.

Physical adsorption of N_2 takes place at the gas/solid interface by forming a monolayer of nitrogen molecules on the surface without contribution of chemical bonds. Figure 2.14 shows the possible adsorption and desorption isotherms for microporous, mesoporous, macroporous and nonporous materials that are generated by measuring the amount of gas adsorbed at different pressures. [113]

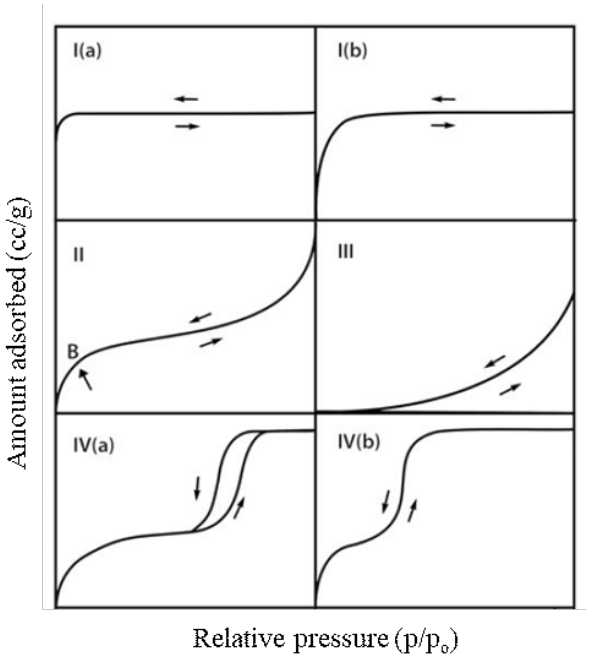

Figure 2.14. Different physisorption isotherms: I(a) and I(b) for microporous materials, II and III for non-porous or macroporous materials and IV for mesoporous materials. [113]

A type I isotherm represents microporous materials. At low relative pressures, N_2 molecules fill micropores and because there are no mesopores or macropores to adsorb more nitrogen, the amount adsorbed does not change with increasing pressure. The difference between type I(a) and I(b) is that pore size distribution in type I(a) is narrowed to pores smaller than 1 nm, whereas type I(b) represents a microporous material with a wider pore size distribution that may include small mesopores (>2.5 nm). [113]

A type II isotherm shows continuous adsorption of a nitrogen monolayer-multilayer on the surface that can be attributed to macroporous or nonporous materials. A sharp knee before point B usually corresponds to a fully formed monolayer. On the other hand, overlapping of monolayers can lead to a less sharp knee and more gradual curvature. [113]

A type III isotherm shows adsorption for a macroporous or nonporous material. The interactions between the solid surface and the nitrogen molecules are so weak that adsorbate molecules are clustered around the most favorable sites on the solid surface. As opposed to type II materials, the amount of gas molecules that type III materials can adsorb onto the surface is finite. [113]

Type IV isotherms correspond to mesoporous materials. In mesoporous materials, the adsorption behavior is explained by both the interaction between adsorbent-adsorbate molecules and the condensed nitrogen molecules in the pores. The region before the sharp increase in amount adsorbed is due to the presence of small and narrow mesopores. Once the small mesopores are filled, larger mesopores start to adsorb the nitrogen molecules on their surface. However, since the pores are relatively large and wide, the amount of gas molecules adsorbed onto the surface increases, which in turn increases the pressure inside these pores. This results in capillary condensation by transforming the adsorbed molecules to liquid, decreasing the volume occupied as a result. This creates empty space in these pores, which can adsorb more nitrogen, producing the sharp increase in the amount of gas molecules adsorbed. Figure 2.15 illustrates the capillary condensation phenomenon. Type IV(a) shows the presence of mesopores larger than 4 nm; with smaller mesopores, a type IV(b) isotherm is observed. [113]

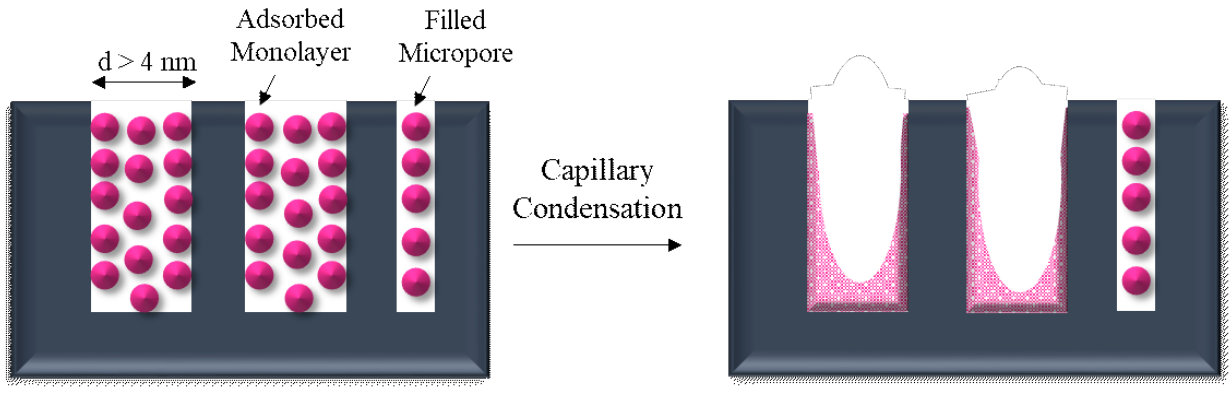

Figure 2.15. Schematics of monolayer adsorption in wide mesopores and capillary condensation.

2.3.1.2 Scanning Electron Microscopy

Scanning electron microscopy (SEM) can be used for a wide variety of organic and inorganic materials to characterize nanometer to micrometer scale features by providing three-dimensional-like topographic images at high magnification. To study a sample by SEM, a finely focused electron beam, which is generated in a vacuum chamber, is scanned across the surface of the sample. Interactions between the electron beam and the sample atoms emit different signals, such as secondary electrons, backscattered electrons and characteristic X-rays. Figure 2.16 illustrates the many different signals obtained from an incident electron beam. In order to image and study a sample using SEM, the sample must be conductive. Non-conductive samples are coated with a thin layer of a conductive material such as Au. The intensity of the signal from each point during scanning determines the brightness of that point. Different contrast effects are obtained by detecting different signal types. Secondary electrons (SEs), which make up one type of beam, are quite low energy (typically <5 eV) and can give information on the topography of the sample. SEs are knocked out of the electron shell of the sample atom when it is impacted by incoming electrons. Backscattered electrons (BSEs), on the other hand, are the result of interactions between the incident beam and the nucleus of the sample's atoms. This beam type can give information about regions with different atomic numbers in the sample. BSEs have higher energies than SEs with energies up to the incident beam energy. The intensity of BSEs is higher when they are emitted from atoms with high atomic numbers (heavy nucleus). In addition, emitted characteristic X-rays can provide qualitative and quantitative information on the composition of the sample through a technique known as energy dispersive X-ray (EDX) spectroscopy. [114]

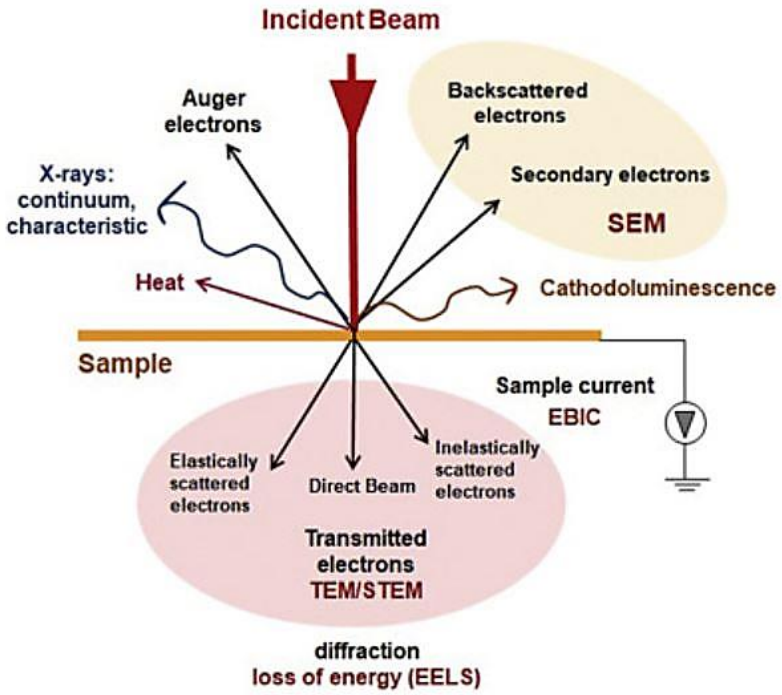

Figure 2.16. Different generated signals as a result of interactions of the sample with the incident electron beam. [115]

The resolution of an SEM image depends on several factors such as the sample material, accelerating voltage, spot size and beam current. The resolution can vary from 1 to 50 nm. [114]

Performing SEM imaging on carbonaceous materials is slightly different from other materials. Carbon's low atomic number results in low contrast images as compared with higher atomic number elements. Carbonaceous materials react weakly with the electron beam and the chances for the electron beam to damage the surface are significant at high accelerating voltages. [115]

2.3.1.3 Transmission Electron Microscopy

Transmission electron microscopy (TEM) is a powerful technique used to characterize microstructures with resolutions reaching the atomic scale. The atomic resolution of a TEM enables the characterization of materials on size scales that may be achievable with only a few

other techniques, like scanning probe microscopy techniques. For TEM, a stationary electron beam impinges onto a certain area of a thin specimen (<200 nm). Electrons can interact with the sample in a number of ways; they can be reflected, scattered, absorbed or pass through the sample uninterrupted. Unscattered and scattered electrons that are transmitted through the specimen can be collected to form an image. The energy of the electrons transmitted through the sample is much higher (80-300 keV) than the electrons emitted from the sample in the SEM, due to the energy of the incident electron beam as a result of the acceleration voltage. The accelerating voltage of a scanning electron microscope is variable, usually in the range 0.5 – 30 kV. Transmitted electrons can provide information about the specimen's internal microstructure, enabling imaging of columns of atoms. Furthermore, crystallographic information of materials can be revealed using electron diffraction in a TEM. Selected area electron diffraction (SAED) and convergent beam electron diffraction (CBED) are two electron diffraction techniques. Similar to SEM, compositional information can be obtained using TEM. EDX spectroscopy and electron energy loss spectroscopy (EELS) are two techniques for characterizing the composition. Another useful variation of TEM is scanning transmission electron microscopy (STEM). When operating in STEM mode, the high intensity electron beam is focused to a point on the sample and scanned across the sample. The electrons that pass through the sample are then collected and translated into an image intensity for that specific pixel. Bright field (BF) and annular dark field (ADF) are the two commonly used STEM imaging techniques. The contrast mechanism in BF STEM is due to mass-thickness and diffraction contrast effects. BF STEM images are formed by collecting the electrons that pass through the sample (only unscattered electrons and electrons scattered with very low angles; i.e., <0-10 mrad). On the other hand, the ADF STEM images are generated by the electrons that are scattered away from the optic axis after being transmitted

through the sample. The ADF detector is located at larger angles (10-50 mrad). High angle annular dark field imaging (HAADF) is another type of image that can be acquired using STEM. HAADF detectors detect electrons scattered with very high angles (>50 mrad). These electrons are also known as incoherently scattered electrons due to Rutherford scattering from the nucleus of the atoms. HAADF imaging is very sensitive to variations in the atomic number of atoms in the sample; hence, the HAADF technique is also known as Z contrast imaging. The contrast in HAADF STEM images is almost entirely due to the mass-thickness effects. TEM samples must be electron transparent which means sample thicknesses should be less than 200 nm and even thinner for atomic resolution. Figure 2.17 compares an SEM and TEM in terms of the source of the signal. [116]

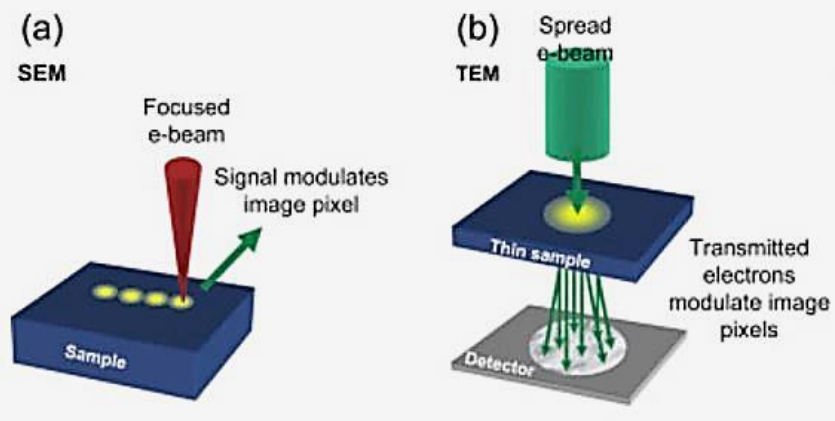

Figure 2.17. Schematics of a) SEM and b) TEM imaging techniques. [116]

2.3.1.4 X-ray Diffraction

X-ray diffraction (XRD) is a method that can be utilized to identify the crystal structure of materials. The principle used in XRD is based on Bragg's law that is shown as Equation 2.22:

$$n\lambda = 2d\sin\theta \qquad (2.22)$$

where n is an integer, λ is the wavelength of the X-rays, d is the crystallographic plane d-spacing and θ is the Bragg angle (between the X-ray incident beam and the family of the (hkl) lattice planes). An incident X-ray beam is impinged on the sample that is tilted through a range of angles. If the sample has long-range order (crystalline), the X-ray beam will diffract generating a pattern that is characteristic to the structure of the sample. Interactions between the incident X-ray beam and the sample produce intense diffracted X-rays by constructive interference when conditions satisfy Bragg's Law. Constructive interference occurs when the difference in the travel path of the incident X-rays, hitting different atomic planes from the same (hkl) family, is equal to an integer multiple of the X-ray wavelength. The diffraction pattern shows a peak for each constructive interaction. Each peak corresponds to diffraction from a particular crystallographic plane. An XRD diffraction pattern plots the intensity of the scattered X-rays vs. the angle of the detector (2θ). Non-crystalline (amorphous) samples create a diffraction pattern

with only a few broad peaks, as there is no long range order in the crystal structure. This means that X-rays are scattered in many directions which leads to the broad peaks in a wide 2theta range instead of high intensity narrow peaks. [117,118]

2.3.1.5 X-ray Photoelectron Spectroscopy

X-ray photoelectron spectroscopy is a surface characterization technique that is used for characterization of the chemical composition and the oxidation state of the elements present in the sample. A monochromatic beam of X-rays is used to excite electrons in the sample; some of these electrons are ejected from the surface while most of them are absorbed by the sample itself on their way out. The ejected electrons are called photoelectrons. Due to inelastic collisions within the sample's atomic structure, photoelectrons originating more than 20-50 Å below the surface cannot escape with sufficient energy to be detected. This is the reason for surface

sensitivity of XPS. The binding energy of the photoelectrons is then calculated as the difference between the kinetic energy of the ejected electrons and the incident X-ray energy. Differences in the electronic structure of the elements present in the sample and their oxidation states lead to different binding energies; this is also called shifting. These shifts can be used to determine chemical and electronic structure information about the sample. [119,120]

2.3.2 Electrochemical Techniques

Electrochemical techniques are used to evaluate the performance of energy storage devices. Properties like current, voltage, resistance, capacitance, cycle life and energy/power density are measured using these techniques.

2.3.2.1 Cyclic Voltammetry

Cyclic voltammetry (CV) is employed in battery or supercapacitor testing. In CV tests, the potential applied to the electrode is scanned from an initial voltage, through a voltage window, up to a switching potential. The potential is scanned with a constant scanning rate and the current produced is measured; CV graphs are called voltammograms. [121]

In the case of supercapacitors, CV is used to calculate the capacitance and to characterize the performance and the charge storage mechanism of a supercapacitor. CV is also used to study the presence of Faradaic reactions in FSs.

In the case of batteries, CV can be used to determine the onset potentials, the charge storage mechanisms, Faradaic reactions present in the cell and maximum current density for electrochemical reactions.

In addition, CV is a useful technique that can be used to determine the maximum applicable voltage to the cell. EDLSs often have a voltammogram with a rectangle shape, while FSs and

batteries have voltammograms with peaks. Each redox reaction takes place at a certain voltage and causes an increase in the current. Therefore, each peak in a CV curve represents an electrochemical reaction. This is demonstrated in Figure 2.18, with two peaks corresponding to either side of a reversible reaction at voltages of E_{pc} (cathodic reaction) and E_{pa} (anodic reaction). Current that is produced between each peak ($i_{capacitive}$) is not a result of redox reactions, but rather the double layer capacitive behavior of the device. Thus, in a perfect EDLS, there are no peaks in the CV curves and they appear rectangular. [86]

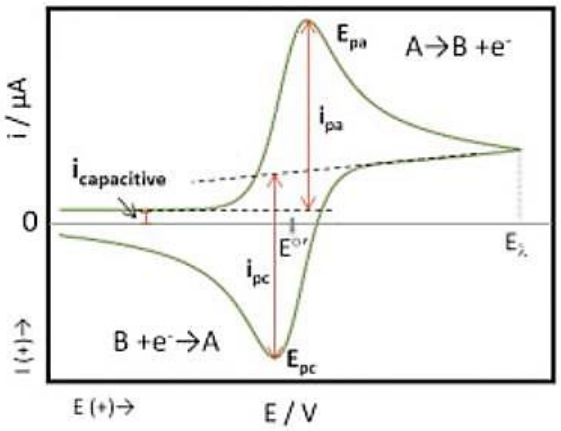

Figure 2.18. An example of a CV curve with anodic and cathodic electrochemical reactions and capacitive current. [121]

The capacitance value of an EDLS can be calculated from a CV curve, using Equations 2.23 and 2.24. [122]

$$C = \frac{Q}{\Delta V} \tag{2.23}$$

$$Q = \int_{Ei}^{Ef} I dt \tag{2.24}$$

where I is the current (in A), Q is the total charge transferred (in coulombs), C is the capacitance (in F) and ΔV is the potential window (in V).

2.3.2.2 Galvanostatic Cycling with Potential Limit

Galvanostatic cycling with potential limit (GCPL) is another technique used to evaluate the life cycle of energy storage devices and to determine battery discharge/charge efficiencies and the capacitance of an EDLS. For ZABs, usually a negative current (discharge) is applied to the cell and the cell voltage is measured. The scanned current is then reversed (charge) and the charging voltage of the battery is measured. For supercapacitors, in GCPL tests, a constant positive current (known as a charging current) is applied to the working electrode (WE) and the potential is measured until the upper limit of the potential is achieved (chosen based on the type of the electrolyte). The same current value is reversed (discharging current) until the lower limit of the potential is reached. The result of a GCPL test is a potential vs. time curve. A symmetric GCPL curve represents a good EDLS where losses from charge to discharge are as small as possible. This behavior can be seen in Figure 2.19. The potential increases linearly during charge/discharge.

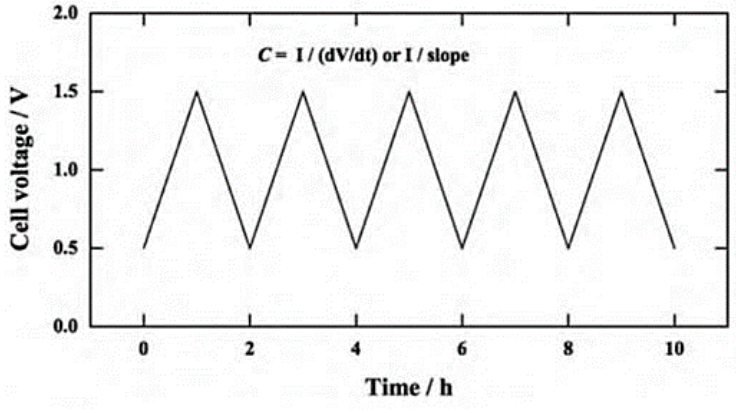

Figure 2.19. Schematic of a GCPL graph for an ideal EDLS. [86]

The efficiency of a ZAB is calculated from Equation 2.24.

$$\text{Efficiency} = \frac{E_{discharge}}{E_{charge}} \times 100 \quad (2.24)$$

The capacitance of a supercapacitor from a GCPL curve is calculated from the slope of the charge/discharge curves, using Equation 2.25. [123]

$$C = \frac{I}{Slope} = \frac{I\,dt}{dV}dV \quad (2.25)$$

where dt is the charge/discharge duration and dV is the change in the potential.

2.3.2.3 Electrochemical Impedance Spectroscopy

Electrochemical impedance spectroscopy (EIS) is used to measure the impedance of an energy storage device by applying a low amplitude alternating voltage, ΔV, to a steady-state potential, V_s. This technique is used to measure the solution resistance and charge transfer resistance (between the electrode and the electrolyte) and to study the species diffusion behavior in the cell. This kind of input signal will result in a sinusoidal output current, ΔI. The impedance is then given by Equations 2.26-2.28. [124]

$$Z(\omega) = \frac{\Delta V}{\Delta I} \quad (2.26)$$

$$\Delta V(\omega) = \Delta V_{max} e^{j\omega t} \quad (2.27)$$

$$\Delta I(\omega) = \Delta I_{max} e^{j(\omega t + \varphi)} \quad (2.28)$$

where ω is the pulsation frequency, ΔV_{max} is the input signal amplitude, φ is the phase angle between the current and voltage, ΔI_{max} is the output signal amplitude, j is the imaginary number and $Z(\omega)$ is the electrochemical impedance. [124] Figure 2.20 schematically shows an EIS plot, also known as Nyquist plot for an ideal EDLS.

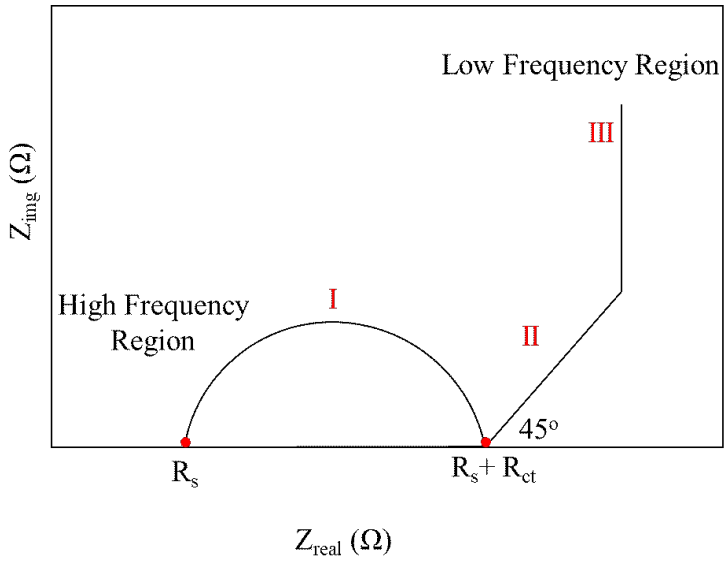

Figure 2.20. Schematic of an EIS graph for an ideal EDLS.

$Z(\omega)$ has one real and one imaginary component; the imaginary aspect represents the capacitor behavior of the cell. An imaginary impedance (Z_{imag}) vs. real impedance (Z_{real}) plot at different frequencies has three main regions. The first region (I) is a semicircle with a radius of R_{ct}, which is the charge transfer resistance. In this region, frequencies are so high that the double layer does not have enough time to expand. The first intercept of the semicircle with the real axis shows the solution resistance R_s and the second intercept is $R_s + R_{ct}$. The second region (II) is linear with a 45° angle. This means that at lower frequencies, the double layer is expanding at the same rate at

which the real part of the solution impedance is evolving. The last part (III) is called the Warburg region in which the frequencies are so low that only the double layer is expanding and Z_{real} remains constant. [125,126]

Chapter 3: Superior Performance of Electrochemical Double Layer Supercapacitor Made with Asphaltene Derived Activated Carbon Fibers

A version of this chapter has been published in the journal Energy Technology:

Z. Abedi, D. Leistenschneider, W. Chen and D.G. Ivey, "Superior Performance of Electrochemical Double Layer Supercapacitor Made with Asphaltene Derived Activated Carbon Fibers," Energy Technol., 2020, vol. 2000588, p. 1.

3.1 Introduction

With the ever-increasing demand for energy, the development of inexpensive energy storage devices is crucial. Electrochemical storage devices include fuel cells, batteries and electrochemical double layer supercapacitors (EDLS). EDLSs are simple, safe and cost effective devices that consist of carbon based electrodes. [127,128] Furthermore, EDLSs can deliver high power densities and have long cycle lifetimes compared with batteries. [49,62,129] As such, they can be used to provide on demand power in hybrid electric vehicles, boosting fuel cell and battery performance. [40,63] The energy storage mechanism for EDLSs involves electrostatically storing electrolyte ions on the surface of the electrodes. [127] Typically, carbon materials are utilized as the EDLS electrodes because of their high conductivity, which facilitates charge adsorption/desorption. One key consideration for fabricating inexpensive EDLS electrodes is the use of an abundant and inexpensive raw material. [4,130–133]

Asphaltene is a high carbon content by-product of the oil sands industry and, as such, is a potential precursor for activated carbon electrodes in EDLSs. Almost 260,000 m^3 of bitumen are produced daily from oil sands operations in Alberta, Canada. [8] Approximately 20 wt% of this bitumen consists of asphaltene, which is considered to be the most polar fraction and heaviest

part of oil sands bitumen. Asphaltene is removed during the bitumen extraction process, because it significantly increases the viscosity of bitumen which is transported via pipelines. [134,135] Current applications of asphaltene include materials for roadwork, roofing and water proofing. [136] However, the demand for asphaltene is lower than the amount produced daily. Because of its low price and high carbon content, asphaltene is a promising precursor for EDLS electrodes. Chemical treatment of the precursors is necessary to increase the specific surface area (SSA) of the electrode material as it is generally believed that capacitive behavior improves with increasing SSA. [53] Although SSA is an important factor, a proportional increase in the capacitance is not guaranteed by increasing the surface area; pore size distribution also affects electrochemical performance. [137] Depending on the electrolyte that is used in the cell, different pore designs may be required to achieve high specific capacitance and specific energy densities. [138] Charge carriers are much smaller in aqueous electrolytes than in organic and ionic liquid electrolytes. As such, microporous (pore size < 2 nm) active materials are preferred for EDLS cells working with aqueous electrolytes. [14] However, for EDLS cells utilizing organic or ionic liquid electrolytes, the presence of mesopores (pore size from 2 to 50 nm) can help the performance by improving charge adsorption/desorption and transport. [139] To achieve an EDLS cell with high electrochemical performance, an optimized SSA and pore size distribution should be developed in the electrode active material. [140] Pores must be small enough to ensure high SSA and large enough to be able to effectively adsorb charge carriers. [141]

The amount of energy delivered by an EDLS can change significantly by changing the maximum voltage applied to the cell according to Equation 3.1:

$$E = \frac{1}{2}CV^2 \quad (3.1)$$

where E is the energy (in J), C is the capacitance of the ELDS (in F) and V is the maximum potential applied to the cell (in V). The power (P) is then calculated by dividing the energy delivered by the discharge duration. When using aqueous solutions as the electrolyte, the maximum potential that can be applied to the cell is lower than the potentials for ionic electrolytes. The use of non-aqueous solutions as the electrolyte can increase the specific energy and power delivered by EDLSs by expanding the voltage window (Equation 3.1). In addition to the wide potential window (up to 4 V), ionic liquids are non-toxic and environmentally compatible. [142,143]

A recent study by Ni et al. reported on the performance of EDLSs fabricated with purchased oxygen and nitrogen doped pitch based carbon fibers. High capacitance values (301 F g^{-1} at a specific current of 1 A g^{-1}) were reported; however, relatively low specific energy and power values were obtained. [144]

For this work, asphaltene powder, as a pentane insoluble residue from the extraction of bitumen in oil sands, was provided by CNOOC Petroleum North America ULC (Nexen) from their Long Lake Upgrader in Alberta. The asphaltene powder was used to produce carbon fibers that were carbonized and then fabricated into EDLS electrodes. Some of the fibers were chemically activated using an alkali hydroxide (KOH) to generate high SSAs as well as narrow pore size distributions. Symmetric full coin cells were prepared from the electrodes and electrochemically tested, using both aqueous (KOH) and ionic liquid ($EMIMBF_4$) electrolytes. The ionic liquid electrolyte was utilized to increase the energy density of the supercapacitor device. Unlike the

work by Ni et al. [144], the fibers were synthesized in the laboratory and were not doped with oxygen or nitrogen.

3.2 Experimental

3.2.1 Preparation and Characterization of Carbon Fibers and Activated Carbon Fibers

As received raw asphaltene powder (RA) was processed into filaments with a diameter of 10 μm via a melt spinning procedure using an AT255 system from Anytester. The powder was melted at 197 °C and forced through a spinneret hole (diameter 0.15 mm) with a N_2 pressure of 400 kPa. To stabilize the fiber structure, in order to prevent melting of the material at elevated temperatures, the fibers were soaked in a 2.7 M HNO_3 solution for 10 min and heat treated in air (40 mL min^{-1}). During the first temperature step, the material was heated to 140 °C at a rate of 0.25 °C min^{-1} and kept at this temperature for 161 min. Afterwards, the temperature was raised to 300 °C at a rate of 0.5 °C min^{-1} and held for 120 min. Stabilized fibers (SF) were then heated to 500 °C in a tube furnace, equipped with a quartz tube, under N_2 flow (80 mL min^{-1}) at a rate of 3 °C min^{-1} and held there for 1 h to become pre-carbonized. After pre-carbonization, some fibers were carbonized (CF) at 800 °C for 2 hours at a heating rate of 3 °C min^{-1}. The remaining fibers were mixed with dry KOH with different mass ratios; i.e., R = (mass of KOH) / (mass of fibers) from 1 to 3. These fibers were then activated and carbonized with the same heating rate as the non-activated fibers. CF and activated carbonized fibers with different R values (ACF-R) were washed with 35 wt% HCl and deionized water multiple times using a vacuum filtration system. The final samples were dried in a vacuum oven at 100 °C for at least 12 h.

Field emission scanning electron microscopy (ZEISS Sigma 300 VP-FESEM) was used to measure the diameters of the fibers after melt spinning and to investigate the surface morphology and composition of the CF and ACF-R samples. Nitrogen physical adsorption/desorption using

an Autosorb-iQ-XR system was employed to determine the SSA and the pore size distribution. Samples were outgassed at 200 ^{o}C for 10 h prior to the test. The SSAs were calculated using both quenched solid density functional theory (QSDFT) and Brunauer-Emmett-Teller (BET) methods. Pore size distributions were calculated from the adsorption branch using the QSDFT method, assuming slit and cylindrical pores, and the total pore volumes were determined at a relative pressure of 0.95. CHNS elemental analysis was done, using a Flash 2000 Organic Analyzer, to evaluate the light element composition of all samples.

3.2.2 Preparation of Electrodes

Electrodes were prepared by mixing 90 wt% of the CF or ACF-R samples, 5 wt% of polytetrafluoroethylene (PTFE, suspension) and 5 wt% of acetylene black at 80 °C in an agate mortar to form a homogeneous paste. After drying the paste in a vacuum oven at 100 ^{o}C for 12 h, electrode films were obtained. Disks, 1.92 cm^2 in area, were sectioned from the films to be used as the electrodes. The mass of the electrodes was 15-25 mg, while the thickness was 100-150 μm.

3.2.3 Preparation of Supercapacitor Cells

Coin cells were prepared by using two electrodes with the same mass and thickness pressed onto stainless steel current collectors with a conductive adhesive paint and a separator between them (Figure 3.1). 100 μL of electrolyte was added to the set-up before sealing; 6 M KOH and 1-ethyl-3-methylimidazolium tetrafluoroborate ($EMIMBF_4$) were used as the aqueous and ionic liquid electrolytes, respectively.

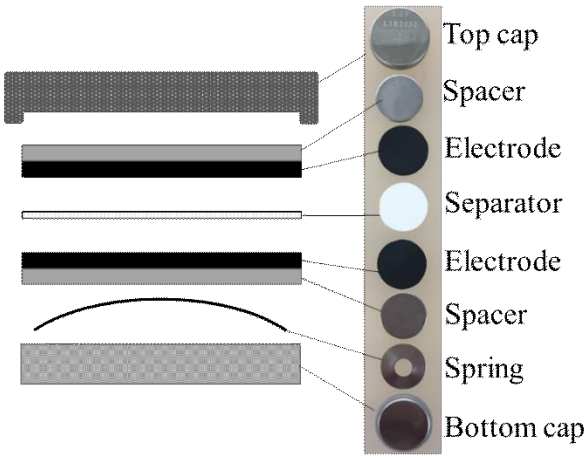

Figure 3.1. Coin cell preparation schematic.

3.2.4 Electrochemical Measurements

Electrochemical tests were conducted to evaluate the capacitive performance, using a VSP potentiostat (Biologic). The tests included cyclic voltammetry (CV, scan rate from 10 to 100 mV s^{-1}), galvanostatic charge/discharge with potential limitation (GCPL, specific currents from 40 mA g^{-1} to 4 A g^{-1}) and electrochemical impedance spectroscopy (EIS, frequency from 50 mHz to 500 kHz).

3.2.5 Methods for Determining Capacitance, Energy and Power Density

The capacitance values reported for this work are for discharge of a single electrode and are calculated from Equation 3.2:

$$C_s = 4\frac{C_t}{m_t} \tag{3.2}$$

where C_s is the specific capacitance of one electrode (in F g^{-1}), C_t is the total capacitance (in F) of the device and m_t is the total mass of the two electrodes (in g). For supercapacitors that behave

ideally, C_t is calculated from the slope of the discharge part of the galvanostatic curves (e.g., GCPL curves) and is given by:

$$C_t = I\frac{\Delta t}{\Delta V} \tag{3.3}$$

where I is the applied current during discharge (in A), Δt is the discharge duration and ΔV is the voltage difference from the start of discharge (after Ohmic drop during self-discharge) to the end.

Specific energy is calculated as:

$$E_s = \frac{I\int_{t(V_{min})}^{t(V_{max})} V(t)\,dt}{3.6\,m_t} \tag{3.4}$$

where E_s is the specific energy of one electrode (in Wh kg^{-1}). [123]

3.3 Results and Discussion

3.3.1 Activation and Microstructure of Carbon/Activated Carbon Fibers

Nitrogen physisorption experiments for CF and SF generate isotherms typical of non-porous materials with fairly low SSAs according to the IUPAC classification (Figure 3.2). The volume of gas adsorbed on SF and CF is quite small during N_2 adsorption and there is no increase in the volume adsorbed at low relative pressures, which indicates the absence of micropores. More details about the pore structure are shown in Table 3.1. The CFs have a relatively small SSA and pore volume. No electrochemical tests were conducted on SF due to its low porosity.

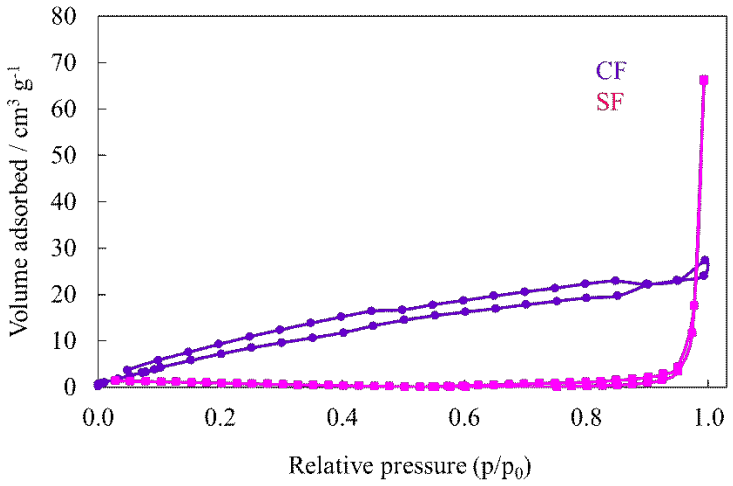

Figure 3.2. Nitrogen adsorption/desorption isotherms at 77 K for CF and SF.

Table 3.1. SSA and pore structure of ACF-R and CF

Sample	**DFT SSA** ($m^2 g^{-1}$)	**BET SSA** ($m^2 g^{-1}$)	**Total pore volume** ($cm^3 g^{-1}$)	**Micropore volume** ($cm^3 g^{-1}$)	**Mesopore volume** ($cm^3 g^{-1}$)
CF	23	43	0.04	0.00	0.04
ACF-1	1715	1091	0.62	0.48	0.09
ACF-2	2290	1640	0.92	0.70	0.15
ACF-3	2689	2290	1.27	0.88	0.29

Mesopore volume calculated as V_{total} - $V_{micropore}$.

According to the IUPAC classification, because of the large increase in the amount of N_2 adsorbed at very low pressures ($p/p_0 < 0.05$) and the quite flat plateau at higher pressures ($p/p_0 > 0.1$), ACF-R can be defined as a microporous material (Figure 3.3(a)). The increase in the volume adsorbed at low pressures from ACF-1 to ACF-2 to ACF-3 indicates an increase in micropore volume ($V_{micropore}$); i.e., $V_{micopore}$ (ACF-3) > $V_{micopore}$ (ACF-2) > $V_{micopore}$ (ACF-1). ACF-3 likely contains some very narrow mesopores as well, as indicated by the knee at a relative

pressure $p/p_0 = 0.1$. The correlation between R and total pore volume and BET SSA for ACF-R (Figure 3.3(b) and 3.3(c)) shows an increase in both total pore volume and BET SSA with increasing R. R = 0 represents CF (non-activated carbonized fiber).

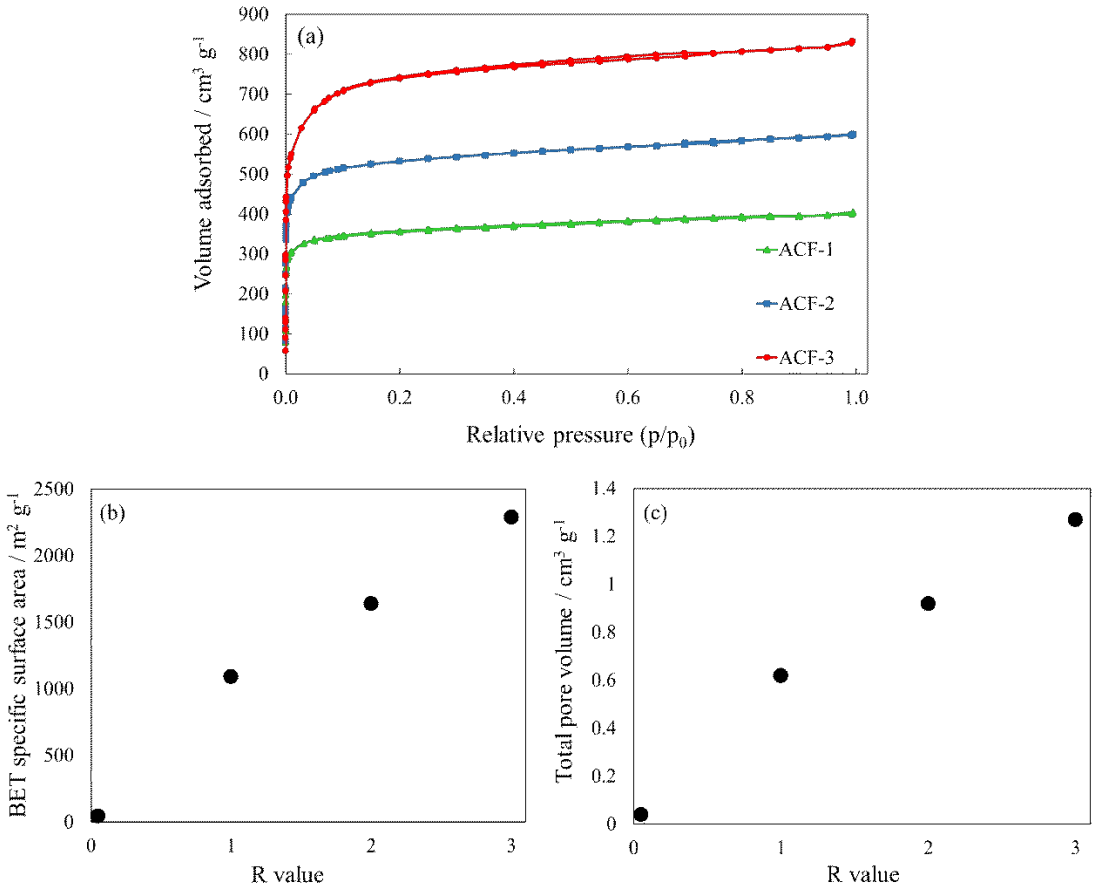

Figure 3.3. (a) Nitrogen adsorption/desorption isotherms at 77 K for ACF-R, (b) BET SSA as a function of R (c) and total pore volume change as a function of R.

It is apparent from Figure 3.4(a) that the majority of pores in ACF-1 fall into the micropore region (pore width between 0.8 nm and 1 nm). In ACF-2, however, the total volume of micropores (pore width between 0.8 nm and 1.1 nm) increases but there is a small amount of narrow mesopores (pore width ~ 2.2 nm). In ACF-3, the micropore volume increases significantly. The total volume of mesopores with the same size as those in ACF-2 increases as

well, meaning that the micropores grow in size and merge to create mesopores while new micropores are being created. Figure 3.4(b) represents the cumulative pore volume for ACF-R.

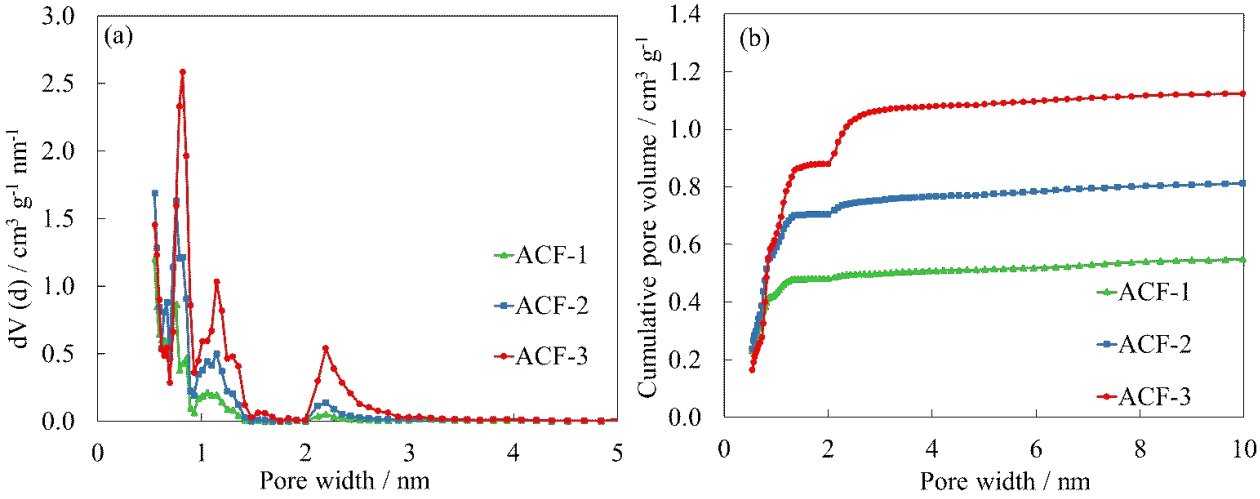

Figure 3.4. Nitrogen adsorption results for ACF-R. QSDFT based (a) pore size distribution and (b) cumulative pore volume.

The BET surface area of ACF-R increases from 1091 $m^2 g^{-1}$ for ACF-1 to 1640 $m^2 g^{-1}$ for ACF-2 to 2290 $m^2 g^{-1}$ for ACF-3 (Table 3.1). As with the SSA, the total pore volume and micropore volume increase with increasing R value. The $V_{micropore} / V_{total}$ ratio decreases as R increases (from ACF-1 (0.77) to ACF-3 (0.69) – Figure 3.5(a)), whereas the $V_{mesopore} / V_{total}$ ratio increases as R increases (from ACF-1 (0.23) to ACF-3 (0.31) – Figure 3.5(b)). Considering the fact ACF-3 has the highest $V_{micropore}$ (0.88 $cm^3 g^{-1}$), it is expected that the presence of more mesopores in ACF-3 should enhance the capacitive performance by improving ion transport in the electrodes.

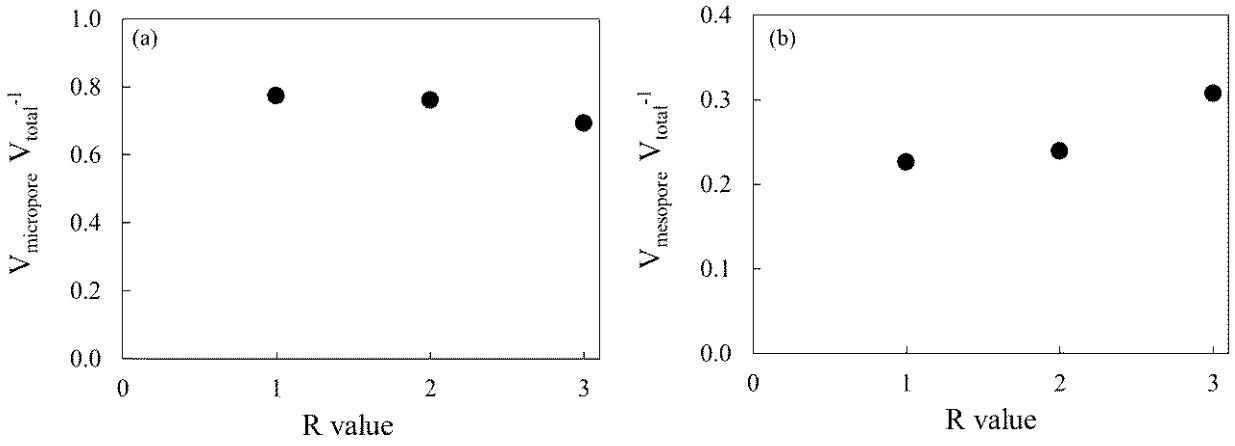

Figure 3.5. Micropore and mesopore evolution for different R values.

The activating agent (KOH) etches the fibers, introducing structural damage (Figure 3.6) and changes the surface morphology of the fibers. The changes in fiber shape, length and surface morphology are more pronounced with increasing KOH content (R value); e.g., ACF-3 fibers are much shorter and distorted with a rough surface relative to CF. SEM images at low and high magnification and energy dispersive x-ray (EDX) maps of the fabricated electrode with ACF-3 (Figure 3.6) show that the fibers have generally retained their shape even after electrode preparation. Also, the O map represents O in the fibers (Table 3.2); all metallic residue and activation agent were removed by washing the fibers with water and HCl. Very small carbon particles in Figure 3.6 are likely acetylene black particles and the presence of F is attributed to PTFE used as the electrode binder.

Table 3.2. CHNS elemental analysis for CF and ACF-R samples (wt%)

Sample	Carbon	Hydrogen	Nitrogen	Sulfur	Oxygen	Total
CF	88.00	0.57	1.50	5.80	2.13	98.00
ACF-1	93.00	0.20	0.20	0.10	3.00	97.00
ACF-2	92.00	0.36	0.10	0.20	3.00	96.00
ACF-3	94.00	0.30	0.07	0.00	2.50	97.00

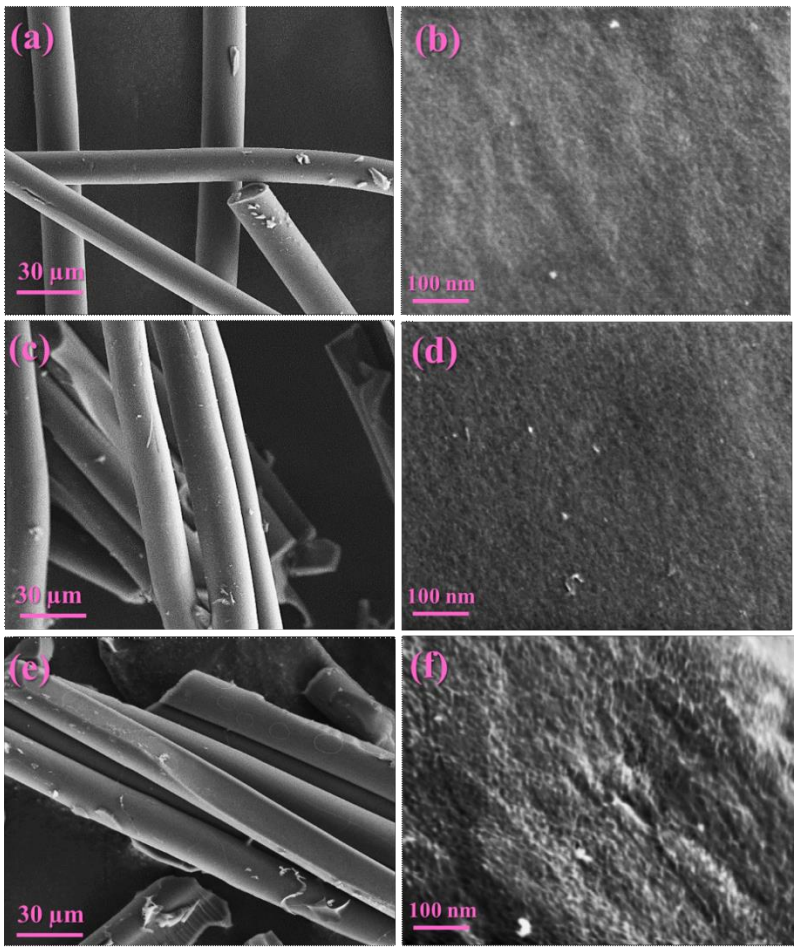

Figure 3.6. SEM secondary electron (SE) images of ACF-R samples. (a) and (b): ACF-1; (c) and (d): ACF-2; (e) and (f): ACF-3.

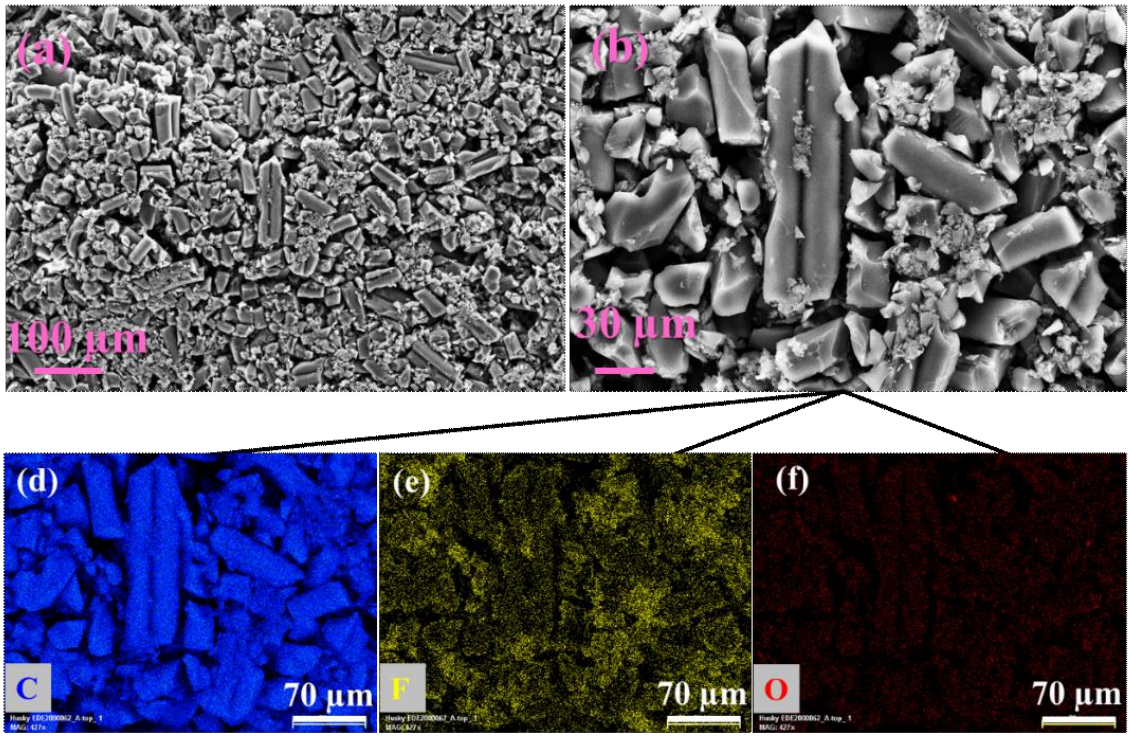

Figure 3.7. SEM SE images and EDX maps of fabricated electrode using ACF-3.

3.3.2 Capacitive Performance of CF and ACF-R in Aqueous Electrolyte

Four EDLS symmetric cells (CF, ACF-1, ACF-2 and ACF-3) were prepared. Two electrodes with the same mass and thickness from the same batch of fibers were used in 100 µl of 6 M KOH as the aqueous electrolyte due to its small ions size and high conductivity. [145] The electrochemical performance of each cell was evaluated by CV, GCPL and EIS measurements.

All CV curves for the ACF-R samples (Figure 3.8(a)) have rectangular shapes at a scan rate of 10 mV s^{-1}, which is characteristic of an ideal double layer capacitor. ACF-3 has the most rectangular CV shape with an almost immediate formation of the plateau after voltage inversion from positive to negative values. Figure 3.8(b) shows CV curves for ACF-3 at different scan rates; these curves are also rectangular. The CV curve for the CF sample is not rectangular and redox peaks are present (Figure 3.8 (a)). The redox peaks for the carbonized precursor may be

related to the presence of sulfur and nitrogen in the precursor. This hypothesis is strengthened by comparing the amounts of sulfur and nitrogen in CF and ACF-R samples (Table 3.2), which are significantly reduced after activation.

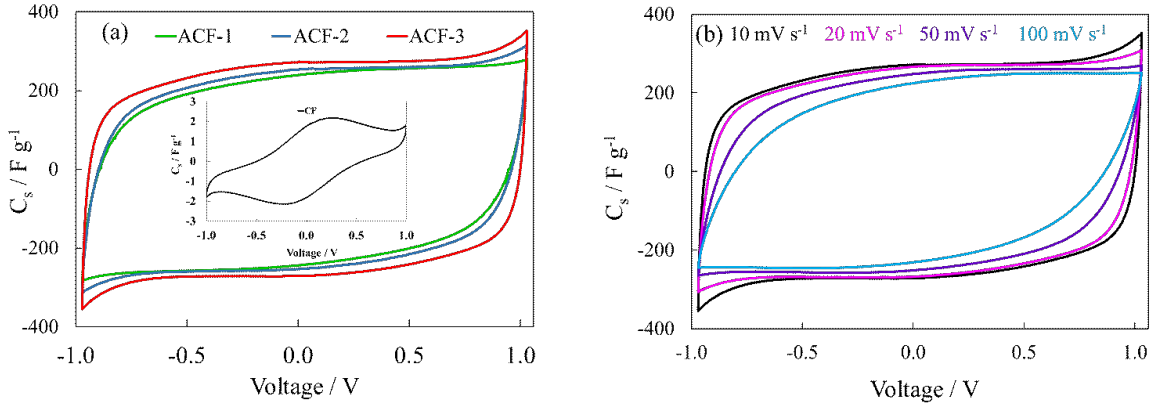

Figure 3.8. (a) CV curves for ACF-R and CF at a scan rate of 10 mV s^{-1} and (b) CV curves for ACF-3 at scan rates from 10 mV s^{-1} to 100 mV s^{-1}.

GCPL tests at different specific currents were conducted to obtain the capacitance of ACF-1, ACF-2 and ACF-3 in aqueous electrolyte cells (Figure 3.9(a) and 3.10). The symmetric shape of the GCPL curves and the almost linear voltage-time dependence of the discharge curves for the activated samples represents nearly ideal capacitive behavior, whereas the carbonized precursor (CF) has poor EDLS performance. Figure 3.9(b) shows GCPL tests for ACF-3 at different specific currents from 40 mA g^{-1} to 4 A g^{-1}. Although the Ohmic drop increases with increasing specific current, both the charge and discharge portions of the curves remain almost linear.

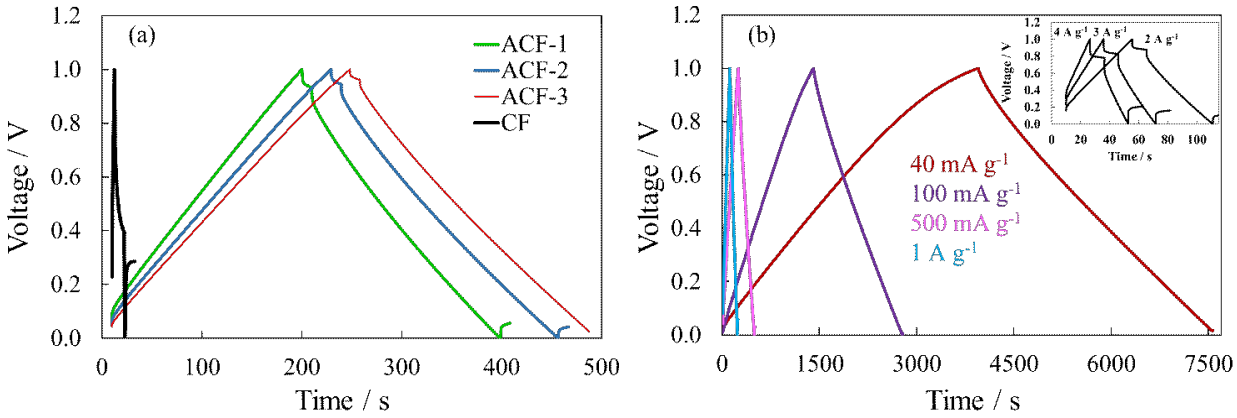

Figure 3.9. (a) GCPL tests for ACF-R and CF at a specific current of 0.4 mA g^{-1} and (b) GCPL tests for ACF-3 at different specific currents from 40 mA g^{-1} to 4 A g^{-1}.

ACF-1 with an SSA of 1091 m^2 g^{-1} has a capacitance of 276 F g^{-1} at 40 mA g^{-1} which drops to 114 F g^{-1} at 4 A g^{-1} (-59%) (Figure 3.10). The capacitance for ACF-2 increases relative to ACF-1 to 315 F g^{-1} at 40 mA g^{-1} and decreases to 164 at 4 A g^{-1} (-48%). ACF-3 performs the best at higher specific currents with a capacitance of 311 F g^{-1} at 40 mA g^{-1} and 222 F g^{-1} at 4 A g^{-1} (a 29% drop). The good performance of ACF-3 may be related to its high SSA which is due to the high micropore volume. Furthermore, the bimodal distribution of pores (both micropores and narrow mesopores) in ACF-3 may facilitate ion transport leading to higher capacitance values at higher specific currents (Figure 3.4 and Figure 3.10).

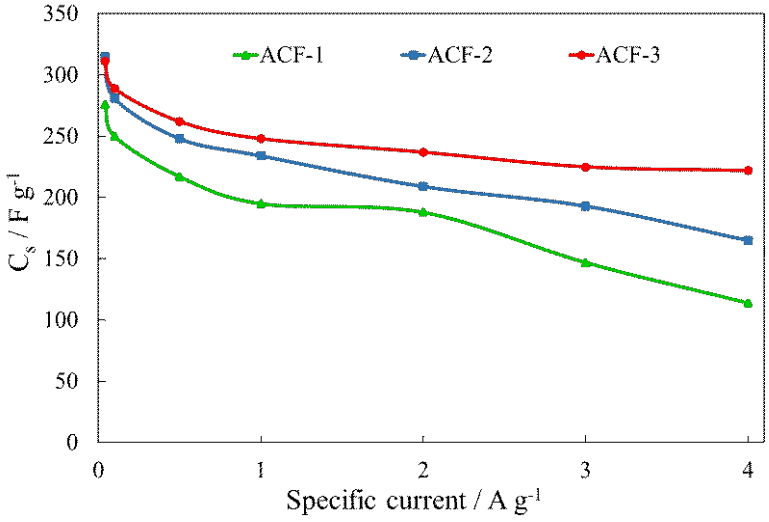

Figure 3.10. Specific capacitances at different specific currents for ACF-R samples.

The cycle life of the ACF-R samples was evaluated by GCPL charge/discharge at a specific current of 1 A g^{-1} for 10,000 cycles and the results are presented in Figure 3.11. Because of the poor capacitive performance of the CFs, extended cycle testing was not performed on this material. The capacitance decays after 10,000 cycles for ACF-1, ACF-2 and ACF-3 are 14%, 10% and 9%, respectively, which indicates the good performance of the ACF-3.

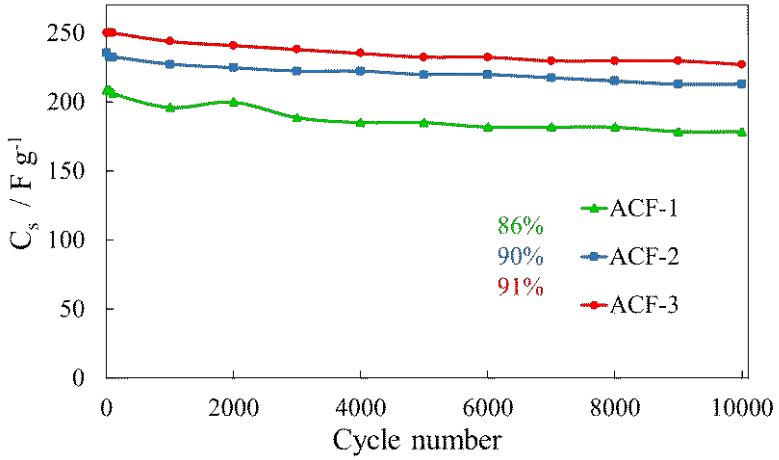

Figure 3.11. Cycling tests for ACF-R samples.

EIS tests for all four samples were performed at a frequency range from 500 kHz to 50 mHz with an alternating potential amplitude of 5 mV (Figure 3.12). ACF-3 behaves as an ideal EDLS with a semicircle at medium frequencies, a linear line with a 45° slope with respect to the real axis at low frequencies and an almost vertical curve at very low frequencies (Warburg region). The diameter of the semicircle provides the charge transfer resistance, R_{ct}, at the electrode/electrolyte interface. The first intercept of the curve with the real axis represents the solution resistance, R_s. The imaginary and real parts of the impedance represent the capacitor and electrolyte solution components of the circuit, respectively. [126]

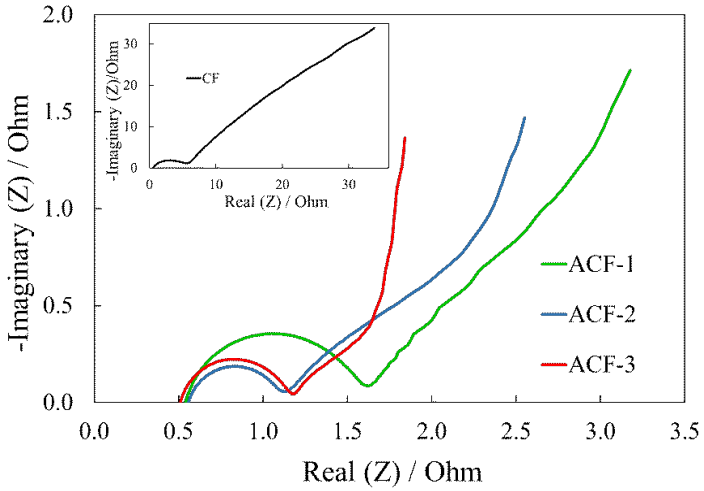

Figure 3.12. EIS tests for ACF-R and CF samples.

For an ideal electrochemical supercapacitor, in the low frequency region of the graph, the double layer extends into the electrolyte and corresponds to where the capacitor part of the circuit dominates. This is the Warburg region represented by an almost vertical line in the graph. The CF sample does not enter the Warburg region (inset of Figure 3.12) and has a much higher R_s than the ACF-R samples. This could be related to the low C content and the high amount of S, O and N according to the CHNS results. ACF-3 shows nearly ideal supercapacitor performance by entering the Warburg region before ACF-1 and ACF-2 in the medium frequency region. ACF-2

has the same R_{ct} as ACF-3 and enters the pure capacitance region later than ACF-3. ACF-1 has a higher R_{ct} than either ACF-3 or ACF-2 and does not enter the Warburg region until very low frequencies are reached. All four samples have the same R_s, which is expected, and confirms the test reliability since the same aqueous solution was used as the electrolyte for all samples. [125,126]

In order to determine whether the KOH/carbon fiber mass ratio (R) had been optimized, the amount of KOH was increased to prepare ACF-4 with an R value of 4. The pore structure of this batch of fibers is given in the supporting information (Table SI3.1 and Figures SI3.1, SI3.2 and SI3.3). Although the highest BET SSA was achieved (2960 $m^2\ g^{-1}$), the micropore volume decreased from 0.88 $cm^3\ g^{-1}$ for ACF-3 to 0.73 $cm^3\ g^{-1}$ for ACF-4 and the mesopore volume increased from 0.29 $cm^3\ g^{-1}$ for ACF-3 to 1.2 $cm^3\ g^{-1}$ for ACF-4. The capacitance behavior of ACF-4 was then evaluated using GCPL tests at different specific currents (Figure SI3.4). The maximum capacitance for ACF-4 was lower than the corresponding values for ACF-2 and ACF-3, coupled with a significant drop in the capacitance values at higher currents. This behavior may be related to the lower micropore volume for ACF-4. Because the best capacitance and rate behavior were achieved with ACF-3, further electrochemical tests were conducted only on ACF-3.

Compared with the work by Ni et al., EDLS cells prepared in this work, using bitumen-derived asphaltene, behave more like ideal supercapacitors, as shown by the rectangular CV curves and symmetric charge/discharge galvanostatic curves. The specific capacitance values, cycle life and resistance values for the cells in aqueous KOH are comparable to the values reported by Ni et al. [144]

3.3.3 Capacitive Performance of ACF-3 in Ionic Liquid Electrolyte

Two electrodes were fabricated from ACF-3; ACF-3 was chosen because of its superior performance in aqueous electrolyte as well as its suitable pore structure that contains some narrow mesopores (more than ACF-1 and ACF-2) for storing larger ions. A symmetric EDLS cell with 100 µl $EMIMBF_4$ (ionic diameter of the ions in $EMIMBF_4$: 0.8 nm for $EMIm^+$ and 0.38 nm for $BF4^-$) as the electrolyte was prepared using the same method described previously; this EDLS cell is denoted as ACF-3-ionic. [51] CV, GCPL and EIS tests were carried out to evaluate the capacitive behavior of the cell. Figure 3.13(a) shows CV curves at scan rates of 5 mV s^{-1} to 100 mV s^{-1}. Similar to ACF-3 performance in the aqueous electrolyte, the CV curves look fairly rectangular at slow and medium scan rates and start to deviate from the rectangular shape at high scan rates. ACF-3-ionic has almost ideal supercapacitor performance with linear galvanostatic charge/discharge curves and small Ohmic drop (Figure 3.13(b)); however, the Ohmic drop increases with increasing specific current. GCPL tests at different specific currents were used to calculate the capacitance values as explained previously; the capacitance values at specific currents from 40 mA g^{-1} to 4 A g^{-1} are shown in Figure 3.13(c). The capacitance value decreases from 205 F g^{-1} at 40 mA g^{-1} to 116 F g^{-1} at 4 A g^{-1} (-43%), which is a smaller drop than for ACF-1 (-59%) and ACF-2 (-48%) in aqueous electrolytes but a larger drop than for ACF-3 (-29%) in the aqueous electrolyte. This result is expected due to the higher viscosity and larger charge carrier sizes for $EMIMBF_4$ compared with 6 M KOH. EIS tests for ACF-3-ionic are shown in Figure 3.13(d). The cell does not enter the Warburg region even at frequencies as low as 10 mHz, which may be attributed to the high viscosity of the electrolyte.

Because of the wide potential window, only limited cycle testing of ACF-3 in the ionic liquid electrolyte was done (48 cycles, Figure SI3.5). The capacitance dropped from 161 F g1 in the first cycle to 120 F g1 (25% decrease) after 48 cycles. The drop may be associated with the

degradation of the electrodes in the ionic liquid. Most of the pores in ACF-3 are micropores (Table 3.1), so once they are even slightly plugged, there is less surface area available to the larger EMIMBF4 electrolyte ions. The ions cannot be stored in the micropores anymore and the only available pores are micropores, leading to reduced capacitance during cycling.

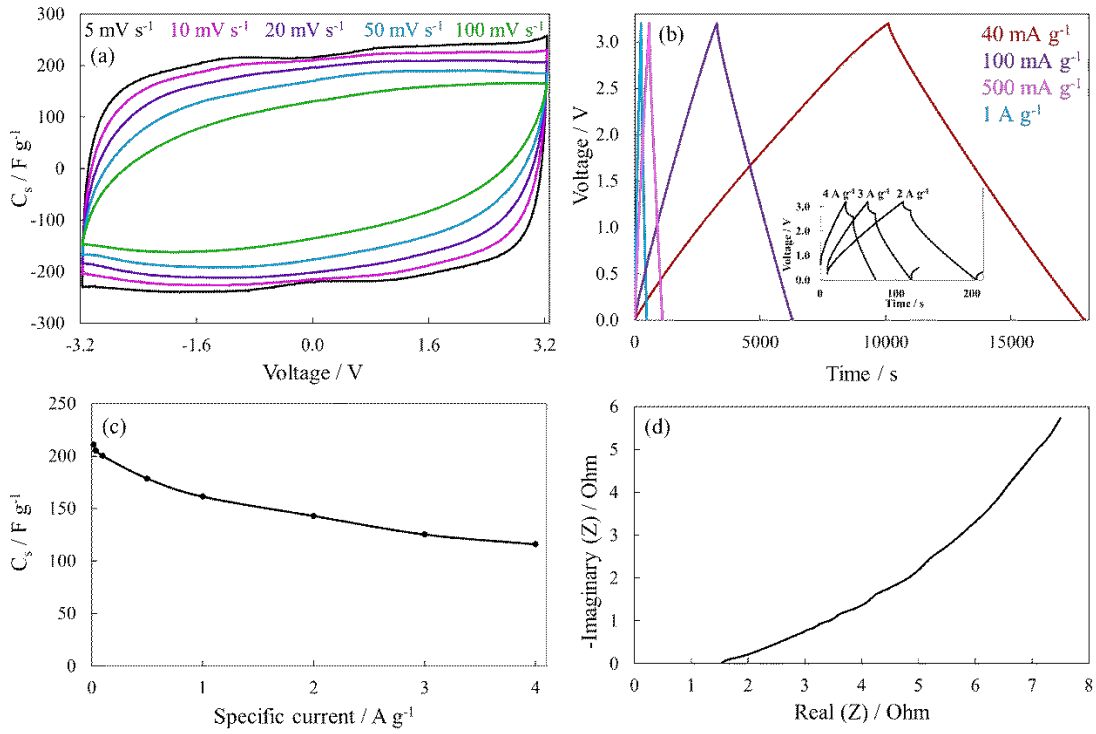

Figure 3.13. Electrochemical tests for ACF-3-ionic: (a) CV curves at different scan rates, (b) GCPL tests at different specific currents, (c) specific capacitance as a function of specific current and (d) EIS test.

3.3.4 Energy and Power Comparison

To compare the specific energy (E_s in Wh kg^{-1}) and specific power (P_s in W kg^{-1}) delivered during discharge, a Ragone plot for all ACF-R samples in aqueous and ionic liquid electrolytes is presented in Figure 3.14(a). ACF-3-ionic has the highest specific energy and power due to its wider potential window compared with the aqueous electrolyte. Specific power for ACF-3-ionic

increases by almost two orders of magnitude (from 27 W kg^{-1} to 2.76 kW kg^{-1}), while E_s decreases to about one third of the highest value (from 58.2 to 17.6 Wh kg^{-1}), when the specific current is increased from 40 mA g^{-1} to 4 A g^{-1} (Figure 3.14(b) and Table 3.3).

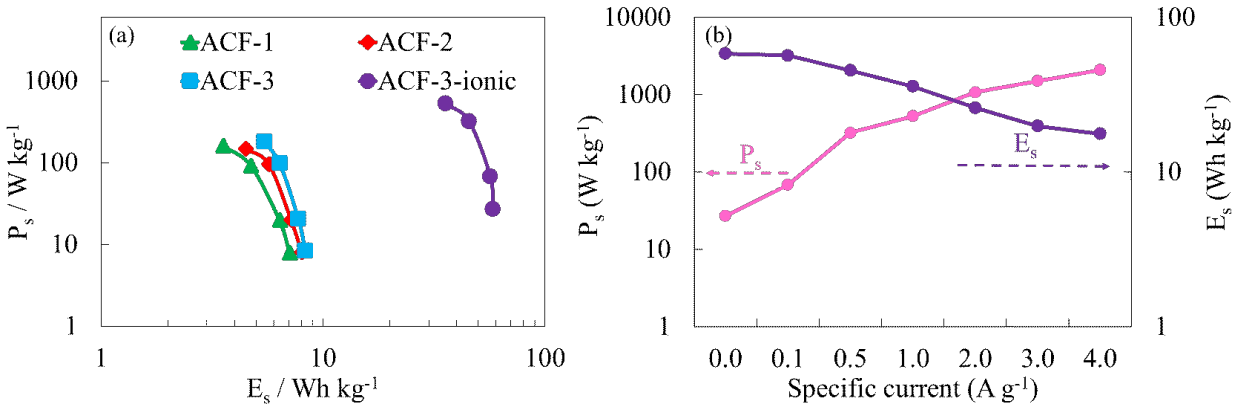

Figure 3.14. (a) Ragone plot for all EDLS cells studied. (b) E_s and P_s for ACF-3-ionic at different specific currents.

Table 3.3. Specific energy (E_s) and specific power (P_s) for all EDLSs at different specific currents

	E_s (Wh kg^{-1})				**P_s (W kg^{-1})**			
Sample	40 mA g^{-1}	100 mA g^{-1}	500 mA g^{-1}	1 A g^{-1}	40 mA g^{-1}	100 mA g^{-1}	500 mA g^{-1}	1 A g^{-1}
ACF-1	7.1	6.4	4.7	3.5	7.9	19.7	91.9	161.0
ACF-2	8.0	7.2	5.7	4.5	8.1	19.9	95.7	148.7
ACF-3	8.3	7.7	6.4	5.4	8.3	20.5	97.6	180.6
ACF-3-ionic	58.2	56.6	45.4	35.7	27.0	68.2	322.3	525.4

The ACF-3-ionic cell has maximum specific energies exceeding those for typical supercapacitors. The performance also overlaps with batteries for some current densities. [17] Specific energy and power values for the capacitors in this work are comparable with other values for carbon nanomaterials, as shown in Table 3.4. E_s and P_s values for EDLS cells in ionic liquid and organic electrolytes reported by Zhang et al. and Miao et al. are similar to the values obtained in this work using the ionic liquid electrolyte. [146,147] The work by Li et al. on biomass-derived carbon yields relatively low specific cell capacitance values; however, a maximum specific power of 468.8 W kg^{-1} at a specific energy of 61.2 Wh kg^{-1} was achieved in an organic electrolyte. [148] Using an aqueous electrolyte, Banda et al. and Ni et al. achieved E_s values much lower than those attainable in non-aqueous electrolytes. [144,149]

Table 3.4. Specific energy (E_s) and specific power (P_s) for EDLS cells made with carbonaceous materials

Material	Electrolyte	E_s (Wh kg^{-1})	P_s (W kg^{-1})
Porous carbon [146]	Organic ($TEAB_4$)	38.0	574.0
Reduced graphene hydrogel [149]	Aqueous (KOH)	7.0	500.0
Poly (ionic liquid)-derived [147]	Organic ($TEAB_4$)	45.0	276.0
Poly (ionic liquid)-derived [147]	Ionic liquid (LiTFSI)	31.8	219.0
Biomass-derived carbon [148]	Ionic liquid ($EMIMBF_4$)	61.2	468.8
Asphaltene based carbon fiber [144]	Aqueous (KOH)	8.0	248.0
This work (at 1 A g^{-1})	Ionic liquid ($EMIMBF_4$)	35.7	525.4

3.4 Conclusions

Carbon fibers for supercapacitor electrodes were prepared from asphaltene, a by-product of bitumen extraction from the oil sands, by melt spinning. Melt-spun asphaltene fibers were stabilized, using a two-step stabilization method, pre-carbonized at 500 ^oC for 1 h and carbonized and activated at 800 ^oC for 2 h. Dry KOH was used to activate the fibers. Three different activation ratios (R= KOH mass/fiber mass) were used, R = 1, 2 and 3, leading to three different final activated fibers (ACF-1, ACF-2 and ACF-3). The capacitive performance of electrodes made with the activated fibers was evaluated in 6 M KOH as the aqueous electrolyte. ACF-1,

ACF-2 and ACF-3 with BET specific surface areas (SSAs) of 1092 $m^2 g^{-1}$, 1640 $m^2 g^{-1}$ and 2290 $m^2 g^{-1}$, respectively, reached capacitance values of 276 F g^{-1}, 315 F g^{-1} and 311 F g^{-1}, respectively, at a specific current of 40 mA g^{-1} in galvanostatic charge/discharge tests. The sample with the best performance in the aqueous electrolyte, ACF-3, was then tested in $EMIMBF_4$ (ionic liquid electrolyte) and reached a capacitance value of 205 F g^{-1} at 40 mA g^{-1}. ACF-3, in the ionic liquid electrolyte, was able to deliver specific power and energy values as high as 525 W kg^{-1} and 35.7 Wh kg^{-1}, respectively, at a specific current of 1 A g^{-1}.

3.5 Supporting Information

Table SI3.1. SSA and pore structure of ACF-4

Sample	DFT SSA ($m^2 g^{-1}$)	BET SSA ($m^2 g^{-1}$)	Total pore volume ($cm^3 g^{-1}$)	Micropore volume ($cm^3 g^{-1}$)	Mesopore volume ($cm^3 g^{-1}$)
ACF-4	3790	2960	1.93	0.73	1.2

* Mesopore volume calculated as V_{total} - $V_{micropore}$

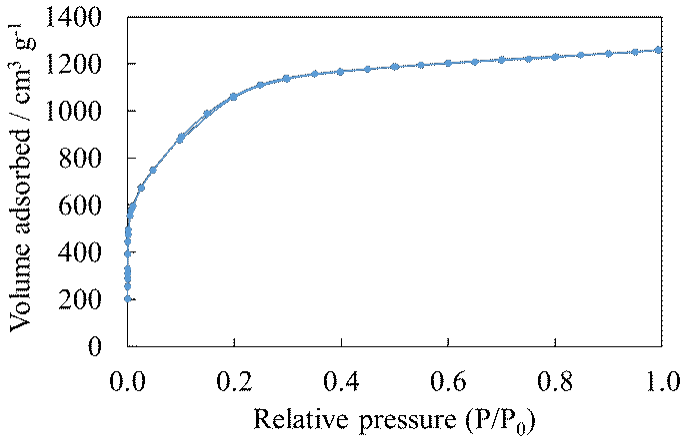

Figure SI3.1. Nitrogen adsorption/desorption isotherms at 77 K for ACF-4.

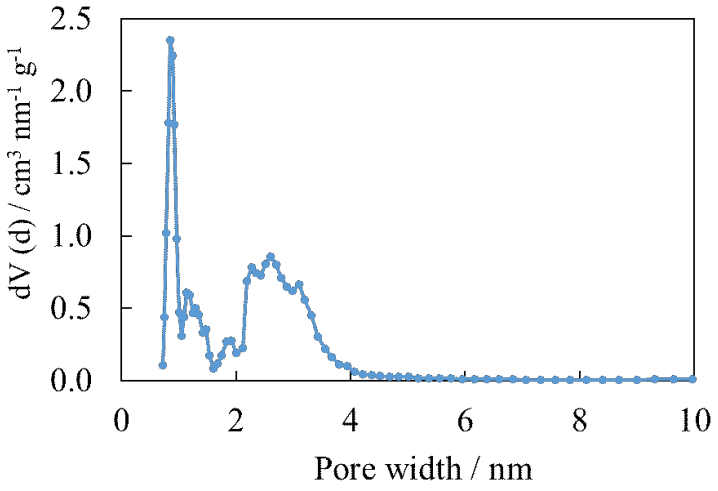

Figure SI3.2. QSDFT based pore size distribution for ACF-4.

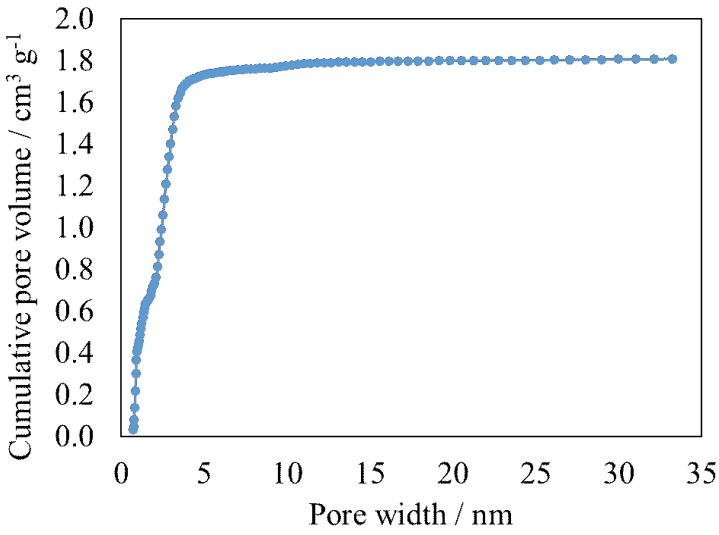

Figure SI3.3. QSDFT based cumulative pore volume for ACF-4.

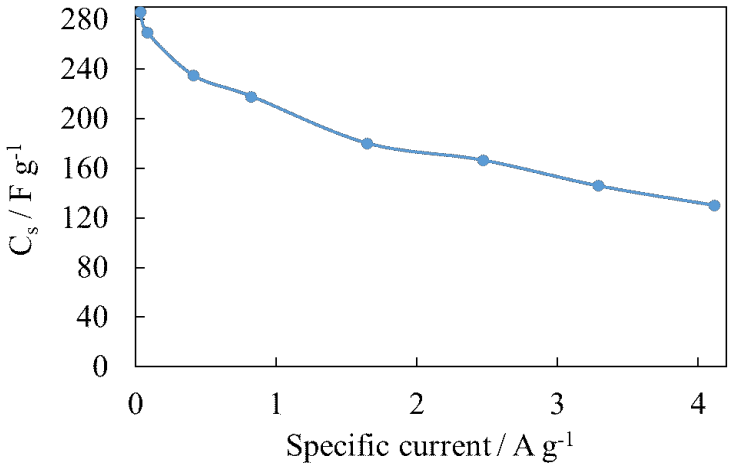

Figure SI3.4. Specific capacitances at different specific currents for ACF-4.

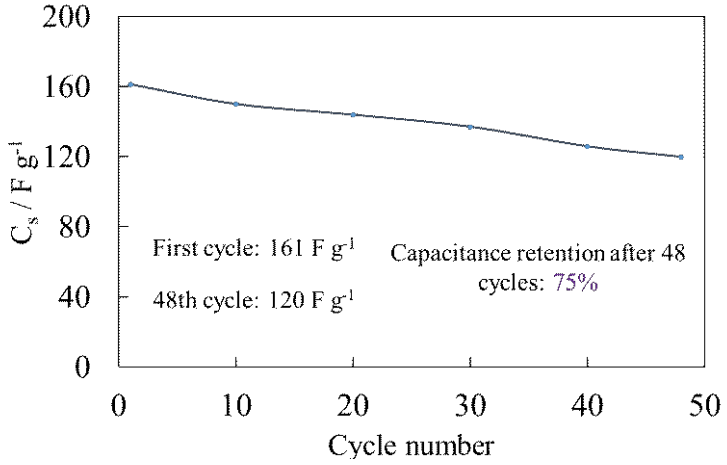

Figure SI3.5. Specific capacitance retention of ACF-3-ionic after 48 cycles.

Chapter 4: Improved Capacitive Behavior of Birnessite Type Mn Oxide Coated on Activated Carbon Fibers

A version of this chapter has been published in the Journal of the Electrochemical Society:

Z. Abedi, D. Leistenschneider, W. Chen and D.G. Ivey, "Improved Capacitive Behavior of Birnessite Type Mn Oxide Coated on Activated Carbon Fibers", J. Electrochem. Soc., 2022, vol. 169, p. 010507.

4.1 Introduction

Electrochemical energy storage devices, such as rechargeable batteries and electrochemical capacitors, have received increasing attention due to their promising performance that can meet current power demands as well as the depletion in supply of fossil fuels. Electrochemical capacitors, that are capable of delivering higher power densities than batteries with reasonably high energy densities, have been shown to be useful for present day energy applications. [63,150,151] Electrochemical capacitors can store energy through either capacitive or pseudocapacitive mechanisms. The first type is also referred to as electrochemical double layer capacitors (EDLCs). EDLCs store energy through physical adsorption/desorption of ions at the electrode surface, while pseudocapacitive electrodes store charge via Faradaic reactions at the surface of the electrodes. [150,152,153]

Metal oxides, including manganese oxide, have been widely studied as inexpensive materials for pseudocapacitor devices. [23] Amongst all manganese oxide phases, birnessite type MnO_2 with a layered birnessite crystal structure shows promise as a material for pseudocapacitors due to its high theoretical specific capacitance (up to 1370 F g^{-1}) that is calculated based on the theoretical charge transfer energy of Mn^{4+} in birnessite to Mn^{3+} and Mn^{2+}. [154–156] However, this

theoretical value is affected by ionic and electronic conductivities, which decrease the practical specific capacitance of birnessite type MnO_2 to 100-300 F g^{-1} in most cases. [157–168]

Asphaltene is a solubility class, which is found in petroleum. It is separated from heavy petroleum by a solvent de-asphalting process. In bitumen production, asphaltene is removed prior to bitumen transport through pipelines to improve bitumen flow. As such, asphaltene has no further value for bitumen processing. Daily production by volume of bitumen in Alberta, Canada is around 260,000 m^3; ~20 wt% of this amount is asphaltene. [8,134,135] Because of its abundance, high carbon content and mainly polyaromatic nature, asphaltene represents a promising precursor for carbon fibers which can be utilized in EDLCs as well as pseudocapacitors. [2,9,169–175]

In this study, efforts are made to increase the specific capacitance of potassium birnessite type MnO_2 (referred to as birnessite type MnO_2 or δ-MnO_2 in this work) closer to its theoretical value by taking advantage of the high carbon content and conductivity of asphaltene based activated carbon fibers (ACF). Other Mn oxide/carbon composite electrodes have been studied in the literature; e.g., MnO_2/PANI by Zhu et al. [169] and MnO_2/carbon nanotubes (CNT) by Zhou et al. [174]. The effect of annealing in N_2 on the pseudocapacitive performance of δ-MnO_2, as well as the charge storage mechanism of this material, are also investigated. Carbon fibers activated using a chemical agent (KOH pellets), with a mass ratio of KOH/ACF = 3, were chosen based on previous work due to their high conductivity, high BET specific surface area (2290 m^2 g^{-1}) and total pore volume of 1.27 cm^3 g^{-1} and good capacitive performance. [9]

4.2 Experimental

4.2.1 Synthesis of Carbon Fibers

Asphaltene powder from bitumen production was processed into filaments, with a diameter of 10 µm, via a melt spinning procedure using an AT255 system from Anytester. Asphaltene was softened at 197 °C inside a box furnace. The soft asphaltene was pressed through a spinneret hole (diameter 0.15 mm) with a N_2 pressure of 400 kPa. The fibres were cooled under ambient conditions. In order to prevent melting of the fibrous material at elevated temperatures, the fibres were soaked in 2.7 M HNO_3 solution for 10 min and heat treated in air (air flow of 400 mL min^{-1}). A two-step temperature program was used. First of all, the material was heated to 140 °C at a rate of 0.5 °C min^{-1} and kept at this temperature for 161 min. Secondly, the temperature was raised to 300 °C with a heating rate of 0.5 °C min^{-1} and held for 120 min to achieve stabilized fibres (SF). The SF were then heated to 500 °C in a tube furnace, equipped with a quartz tube, under N_2 flow (80 mL min^{-1}), at a rate of 3 °C min^{-1} and held for 1 h to become pre-carbonized. Pre-carbonized fibers were mixed with dry KOH pellets with a KOH/fiber mass ratio of 3 and then carbonized and chemically activated at 800 °C for 2 h under the same N_2 flow and heating rate as for pre-carbonization. A final step of washing the fibers with a dilute HCl solution was employed to achieve the final activated carbon fibers.

4.2.2 Synthesis of δ-MnO_2 Powder and δ-MnO_2 Coated Activated Carbon Fibers

δ-MnO_2 powder was prepared by gradually adding and stirring a 2/3 molar ratio of $KMnO_4$/$MnSO_4(H_2O)$ in a mixture of 25 mL of deionized water and 100 mg of NaOH at 80 °C for 35 min. Three different batches of as prepared δ-MnO_2 powder (referred to as as-δ-MnO_2) were annealed at 300 °C, 400 °C and 500 °C in a tube furnace under N_2 flow (80 mL min^{-1}) with a heating rate of 5 °C min^{-1} and held for 3 h. These samples are denoted as 300-δ-MnO_2, 400-δ-MnO_2 and 500-δ-MnO_2, respectively. δ-MnO_2 was coated on ACF by adding 80 mg of ACF to the stirring solution (referred to as ACF-as-δ-MnO_2). ACF-as-δ-MnO_2 was then annealed at 400

°C (ACF-400-δ-MnO_2) in the same N_2 flow with the same heating rate as explained above and held there for 3 h. 400 °C was chosen for annealing ACF-as-δ-MnO_2 because annealing the δ-MnO_2 powder at 400 °C significantly improves the capacitive performance (discussed in the first paragraph of the Capacitive Performance section).

4.2.3 Preparation of the Electrodes

A mixture of 90 wt% active material (ACF, Mn oxide powder or δ-MnO_2 coated ACF), 5 wt% carbon black and 5 wt% polytetrafluoroethylene (PTFE, suspension) was prepared by mixing the components at 70 °C using an agate mortar and pestle to form homogeneous electrode films. The electrode films were then pasted onto a carbon paper (Fuel Cell Store: Toray Paper 060-TGP-H-060) as the structural support. Initial electrochemical testing was done with the Mn oxide powders (as-δ-MnO_2, 300-δ-MnO_2, 400-δ-MnO_2 and 500-δ-MnO_2) to determine the optimum annealing condition and the effects of annealing. After finding the optimum annealing temperature (400 °C), more electrochemical and characterization tests were conducted on ACF-400-δ-MnO_2. The mass loadings for each electrode prepared with Mn oxide powder and δ-MnO_2 coated ACF were ~7 mg cm^{-2} and 4 mg cm^{-2}, respectively. Mass loading includes the mass of active material (Mn oxide powder or δ-MnO_2 coated ACF), PTFE and carbon black.

4.2.4 Preparation of Pseudocapacitor Cells

For half-cell tests, 1 cm^2 pieces of prepared electrodes were used as the working electrode. A Pt wire counter electrode and Hg/HgO reference electrode were used in 100 ml of 1 M Li_2SO_4 as the electrolyte.

Coin cells were employed for full-cell electrochemical testing of the prepared electrodes. The electrodes were cut into 1.92 cm^2 disks; each disk had a thickness of 150-200 µm. Two electrode disks with equal mass and thickness were pressed onto stainless steel current collectors, using a

conductive adhesive paint (a mixture of carbon black, PTFE and reagent alcohol) and were sealed with a separator that was soaked in 100 μL of 1 M Li_2SO_4.

A half-cell configuration was used to determine the proper voltage window as well as the presence of any redox reactions. A full-cell configuration was used to investigate the capacitive behavior and charge storage mechanism.

4.2.5 Materials Characterization

The crystal structures of δ-MnO_2 and annealed δ-MnO_2 were determined by X-ray diffraction (XRD), using a Rigaku Ultima IV with Cu K_α radiation with a scanning speed of 3 deg min^{-1} and a step size of 0.05 deg (zero background sample holders were used). The specific surface area (SSA) and pore size distribution of ACF were obtained through N_2 physical adsorption/desorption at 77 K using an Autosorb-iQ-XR system. Samples were outgassed at 100 ^oC for 4 h prior to the measurements. Quenched solid density functional theory (QSDFT) and Brunauer–Emmett–Teller (BET) methods were used to calculate the SSA. Pore size distribution was calculated from the adsorption curve using the QSDFT method, assuming slit and cylindrical pores, and the total pore volume was determined at a relative pressure of 0.95. Microstructure and composition of the samples were studied by field emission scanning electron microscopy (ZEISS Sigma 300 VP-FESEM), using both secondary electron (SE) images and energy dispersive X-ray (EDX) analysis. X-ray photoelectron spectroscopy (XPS) (PHI VersaProbe III scanning XPS Microprobe), with a monochromatic Al X-ray source operated at 210 W and a pass energy of 20 eV, was employed to determine the oxidation state of Mn oxide samples. Background subtraction was done using a Shirley-type background. Transmission electron microscopy (TEM), selected area electron diffraction (SAED) and EDX analysis, using a JEOL JEM-ARM200F microscope operating at an accelerating voltage of 200 kV, were done for

further microstructural and crystal structure analysis at a finer scale. CHNS elemental analysis, using a Flash 2000 Organic Analyzer, was utilized to evaluate the light element composition of ACF.

4.2.6 Electrochemical Measurements

A Biologic VSP potentiostat was used to investigate the capacitance performance of prepared coin cells. Cyclic voltammetry (CV with scan rates from 1 mV s^{-1} to 500 mV s^{-1}), galvanostatic charge/discharge with potential limitation (GCPL, specific currents from 40 mA g^{-1} to 4 A g^{-1}) and electrochemical impedance spectroscopy (EIS, frequency range from 50 mHz to 500 kHz) were utilized. To ensure that the results were repeatable, electrochemical tests for each sample were conducted at least three times.

4.2.7 Calculations

The capacitance from the discharge behavior of a single electrode (full-cell) at a constant current was determined from Equation 4.1. [123]

$$C_s = 4I\frac{\Delta t}{\Delta V\, m_t} \tag{4.1}$$

I is the current (A), C_s is the specific capacitance of the single electrode (F g^{-1}), Δt is the discharge duration (s), ΔV is the discharge voltage window (V) and m_t is the mass of active material in both electrodes (g).

Specific energy and power values were calculated from Equation 4.2 and Equation 4.3, respectively: [176]

$$E_s = \frac{\int_{t(V_1)}^{t(V_2)} V(t)\, dt}{3.6\, m_t} \tag{4.2}$$

$$P_s = \frac{\int_{t(V_1)}^{t(V_2)} V(t)\,dt}{3.6\, m_t\, \Delta t} \quad (4.3)$$

E_s and P_s are the specific energy (Wh kg^{-1}) and specific power (W kg^{-1}) of both electrodes used in the coin cell, respectively, and V_2-V_1=ΔV.

4.3 Results and Discussion

4.3.1 Characterization of Activated Carbon Fibers (ACF)

The nitrogen adsorption isotherm for ACF is shown in Figure 4.1(a) and the interpretation is based on the IUPAC classification for microporous materials. [113] For low relative pressures ($P\ P_0^{-1} < 0.05$, P = the equilibrium pressure and P_0 = the saturation vapor pressure of nitrogen at 77 K) there is a sharp increase in adsorbed volume with increasing pressure, followed by an almost flat plateau at higher relative pressures ($P\ P_0^{-1} > 0.1$). [113] The majority of the pores (0.88 $cm^3\ g^{-1}$ or 69.3 % of the total pore volume of 1.27 $cm^3\ g^{-1}$) are micropores with 0.29 $cm^3\ g^{-1}$ of narrow mesopores with a pore width just above 2 nm (Figure 4.1(b)). The BET SSA for ACF is 2290 $m^2\ g^{-1}$. SEM secondary electron (SE) images (Figure 4.1(c) and 4.1(d)) show that even after chemical activation, the fibers still retain their fiber shape with a rough and non-homogeneous surface morphology. The amount of carbon, hydrogen, nitrogen and sulfur in ACF, determined from CHNS analysis, are presented in Figure 4.1(e). The presence of some K from the activation step is the reason that the total mass percentage is not 100%.

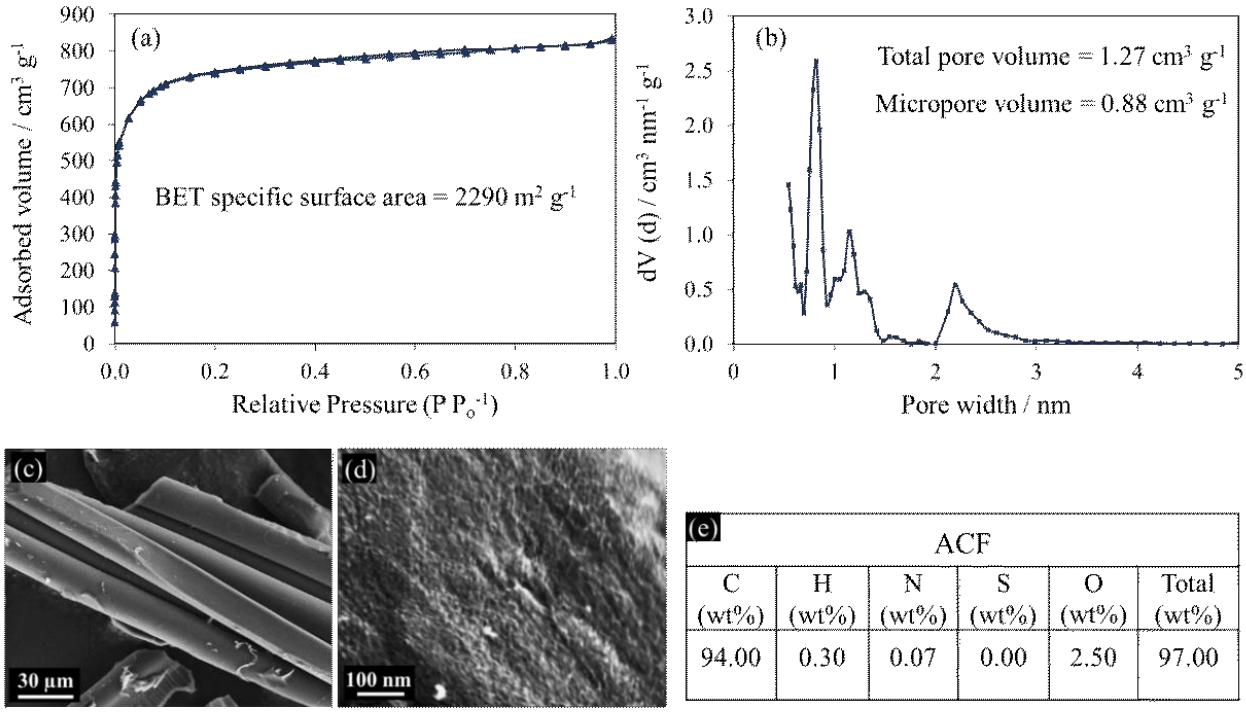

(e)

ACF					
C (wt%)	H (wt%)	N (wt%)	S (wt%)	O (wt%)	Total (wt%)
94.00	0.30	0.07	0.00	2.50	97.00

Figure 4.1. Microstructural details for ACF: a) Nitrogen adsorption/desorption isotherm at 77 K, b) pore size distribution calculated from the adsorption curve by the QSDFT method, c) and d) SEM SE images at low and high magnification and e) CHNS elemental analysis.

4.3.2 Characterization of Mn Oxide Powder and δ-MnO_2 Coated ACF

SEM SE images for as-prepared and annealed Mn oxide powder and δ-MnO_2 coated ACF samples are shown in Figure 4.2. As-δ-MnO_2 has a flake-like microstructure (Figure 4.2(a)) which changes to some degree during annealing. There is very little change on annealing to 400 ^oC; the nano-flake type morphology present in the as-prepared powder is maintained for the 300-δ-MnO_2 (Figure 4.2(b)) and 400-δ-MnO_2 (Figure 4.2(c)) samples. There is a distinct change in morphology at 500 ^oC (Figure 4.2(d)), which correlates with a phase transformation, as discussed in the XRD results. The SEM SE image of ACF-as-δ-MnO_2 shows that the surface of the fibers is fully coated with δ-MnO_2 (Figure 4.2(e)) and the coating has the same morphology as as-δ-

MnO_2 (Figure 4.2(f)). Annealing ACF-as-δ-MnO_2 at 400 °C (Figure 4.2(g) and (h)) leads to a δ-MnO_2 coating morphology similar to that for the 400-δ-MnO_2 powder samples.

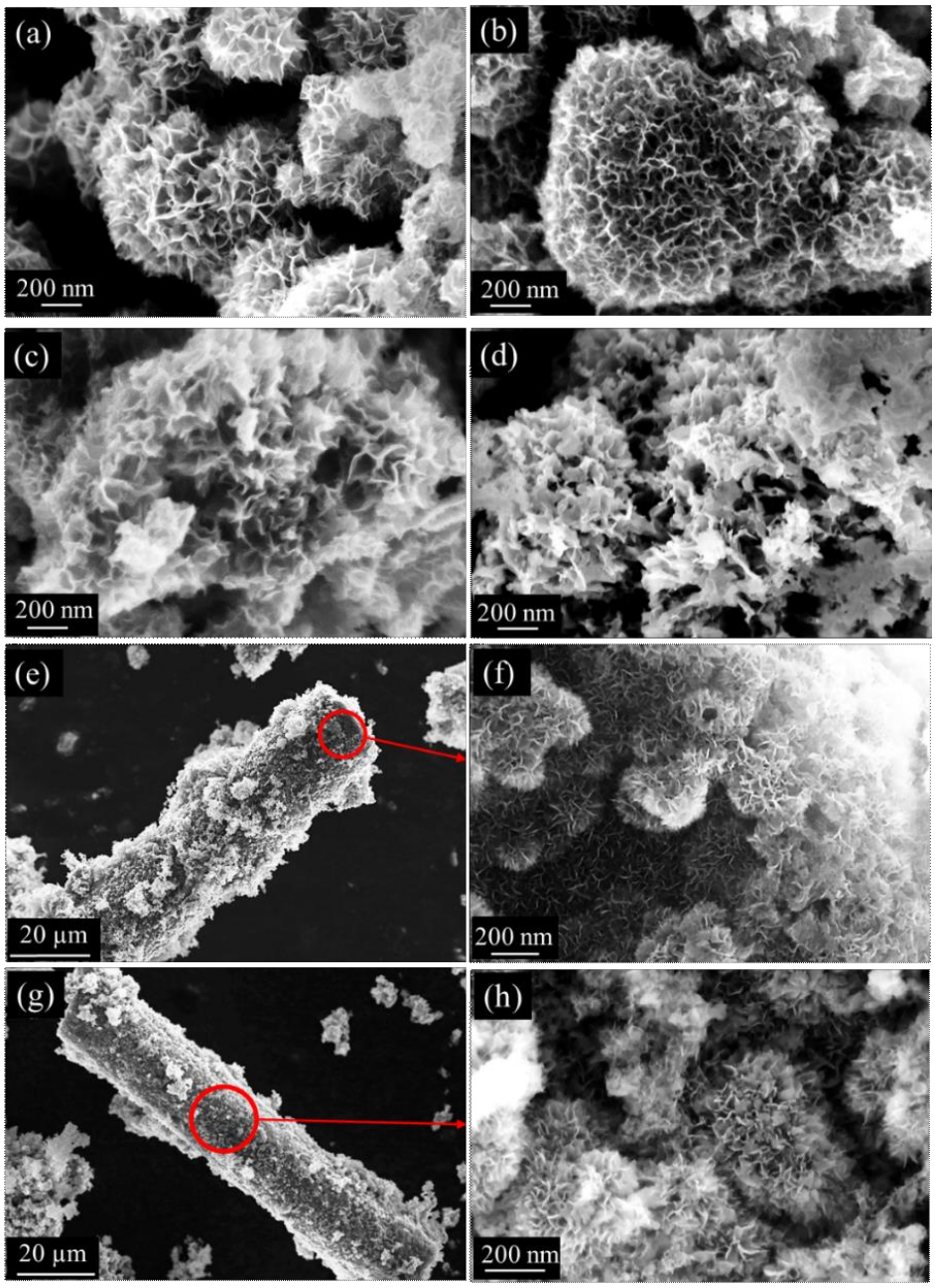

Figure 4.2. SEM SE images of a) as-δ-MnO_2, b) 300-δ-MnO_2, c) 400-δ-MnO_2, d) 500-δ-MnO_2, e) and f) ACF-as-δ-MnO_2 and e) and g) ACF-400-δ-MnO_2.

XRD patterns for as-prepared and annealed samples are shown in Figure 4.3. The as-δ-MnO_2, 300- δ-MnO_2 and 400-δ-MnO_2 samples have very similar XRD patterns which can be indexed to potassium birnessite hydrate ($K_{0.23}MnO_2(H_2O)_{0.7}$, JCPDS: 80-1098; monoclinic with a = 0.52 nm, b = 0.28, c = 0.72 nm and β = 100.76°). The XRD pattern for 500-δ-MnO_2 is different from the rest of the samples and can be indexed to a combination of Mn_3O_4 (JCPDS: 01-1127; tetragonal with a = b = 0.58 nm and c = 0.94 nm) and $KMnO_2$ (JCPDS: 12-0706; tetragonal with a = b = 0.98 nm and c = 0.29 nm). Upon annealing at 300 °C and 400 °C, peaks at 12.55° and 25.23° which correlate to the (001) and (002) crystallographic planes of $K_{0.23}MnO_2(H_2O)_{0.7}$, respectively, become less intense particularly at 400 °C, which is an indication of reduced crystallinity for the annealed samples compared with as-δ-MnO_2. The loss in peak intensity is proposed to correspond to partial removal of oxygen atoms (due to annealing is a N_2 reducing environment) and H_2O molecules from the structure. Similar to the discussion by Ma et al. [177], the (001) reflection of as-δ-MnO_2 represents the layered structure of birnessite MnO_2 and the (002) reflection is from the hydrated cation (potassium in this case) layers, inserted between the (001) layers. Pure δ-MnO_2 (JCPDS: 18-0802) does not have a reflection at 2theta ~25°. Thus, the reduction in the (002) peak intensity for as-δ-MnO_2 during annealing is likely due to removal of the hydrated molecules (present in the form of hydrated K^+) and the decrease in the (001) peak intensity is due to partial removal of O from the δ-MnO_2 microstructure. To summarize, it is proposed that annealing at temperatures less than 400 °C leads to a decrease in the crystallinity of δ-MnO_2 and damage to the microstructure, which may enhance pseudocapacitive activity. Annealing at 500 °C results in phase transformation to Mn_3O_4 and $KMnO_2$.

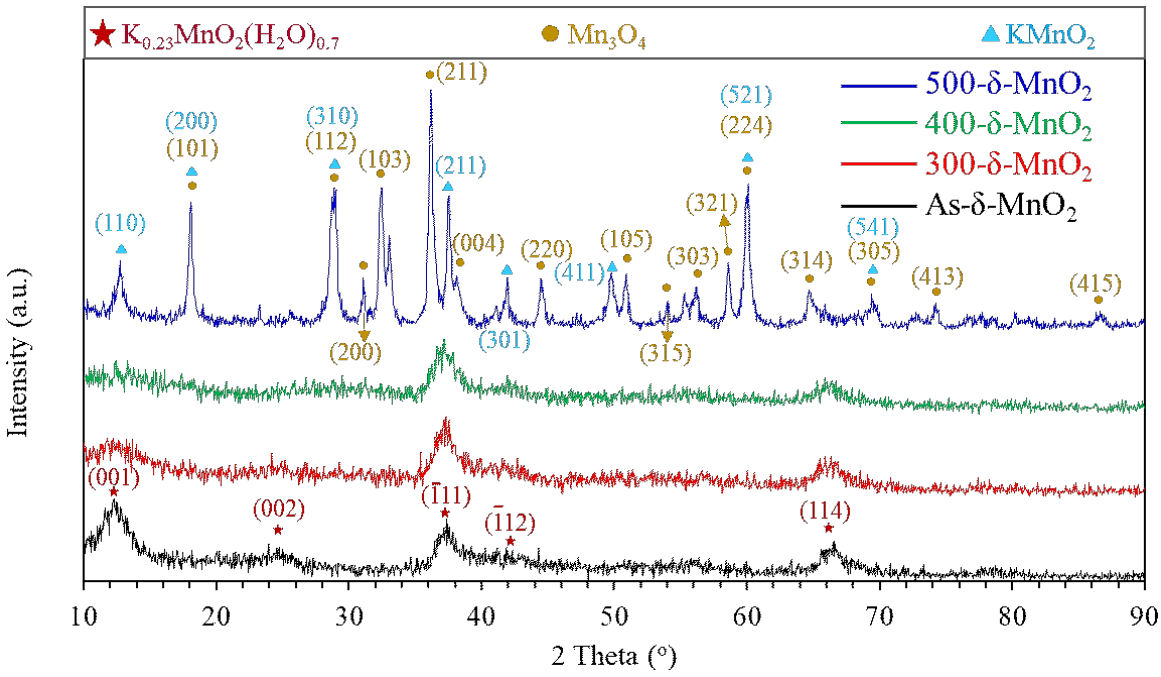

Figure 4.3 XRD patterns for Mn oxide samples. PDF files – potassium birnessite hydrate ($K_{0.23}MnO_2(H_2O)_{0.7}$): 80-1098, Mn_3O_4: 01-1127 and $KMnO_2$: 12-0706.

The as-δ-MnO_2 and 400-δ-MnO_2 samples were further characterized using TEM, because of the subtle changes in structure detected by XRD. TEM EDX analysis of as-δ-MnO_2 (supporting information, Figure SI4.1) shows overlapping Mn, O and K maps, confirming the potassium birnessite MnO_2 structure. TEM and high resolution TEM (HRTEM) images for the as-δ-MnO_2 and 400-δ-MnO_2 samples are shown in Figure 4.4(a)-(b) and 4(e)-(f), respectively. The nano-flakes that were observed in the SEM images are also present in the TEM images of the two samples (Figure 4.4(a) and 4.4(e)). SAED patterns for both as-δ-MnO_2 (Figure 4.4(d)) and 400-δ-MnO_2 (Figure 4.4(g)) show three fairly weak diffraction rings, with d-spacings of 0.240 nm, 0.211 nm and 0.138 nm. These can be indexed to potassium birnessite MnO_2 ($K_{0.23}MnO_2(H_2O)_{0.7}$, JCPDS). Figure 4.4(c) shows a single crystal SAED pattern from as-δ-MnO_2 with a [001] orientation. The diffraction rings are more well-defined in the diffraction

pattern for as-δ-MnO_2 than for 400-δ-MnO_2, which is consistent with the XRD patterns, and indicates a decrease in crystallinity due to the loss of oxygen and hydrated molecules during the annealing. The layered structure of birnessite, from the (001) planes with a d-spacing ~0.70 nm, is more distinct for 400-δ-MnO_2 compared with as-δ-MnO_2. This may be related to the removal of the hydrated cation (K^+) layer ((002) planes) from the microstructure after annealing which makes the (001) planes of the birnessite easier to image.

The oxidation state of Mn in as-δ-MnO_2 and 400-δ-MnO_2 was determined by XPS analysis (Figure 4.4(h)-4(k)). As an example, the survey spectrum for the as-δ-MnO_2 is shown in Figure SI4.2. Peak splitting of the Mn 3s and 2p spectra was used to determine the oxidation state. The C 1s spectrum is attributed to alkyl carbon (C-C, C-H) and was set to a binding energy of 285.0 eV to calibrate all XPS spectra. Due to fewer unpaired electrons in the 3d orbital, splitting of the 3s peak decreases with increasing Mn valence. The peak splitting reported by Gorlin and Jaramillo and Ilton et al. for a Mn^{4+} 3s peak is in the range of 4-4.5 eV. [178,179] The Mn 3s region for both samples consists of two peaks with peak splitting of 4.54 eV (Figure 4.4(h) and 4(j)). The high resolution Mn 2p spectrum shows two peaks with peak splitting of 11.46 eV for as-δ-MnO_2 and two peaks with peak splitting of 11.44 eV for 400-δ-MnO_2 sample (Figure 4.4(i) and 4.4(k)). According to Wu et al., peak splitting for Mn 2p is 11.5 eV for a valence of 4^+, while Zhang et al. indicate peak splitting for Mn 2p of 11.6 eV for the same valence. [164,180] The peak splitting for both the Mn 3s and 2p spectra for as-δ-MnO_2 and 400-δ-MnO_2 coincides with an oxidation state of 4^+ for Mn, confirming that no phase transformation occurs during the annealing step. [16,120,163,164,178,181]

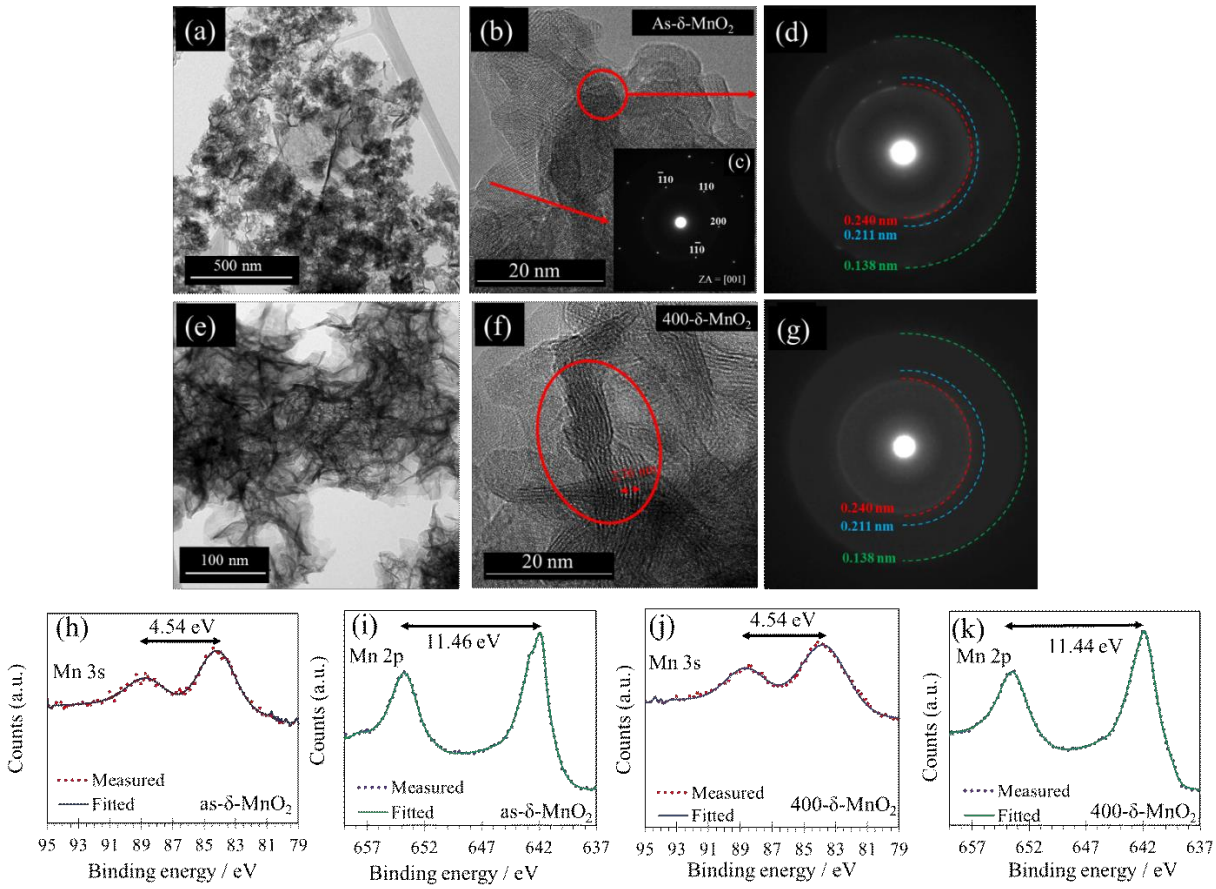

Figure 4.4. a)-d) TEM, HRTEM and SAED analysis for as-δ-MnO_2, d)-g) TEM, HRTEM and SAED analysis for 400-δ-MnO_2, (h) Mn s and (i) Mn 2p XPS spectra for as-δ-MnO_2 and (j) Mn 3s and (k) Mn 2p spectra for 400-δ-MnO_2.

N_2 adsorption/desorption isotherms for as-δ-MnO_2, 300-δ-MnO_2 and 400-δ-MnO_2 represent isotherms for nonporous or macroporous materials (Figure 4.5(a), type II isotherm [113]). 400-δ-MnO_2 has the highest adsorbed volume at all relative pressures. The SSA of δ-MnO_2, calculated using the BET method, increases by annealing at 300 ^oC and 400 ^oC (Figure 4.5(b)). The BET SSA values for as-δ-MnO_2 and 400-δ-MnO_2 are 88 $m^2\ g^{-1}$ and 141 $m^2\ g^{-1}$, respectively. Similar to SSA, the total pore volume for 400-δ-MnO_2 is higher than the total pore volume for as-δ-MnO_2 (0.20 $cm^3\ g^{-1}$ for as-δ-MnO_2 and 0.43 $cm^3\ g^{-1}$ for 400-δ-MnO_2). Figure 4.5(c) shows that

400-δ-MnO_2 has the highest cumulative pore volume and total pore volume. In addition, most of the total pore volume for all three samples is from mesopores and macropores. Pore size distribution results show that annealing at 400 ^oC leads to an increase in the mesopore volume (at all pore widths). The increase in the SSA and total pore volume by annealing at 400 ^oC and 300 ^oC is likely due to the partial removal of oxygen, the removal of the hydrated molecules and the introduction of O deficient defects in the microstructure. The BET SSA values for ACF-400-δ-MnO_2, 400-δ-MnO_2 and ACF are 179 $m^2 g^{-1}$, 141 $m^2 g^{-1}$ and 2290 $m^2 g^{-1}$, respectively (Figure SI4.3). Both ACF-400-δ-MnO_2 and 400-δ-MnO_2 have type II isotherms (nonporous or macroporous materials). The MnO_2 coated carbon fiber sample (ACF-400-δ-MnO_2) has a significantly lower SSA than the bare fibers (ACF) because of the good coverage of MnO_2 on the fibers, which limits fiber exposure. ACF-400-δ-MnO_2 has a higher SSA than the annealed MnO_2 powder (400-δ-MnO_2) since some of the carbon fibers are exposed in ACF-400-δ-MnO_2, providing some contribution from the fibers (ACF).

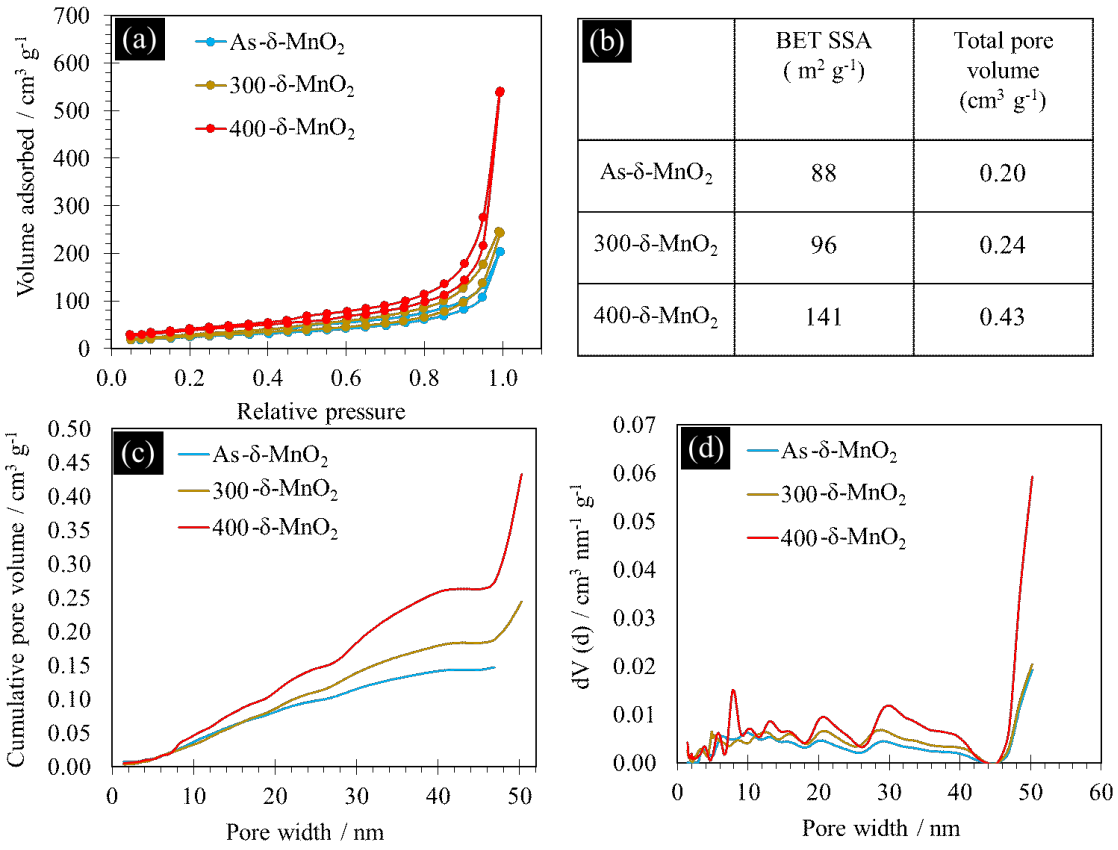

(b)	BET SSA (m^2 g^{-1})	Total pore volume (cm^3 g^{-1})
As-δ-MnO_2	88	0.20
300-δ-MnO_2	96	0.24
400-δ-MnO_2	141	0.43

Figure 4.5. N_2 physisorption test results for as-δ-MnO_2, 300-δ-MnO_2 and 400-δ-MnO_2 at 77 K. (a) adsorption/desorption isotherm, (b) BET specific surface area and total pore volume, (c) cumulative pore volume and (d) pore size distribution.

4.3.3 Capacitive Performance

To investigate the effect of annealing on the capacitive performance of the as-δ-MnO_2 and annealed samples, CV (scan rate: 10 mV s^{-1}) and GCPL (0.04-4 A g^{-1}) tests were conducted on the powder samples (Figure SI4.4). The CV test results (Figure SI4.4(a)) indicate that 400-δ-MnO_2 has the largest area under the curve which means that 400-δ-MnO_2 has the highest specific capacitance amongst the samples. This is in agreement with the specific capacitance values obtained from the GCPL tests (Figure SI4.4(b)) which show that 400-δ-MnO_2 has the highest specific capacitance at all specific currents (i_s). Specific capacitance values for 400-δ-MnO_2 are

195 and 117 F g^{-1} at 0.04 and 4 A g^{-1}, respectively, which are improved compared with as-δ-MnO_2 (155 and 100 F g^{-1} at 0.04 and 4 A g^{-1}, respectively). It is proposed that annealing at 400 ^oC removes hydrated molecules and O from the (002) and (001) crystallographic planes of as-δ-MnO_2, providing more adsorption/desorption and intercalation sites for the electrolyte species (Li^+). Thus, 400 ^oC was chosen for annealing of ACF-as-δ-MnO_2.

Half-cell tests, in a three-electrode configuration with a Pt wire counter electrode and a Hg/HgO reference electrode, were conducted on ACF-400-δ-MnO_2 to investigate the presence of redox reactions and the stability of the electrodes at different voltage windows. Figure 4.6(a) shows the half-cell CV tests for ACF-400-δ-MnO_2 at a scan rate of 10 mV s^{-1}, which indicate that the electrode is stable up to a voltage of 1 V vs. Hg/HgO. In fact, scanning at up to at least 0.8 V vs. Hg/HgO is necessary to observe the redox peaks (both charge and discharge peaks at ~0.6 V vs. Hg/HgO). The oxygen evolution reaction (OER) that starts at ~1 V vs. Hg/HgO and creates a spike in the current is the limiting factor for the voltage window. It was also observed that the electrode made with ACF-400-δ-MnO_2 needs to be cycled at least 10 times for the redox peaks to appear; the first cycle does not show any peaks. Electrolyte penetration in the electrode material becomes easier due to wetting of the electrode during the first few cycles, which enhances the redox reactions (Li^+ intercalation) occurring at the surface of the electrode. By cycling the electrode (using CV) up to 200 cycles, the peak position and intensity remain almost the same (Figure 4.5(b)). The intensity of the redox peak is relatively low and the overall CV curves look semi-rectangular which is likely due to the presence of double layer capacitance (from ACF) in addition to pseudocapacitance (from δ-MnO_2).

CV curves, measured from the symmetric full-cell configuration, look almost rectangular for all scan rates. Because of the symmetric nature of the full-cell design, the redox peaks are not fully

visible in the CV curves (Figure 4.6(c)). The specific capacitance values at different i_s values were calculated from the GCPL tests in full-cell configurations (Figure 4.6(d)). C_s values for both ACF-400-δ-MnO_2 and 400-δ-MnO_2 decrease as i_s increases, which is likely because the time available for Li^+ intercalation/de-intercalation reactions is not adequate at high i_s. Coating 400-δ-MnO_2 on ACF leads to a considerable increase in C_s (at all i_s values) compared with 400-δ-MnO_2 (powder). C_s values for ACF-400-δ-MnO_2 and 400-δ-MnO_2 are 328 F g^{-1} and 195 F g^{-1} (at 0.4 A g^{-1}), respectively, which drop to 251 F g^{-1} and 117 F g^{-1}, respectively, by increasing i_s to 4 A g^{-1}. This improvement in capacitive behavior is likely due to the direct growth of δ-MnO_2 on ACF. It has been shown that ACF has desirable conductivity and porosity. [9] The direct growth provides a synergistic effect between the high conductivity of ACF and high theoretical capacitance value of δ-MnO_2. The cycling behavior of ACF-400-δ-MnO_2 is much more stable than that of 400-δ-MnO_2 (Figure 4.6(e)). ACF-400-δ-MnO_2 retains ~94% of its initial C_s at 1 A g^{-1} after 10,000 cycles (initial and final C_s values are 296 F g^{-1} and 279 F g^{-1}, respectively) while 400-δ-MnO_2 only retains 64% of its initial C_s (initial and final C_s values are 154 and 98 F g^{-1}, respectively) after 10,000 cycles. The excellent cycling behavior of ACF-400-δ-MnO_2 is probably a result of the direct growth of δ-MnO_2 on ACF that has led to efficient absorption/desorption of Li^+. Charge/discharge (GCPL) curves at 100 and 10,000 cycles are quite symmetric; no obvious plateau is observed (Figure 4.6(f)). Also a minor degradation in the capacitive behavior is indicated by no major change in the iR drop and GCPL shapes that are quite identical for 100 cycles and 10,000 cycles.

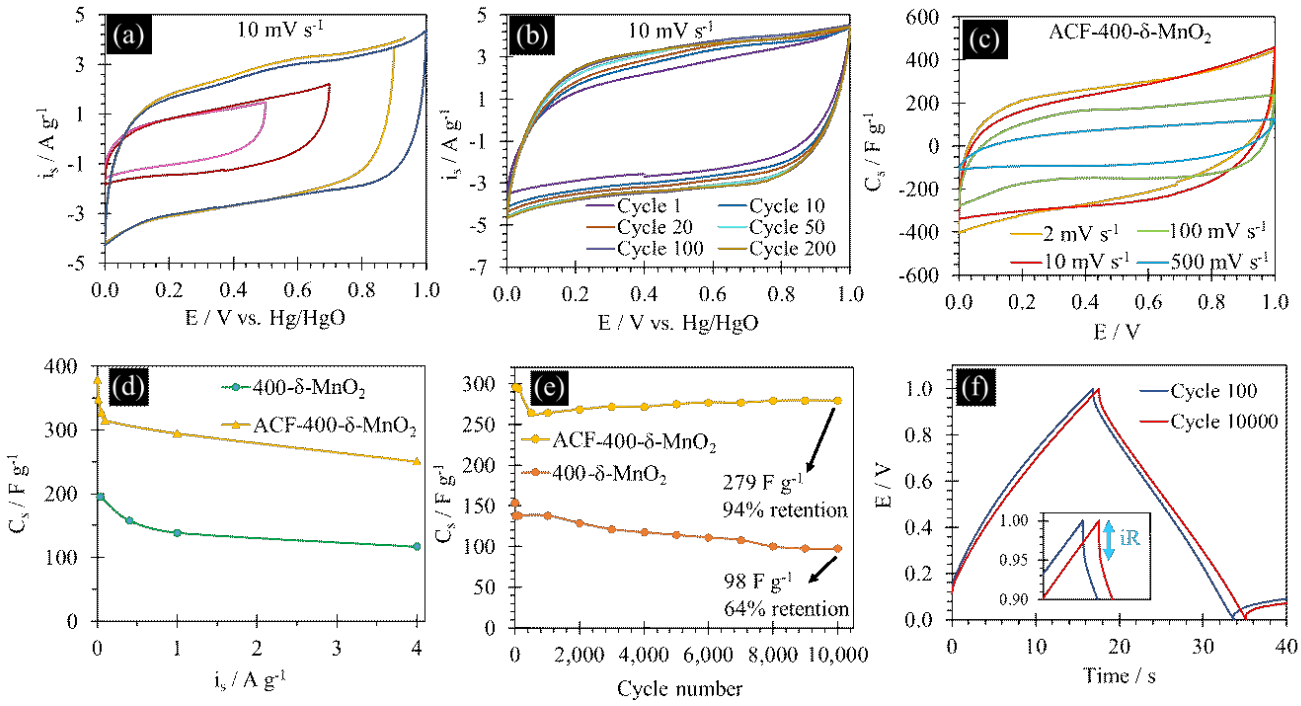

Figure 4.6. Electrochemical tests results. (a) and (b) Half-cell CV tests at a scan rate of 10 mV s^{-1}, (c) full-cell CV tests at scan rates 2-500 mV s^{-1}, (d) specific capacitance values calculated from the GCPL tests for ACF-400-δ-MnO_2 and 400-δ-MnO_2, (e) charge/discharge cycling test results at 1 A g^{-1} and (f) GCPL curves for cycle numbers 100 and 10,000.

The presence of redox peaks in the half-cell CV test results and the quite symmetric GCPL curves indicate a more pseudocapacitive behavior rather than pure battery or pure double layer capacitor behavior. [67]

The performance of ACF-400-δ-MnO_2 in Li_2SO_4 is superior to that of ACF in terms of the CV tests results at all scan rates (Figure SI4.4(c)); the capacitance is lower and the CV area is smaller for ACF. Because the performance of ACF-400-δ-MnO_2 is better than that of ACF or 400-δ-MnO_2 alone and all the calculated capacitance values for ACF-400-δ-MnO_2 are normalized by the total mass of ACF and 400-δ-MnO_2, it is concluded that the direct growth of 400-δ-MnO_2 on ACF is effective and improves capacitive performance.

The mass of ACF is small compared with 400-δ-MnO_2 in ACF-400-δ-MnO_2 (19 wt% ACF and 81% 400-δ-MnO_2) and the ACF surface is fully coated. As such, the contribution of ACF to the capacitive behavior is likely negligible, although it provides a conductive substrate for 400-δ-MnO_2.

A Ragone plot for ACF-400-δ-MnO_2 and 400-δ-MnO_2, that includes the specific energy and power values calculated from the GCPL tests, is given in Figure SI4.5. Values were normalized by the total mass of both electrodes in a coin cell device. Coating 400-δ-MnO_2 on ACF increases the energy and power values significantly when compared with the 400-δ-MnO_2 powder itself. For example, ACF-400-δ-MnO_2 can deliver a specific power of ~7 kW kg^{-1} at a specific energy of ~4.2 Wh kg^{-1} (at 1 A g^{-1}), while 400-δ-MnO_2 only delivers 240 W kg^{-1} at 2.4 Wh kg^{-1} (at 1 A g^{-1}). This significant improvement in the energy and power values is likely due to the intimate coating of 400-δ-MnO_2 on ACF.

To investigate the charge storage mechanism, SEM and XRD analysis were conducted on electrodes prepared with ACF-400-δ-MnO_2, in three different stages: pristine, charged and discharged. Charged and discharged electrodes were cycled for 50 times before they were fully charged or discharged (Figure SI4.6). SEM images of the pristine electrode (Figure SI4.6(a)), charged electrode (Figure SI4.6(c)) and discharged electrode (Figure SI4.6(e)) show the 400-δ-MnO_2 coated ACF amongst PTFE, carbon black and 400-δ-MnO_2 particles. The high magnification SEM image of the pristine electrode (Figure SI4.6(b)) shows the nano-flake morphology of 400-δ-MnO_2 that was previously observed in the ACF-400-δ-MnO_2 sample (Figure 4.2(h)). The nano-flake like morphology of the 400-δ-MnO_2 coating on ACF was retained in the charged (Figure SI4.6(d)) and discharged (Figure SI4.6(f)) electrodes. The XRD patterns for the pristine, charged and discharged electrodes have two main peaks at ~18° and 25°

which correspond to the peaks in the carbon paper used for preparing the electrodes. It is noteworthy that 400-δ-MnO_2 XRD pattern (Figure 4.3) showed a mostly amorphous/nanocrystalline structure with two weak peaks at ~37.5º and ~67º. Because of interference from the carbon paper, the peaks from 400-δ-MnO_2 in the pristine, charged and discharged electrodes are even less intense. However, for all three samples, there is a peak at ~37.5º that corresponds to the (-111) plane of birnessite (compare Figure SI4.6(g) with Figure 4.3). The almost identical XRD patterns for the pristine, charged and discharged electrodes mean that no phase transformation occurs during charge/discharge of the electrodes.

The retention of the flake-like morphology, along with the XRD results, show that Li^{+1} intercalation takes place during charge and discharge, respectively, with no phase transformation.

A comparison between the results from this work and the literature for MnO_x pseudocapacitors in aqueous electrolytes is presented in Table 4.1. Demarconnay et al. have investigated the charge storage mechanism of birnessite-type MnO_2 with a specific capacitance of 150 F g^{-1} at 5 mV s^{-1}. [176] Deng et al. have investigated supercapacitor devices made with wheat flour derived carbon foam/δ-MnO_2 composites (WFCF/MnO_2) that reached specific capacitance values as high as 146 F g^{-1} at 1 A g^{-1} with a capacitance retention of 70% after 5000 cycles. The specific value reported in this work at 1 A g^{-1} (296 F g^{-1}) is higher than the one reported by Deng et al. (146 F g^{-1}). This could be due to the annealing step employed in this work that modified the microstructure, improving the capacitance of δ-MnO_2. [182] Ma et al. have fabricated pseudocapacitor devices with high stabilities that can reach a specific capacitance of 350 F g^{-1} at 1 A g^{-1} with a capacitance retention of 90% after 10,000 cycles. [183] Although the capacitance retention in this work is superior to that reported by Ma et al., the specific capacitance values reported by Ma et al. are higher than the ones reported here. This could be related to a couple of

factors: 1) the core-shell δ-MnO_2/carbon nanowires structure used in the work by Ma et. al., may have improved the conductance, SSA and porosity and, therefore, the performance of the device. 2) The capacitance values in Table 4.1 are normalized to the mass of active material and it is not clear whether the mass utilized by Ma et al. is just for MnO_x or the total mass. The total mass of the electrode was used for the current study. Chen et al. have fabricated flexible pseudocapacitor electrodes, employing electrodeposition of MnO_2 on carbon nanotube (CNT) films, which were activated by electrochemical anodic oxygen evolution that introduced some internal space into the films. [184] CNT/MnO_2 films reached a maximum specific capacitance of 300 F g^{-1} at a specific current of 0.1 A g^{-1} which dropped to 120 F g^{-1} at a specific current of 2 A g^{-1}. The capacitance retention of the device, tested at 0.5 mA cm^2, was 75% after 1600 cycles. [184] The higher specific capacitance values reported in this work (296 F g^{-1} at 1 A g^{-1}) may be due to the direct growth of δ-MnO_2 on ACF used for the electrodes compared with CNTs utilized in the work by Chen et al., as well as the microstructural defects in the annealed δ-MnO_2.

Table 4.1. Specific capacitance and capacitance retention comparison

Electrode material	**Electrolyte**	**Specific current or scan rate**	**Initial specific capacitance (F g^{-1})**	**Capacitance retention**
Birnessite MnO_2 powder [176]	0.1 M Na_2SO_4	5 mV s^{-1}	150	---
Carbon foam/δ-MnO_2 composites [182]	6 M KOH	1 A g^{-1}	146	70% after 5000 cycles
MnO_x@C@MnO_x [183]	6 M KOH	1 A g^{-1}	350	90% after 10000 cycles
CNT/MnO_2 [184]	1 M Na_2SO_4	0.1 A g^{-1}	300	75% after 1600 cycles
This work δ-MnO_2/carbon fiber	1 M Li_2SO_4	1 A g^{-1}	296	94% after 10,000 cycles

A recent study by Sun et al. has shown that annealing of as-prepared δ-MnO_2 in N_2 can result in an increase in the conductivity of the material. [185] However, there was no discussion on any structural changes, as shown in this work. The XRD patterns in the work by Sun et al. were measured in the range of 2θ equal to 15°-90° and do not show the (001) peak for birnessite type MnO_2 at ~12.5°. Also, no comparison (using TEM or XPS) of structural changes between the as-prepared δ-MnO_2 and the annealed samples was done by Sun et al.

In this work, annealing at low temperatures (400 °C) resulted in reduced crystallinity, providing more available sites for electrolyte ion intercalation, leading to improved pseudocapacitive performance compared with as-prepared birnessite type MnO_2. It has been shown previously that

amorphous materials have improved capacitive properties due to defects and increased disorder in the microstructure. [186–188]

4.4 Conclusions

Asphaltene based carbon fibers were chemically activated (ACF) to reach specific surface areas as high as 2290 $m^2 g^{-1}$. Birnessite type MnO_2 was directly grown on ACF to fabricate pseudocapacitor electrodes. Mn oxide was synthesized through precipitation methods, producing birnessite type-MnO_2 (δ-MnO_2). The capacitance of as-prepared birnessite type MnO_2 was relatively low, but was improved by annealing to modify the crystal structure. Annealing at 400 ^oC (400-δ-MnO_2) provided the best capacitive performance, so this material was directly coated on ACF to fabricate composite electrodes. The composite electrode had improved performance over MnO_2 powder alone; the capacitance increased from 140 F g^{-1} to 296 F g^{-1} at 1 A g^{-1} for electrodes made with δ-MnO_2 coated ACF (ACF-400-δ-MnO_2); ~94% of the initial capacitance was retained after 10,000 charge/discharge cycles. This composite device also delivered a specific energy of 1.27 kW kg^{-1} at a specific energy of ~6 Wh kg^{-1} (at 1 A g^{-1}). The good performance of ACF-400-δ-MnO_2 is attributed to the high conductivity of ACF that helps compensate for the low conductivity of MnO_2. Annealing at 400 ^oC introduced defects into the microstructure of δ-MnO_2 by reducing the crystallinity, thereby generating additional active sites for charge/discharge reactions. Intercalation of the electrolyte's ions (Li^{+1}) is believed to be the main reaction involved during charge/discharge.

4.7 Supporting Information

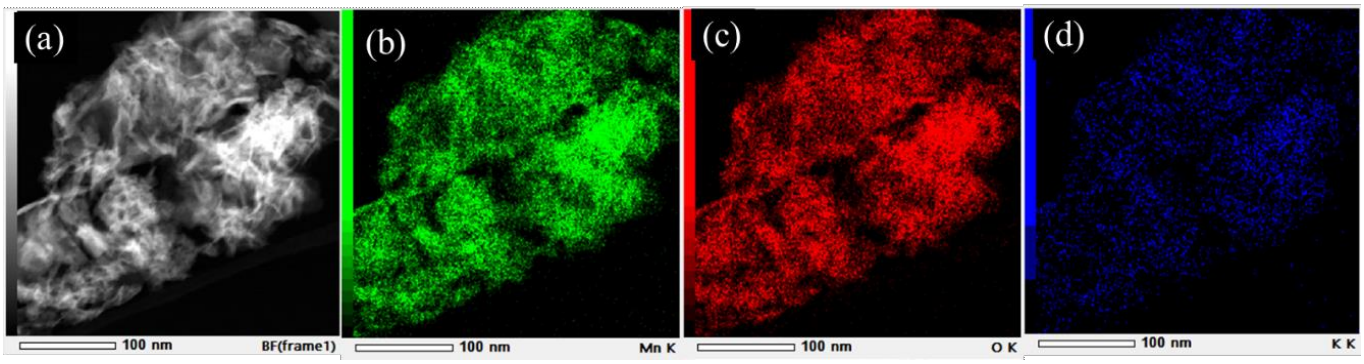

Figure SI4.1. STEM ADF image and EDX maps of as-δ-MnO_2.

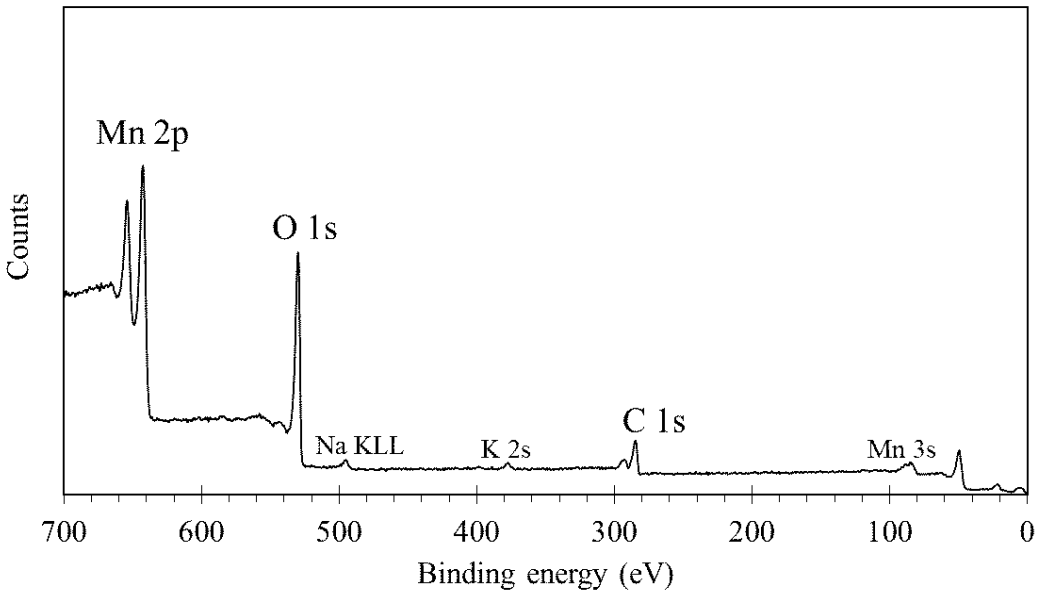

Figure SI4.2. XPS survey spectrum for as-δ-MnO_2.

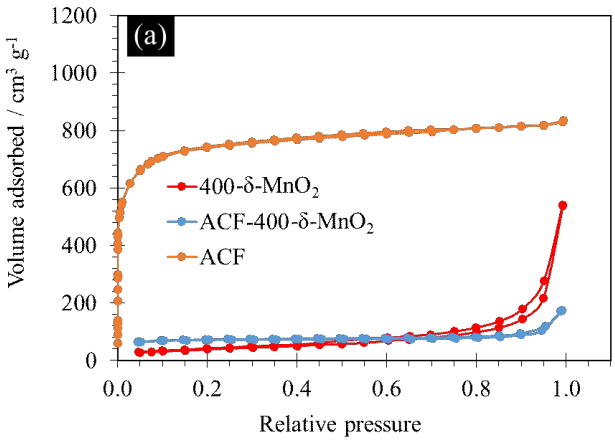

(b)	BET SSA (m^2 g^{-1})
400-δ-MnO_2	141
ACF	2290
ACF-400-δ-MnO_2	179

Figure SI4.3. N_2 physisorption comparison for ACF, 400-δ-MnO_2 and ACF-δ-MnO_2. (a) Isotherms and (b) BET SSA.

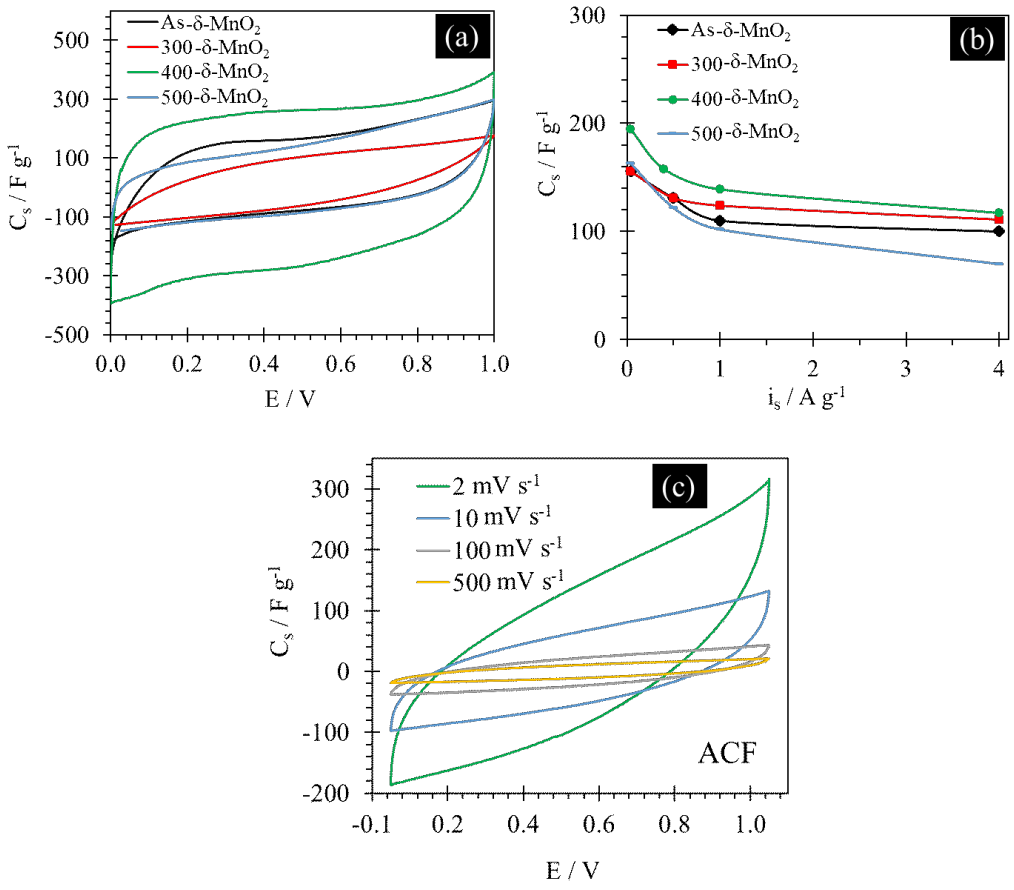

Figure SI4.4. (a) CV curves at 10 mV s^{-1}, (b) specific capacitance values (obtained from GCPL test results) for as-δ-MnO_2 and annealed samples and (c) CV curves at different scan rates for ACF measured in full-cell configurations.

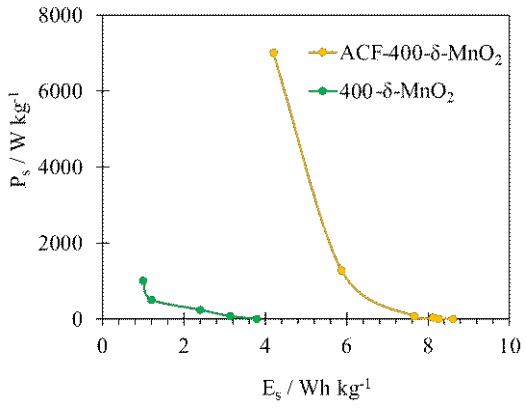

Figure SI4.5. A Ragone plot for ACF-400-δ-MnO_2 and 400-δ-MnO_2.

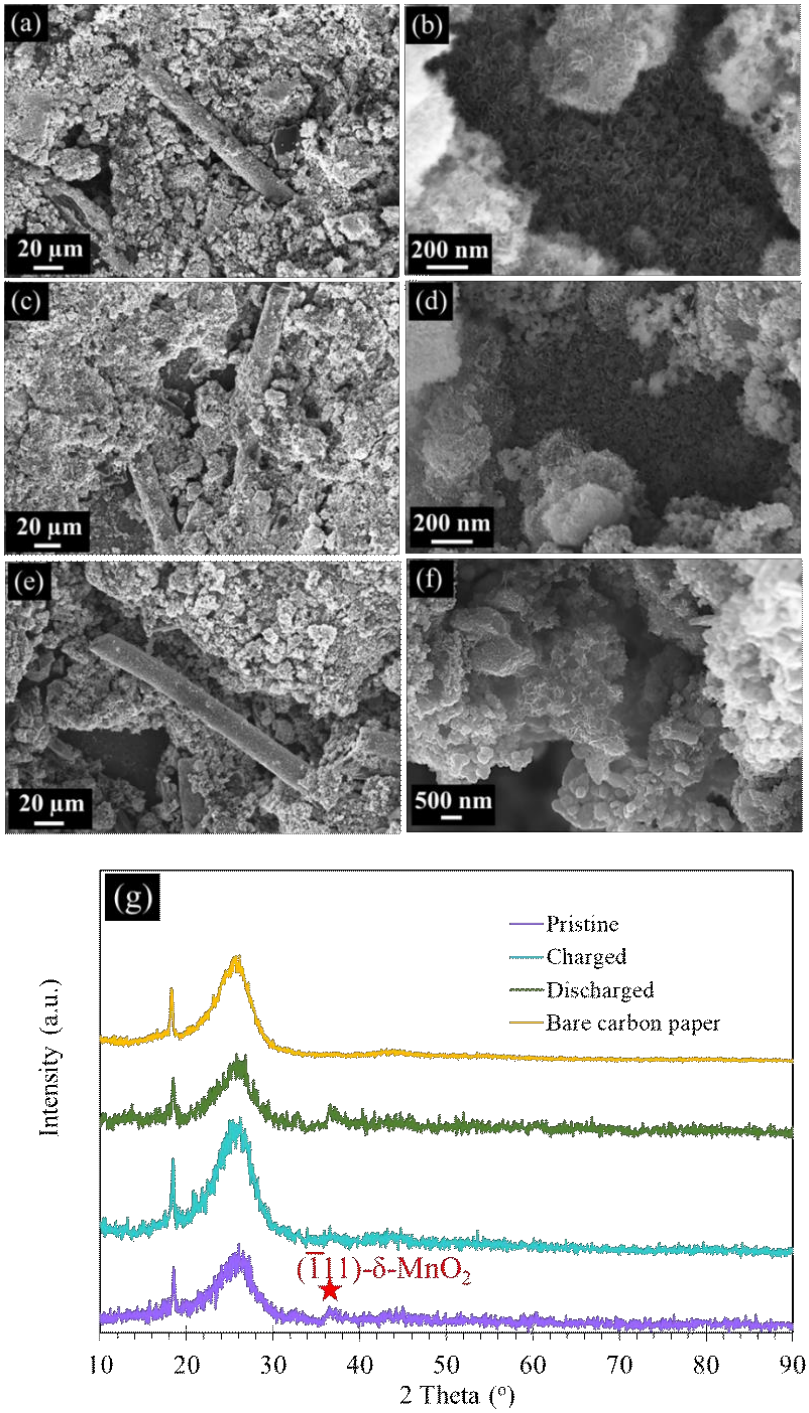

Figure SI4.6. SEM and XRD analysis of pristine, charged and discharged electrodes made with ACF-400-δ-MnO_2. (a) and (b): pristine electrode, (c) and (d): charged electrode, (e) and (f) discharged electrode and (g) XRD patterns.

Chapter 5: Spinel Type Mn-Co Oxide Coated Carbon Fibers as Efficient Bifunctional Electrocatalysts for Zinc-air Batteries

A version of this chapter has been published in the journal Batteries and Supercaps:

Z. Abedi, D. Leistenschneider, W. Chen and D.G. Ivey, "Spinel Type Mn-Co Oxide Coated Carbon Fibers as Efficient Bifunctional Electrocatalysts for Zinc-air Batteries", Batter. Supercaps, 2022, vol. 5, p. e202100339.

5.1 Introduction

Zinc-air batteries (ZABs) are considered as a safe and inexpensive energy storage solution as the world becomes less dependent on fossil fuels and moves toward renewable energy technologies. Compared with other commonly used batteries like Pb-acid batteries and Li-ion batteries, ZABs are low cost, non-polluting and safe. They can provide energy densities as high as 1048 Wh kg^{-1}. ZABs are currently used in hearing aids, navigation lights and railway signals. Their limited use is mainly because of their poor cycling behavior and low discharge/charge efficiencies. [26,189,190]

A metallic zinc electrode, an air electrode and a typical electrolyte, consisting of 6 M KOH + ~0.25 M Zn^{2+}, are the main components of a ZAB. The air electrode is usually carbon based; this electrode is often referred to as the gas diffusion layer (GDL). The oxygen reduction reaction (ORR) and oxygen evolution reaction (OER) take place at the surface of the air electrode during discharge and charge, respectively. Equation 1 shows the ORR; Equation 5.1 in reverse is the charge reaction (OER). [26,29,30,191,192]

$$O_2 + 2H_2O + 4e^- \xrightarrow{\text{discharge}} 4OH^- \qquad (5.1)$$

Nano-scale carbonaceous materials such as graphene nanosheets or powder, carbon nanotubes (CNTs) and nano scale carbon fibers are usually used to prepare air electrodes. Electrocatalysts are coupled with the air electrode via different methods like electrodeposition or atomic layer deposition (ALD). Preparation steps for these nano-scale carbon based materials are often costly and time consuming. A cost-effective carbonaceous precursor with a facile preparation method is desirable for preparing air electrodes. Asphaltene is a carbon rich and inexpensive (more supply than demand) by-product of partial upgrading of bitumen extracted from the oil sands. Asphaltene currently has no further value other than low quality fuel or landfill; however, it can be utilized to prepare micron-scale carbon fibers (CFs). [8,9,18,19,33,134,136,193–196]

Electrocatalysts in the air electrode play a vital role in improving the efficiency and cycling behavior of a ZAB, which tend to be limited by the inherent poor kinetics of the ORR and OER reactions that take place at the air electrode. Transition metal oxides have been employed as ORR/OER electrocatalysts in ZABs as alternatives to precious metals like Pt or Ru. Transition metal oxides, such as Mn, Co, Ni and Fe oxides demonstrate promising bifunctional catalytic activity towards ORR and OER. Their low cost, safety, abundance and ease of handling make them desirable for use as electrocatalysts in ZABs. Co based transition metal oxides have been shown to demonstrate strong OER catalytic activity, while Mn based transition metal oxides have good ORR catalytic activity. As such, combining the two oxides into Mn-Co mixed oxides has generated significant interest as bifunctional catalysts for metal-air batteries. [10,13,19,26,197,198]

In this work, carbon fibers (8-12 μm in diameter) are prepared through melt-spinning from asphaltene. These fibers are then coated with Mn-Co mixed oxides as bifunctional electrocatalysts for ZABs. Homemade GDLs are prepared, using the coated CFs. This work

shows that 1) costly nano-scale carbonaceous materials are not needed to prepare air electrodes or electrocatalysts, 2) ORR catalytic activity of homemade air electrodes, prepared with asphaltene based CFs (not coated with Mn-Co electrocatalyst), is similar to that of commercially available GDLs while presenting superior OER activity and 3) Mn-Co mixed oxide coated CFs display comparable or better cycling behavior and efficiency relative to similar metal oxide/carbon based electrodes in the recent literature. These electrodes are fabricated using a cost-effective procedure.

5.2 Experimental

5.2.1 Carbon Fiber Synthesis

Carbon fiber synthesis was done based on process developed by Zuo et al. [175] and Leistenschneider et al. [171] In a typical procedure, as-received asphaltene powder was processed into asphaltene fibers by a melt-spinning process. Melt spinning was done using an AT255 system from Anytester. Asphaltene powder was melted at 197 oC in a N2 atmosphere. The soft asphaltene powder was then pressed through a spinneret hole with a diameter of 15 µm and a N2 gas pressure of 400 kPa and collected on a rotating drum with a speed of 200 rpm. Afterwards, asphaltene fibers were cooled under ambient conditions. A one-step oxidation process was performed on the fibers followed by soaking in 3.2 M HNO3 for 10 min to prevent melting at elevated temperature. The fibrous material was heated to 300 °C at a heating rate of 1.5 °C min-1 and kept at this temperature for 120 min. Oxidized fibers were then divided into three batches; each batch was carbonized at 500 oC (CF-500), 800 oC (CF-800) or 1500 oC (CF-1500) for 2 h in N2. 1500 oC is the maximum temperature attainable by the furnace.

5.2.2 Electrocatalyst Coating Synthesis

CF-1500 was chosen as the substrate for Mn-Co mixed oxide coatings due to its superior ORR/OER catalytic activity compared with fibers carbonized at the other temperatures (see discussion in Section 4). 80 mg of carbonized fibers (CF-1500) were soaked in 20 ml of 28 wt% NH_4OH for 10 min to introduce N containing groups onto the surface of the carbonized fibers; the aim was to provide nucleation sites for the electrocatalyst coating. The fibers were then sonicated in a mixture of 30 ml of reagent alcohol, 100 mg of NaOH and a 500 mg mixture of Mn(II) acetate ($Mn(Ac)_2$ or $C_4H_6MnO_4$) and Co(II) acetate ($Co(Ac)_2$ or $C_4H_6CoO_4$) salts. The sonication time was varied from 0 h (MnCo-no sonication) to 6 h (MnCo-6h). The mass ratio of acetate salts, i.e., $Mn(Ac)_2/Co(Ac)_2$, in the sonication solution was 1:1 (250 mg of each salt). The sonication method in this work is similar to the one reported by Li et al. [199] for N-doped carbon nanotubes (N-CNT).

The sonication time that led to the best ORR/OER catalytic activity and full cell ZAB performance (5 h, discussed in Section 4) was chosen to prepare Mn-Co mixed oxide decorated CF-1500. Three mass ratios of acetate salts ($Mn(Ac)_2/Co(Ac)_2$) in the sonication solution were tested, i.e., 2:1 (333.33 mg of Mn salt and 166.67 mg of Co salt), 1:2 (166.67 mg of Mn salt and 333.33 mg of Co salt) and 1:1 (250 mg of Mn salt and 250 mg of Co salt), to investigate the effect of salts ratio. These samples are denoted as MnCo-5h-2:1, MnCo-5h-1:2 and MnCo-5h-1:1, respectively.

5.2.3 Electrode Preparation

Carbon fiber electrodes that were carbonized at different temperatures (without Mn-Co mixed oxide) were prepared by pasting a mixture of 90 wt% CF, 5 wt% polytetrafluoroethylene (PTFE) and 5 wt% carbon black onto carbon paper (Fuel Cell Store: Toray Paper 030-TGP-H-030).

Electrodes consisting of Mn-Co mixed oxide decorated CF-1500 fibers were prepared by pasting a mixture containing 90 wt% Mn-Co mixed oxide decorated CF-1500, 5 wt% PTFE and 5 wt% carbon black onto a hydrophobic carbon paper (Fuel Cell Store: Toray Paper 060-TGP-H-060). The carbon paper provided structural support and helped prevent electrolyte leakage during operation. Mass loading for each electrode was ~10 mg cm^{-2} of CF or Mn-Co mixed oxide coated CF-1500.

The electrochemical performance of the prepared electrodes, in both half-cell and full-cell configurations, was compared with electrodes fabricated with Pt-RuO_2 benchmark catalysts (referred to as Pt-Ru in this work). [22] The latter electrodes were spray coated on commercial GDL (Fuel Cell Store: Toray Paper 060-TGP-H-060) with a mass loading of ~0.5 mg cm^{-2}. The spray coating suspension was prepared by mixing 50 mg of Pt-RuO_2 powder (nominally 30 wt% Pt and 15 wt% RuO_2 combined with carbon black, purchased from Alfa Aesar), 1 ml of ethanol, 0.1 ml Nafion 5% and 2 ml of deionized water (DIW).

5.2.4 Materials Characterization

The crystal structure of CF was determined by X-ray diffraction (XRD), using a Rigaku Ultima IV system with Cu K_α radiation, a scanning speed of 3˚ min^{-1} and a step size of 0.05˚. Zero background sample holders were utilized. The microstructure and composition of the samples were determined through field emission scanning electron microscopy (ZEISS Sigma 300 VP-FESEM), using both secondary electron (SE) images and energy dispersive X-ray (EDX) analysis. X-ray photoelectron spectroscopy (XPS) (PHI VersaProbe III scanning XPS Microprobe), with a monochromatic Al X-ray source operated at 210 W and a pass energy of 20 eV, was employed to determine the oxidation state of Mn and Co in the Mn-Co mixed oxide coatings. All XPS spectra were calibrated using the C 1s peak at a binding energy of 285.0 eV

and the background was fitted using a Shirley approach. Transmission electron microscopy (TEM) and selected area electron diffraction (SAED), using a JEOL JEM-ARM200F microscope operating at an accelerating voltage of 200 kV, was utilized for further microstructural and crystal structure analysis at a finer scale. CHNS elemental analysis, with a Flash 2000 Organic Analyzer, was employed to evaluate the light element composition of the carbon fibers.

5.2.5 Electrochemical Measurements

A Biologic VSP potentiostat was used to investigate the ORR and OER catalytic activity of the CFs and Mn-Co mixed oxide coated CFs as well as full-cell ZAB performance. Linear sweep voltammetry (LSV at 5 mV s^{-1}) in a half-cell configuration with a Pt wire counter electrode and Hg/HgO reference electrode (+0.098 V vs. SHE) was utilized to determine the ORR and OER catalytic activity. Galvanostatic cycling with potential limitation (GCPL) at current densities (j) of ± 2 mA cm^{-2}, ± 5 mA cm^{-2}, ± 10 mA cm^{-2} and ± 20 mA cm^{-2} in a full-cell configuration with a 2 cm $\times$ 6 cm zinc sheet counter electrode was employed to determine the full cell charge and discharge potentials, potential gaps and efficiencies at each current density and the cycling behavior of the battery. 1M KOH and 6M KOH + 0.25 M ZnO were used as the electrolytes for half-cell and full-cell tests, respectively.

Onset potentials for ORR and OER are defined as the potentials at which current densities of -10 mA cm^{-2} and +10 mA cm^{-2} are achieved, respectively. The efficiency of each ZAB cell is defined as the discharge potential divided by the charge potential, i.e., V_{ORR}/V_{OER}, at the same discharge/charge current density. The potential gap is defined as $\Delta V = V_{OER} - V_{ORR}$ and the maximum current density achieved is defined as the current density at -0.5 V vs. Hg/HgO for ORR and at 0.9 V vs. Hg/HgO for OER.

5.3 Results and Discussion

5.3.1 Carbon Fiber Characterization and Catalytic Activity

XRD patterns for all three CFs correspond to the patterns for natural graphite (Figure 5.1). [200] The two main peaks at 26.5° and 44.4° can be indexed to the (002) and (101) planes, respectively (PDF#13-0148; hexagonal with a = 2.462 Å and c = 6.701 Å). [201] These two peaks are the sharpest and the strongest for CF-1500, which means that carbonization at 1500 ºC leads to the most graphitized structure with the highest carbon content CFs. It has been shown previously that higher carbonization temperatures for C based materials lead to increased graphitization. [202] Also, amongst all C based materials, graphite based ones (such as carbon nanotubes, sheets and powder) tend to show the best ORR/OER catalytic activity with long term operation stability. [34] In addition, a study by Ross et al. demonstrated that graphitized carbon has a reduced corrosion rate in harsh alkaline electrolytes, which could improve the cycling behavior of a ZAB in alkaline electrolytes. [203] For these reasons, 1500 ºC was chosen as the carbonization temperature for the fibers.

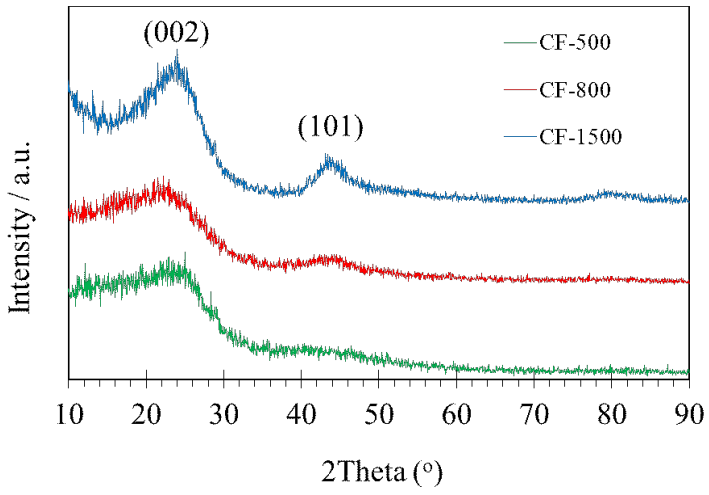

Figure 5.1. XRD patterns for CF carbonized at 500 ºC, 800 ºC and 1500 ºC.

Half-cell LSV curves in O_2 saturated 1 M KOH are shown in Figure 5.2. The ORR and OER activity increase as the carbonization temperature increases, which is related to an increase in graphitization degree. Graphite has been shown previously to provide active sites for ORR/OER. [22] The CF-1500 sample has the highest activity towards both ORR and OER with ORR and OER onset potentials of -0.23 V vs. Hg/HgO and 0.68 V vs. Hg/HgO, respectively. Also, the ORR activity of CF-1500 is comparable to that of commercial GDL. CF-1500 has a lower absolute onset potential than commercial GDL, while commercial GDL has a slightly higher maximum current density than CF-1500 (Figure 5.2(a)). The OER activity of CF-1500 is significantly better than that for commercial GDL; CF-1500 has a lower onset potential and a significantly higher maximum current density. The superior OER catalytic activity for electrodes made with CFs compared with commercial GDL is likely due to the presence of S and N containing groups in the CFs which can enhance OER catalytic activity. [204] Both S and N are present in the CF precursor, as reported previously, and the amounts were measured via CHNS analysis (Table SI5.1). [9,171]

CF-1500 was chosen as the substrate for Mn-Co mixed oxide ORR/OER bifunctional catalysts due to its promising catalytic activity and high graphitization degree (Figure 5.1).

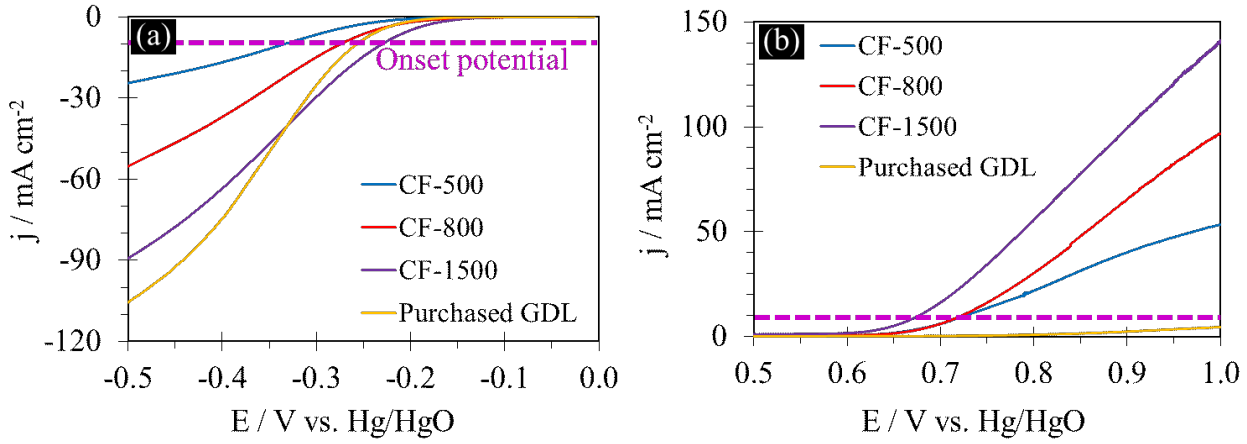

Figure 5.2. LSV tests at 5 mV s^{-1} showing (a) ORR and (b) OER catalytic activity of commercial GDL and homemade air electrodes prepared with CF-500, CF-800 and CF-1500.

5.3.2 Mn-Co Mixed Oxide Coated Carbon Fiber Characterization and Catalytic Activity

SEM SE images and EDX maps of Mn-Co mixed oxide coated CFs, prepared with no sonication, are shown in Figure 5.3(a)-(d) and exhibit a discontinuous coating on the fibers with a particle size in the 1 µm to 15 µm range. Mn, Co and O signals overlap, which indicates that a Mn-Co mixed oxide was produced. Sonication of the CF-1500 in the salt solution was done in an attempt to improve the quality of the mixed oxide coating on the fibers. The sonication time was varied from 1 h to 6 h and the corresponding SEM images and EDX maps are shown in Figure 5.3. Coating uniformity increased with increasing sonication time; for times 3 h or longer the entire fiber surface is covered with the mixed metal oxide. The oxide coating thickness increases with increasing sonication time, which can cause conductivity and charge transfer issues due to the insulating nature of the oxide. [205] Increasing the sonication time also creates patches of thicker oxide on the surface of the fibers (Figure 5.3(a, e, i, m, q and u)). This may not be a major issue in terms of conductivity and electron/species transfer due to the small amount of Mn-Co oxide catalyst relative to the carbon fibers. EDX quantitative analysis (Table 5.1) was done for each of

the areas shown in the SEM images in Figure 5.3; the sample subjected to 5 h of sonication had the highest amounts of Mn and Co. The amount of Mn-Co oxide coating increases with increasing sonication time up to 5 h and then levels off for longer times (6 h). Longer sonication times may result in some delamination of the oxide coating from the fibers leading to a decrease in the amount of oxide coating. The data in Table 5.1 indicates that the Mn:Co ratio is close to 1:1 for all samples, with the possible exception of the 4 h sample. The 1:1 ratio corresponds with the Mn:Co ratio of the salts used in the sonication solution.

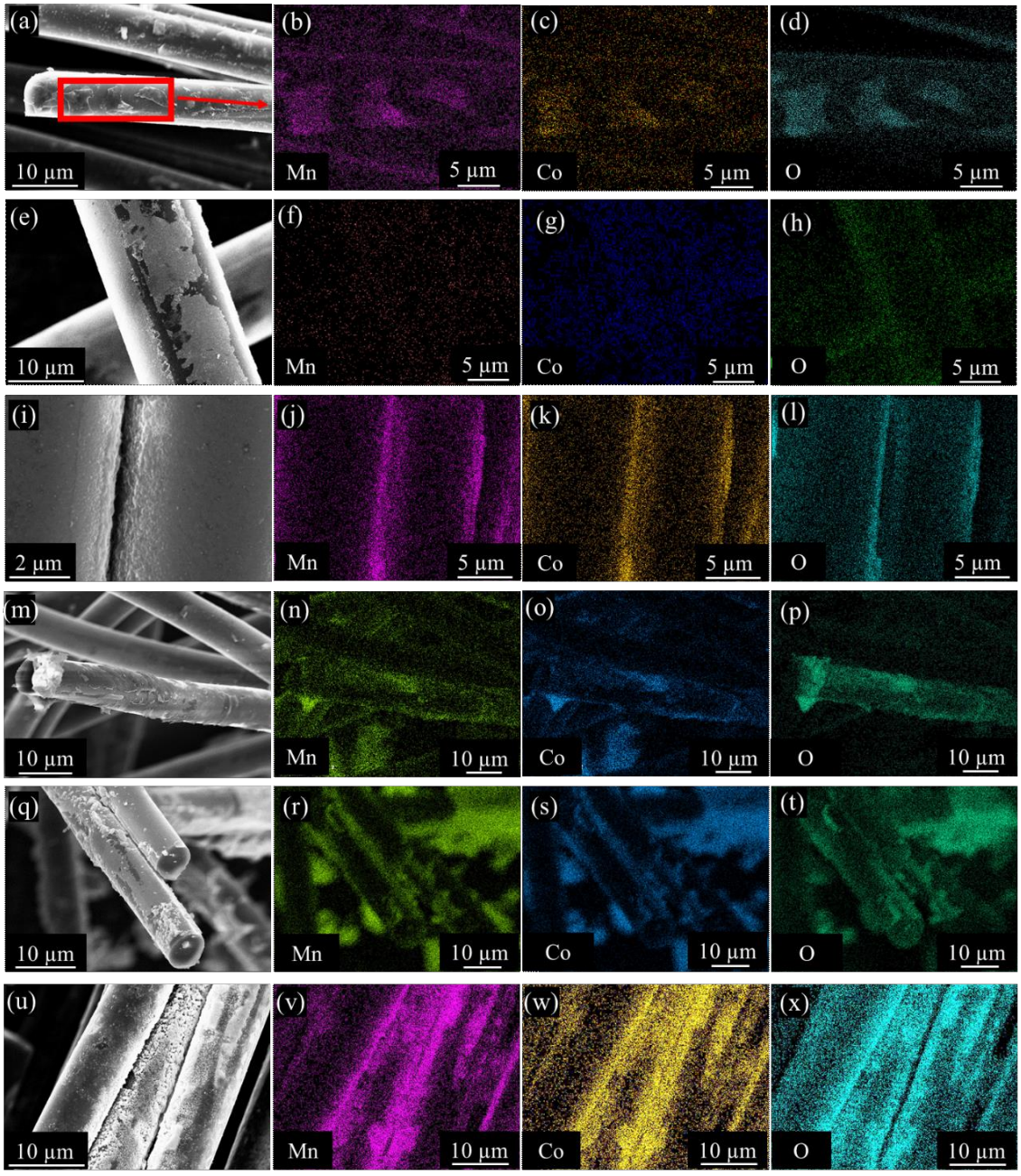

Figure 5.3. SEM SE images and EDX maps of Mn-Co mixed oxide coated carbon fibers with (a)-(d) no sonication, (e)-(h) 1 h, (i)-(l) 3 h, (m)-(p) 4 h, (q)-(t) 5 h and (u)-(x) 6 h of sonication.

Table 5.1. EDX quantitative analysis of Mn-Co mixed oxide coated CF-1500*

	Atomic %			Mass %		
Sample	Mn	Co	O	Mn	Co	O
1 h	0.25	0.25	6.3	1.1	1.2	5
3 h	0.39	0.35	13.2	1.6	1.6	16
4 h	0.51	0.72	10.1	2.1	3.2	12.3
5 h	1.63	1.85	17.6	6.2	7.6	19.5
6 h	1.0	1.0	16.6	4.2	4.2	19.3

* The amount of C, or other residual elements (e.g., S and N), is not included, therefore, the amounts do not add to 100%

LSV half-cell tests were carried out for the coated fiber electrodes and the Pt-Ru spray coated electrode (Figure 5.3). Among the sonicated samples, MnCo-5h has the lowest absolute ORR onset potential of -0.08 V vs. Hg/HgO and the lowest OER onset potential of 0.32 V vs. Hg/HgO (Table 5.2). These values compare favorably with Pt-Ru, with an ORR onset potential of -0.06 V vs. Hg/HgO and an OER onset potential of 0.63 V vs. Hg/HgO. In fact, the OER onset potential for MnCo-5h is significantly better than the value for Pt-Ru. MnCo-5h also has the highest ORR current density of -571 mA cm^{-2} at -0.5 V vs. Hg/HgO. Its maximum OER current density is the lowest (139 mA cm^{-2}) among all sonicated samples, but still exceeds the value for Pt-Ru. The half-cell test results indicate that a sonication time of 5 h is optimal for yielding the most efficient bifunctional electrocatalyst. MnCo-5h sample also has the largest amount of Mn-Co oxide coating on the CFs (Table 5.1).

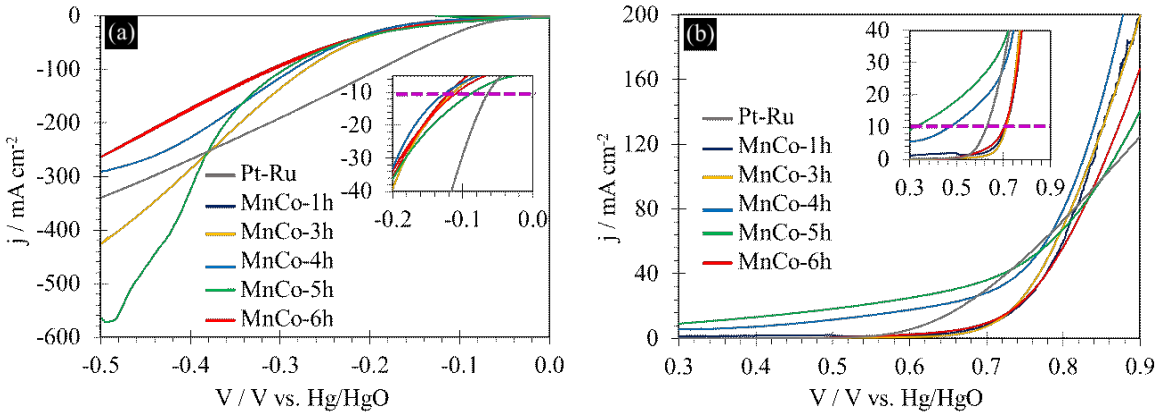

Figure 5.4. LSV half-cell test results at 5 mV cm^{-2}. (a) ORR and (b) OER catalytic activities for Mn-Co mixed oxide coated CF-1500 with different sonication times and the Pt-Ru electrode.

Table 5.2. ORR/OER onset potentials and maximum current densities for Mn-Co mixed oxide coated CF-1500 with different sonication times and Pt-Ru

	Sample					
	1 h	3 h	4 h	5 h	6 h	Pt-Ru
ORR onset potential (V vs. Hg/HgO)	-0.14	-0.11	-0.12	-0.08	-0.11	-0.06
OER onset potential (V vs. Hg/HgO)	0.7	0.7	0.47	0.32	0.7	0.63
Maximum ORR current density (mA cm^{-2})	-334	-422	-291	-571	-263	-334
Maximum OER current density (mA cm^{-2})	200	200	199	139	167	126

ZAB full-cell tests were done for the same samples as the half-cell tests (Figure 5.5) and the behavior is similar to the LSV tests. MnCo-5h has the best bifunctional catalytic performance among all samples tested including Pt-Ru. MnCo-5h has a potential gap of 0.74 V and an efficiency of 62.6% at 10 mA cm^{-2}, while Pt-Ru has a potential gap of 0.77 V and an efficiency of 61.9% at the same current density. The potential gap increases to 0.83 V and the efficiency

decreases to 58.9% when the current density is increased to 20 mA cm^{-2}. This performance is still better than that for Pt-Ru at 20 mA cm^{-2} (Table 5.3).

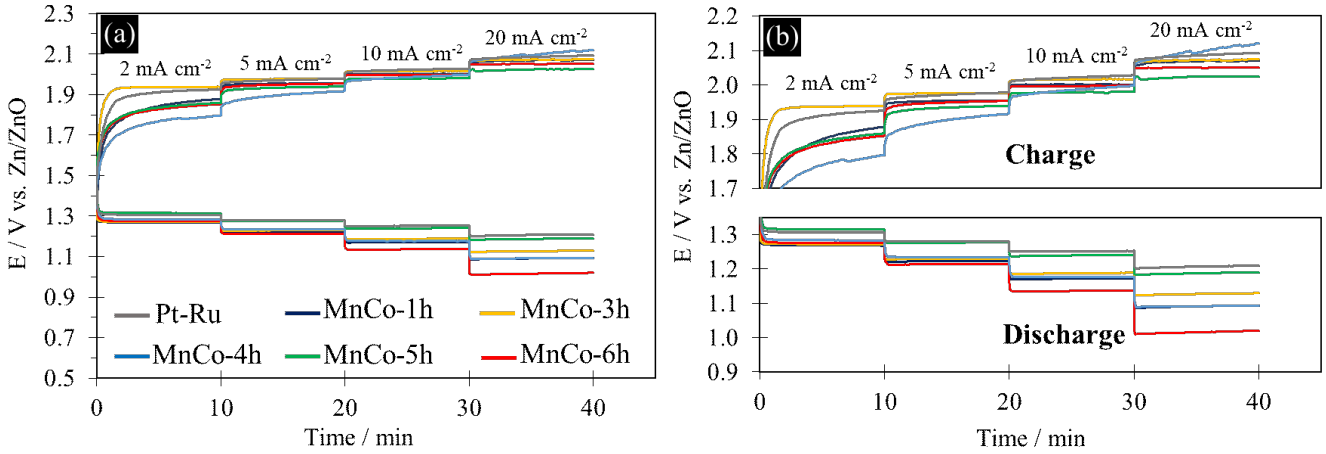

Figure 5.5. (a) ZAB full-cell test results and (b) enlarged view of full-cell test results for Mn-Co mixed oxide coated CF-1500 with different sonication times and Pt-Ru.

Table 5.3. Voltage gaps and efficiencies measured from the full-cell tests for Mn-Co mixed oxide coated CF-1500 with different sonication times and Pt-Ru

		Sample					
		1 h	3 h	4 h	5 h	6 h	Pt-Ru
10 mA cm^{-2}	Voltage gap (V)	0.83	0.83	0.80	0.74	0.87	0.77
	Efficiency (%)	58.5	58.9	59.6	62.6	56.5	61.9
20 mA cm^{-2}	Voltage gap (V)	0.98	0.94	1.01	0.83	1.03	0.88
	Efficiency (%)	52.7	54.6	51.9	58.9	49.8	57.9

Because of the promising catalytic performance of MnCo-5h, other electrodes were fabricated by varying the Mn and Co salt composition while maintaining the sonication time at 5 h. The Mn:Co salt mass ratio was changed to 1:2 and 2:1.

LSV half-cell tests were done and the results, including those from the Pt-Ru electrode, are shown in Figure 5.6. Of the 3 Mn:Co ratios tested, the sample with a Mn:Co salt ratio of 1:2 has the best ORR (Figure 5.6(a)) and OER (Figure 5.6(b)) catalytic activity. MnCo-5h-1:2 has a lower absolute ORR onset potential than either MnCo-5h-1:1 or MnCo-5h-2:1 and an maximum absolute current density higher than MnCo-5h-2:1 and comparable to MnCo-5h-1:1. In fact, MnCo-5h-1:2 also has an absolute ORR onset potential slightly lower than that for Pt-Ru and a maximum absolute current density much higher than that for Pt-Ru (Table 5.4). MnCo-5h-2:1 has an onset OER onset potential that is comparable to Pt-Ru. All Mn-Co samples have better OER activity than Pt-Ru, both in terms on onset potential and maximum current density (Figure 5.6 and Table 5.4). MnCo-5h-1:2 has the lowest OER onset potential (0.28 V vs. Hg/HgO) and the highest maximum OER current density (293 mA cm^{-2}).

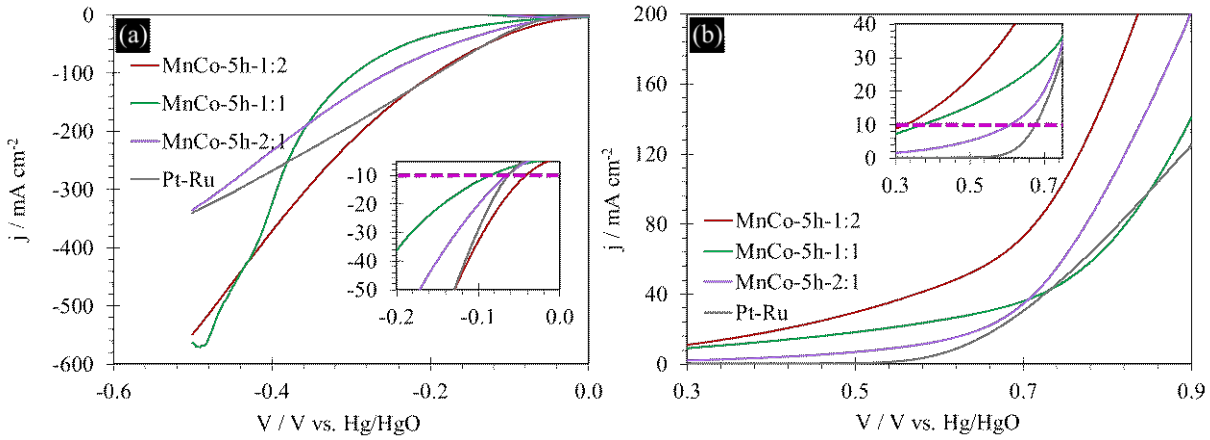

Figure 5.6. (a) ORR and (b) OER LSV half-cell test results at 5 mV cm^{-2} for different Mn:Co salt mass ratios and Pt-Ru.

Table 5.4. ORR/OER onset potentials and maximum current densities for different Mn:Co salt ratios and Pt-Ru

	Sample			
	1:1	1:2	2:1	Pt-Ru
ORR onset potential (V vs. Hg/HgO)	-0.08	-0.04	-0.06	-0.06
OER onset potential (V vs. Hg/HgO)	0.32	0.28	0.56	0.63
Maximum ORR current density (mA cm^{-2})	-571	-549	-335	-334
Maximum OER current density (mA cm^{-2})	139	293	202	126

ZAB full-cell tests were done on the same 4 electrodes (Figure 5.7) and similar behavior to the half-cell tests was obtained. Efficiencies and potential gaps were calculated and are shown in Table 5.5. MnCo-5h-1:2 has a potential gap of 0.72 V and an efficiency of 63.7% at 10 mA cm^{-2}, while Pt-Ru has a potential gap of 0.77 V and an efficiency of 61.9% at the same current density. The potential gap for MnCo-5h-1:2 increases to 0.82 V and the efficiency decreases to 60.0% for

a current density of 20 mA cm^{-2}. This performance is still better than that for Pt-Ru with an efficiency of 57.9% and a voltage gap of 0.88 V at 20 mA cm^{-2} (Table 5.5).

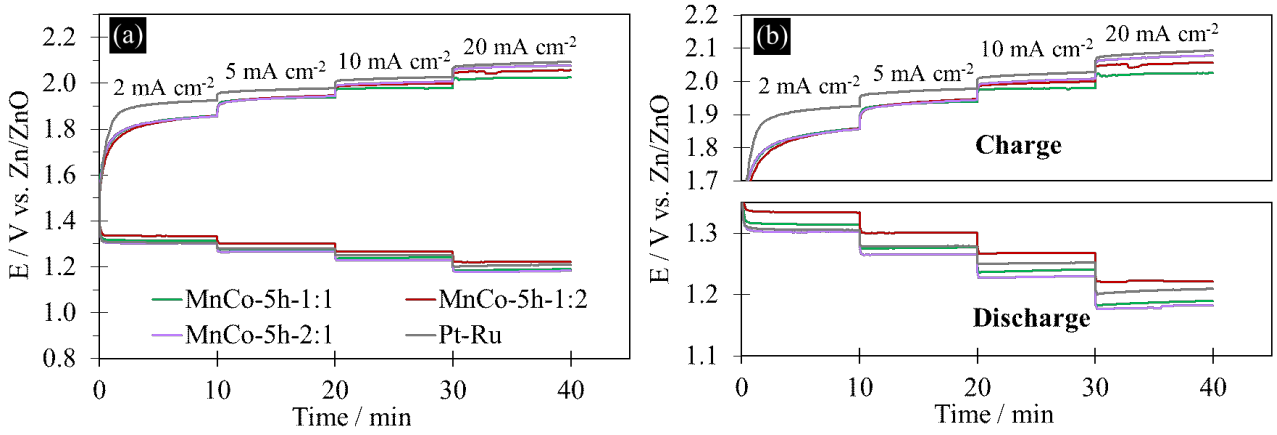

Figure 5.7. (a) ZAB full-cell test results and (b) enlarged view of full-cell test results for different Mn:Co salt ratios and Pt-Ru.

Table 5.5. Voltage gaps and efficiencies measured from full-cell tests for different Mn:Co salt ratios and Pt-Ru

		Sample			
		1:1	1:2	2:1	Pt-Ru
10 mA cm^{-2}	Voltage gap (V)	0.74	0.72	0.77	0.77
	Efficiency (%)	62.6	63.7	61.5	61.9
20 mA cm^{-2}	Voltage gap (V)	0.83	0.82	0.89	0.88
	Efficiency (%)	58.9	60.0	57.0	57.9

Because of its promising bifunctional catalytic performance, MnCo-5h-1:2 was chosen for further materials characterization (SEM/EDX) and electrochemical testing (cycling).

The SEM SE image and EDX maps for MnCo-5h-1:2 (Figure 5.8) show that the Mn-Co mixed oxide coating covers the entire surface of the fibers with some patches of thicker coating. EDX quantitative analysis, from different areas, gives a Mn:Co atomic ratio of ~1:2, which corresponds to the Mn:Co salt ratio in the solution used for deposition. A representative SAED pattern is presented in Figure 5.8(e) and consists of concentric rings, which indicate that the oxide is polycrystalline. The pattern can be indexed to $MnCo_2O_4$ with a cubic spinel structure (PDF#23-1237, a = 8.269 Å). A schematic of the cubic spinel crystal structure is presented in Figure 5.8(f), illustrating some of the tetrahedral and octahedral sites that act as active sites for O_2 donor-acceptor chemisorption. The tetrahedral cations fill 1/8 of the tetrahedral holes and the octahedral cations fill 1/2 of the octahedral holes.

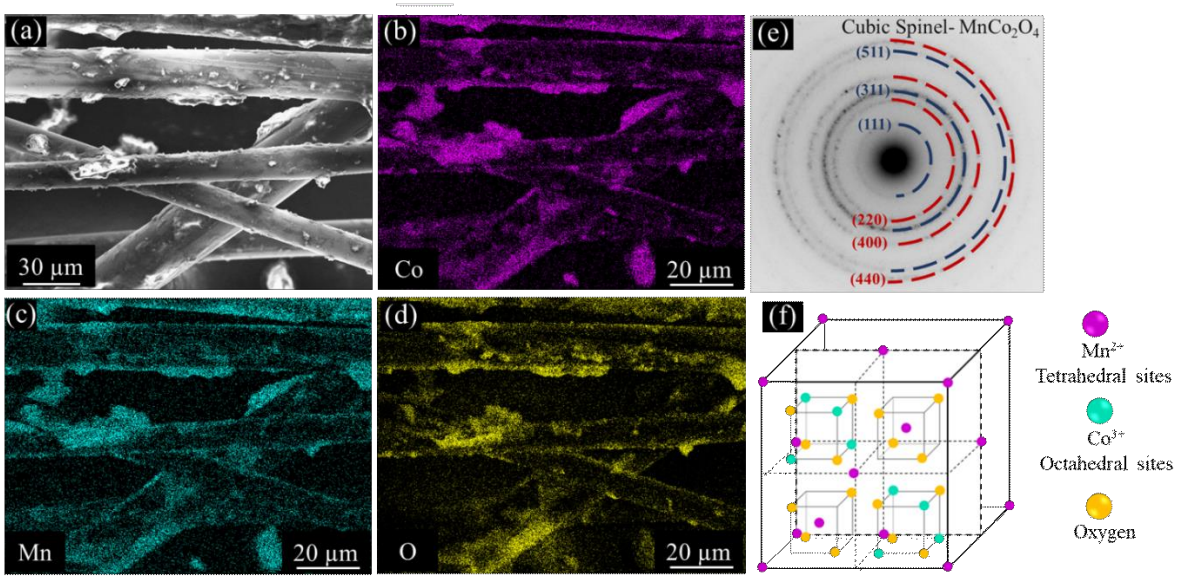

Figure 5.8. (a) SEM, (b)-(d) EDX and (e) SAED analysis of MnCo-5h-1:2. (e) Schematic of the spinel structure, showing some of the octahedral and tetrahedral sites.

The identification of the Mn-Co spinel phase was further confirmed through XPS analysis of MnCo-5h-1:2 (Figure 5.9). Figure 5.9(a) shows the survey spectrum; the Mn and Co peaks are

from the coating, the C peak is from the CF and the O peaks are from both CF and the Mn-Co oxide coating. The Na peak is likely from NaOH in the solution used for oxide coating and/or residual surface contamination. The peaks from the catalyst coating are relatively weak because of the small amount of catalyst compared with the carbon fibers.

High resolution spectra for Co and Mn are shown in Figure 5.9. The peak splitting for the Mn 3s spectrum (5.7 eV, Figure 5.9(b)) and the peak positions in the Mn 2p spectrum (Figure 5.9(c)) were used to estimate the Mn valence in the Mn-Co oxide spinel phase. Clark et al. [16] and Gorlin and Jaramillo [179] have demonstrated a relationship between Mn 3s peak splitting and the oxidation state of Mn. Based on these studies, the Mn 3s peak splitting of 5.7 eV may correspond to an oxidation state of 2+. The Mn 2p spectrum contains two main peaks that represent Mn $2p_{3/2}$ and Mn $2p_{1/2}$ at binding energies of 641.8 eV and 653.3 eV, respectively, which can be assigned to Mn^{2+}. [178,181,206,207] Deconvolution of the Co 2p spectrum leads to four components (Figure 5.9(d)). The peaks at binding energies of 780.7 eV and 796.5 eV correspond to Co $2p_{3/2}$ and Co $2p_{1/2}$, respectively. [208] The binding energies of the $2p_{3/2}$ and $2p_{1/2}$ shake-up satellite peaks were used to estimate the Co oxidation state. The satellite peak positions for Co $2p_{3/2}$ and $2p_{1/2}$ are 785.1 eV and 802.6 eV, respectively, which indicates the presence of Co^{3+} in MnCo-5h-1:2. From the XPS analysis results, it can be concluded that Mn and Co in the Mn-Co oxide coating have oxidation states of 2+ and 3+, respectively, rather than mixed oxidation states. This corresponds to a chemical formula for the spinel phase of $MnCo_2O_4$.

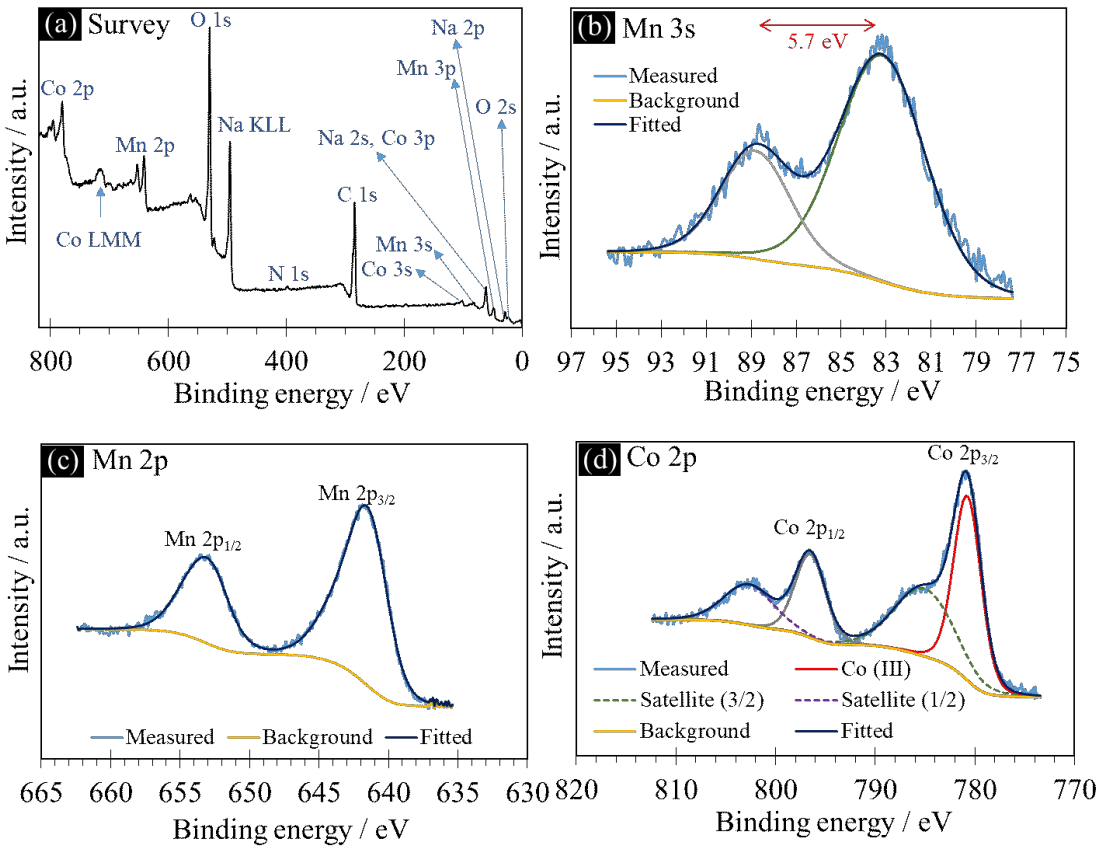

Figure 5.9. XPS analysis results for MnCo-5h-1:2. (a) Overall survey spectrum, (b) Co 2p spectrum, (c) Mn 3s spectrum and (d) Mn 2p spectrum.

The good ORR/OER bifunctional catalytic activity of MnCo-5h-1:2 is proposed to be related to its spinel crystal structure (Figure 5.8(e)). The presence of both tetrahedral and octahedral sites (filled with Mn and Co cations, respectively) in the Mn-Co spinel structure provides donor-acceptor chemisorption sites (active sites) for O_2, which can provide efficient catalytic activity towards ORR/OER. [205]

The MnCo-5h-1:1 and MnCo-5h-2:1 samples were also characterized, using electron diffraction in the TEM and XPS (Figure SI5.1 and 5.13). Both samples have SAED patterns similar to MnCo-5h-1:2 and the patterns can be indexed to a cubic spinel structure (Supporting

Information, Figure SI5.1(a) and 5.12(b)). High resolution XPS spectra for MnCo-5h-1:1 and MnCo-5h-2:1 are shown in Figure SI5.2(a)-(f) and the oxidation states for Mn are summarized in Figure SI5.1(g). The Mn oxidation state was determined from the Mn 3s peak splitting and 2p peak positions. Manganese in both samples has an overall oxidation state of ~2.6, which corresponds to a mixed of 2+ and 3+ valences. The Mn $2p_{3/2}$ spectrum can be deconvoluted into two components with binding energies of 641.2 eV (Mn^{2+}) and 642.8 eV (Mn^{3+}) for MnCo-5h-1:1 and 641.1 eV (Mn^{2+}) and 642.8 eV (Mn^{3+}) for the MnCo-5h-2:1. The Co $2p_{3/2}$ spectra can be deconvoluted into two peaks at 780.4 eV (Co^{3+}) and 784.8 eV (Co^{2+}) for MnCo-5h-2:1 and 780.3 eV (Co^{3+}) and 784.8 eV (Co^{2+}) for MnCo-5h-1:1. In both MnCo-5h-2:1 and MnCo-5h-1:1, Mn and Co exist in the 2+ and 3+ oxidation states. [16,179]

The better catalytic activity for MnCo-5h-1:2, compared with MnCo-5h-1:1 and MnCo-5h-2:1, can be attributed to differences in the oxidation states. For MnCo-5h-1:2, Co exists exclusively in the 3+ state with Mn exclusively in the 2+ state. For both MnCo-5h-2:1 and MnCo-5h-1:1, Mn and Co have mixed oxidation states of 2+ and 3+.

In the $MnCo_2O_4$ spinel structure (MnCo-5h-1:2), Mn as Mn^{2+} occupies the tetrahedral sites and Co as Co^{3+} occupies the octahedral sites. In the MnCo-5h-1:1 and MnCo-5h-2:1 spinel structures, the tetrahedral and octahedral sites are occupied by both Mn^{2+} and Co^{2+}. It is proposed that a Mn-Co mixed oxide electrocatalyst with a spinel crystal structure, with Mn in the 2+ oxidation state and Co in the 3+ state (MnCo-5h-1:2), has better bifunctional catalytic activity than a spinel structure where Mn and Co both have mixed oxidation states of 2+ and 3+ (MnCo-5h-2:1 and MnCo-5h-1:1). There are conflicting reports in the literature regarding oxidation state and catalytic activity. Some recent papers indicate that higher oxidation states for Mn (3+/4+) lead to better ORR catalytic activity; e.g., the work by Li et al. [209] and the study by We et al.

[210]. On the other hand, there are other recent studies; e.g., Cheng et al. [211], that show that a lower Mn oxidation state is preferred for ORR catalytic activity. In any case, for the samples in this study, the combination of Mn^{2+} Co^{3+} provided superior bifunctional catalytic activity. It is also noteworthy that most recent articles claim that the presence of Co^{3+} in the spinel structure is beneficial in terms of OER performance. [212]

The cycling performance of batteries prepared using MnCo-5h-1:2 and Pt-Ru as the air electrodes and a zinc sheet (2 cm × 6 cm) as the counter electrode was tested at a current density of 10 mA cm^{-2} for 200 charge/discharge cycles. This corresponds to a total cycling time of 100 h with charge and discharge durations of 10 min each and a 5 min rest period after each charge and discharge step (Figure 5.10). During the first 4 cycles, the ORR potential decreases and the OER potentials increases slightly for MnCo-5h-1:2. This may be due to oxidation of the CFs upon exposure to the alkaline electrolyte. [203] MnCo-5h-1:2 cycling performance is very stable without any major fluctuations during subsequent cycles, with initial discharge and charge potentials of 1.27 V vs. Zn/ZnO and 1.99 V vs. Zn/ZnO, respectively, and final values after 200 cycles of 1.22 V vs. Zn/ZnO and 2.02 V vs. Zn/ZnO, (Figure 5.10(c)). The initial efficiency is 63.7% and the final efficiency is 58.9%, which corresponds to only a 7.5% decrease in efficiency. The electrode with Pt-Ru is not stable during cycling with initial and final efficiencies of 61.9% and 43.2%, respectively, after 200 cycles, which represents a 30.2% drop in efficiency. A power curve comparison for MnCo-5h-1:2 and Pt-Ru is presented in Figure 5.10(d). The power curve for MnCo-5h-1:2 reaches a maximum power density of 127 mW cm^{-2} at 198 mA cm^{-2} which is slightly better than the maximum power density of 121 mW cm^{-2} for Pt-Ru at 223 mA cm^{-2}.

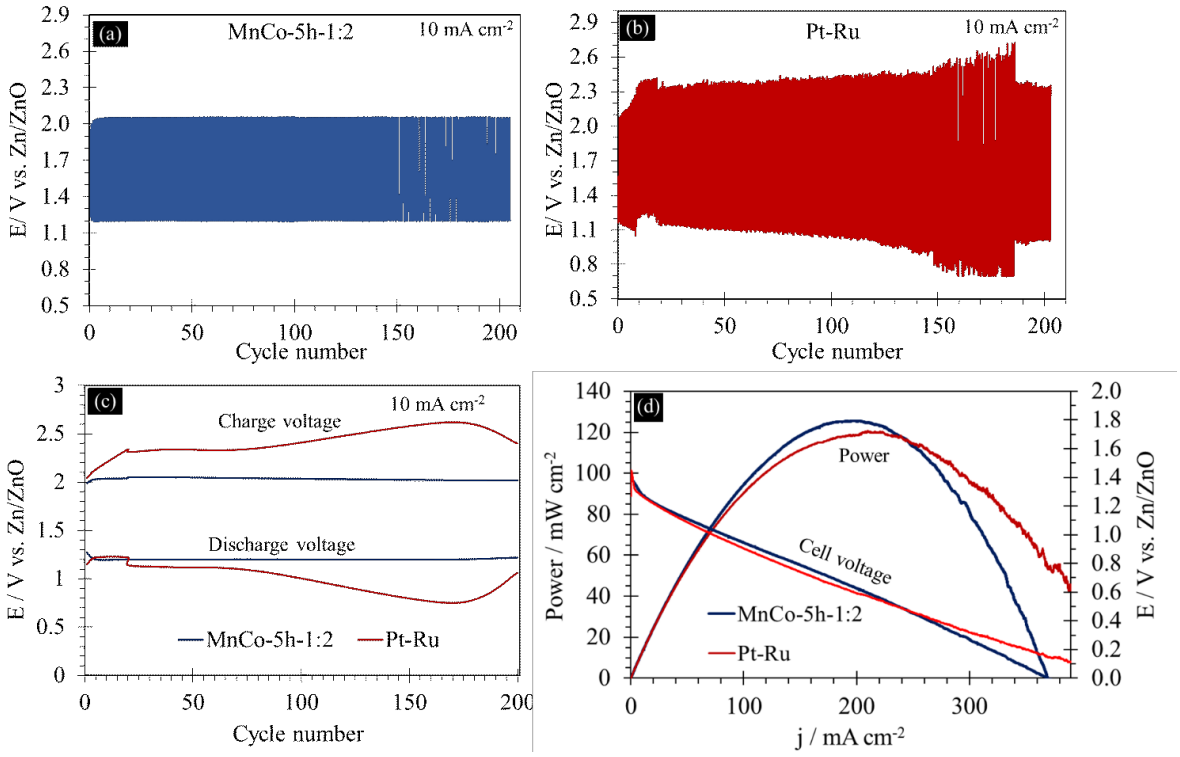

Figure 5.10. Cycling tests at 10 mA cm^{-2} for (a) MnCo-5h-1:2 and (b) Pt-Ru. (c) Charge and discharge potentials for both cells during cycling. (d) Polarization and power comparison.

MnCo-5h-1:2 electrodes were characterized using SEM/EDX analysis before and after cycling (Figure 5.11). SEM SE images (Figure 5.11(a)-(c)) and K maps (Figure 5.11(e) and 5.12(f)) for the electrodes after 10 and 200 cycles show that K coverage, likely in the form of potassium carbonate, increases with cycling. However, battery performance was not adversely affected as there was very little change from the 10^{th} to the 200^{th} cycle. This is due in part to the size of the carbon fibers (~10 µm in diameter) which results in a more open air electrode with relatively large voids and pores that are visible to the human eye (Figure 5.11(a)-(c)). The large voids aid oxygen delivery and removal during ORR and OER when the battery is discharged or charged, leading to a stable cycling behavior. Oxidation of carbon fibers and carbon black added during electrode fabrication is likely responsible for the small performance degradation during the initial

cycles. After 200 cycles, the amount of Mn and Co from the EDX analysis (Figure 5.11(d)) decreases due to the increased coverage of K; however, the Mn:Co ratio remains approximately constant. There is a small amount of Zn on the surface of the cycled electrodes, as ZnO, and this is likely due to presence of soluble zincate ($Zn(OH)_4^{2-}$) species in the electrolyte.

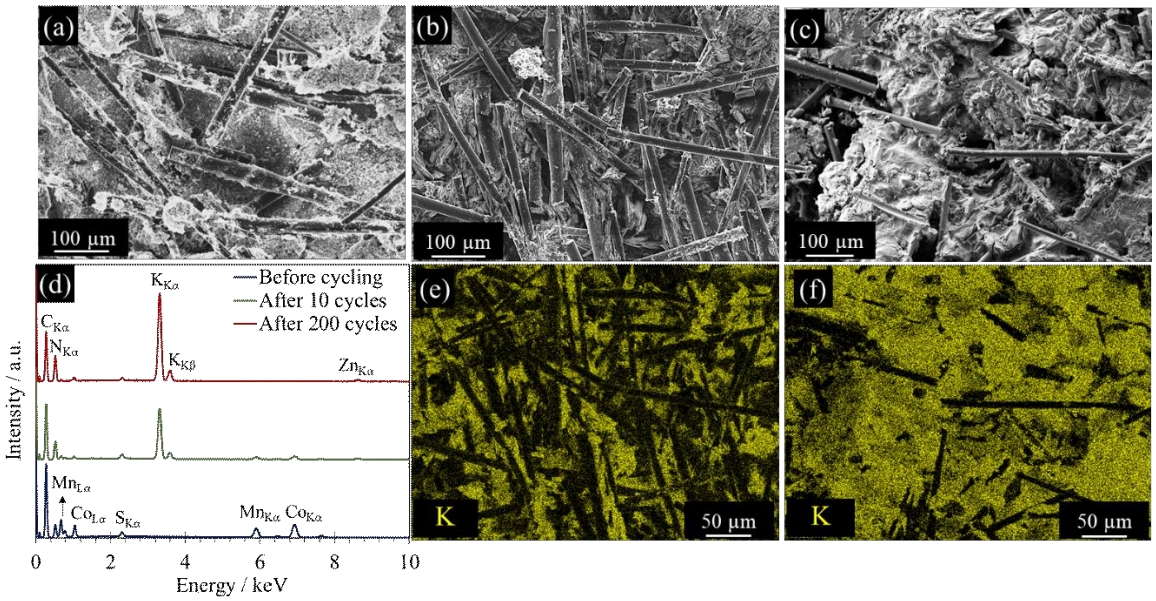

Figure 5.11. SEM images and EDX analysis of MnCo-5h-1:2 electrodes before and after battery cycling. (a) SE image before cycling, (b) SE image after 10 cycles, (c) SE image after 200 cycles, (d) EDX spectra from the areas shown in the SEM images, (e) K EDX map for the electrode after 10 cycles and (f) K EDX map for the electrode after 200 cycles.

It is apparent that MnCo-5h-1:2 is very stable as a bifunctional catalyst after cycling at 10 mA cm^{-2} for 200 cycles. Furthermore, the performance of MnCo-5h-1:2 is superior to that of other bifunctional transition metal oxide/carbon based catalysts reported in the recent literature (Table 5.6). As an example, Co-Mn-Ni nanorods were prepared by Wang et al. and cycled in a ZAB containing 6 M KOH + 0.2 M $Zn(Ac)_2$ electrolyte at 10 mA cm^{-2}. [207] Only final efficiency values were provided in their work, but a significant increase in the OER potential and a

decrease in the ORR potential were reported. Aasen et al. prepared $(Co,Fe)_3O_4$/CNT bifunctional catalysts on GDL that were cycled at both 10 and 20 mA cm^{-2} in 6 M KOH + 0.25 M ZnO. [213] The reported cycling performance was quite stable; however, ORR/OER half-cell catalytic activities for MnCo-5h-1:2 in this work are superior. In addition, synthesis of MnCo-5h-1:2 is more cost-effective since no costly carbonaceous precursors like CNTs are required. Another example is the work by Cano et al., where $NiCo_2O_4$ catalysts on a Ni based GDL were prepared and cycled in 6 M KOH at 10 mA cm^{-2}. [214] However, significant performance losses were reported after 50 h of cycling (~55.6% efficiency). Performance then declined more rapidly until 100 h with a final discharge potential of ~0.1 V vs. Zn/ZnO. The discharge potential for MnCo-5h-1:2 is 1.19 V vs. Zn/ZnO after 200 cycles.

Table 5.6. Comparison of bifunctional transition metal oxide/carbon based catalysts recently reported in the literature

Catalyst/air electrode material	**Battery/cell characterization**	**Cycling current density (j, mA cm^{-2})**	**Initial efficiency**	**Final efficiency**	**Number of cycles, cycling duration (h)**
$MnCo_2O_4$/CF (this work)	6 M KOH + 0.25 M ZnO, ambient air	10	63.7	58.9	200, 100
Co–Mn–Ni nanorods [207]	6 M KOH + 0.2 M $Zn(Ac)_2$, ambient air	10	---	57.4	100, 16.7
MnO_x + CoFe on GDL [26]	6 M KOH + 0.25 M ZnO, ambient air	10	59	57	200, 100
$(Co,Fe)_3O_4$/CNT on GDL [213]	6 M KOH + 0.25 M ZnO, ambient air	10	59.1	58.5	200, 100
Co-Fe [197]	6 M KOH+0.25 M ZnO, ambient air	5	~56	~56	20, 20
$NiCo_2O_4$ on Ni-GDL [214]	6 M KOH, ambient air	10	~59.1	Battery failed after 75 cycles	100, 100

5.4 Conclusions

Highly stable and efficient Mn-Co oxide/carbon fiber bifunctional catalyst/air electrodes were synthesized through a facile and cost-effective method. Asphaltene as a by-product of oil sands industry was used to prepare carbon fibers (CFs) which were then coated with Mn-Co oxide, identified as cubic spinel $MnCo_2O_4$, via a simple sonication method as the bifunctional catalyst. Several sonication times and Mn:Co ratios were examined in terms of their catalytic activity

towards ORR/OER, charge/discharge efficiencies in full-cell Zn-air batteries and cycling behavior. A sonication time of 5 h with a Mn:Co ratio of 1:2 provided the best performance. The ORR onset potential for this sample (MnCo-5h-1:2) measured from LSV tests in a half-cell (three electrode) configuration was -0.04 V vs. Hg/HgO with a maximum current density of -549 mA cm^{-2}. Its activity towards OER was also outstanding with an OER onset potential of 0.28 V vs. Hg/HgO and a maximum current density of 293 mA cm^{-2}. Discharge/charge efficiencies for MnCo-5h-1:2 were 63.7% and 60.0% at 10 mA cm^{-2} and 20 mA cm^{-2}, respectively. MnCo-5h-1:2 was very stable during cycling at 10 mA cm^{-2}, without any major fluctuations in discharge/charge potentials, and a final efficiency of 58.6% (after 200 cycles). The cycling performance was also superior to that of Pt-Ru electrodes, which had initial and final efficiencies of 61.9% and 43.2%, respectively, under the same conditions. The excellent battery performance is proposed to be due to the inherent ORR/OER bifunctional activity of Mn-Co mixed oxides and its direct and intimate growth on the CFs.

5.5 Supporting Information

Table SI5.1. CHNS analysis results for CF-1500

CF-1500			
C (wt%)	H (wt%)	N (wt%)	S (wt%)
94.05	0.03	0.31	1.54

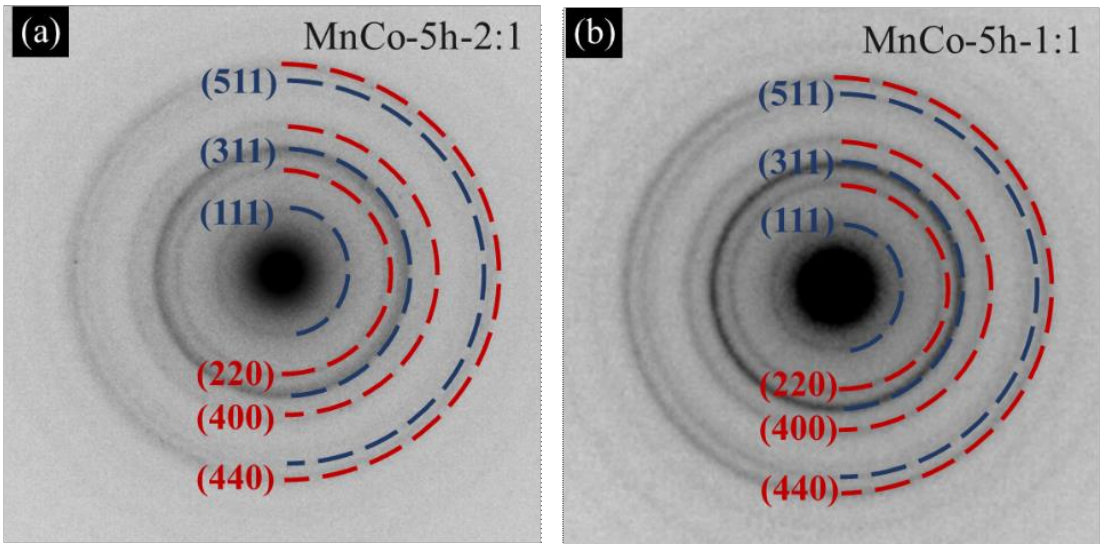

Figure SI5.1. SAED patterns for (a) MnCo-5h-2:1 and (b) MnCo-5h-1:1. The patterns are indexed to a cubic spinel structure.

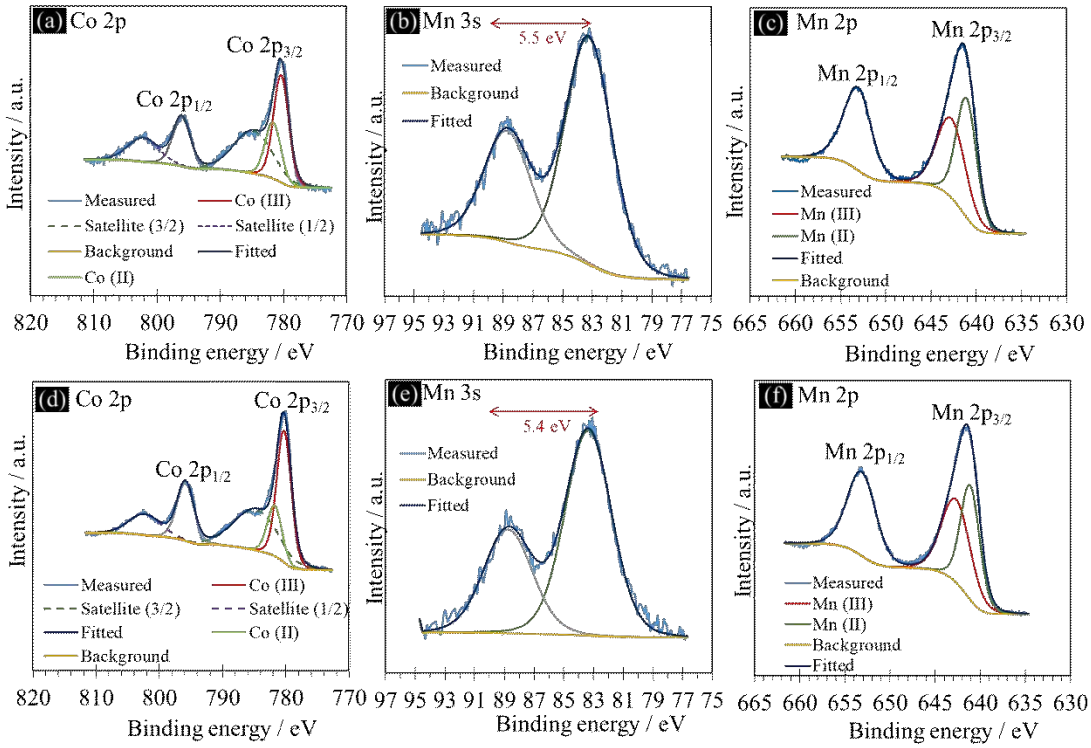

(g)

Sample	Mn 3s peak splitting / eV	Mn oxidation state
1:2	~5.7	~2
1:1	~5.4	~2.6
2:1	~5.5	~2.6

Figure SI5.2. (a)-(c) XPS data for MnCo-5h-2:1. (d)-(f) XPS data for MnCo-5h-1:1. (g) Mn 3s peak splitting and oxidation states for all three MnCo-5h samples.

Chapter 6: Zinc-Air Batteries with Efficient and Stable $MnCo_2O_4$/Carbon Fiber Bifunctional Electrocatalyst and Poly(acrylic Acid) (PAA) Based Gel Electrolyte

A version of this chapter has been published in the journal American Chemical Society Applied Energy Materials:

Z. Abedi, J. Cui, W. Chen and D.G. Ivey, "Zinc-Air Batteries with Efficient and Stable MnCo2O4/Carbon Fiber Bifunctional Electrocatalyst and Poly(acrylic Acid) (PAA) Based Gel Electrolyte" ACS Appl. Energy Mater., 2022.

6.1 Introduction

Rechargeable (secondary) zinc-air batteries (ZABs) are cost effective and promising candidates for sustainable energy storage devices because of their high energy density, safe operation and long shelf life (when sealed). [12,189,215] A metallic Zn electrode, an air electrode that is usually carbon based and an alkaline electrolyte are the main components of a ZAB. [26] Development of rechargeable ZABs is constrained by the sluggish kinetics of the reactions that take place at the air electrode, which limit the round-trip efficiency of the device. [198] This necessitates the use of electrocatalysts for the air electrode reactions. [2,216] The oxygen reduction reaction (ORR) and oxygen evolution reaction (OER) take place at the air electrode during discharge and charge of a ZAB, respectively. [33,217] Traditionally, precious metal based electrocatalysts like Pt and Ru have been used to improve the performance of ZABs; however, their high cost, scarcity and cycling instability make their use for large scale applications impractical. [19] Transition metal oxides have been investigated as effective electrocatalysts for ZABs; e.g., Mn and Co oxides show promising catalytic activity towards ORR and OER,

respectively. However, they suffer from low electrical conductivity which can further negatively affect the reaction kinetics and cause more overpotential. [12,19],[218]

Carbon based structures, like carbon nanotubes (CNT), carbon fibers (CF) and graphite, have been used as the conductive support for transition metal oxides in energy storage devices; carbonaceous materials can also be used to prepare homemade air electrodes for ZABs. [3,7,34,39,130,131] The use of homemade air electrodes in ZABs allows for precise electrode design in terms of the porosity and mass loading to improve battery performance.

Low cost micron-scale carbon fibers can be synthesized from asphaltenes, which is an inexpensive and carbon rich by-product of the oil sands industry, as discussed in previous works. [9,23,171,175] A spinel-type $MnCo_2O_4$ coated CF ($MnCo_2O_4$/CF) bifunctional electrocatalyst was developed in a previous study by some of the current authors. The catalyst exhibited excellent charge/discharge efficiencies with stable cycling behavior in a 6 M KOH + 0.25 M ZnO aqueous electrolyte. [12]

Many challenges have been reported regarding the use of aqueous electrolytes in ZABs, such as evaporation of the electrolyte, cell leakage and flooding. [25,38] Since the electrolyte plays an important role in the performance of the device, new electrolyte materials can be designed to address the issues associated with aqueous electrolytes. Gel polymer electrolytes (GPEs) are promising candidates to replace aqueous electrolytes. GPEs are a class of polymers, known as hydrogels. Hydrogels are capable of absorbing considerable amounts of water, without dissolving. This property enables GPEs to hold alkaline solutions and to be used as the electrolyte in solid-state ZABs. [219,220]

Issues associated with ZABs that use GPEs include limited power densities and cycling stability, as well as poor discharge/charge performance at higher current densities due to degradation of

the polymer structure. [21,38] Polymers, like polyvinyl alcohol (PVA) and polyacrylic acid (PAA), have been used previously as the gel polymer matrix. In 2015, Fu et al.[221] and Xu et al.[222] introduced flexible ZABs with PVA based alkaline electrolytes which suffered from poor cycling stability even at current densities as low as 0.01-0.1 mA cm^{-2}. Chen et al.[223] investigated the extension of cycle life of ZABs with PVA based electrolytes. The best performing cell could be cycled for 160 h, but the current density utilized for cycling was only 2 mA cm^{-2} and the maximum power density delivered by the cell was ~70 mW cm^{-2}. Miao et al.[224] used PAA based GPEs for ZABs with a La based electrocatalyst. The best performing cell delivered a power density of ~55 mW cm^{-2} and was cycled for 100 cycles at 5 mA cm^{-2}, but the cycling duration was only ~17 hours. In the work by Roy et al.[225], 150 cycles at 5 mA cm^{-2} were achieved for a solid-state ZAB with a PAA based GPE; the cell showed stable performance with a roundtrip efficiency of 60.0% but the cycling duration was only 25 h. In the study by Tran et al.[38], ZABs with PAA based electrolytes ran for 120 cycles (60 h) at 5 mA cm^{-2}. Recently, Song et al.[21] investigated the failure mechanism of PAA based GPEs in ZABs. The OH^- content, oxidation of carbon in the air electrode and passivation of the Zn electrode were reported as the most important reasons causing battery failure.

The search for a high power ZAB with a solid-like and flexible GPE, with good performance at higher current densities and a stable cycle life, was the starting point of this work, since most studies on solid-state ZABs use relatively low current densities. Several ZAB cells were prepared with homemade air electrodes that were fabricated with $MnCo_2O_4$/CF as the bifunctional ORR/OER electrocatalyst. The 3D structure of the homemade electrodes was engineered in such a way to provide maximum penetration of the GPE into the electrode by using micron-scale carbon fibers (diameter ~10 μm) that provide voids and porosity between the fibers for the air

electrode. Hydrogel electrolytes with a PAA polymer matrix and different amounts of crosslinker (N,N'-methylenebis (acrylamide) (MBAA)) were used to optimize the hydrogel electrolyte for a rechargeable ZAB with the $MnCo_2O_4$/CF electrocatalyst. The discharge/charge performance and efficiency, cycle life and power output of the fabricated ZABs were investigated. In addition, materials characterization of the electrocatalyst and hydrogel electrolytes was carried out.

6.2 Experimental

6.2.1 Bifunctional Electrocatalyst Synthesis

$MnCo_2O_4$ coated carbon fibers ($MnCo_2O_4$/CF) were used as the bifunctional electrocatalyst in this work. The fabrication process for this electrocatalyst was developed in a previous study. [12] Details regarding carbon fiber preparation can be found in the recent literature. [9,171,175] To summarize, after soaking 80 mg of carbon fibers, carbonized at 1500 ^oC, in ~20 ml of 28 wt% NH_4OH for 10 min, the NH_4OH soaked fibers were sonicated for 5 h in a solution containing 30 ml of reagent alcohol, 100 mg of NaOH, 166.67 mg of Mn(II) acetate ($Mn(Ac)_2$ or $C_4H_6MnO_4$) and 333.33 mg of Co(II) acetate ($Co(Ac)_2$ or $C_4H_6CoO_4$) salts. The purpose of the sonication step was to coat the CFs with a $MnCo_2O_4$ electrocatalyst layer.

A mixture containing 90 wt% $MnCo_2O_4$/CF, 5 wt% polytetrafluoroethylene (PTFE) and 5 wt% carbon black was pasted on a hydrophobic carbon paper (Fuel Cell Store: Toray Paper 060-TGP-H-060) to prepare air electrodes for half-cell and full-cell tests. The carbon paper was mainly used to provide structural support for the catalyst layer. Mass loading for each electrode was ~10 mg cm^{-2} of the electrode mixture.

In order to compare the electrochemical performance of the samples prepared in this work with the benchmark Pt-RuO_2 electrocatalyst, a spray coating method was used to prepare electrodes with Pt-RuO_2. 50 mg of Pt-RuO_2 powder (30 wt% Pt and 15 wt% RuO_2 combined with carbon

black, purchased from Alfa Aesar), 2 ml of deionized water, 0.1 ml of Nafion 5% and 1 ml of ethanol were sonicated for 0.5 h to form the spray coating suspension (hereafter referred to as Pt-Ru). The suspension was then spray coated on the same carbon paper used for $MnCo_2O_4$/CF. Mass loading for each electrode was ~1 mg cm^{-2}.

All the prepared electrodes were dried in a Lindberg/Blue M™ Moldatherm™ box furnace at 350 ^oC prior to use.

6.2.2 Electrolyte Synthesis

Hydrogel electrolytes, containing poly(acrylic acid) (PAA), different concentrations of crosslinker and KOH were prepared. PAA was used as the host polymer. N,N'-methylenebis(acrylamide) or MBAA was used in the hydrogel electrolyte as a crosslinker and potassium persulfate ($K_2S_2O_8$ (KPS)) was used as a thermo-initiator. Acrylic acid, MBAA and KPS were purchased from Sigma-Aldrich, while KOH and ZnO were purchased from Fisher Scientific. Four different electrolytes were prepared with different concentrations (20, 30, 40 and 50 mM) of MBAA. To prepare the electrolytes, 6.5 M KOH, 0.5 M acrylic acid, 0.2 M ZnO, 20-50 mM MBAA and 1.5 mM KPS were mixed using a vortex mixer. The electrolyte mixture was then kept at 60 ^oC for 1 h for the polymerization reaction to complete and then cooled overnight to room temperature. Hydrogel electrolytes with the different MBAA concentrations are denoted as Hydrogel-20-mM, Hydrogel-30-mM, Hydrogel-40-mM and Hydrogel-50-mM, respectively.

An aqueous electrolyte (6 M KOH + 0.25 M ZnO) was also used for full-cell battery testing in order to compare the performance of the prepared electrodes in hydrogel and aqueous electrolytes. 150 ml of 1 M KOH was used as the electrolyte in the half-cell configuration.

6.2.3 Battery Testing Configuration

Half-cell tests were conducted in ~150 ml of O_2 saturated 1 M KOH, with a Pt wire as the counter electrode and Hg/HgO (+0.98 V vs. SHE, in 1 M NaOH) as the reference electrode, to investigate the ORR/OER catalytic performance of the prepared electrodes. O_2 gas was bubbled into the electrolyte with a flow rate of 0.05 standard liters per min (SLPM) for 0.5 h prior to and during the testing.

Full-cell testing was conducted using the prepared air electrode as the working electrode and a 1 cm x 3 cm Zn sheet as the counter electrode in both hydrogel and aqueous (6 M KOH + 0.25 M ZnO) electrolytes. The cells were sealed by wrapping them in film (Bemis™ Parafilm™ M Laboratory) to prevent any water evaporation. Oxygen was supplied through exposure of the cells to ambient air. The discharge/charge performance, efficiency, cycling behavior, power values and conductivity of the electrolytes were measured in the full-cell configuration.

6.2.4 Materials Characterization

Field emission scanning electron microscopy (FE-SEM) coupled with energy dispersive X-ray (EDX) spectroscopy was used to study the microstructure and composition of the samples (ZEISS Sigma 300 VP-FE-SEM). Transmission electron microscopy (TEM), high resolution TEM (HRTEM) and selected area electron diffraction (SAED), using a JEOL JEM-ARM200F microscope operating at an accelerating voltage of 200 kV, were utilized for further microstructural and crystal structure analysis at a finer scale. Rheological properties of the hydrogel electrolytes were determined using a Kinexus Lab$^+$ rheometer. A frequency sweep from 0.01 Hz to 10 Hz at 1% strain was conducted to determine the elastic and viscous shear moduli as well as the complex viscosities. X-ray photoelectron spectroscopy (XPS) with a monochromatic Al X-ray source, using a PHI VersaProbe III scanning XPS Microprobe operated

at 210 W and a pass energy of 20 eV was used to further examine the elements present in the $MnCo_2O_4$/CF catalyst as well as their oxidation states.

6.2.5 Electrochemical Measurements

To determine the electrochemical performance of the prepared electrodes, a Biologic VSP potentiostat was employed. Linear sweep voltammetry (LSV) with a scan rate of 5 mV s^{-1} was utilized in a half-cell configuration to investigate the bifunctional catalytic activity of the prepared electrodes. Galvanostatic cycling with potential limitation (GCPL) tests were conducted to determine the full-cell battery performance and the cycling behavior at current densities (j) of ± 2 mA cm^{-2}, ± 5 mA cm^{-2}, ± 10 mA cm^{-2} and ± 20 mA cm^{-2} in a full-cell configuration. The cut-off voltages for GCPL tests were 0.5 V and 3 V vs. Zn/ZnO for discharge and charge, respectively. Electrochemical impedance spectroscopy (EIS) tests were utilized to measure the electrolyte resistance and the charge transfer resistance at the electrode/electrolyte interface. EIS tests for all samples were performed at a frequency range from 500 kHz to 50 mHz with an alternating potential amplitude of 5 mV.

Onset potentials for ORR and OER in the half-cell tests are defined as the potentials (V vs. Hg/HgO) corresponding to current densities of -10 mA cm^{-2} and +10 mA cm^{-2}, respectively. The maximum current densities (half-cell) are defined as the current densities at -0.5 V vs. Hg/HgO for ORR and at 0.9 V vs. Hg/HgO for OER. The efficiency of each full-cell ZAB is defined as the discharge potential divided by the charge potential, i.e., V_{ORR}/V_{OER}, at the same discharge/charge current density. The potential gap in the full-cell tests are defined as $\Delta V = V_{OER} - V_{ORR}$.

6.3 Results and Discussion

6.3.1 Materials Characterization of the $MnCo_2O_4$/CF Electrocatalyst

An SEM secondary electron (SE) image of the $MnCo_2O_4$/CF sample and corresponding EDX maps are shown in Figure 6.1(a)-(d). In addition to coating the surface of the CF, $MnCo_2O_4$ forms larger particles that grow into each other to form islands (Figure 6.1(a)). EDX maps for Mn, Co and O overlap, which confirms the formation of the mixed Mn and Co oxide (Figure 6.1(b)-(d)). A TEM SAED pattern from several $MnCo_2O_4$ particles is shown in Figure 6.1(e). Several rings are visible, which indicate the polycrystalline nature of $MnCo_2O_4$, and these can be indexed to cubic spinel type $MnCo_2O_4$ (PDF#23-1237, a= 8.269 Å). Figure 6.1(f) shows a TEM bright field (BF) image from an area containing $MnCo_2O_4$ grains, which are less than 10 nm in size. A HRTEM image (Figure 6.1(g)), acquired from the area shown in Figure 6.1(f), shows (220) and (311) type crystallographic planes from $MnCo_2O_4$. In summary, the formation of $MnCo_2O_4$ on the CFs is confirmed by electron microscopy.

Detailed XPS analysis can be found in previous work. [12] However, the overall survey spectrum, Mn 3s and 2p spectra and Co 2p spectra are presented in Figure 6.1(h)-(k), respectively. Mn 3s peak splitting (5.7 eV), Mn 2p peak positions (Mn $2p_{3/2}$ and Mn $2p_{1/2}$ at binding energies of 641.8 and 653.3 eV), Co 2p peak positions (780.7 and 796.5 eV corresponding to Co $2p_{3/2}$ and Co $2p_{1/2}$) and shake-up satellite peaks (Co $2p_{3/2}$ at 785.1 and $2p_{1/2}$ at 802.6 eV) were used to identify the oxidation states of Mn and Co in the catalyst. Mn and Co cations exist in oxidation states of 2+ and 3+, respectively, which correspond with the $MnCo_2O_4$ chemical formula and confirm the TEM analysis.

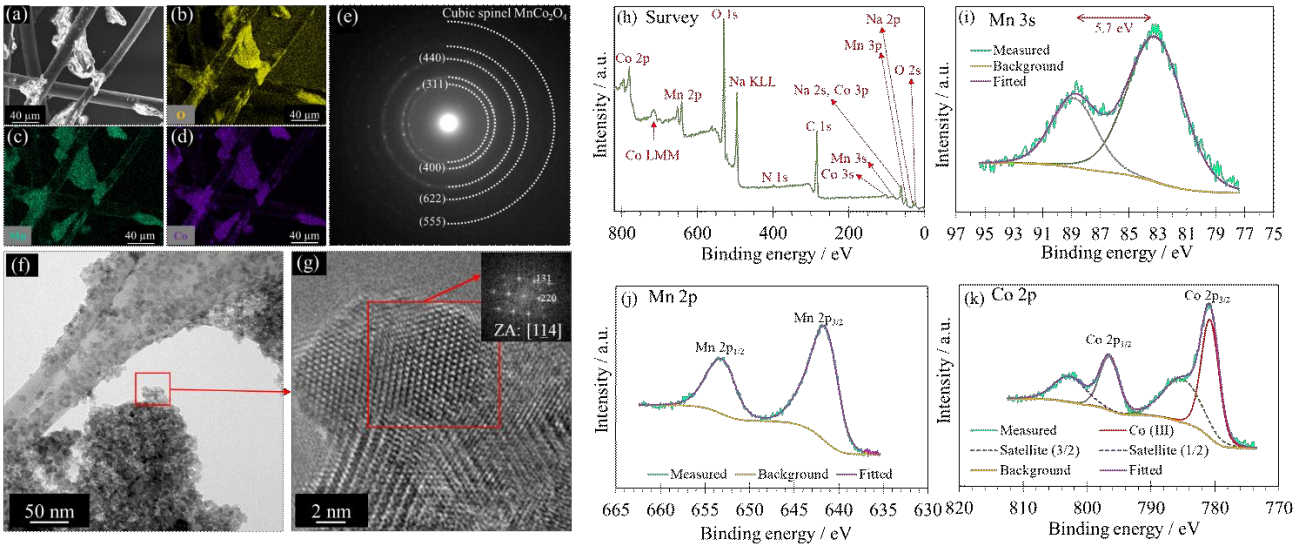

Figure 6.1. Electron microscopy and XPS characterization of $MnCo_2O_4$/CF. (a) SEM SE image, (b)-(d) EDX maps, (e) SAED pattern of the entire region shown in (f), (f) TEM BF image, (g) HRTEM image of the area indicated by the square in (f) with fast Fourier transform (FFT) of the highlighted particle shown in the inset, (h) overall XPS survey spectrum, (i) Mn 3s XPS spectrum, (j) Mn 2p XPS spectrum and (k) Co 2p XPS spectrum.

6.3.2 PAA-KOH Hydrogel Electrolyte Characterization

First of all, a visual test was performed with the prepared electrolytes. The hydrogel electrolytes with different amounts of crosslinker were synthesized in 50 ml laboratory tubes. After synthesis, the electrolytes were moved from the tubes to glass plates. After ~5 min, Hydrogel-20-mM was the only one that did not retain the tube shape and leaked out of the tube as shown by the red arrow in Figure 6.2(a).

The rheological properties of the synthesized hydrogels were examined by a frequency sweep test in the 0.01-10 Hz range at 1% maximum strain to assess the mechanical properties (Figure 6.2 (b) and 2(c)). First, the elastic (G') and viscous (G'') shear moduli were determined. G' represents the reversibly stored energy and the mechanical strength, while G'' represents the

irreversibly lost energy by viscous flow. Then the ratio of G''/ G' = tan(δ) was examined, where δ is the phase angle. G''/ G' < 1 corresponds to a gel (solid-like state), while G''/ G' > 1 represents a sol (liquid-like state). [38,226–228] G' is larger than G'' for all the hydrogel electrolytes over the entire frequency range, so they all qualify as gels. Hydrogel-20-mM has the lowest G''/ G' ratio (Figure 6.2(b)). Complex viscosity was calculated as a function of G' and G'' and is shown in Figure 6.2(c). Hydrogel-50-mM has the highest viscosity while Hydrogel-20-mM has the lowest. Because the complex viscosity is a function of frequency for all the synthesized hydrogel electrolytes (complex viscosity decreases with increasing frequency), they all can be categorized as gels. [229] Hydrogel-20-mM was not chosen for further testing in full-cell ZAB cells, since the visual experiment revealed that it did not retain the tube shape. As such, Hydrogel-20-mM does not qualify as a GPE for the all solid-state cells. Hydrogels with crosslinker concentrations ≥30 mM were tested as the ZAB electrolytes.

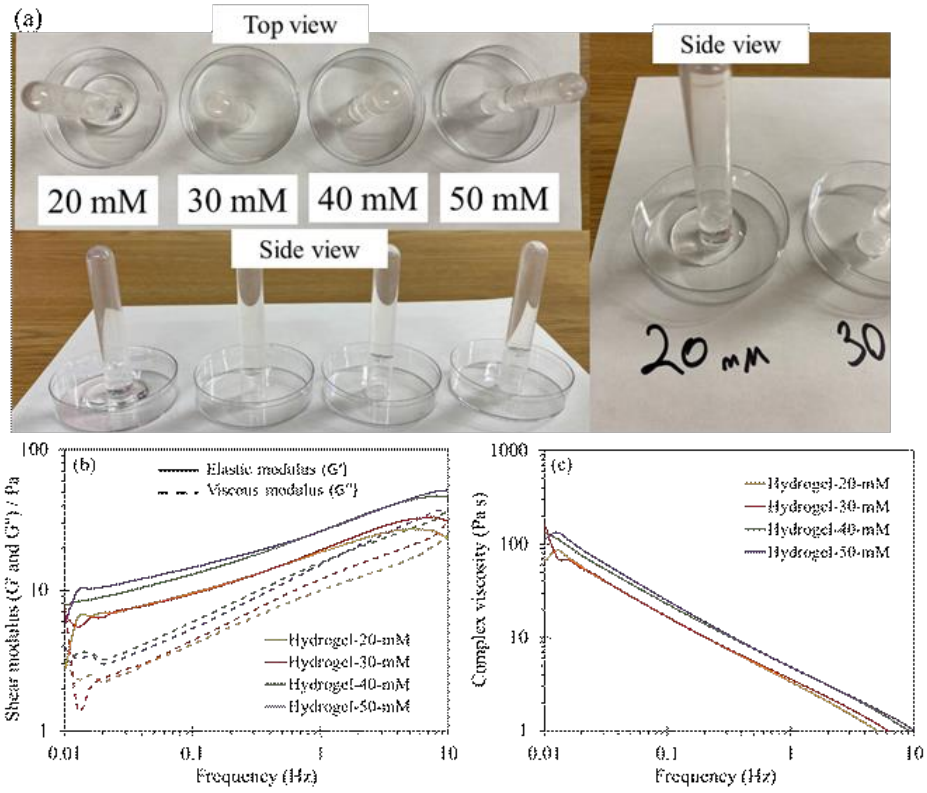

Figure 6.2. Rheological properties of the hydrogel electrolytes with different amounts of MBAA. (a) Visual examination, (b) elastic (G') and viscous (G'') moduli and (c) complex viscosity as a function of frequency determined by a frequency sweep test.

Half-cell (1 M KOH, O2 saturated aqueous solution) LSV curves for MnCo2O4/CF and the benchmark Pt-Ru electrocatalyst are shown in Figure 6.3. The ORR onset potential for MnCo2O4/CF is -0.04 V vs. Hg/HgO, which is slightly better than the onset potential for Pt-Ru (-0.06 V vs. Hg/HgO) (Figure 6.3(a)). The maximum current density, for the potential range of 0 V to -0.5 V vs. Hg/HgO, in the ORR half-cell test for MnCo2O4/CF is -548.7 mA cm-2, which is superior to the maximum current density by Pt-Ru (-333.6 mA cm-2). The OER onset potential and maximum current density for MnCo2O4/CF are 0.28 V vs. Hg/HgO and 292.6 mA cm-2, respectively, which are significantly improved compared with the corresponding values for Pt-Ru (0.63 V vs. Hg/HgO and 126.0 mA cm-2, Figure 6.3(b)). The catalytic activity of

MnCo2O4/CF towards both ORR and OER, in terms of both the onset potential and the maximum current density, is better than that of Pt-Ru. This is due, in part, to the design of the homemade air electrode and the materials utilized. The carbon fibers helped improve the electronic conductivity of the air electrode, by offsetting the poor conductivity of MnCo2O4. In addition, the use of relatively large carbon fibers (~10 µm in diameter) provided voids and pores within the air electrode which facilitated oxygen diffusion through and electrolyte penetration into the air electrode. The half-cell tests results are summarized in Table 6.1.

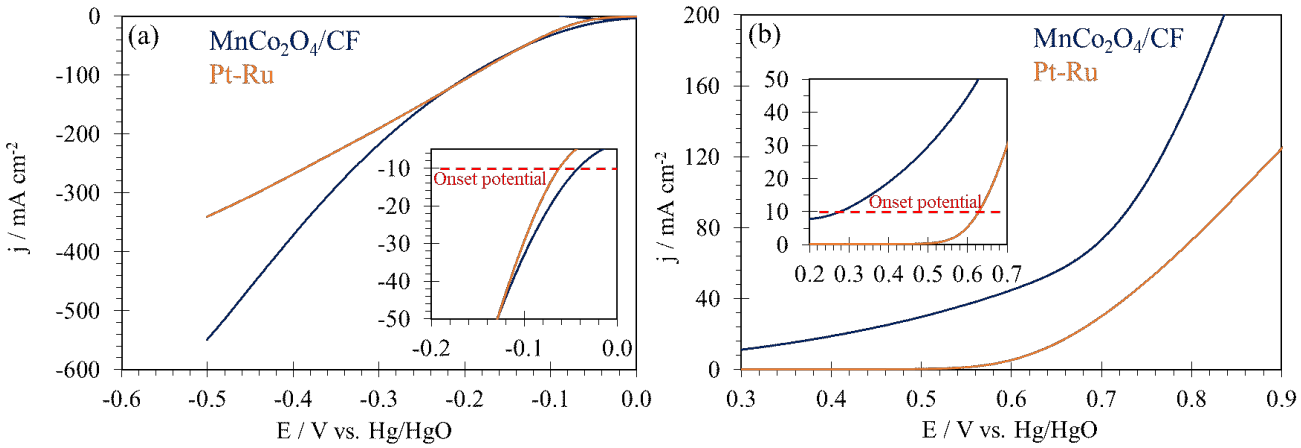

Figure 6.3. (a) ORR and (b) OER half-cell LSV tests results for $MnCo_2O_4$/CF and Pt-Ru in O_2 saturated 1 M KOH.

Table 6.1. Half-cell test results for $MnCo_2O_4$/CF and Pt-Ru in O_2 saturated 1 M KOH

Half-cell results in O_2 saturated 1 M KOH	**$MnCo_2O_4$/CF**	**Pt-Ru**
ORR onset potential (V vs. Hg/HgO)	-0.04	-0.06
OER onset potential (V vs. Hg/HgO)	0.28	0.63
Maximum ORR current density (mA cm^{-2})	-548.7	-333.6
Maximum OER current density (mA cm^{-2})	292.6	126.0

6.3.3 Full Cell Zinc-air Battery Testing

ZAB full-cell tests were conducted on batteries made with an air electrode consisting of $MnCo_2O_4$/CF or Pt-Ru and either a hydrogel electrolyte, with different crosslinker concentrations plus KOH and ZnO ($MnCo_2O_4$/CF-Hydrogel or Pt-Ru-Hydrogel), or an aqueous electrolyte with 6 M KOH and 0.25 M ZnO ($MnCo_2O_4$/CF-Aqueous or Pt-Ru-Aqueous) (Figure 6.4). The efficiency and voltage gaps for all the samples are shown in Table 6.2. Of all $MnCo_2O_4$/CF air electrodes coupled with hydrogel electrolytes with different crosslinker concentrations, Hydrogel-30-mM has the highest efficiency at all current densities. For this reason, Pt-Ru was tested with Hydrogel-30-mM as well. $MnCo_2O_4$/CF-Hydrogel-30-mM has efficiencies of 62.6% and 61.1% with voltage gaps of 0.77 V and 0.84 V, at 10 mA cm^{-2} and 20 mA cm^{-2}, respectively. Similar to the half-cell tests results, $MnCo_2O_4$/CF-Hydrogel-30-mM has superior discharge/charge performance to Pt-Ru-Hydrogel-30-mM, which has efficiencies of 61.3% and 55.1% and voltage gaps of 0.79 V and 0.97 V at 10 mA cm^{-2} and 20 mA cm^{-2}, respectively. In the aqueous electrolyte, $MnCo_2O_4$/CF has better performance, with an efficiency of 63.7% at 10 mA cm^{-2}, than Pt-Ru with an efficiency of 61.9% at the same current density. The better charge/discharge battery performance of $MnCo_2O_4$/CF in both aqueous and hydrogel

electrolytes, compared with Pt-Ru, is attributed to the well-engineered design of the homemade $MnCo_2O_4$/CF air electrode that provides a 3D structure due to the relatively large size of the carbon fibers (~10 μm in diameter) with macro-pores for a better air/electrode/electrolyte interface.

Based on the rheology results, as the crosslinker concentration increases the viscosity of the hydrogel increases and it becomes stiffer. In other words, $viscosity_{(Aqueous)} < viscosity_{(Hydrogel\text{-}30\text{-}mM)} < viscosity_{(Hydrogel\ 40\text{-}mM)} < viscosity_{(Hydrogel\text{-}50\text{-}mM)}$. For both $MnCo_2O_4$/CF and Pt-Ru, the general trend in terms of battery performance is that as the viscosity of the electrolyte increases (from Aqueous to Hydrogel-50-mM), the performance of the battery degrades. The efficiency values at 10 and 20 mA cm^{-2}, that are presented Table 6.2, decrease while the voltage gaps increase as the viscosity of the electrolyte increases. For example, at 10 mA cm^{-2}, $MnCo_2O_4$/CF has an efficiency of 63.7% in the aqueous electrolyte, 62.6% in Hydrogel-30-mM, 61.9% in Hydrogel-40-mM and 61.2% in Hydrogel-50-mM. As the electrolyte becomes more viscous, its penetration into the porous air electrode becomes more difficult, reducing the contact area between the electrolyte and the air electrode (Figure 6.5). It is well established that the ion transport rate decreases as the viscosity increases. [230,231] Therefore, degradation of battery performance by increasing the viscosity of the electrolyte is likely due to the decreased electrode/electrolyte contact, which is also known as the three-phase boundary (air/electrolyte/electrocatalyst), as well as a decrease in the ion (mainly OH^- and Zn^{2+}) transport rate and O_2 diffusion. [232,233]

The expanded view of the full-cell battery performance for $MnCo_2O_4$/CF in hydrogel electrolytes with different crosslinker concentration (Figure 6.4(b)) shows that the charge/discharge voltages at low current densities (e.g., 2 mA cm^{-2}) are very similar. At higher current densities, such as 20

mA cm^{-2}, the differences between the charge/discharge potentials for $MnCo_2O_4$/CF in hydrogel electrolytes with different crosslinker concentrations become more significant. This is likely due to the effect of ion (OH^-, Zn^{2+}) or dissolved gas (O_2) diffusion in the different electrolytes. The effect of diffusion in the electrolyte on the battery performance is not significant at low current densities (e.g., 2 mA cm^{-2}) because the charge/discharge rates are slow enough to provide enough time for the diffusing species to move either towards or away from the air electrode. Ion species diffusion is more important at higher current densities (e.g., 20 mA cm^{-2}), since diffusion rates are not fast enough to respond to the higher ORR/OER rates. As such battery performance degrades. Diffusion is less restricted in Hydrogel-30-mM compared with Hydrogel-40-mM and Hydrogel-50-mM, which leads to a higher discharge voltage and lower charge voltage for Hydrogel-30-mM at high current densities. For example, the charge and discharge voltages at 10 mA cm^{-2} are 1.98 V and 1.24 V vs. Zn/ZnO for $MnCo_2O_4$/CF-Hydrogel-30-mM and 2.02 V and 1.23 V for $MnCo_2O_4$/CF-Hydrogel-50-mM.

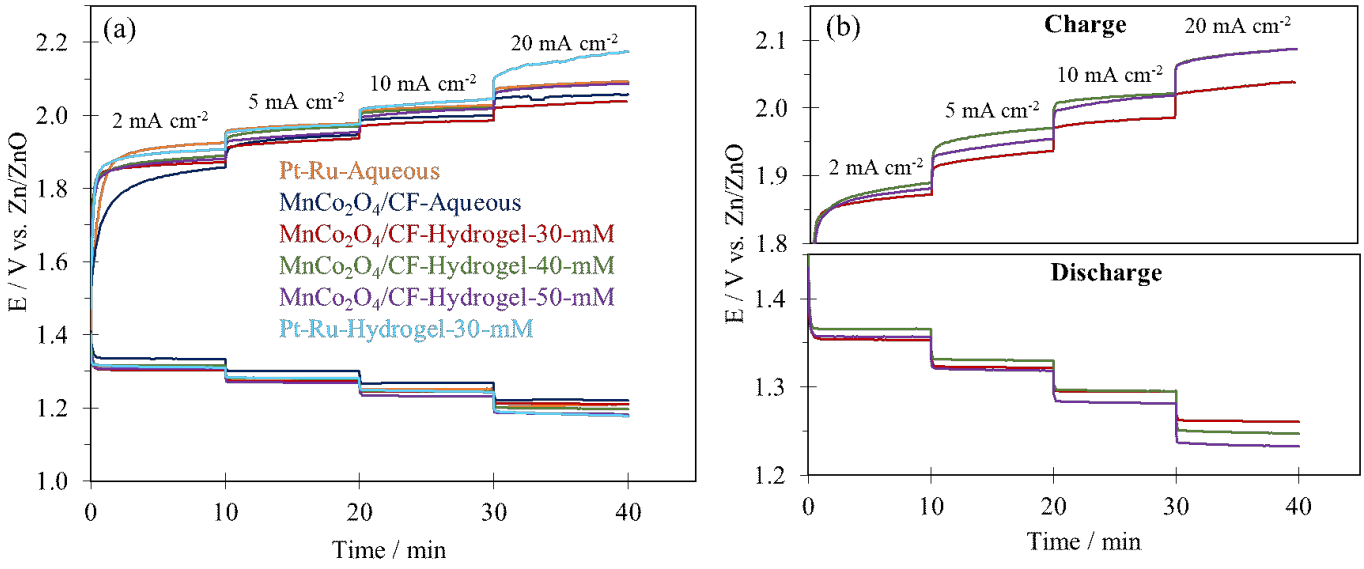

Figure 6.4. ZAB (a) full cell tests results and (b) expanded view of full cell tests results at different current densities for $MnCo_2O_4$/CF and Pt-Ru in aqueous and hydrogel electrolytes.

Table 6.2. Full-cell tests results for $MnCo_2O_4$ and Pt-Ru in hydrogel and aqueous electrolytes

Full-cell results		**Pt-Ru**		**$MnCo_2O_4$/CF**			
		Aqueous	Hydrogel-30-mM	Aqueous	Hydrogel-30-mM	Hydrogel-40-mM	Hydrogel-50-mM
j = 10 mA cm^{-2}	Voltage gap (V)	0.77	0.79	0.72	0.74	0.77	0.78
	Efficiency (%)	61.9	61.3	63.7	62.6	61.9	61.2
j = 20 mA cm^{-2}	Voltage gap (V)	0.88	0.97	0.82	0.74	0.88	0.90
	Efficiency (%)	57.9	55.1	60.0	61.1	57.7	56.7

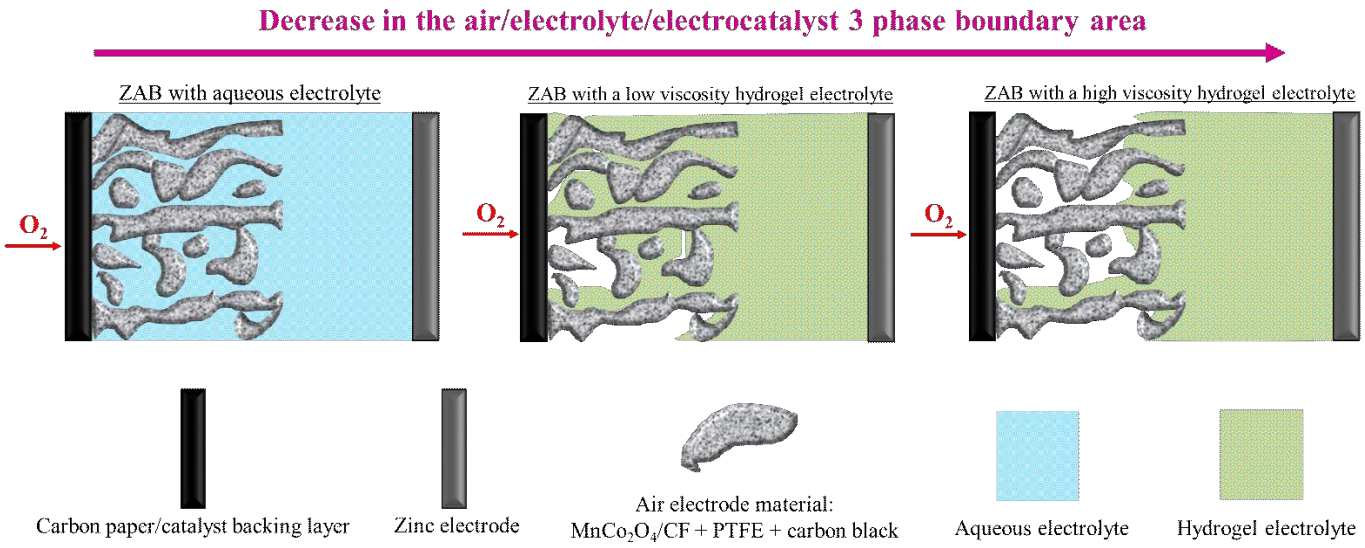

Figure 6.5. Schematics of the effect of electrolyte viscosity on the electrode/electrolyte/air three phase boundary area.

EIS measurements were acquired from the full-cell ZAB configuration, using MnCo2O4/CF as the air electrode, and are shown in Figure 6.6. Because the electrode materials for all the samples were the same, the first intercept of the EIS curves with the x axis represents the electrolyte resistance (Relectrolyte). Typically, in an EIS test at high frequencies, the effect of diffusion of the species in the electrolyte is minimal; this effect becomes dominant at lower frequencies. [125] However, Figure 6.6(b)-(d) shows that the diffusion region for MnCo2O4/CF-Hydrogel-40-mM and MnCo2O4/CF-Hydrogel-50-mM is expanded to the high frequency region, so that the semicircle in the high frequency region is not observed. The Rct value for MnCo2O4/CF-Hydrogel-30-mM was calculated as ~0.3 Ω based on fitting of the data (EC-Lab) (Figure 6.6(b)). However, Rct could not be determined for MnCo2O4/CF-Hydrogel-40-mM and MnCo2O4/CF-Hydrogel-50-mM. Nevertheless, comparison of Figure 6.6(b), (c) and (d) suggests that: 1) the Warburg region with the 45o line, for Hydrogel-40-mM and Hydrogel-50-mM, has expanded to the high frequency region which is why the semicircle in this region is not visible. This result

indicates that diffusion of the charge carrier species within these electrolytes is a limiting factor in terms of the battery performance, even at very high frequencies. In addition, the increase in viscosity of the hydrogel electrolytes, by increasing the crosslinker concentration, results in a decrease in the electrode/electrolyte/air three-phase boundary area. As such, the electrolyte resistance increases. Relectrolyte values for Hydrogel-30-mM, Hydrogel-40-mM and Hydrogel-50-mM were determined as 1.1 Ω, 1.2 Ω and 1.26 Ω, respectively.

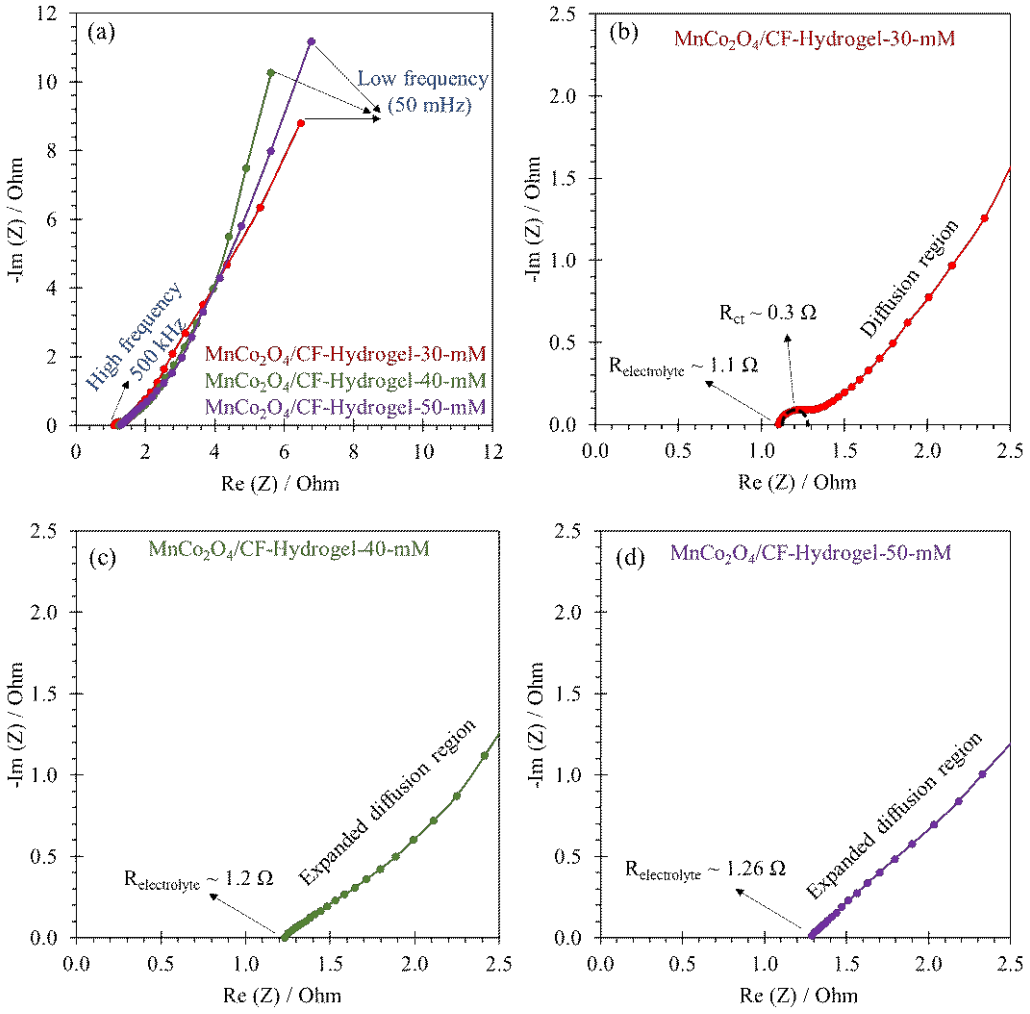

Figure 6.6. EIS tests results for $MnCo_2O_4$/CF in (a) different hydrogel electrolytes. Expanded views for (b) Hydrogel-30-mM, (c) Hydrogel-40-mM and (d) Hydrogel-30-mM.

$MnCo_2O_4$/CF-Hydrogel-30-mM and Pt-Ru-Hydrogel-30-mM were tested for 200 cycles (100 h) at 10 mA cm-2 to investigate the cycling behavior of the batteries. Each cycle includes 10 min of discharge, 5 min of rest and 10 min of charge followed by another 5 min of rest. $MnCo_2O_4$/CF-Hydrogel-30-mM had stable cycling behavior with no major fluctuations in the discharge/charge voltage up to ~130 cycles; there is gradual degradation after ~130 cycles (Figure 6.7(a)). On the other hand, Pt-Ru-Hydrogel-30-mM was not stable during cycling as charge performance started to degrade after ~20 cycles. The battery failed at ~110 cycles (discharge failure occurred at ~100

cycles and charge failure at ~110 cycles (Figure 6.7(b)). Cell failure in this work is defined by the charge voltage exceeding 3.0 V vs. Zn/ZnO and/or the discharge voltage dropping to lower than 0.5 V vs. Zn/ZnO. Initial and final discharge and charge voltages and efficiencies are presented in Table 6.3. Initial and final efficiencies for $MnCo_2O_4$/CF-Hydrogel-30-mM are 62.6% and 56.1% (6.5% difference), respectively, while the initial efficiency for Pt-Ru-Hydrogel-30-mM is 61.3% and the final efficiency is not defined for this battery due to battery failure. An expanded view of the discharge/charge behavior for $MnCo_2O_4$/CF-Hydrogel-30-mM shows the minor changes in the discharge/charge voltages at three different stages (0-10, 90-100 and 190-200 cycles (Figure 6.7(c)). Figure 6.7(d) shows superimposed curves from Figure 6.7(a) and 7(b) to better illustrate the changes in the discharge/charge voltages during cycling for $MnCo_2O_4$/CF-Hydrogel-30-mM and Pt-Ru-Hydrogel-30-mM, for the entire 200 cycles.

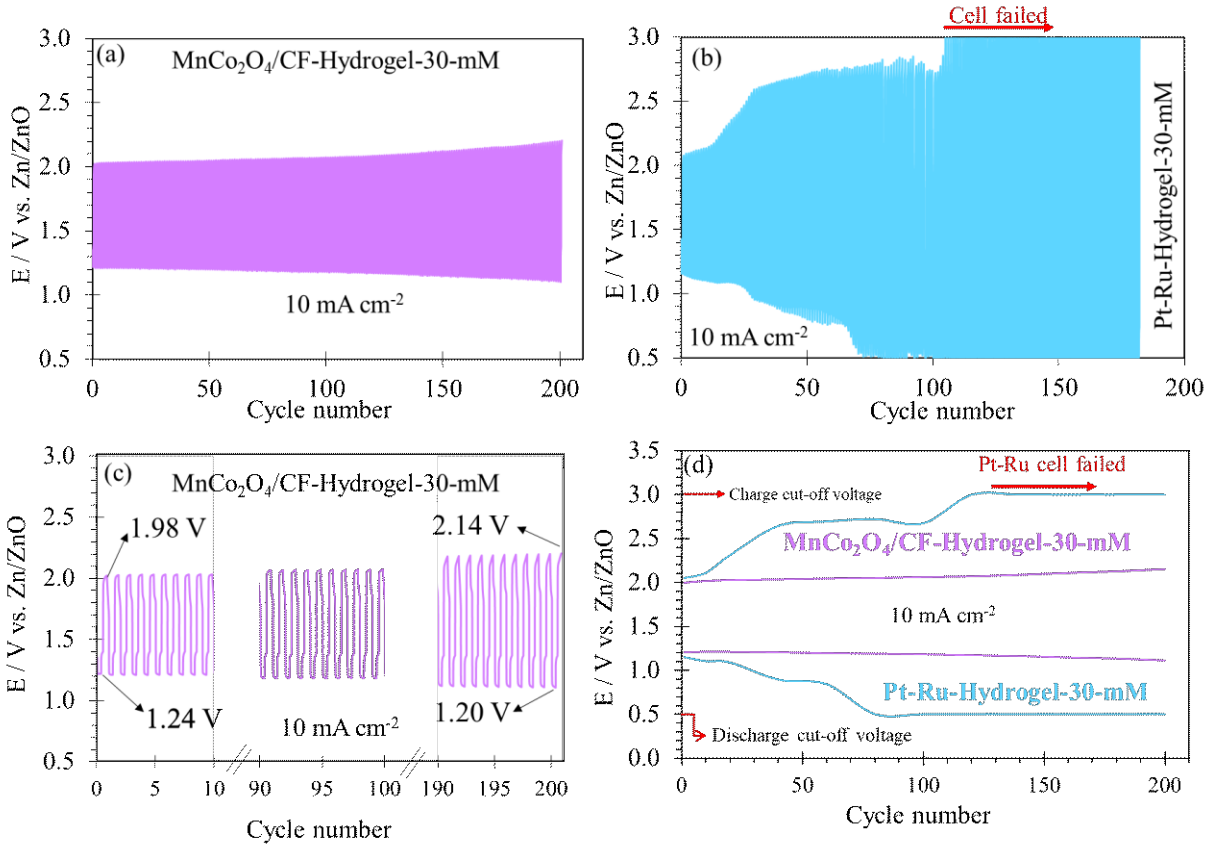

Figure 6.7. Cycling test results for (a) $MnCo_2O_4$/CF-Hydrogel-30-mM and (b) Pt-Ru-Hydrogel-30-mM at 10 mA cm^{-2}. (c) High resolution discharge/charge voltages for $MnCo_2O_4$/CF-Hydrogel-30-mM at three different stages during cycling and (d) discharge/charge voltages for both catalysts for 200 cycles.

Table 6.3. Cycling test results for $MnCo_2O_4$/CF-Hydrogel-30-mM and Pt-Ru-Hydrogel-30-mM at 10 mA cm^{-2}

	$MnCo_2O_4$/CF-Hydrogel-30-mM	**Pt-Ru-Hydrogel-30-mM**
Initial discharge voltage (V)	1.24	1.25
Final discharge voltage (V)	1.20	Failed
Initial charge voltage (V)	1.98	2.04
Final charge voltage (V)	2.14	Failed
Initial efficiency (%)	62.6	61.3
Final Efficiency (%)	56.1	Failed

Since the cycling tests for both the $MnCo_2O_4$/CF and Pt-Ru catalysts were conducted in the Hydrogel-30-mM electrolyte, the performance difference is attributed to the catalysts. A previous study has revealed that $MnCo_2O_4$/CF has very stable cycling behavior in alkaline aqueous electrolytes with only a 4.8% drop in the efficiency after 200 cycles when tested at 10 mA cm^{-2} for 100 h, while the cycling behavior of Pt-Ru was very unstable, mainly due to the oxidation of Pt during OER. [12] Furthermore, the corrosion of carbon in an alkaline environment, mainly in the form of potassium carbonate (K_2CO_3) formation, is a major reason for the performance drop of ZABs. Potassium carbonate particles can plug the porosity of the electrodes limiting access to three phase boundaries. [2,12,22]

SEM/EDX analysis was conducted on pristine and cycled (200 times) $MnCo_2O_4$/CF electrodes, to investigate any morphology changes due to the formation of potassium carbonate (Figure 6.8). The SEM SE image of the pristine electrode (Figure 6.8(a)) shows the distribution of carbon fibers as well as some regions that include carbon black, PTFE and excess $MnCo_2O_4$ that has not

coated the carbon fibers. The EDX maps for this electrode confirm the presence of Mn, Co and O and show that these signals overlap (Figure 6.8(c)-(e)). An SEM SE image and corresponding EDX maps for the cycled electrode are shown in Figure 6.8(f)-(j)). The carbon fibers in the air electrode are still intact. There is no K signal in the EDX spectrum of the cycled electrode (Figure 6.8(k)) and there is no excess C in the porosity (Figure 6.8(g)), which indicates that there is little or no potassium carbonate formation. As such, carbon corrosion is not the primary reason for the drop in efficiency during cycling. The EDX spectrum (Figure 6.8(k)) acquired from the area shown in Figure 6.8(a) of the pristine electrode confirms the presence of Mn, Co, O and C. A small amount of S from the CF precursor and Na from the sonication step are present in the pristine electrode. The EDX spectrum of the area shown in Figure 6.8(f) of the cycled electrode is also presented in Figure 6.8(k) and confirms the presence of Mn, Co and C after cycling. Other possible reasons for performance loss during cycling include degradation of the polymer matrix and changes in the electrolyte concentration. [21,38]

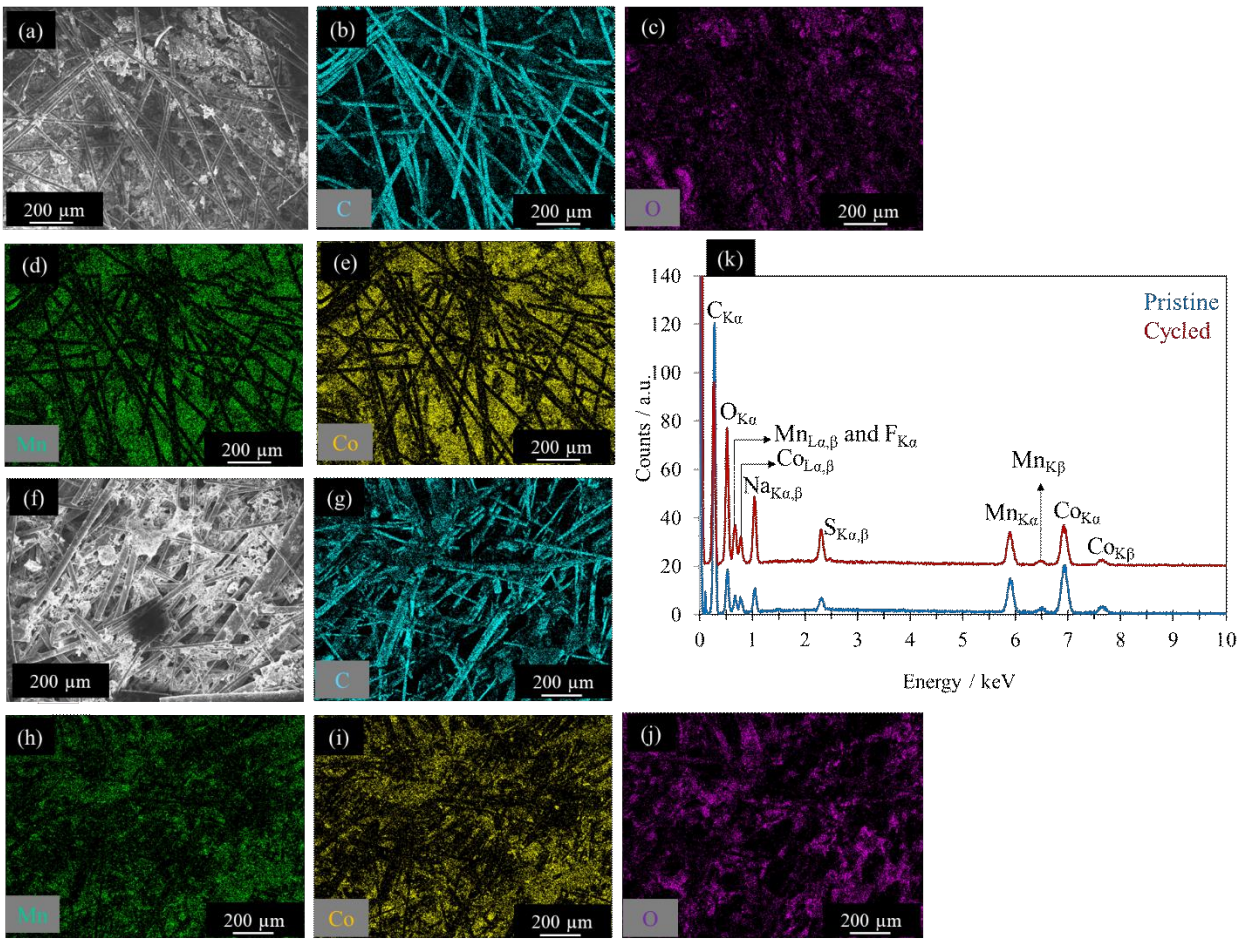

Figure 6.8. SEM/EDX analysis on (a)-(e) pristine and (f)-(j) cycled $MnCo_2O_4$/CF electrodes and (j) the EDX spectra from the areas shown in (a) and (f).

Power density and cell potential plots, as a function of discharge current density, for $MnCo_2O_4$/CF-Hydrogel-30-mM, Pt-Ru-Hydrogel-30-mM, $MnCo_2O_4$/CF-Aqueous and Pt-Ru-Aqueous, are shown in Figure 6.9. The maximum power density achieved for $MnCo_2O_4$/CF-Hydrogel-30-mM is 240 mW cm^{-2}, which is considerably larger than that for Pt-Ru-Hydrogel-30-mM (165 mW cm^{-2}) (Figure 6.9(a)). The maximum power densities achieved for both catalysts in the hydrogel electrolyte are also significantly higher than the ones achieved for the same catalysts in the aqueous electrolyte; i.e., 127 mW cm^{-2} for $MnCo_2O_4$/CF-Aqueous and 121 mW cm^{-2} for Pt-Ru-Aqueous (Figure 6.9(b)). Power densities at current densities lower than

~100 mA cm^{-2} are similar for both the hydrogel and aqueous electrolytes, but power densities at larger current densities are higher for the hydrogel electrolyte compared with aqueous electrolyte. At low current densities, the effect of O_2 diffusion from ambient air into the air electrode on the battery performance is minimal, while at higher current densities O_2 diffusion limits the performance of the battery for both electrolytes. At high current densities, it is believed that since the hydrogel electrolyte does not completely fill the porosity of the air electrode (deep within the electrode) (Figure 6.5), it is easier for O_2 to diffuse from ambient air from the backside of the air electrode to the three phase boundary regions. The aqueous electrolyte more readily fills the porosity of the air electrode, which can limit the three phase boundary area and O_2 diffusion and reduce the power density at higher current densities. In addition, the improved three phase boundary area access that the hydrogel electrolyte provides results in a higher discharge voltage for the catalysts at high current densities. The cell voltage for the catalysts in both the aqueous and hydrogel electrolyte starts at ~1.4 V vs. Zn/ZnO for low current densities and drops in a similar manner with increasing current density until ~100 mA cm^{-2}. The potential drop with increasing current density is more significant for the aqueous electrolyte. For example, at a current density of 300 mA cm^{-2}, the cell voltages for $MnCo_2O_4$/CF-Hydrogel-30-mM and $MnCo_2O_4$/CF-aqueous are ~0.8 V vs. Zn/ZnO and ~0.3 V vs. Zn/ZnO, respectively. Furthermore, the cell voltage for Pt-Ru-Hydrogel-30-mM drops significantly with increasing current density and reaches zero (battery failure) at ~330 mA cm^{-2}.

Figure 6.9(a) also indicates a lower ohmic overpotential for $MnCo_2O_4$/CF-Hydrogel-30-mM compared with Pt-Ru-Hydrogel-30-mM. The ohmic overpotential is due to a combination of resistances from the electron flow, proton flow, and electrical contact. The only difference between the two batteries in Figure 6.9(a) is the air electrode. For the Pt-Ru-Hydrogel-30-mM

system, the battery becomes diffusion limited at high current densities, which is not the case for $MnCo_2O_4$/CF-Hydrogel-30-mM. This is likely because of the different designs for the air electrode. The Pt-Ru catalyst is essentially deposited (sprayed) only on the surface of the air electrode which can limit charge transfer at the surface of the electrode. $MnCo_2O_4$ coats the carbon fibers throughout the entire active region of the air electrode. This facilitates electron/charge transfer to/from the air electrode which improves (lowers) the ohmic overpotential.

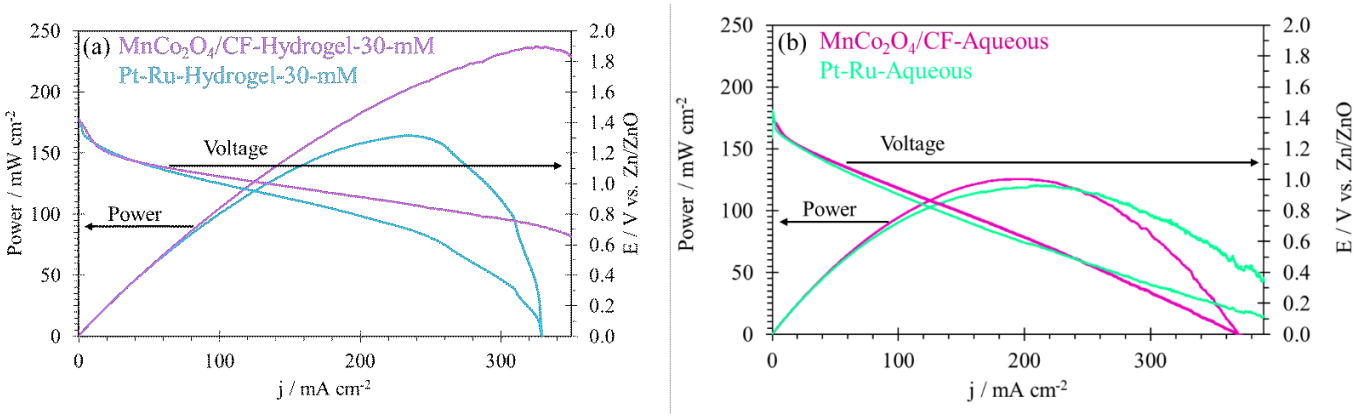

Figure 6.9. Power and cell voltage for ZAB cells with (a) hydrogel and (b) aqueous electrolytes.

The results presented here indicate that using well engineered homemade air electrodes for ZABs with GPE can provide stable batteries with good performance and high power densities. Table 6.4 presents a comparison between the results of this work and the recent literature with GPEs. The power output and cycling performance of batteries with $MnCo_2O_4$/CF as the bifunctional electrocatalyst and PAA as the hydrogel electrolyte ($MnCo_2O_4$/CF-Hydrogel-30-mM) are superior to previously reported rechargeable ZABs. A direct comparison can be made with the studies listed in Table 6.4, as they all used similar electrolytes and transition metal oxide based electrocatalysts. A comparison with several ZABs using aqueous electrolytes is also provided in Table 6.4. Table 6.4 shows that the cycling behavior and the power output for the aqueous

batteries is generally superior to the solid-state ones (with the exception of this work). For example, the work by Wang et al. [234] reported a maximum power output of 231 mW cm^{-2} for a ZAB with an aqueous alkaline electrolyte, however, this cell had a stable charge/discharge performance for only 25 h. The use of micron-scale carbon fibers in this work generated a porous 3D design for the air electrode with a maximum power output of 240 mW cm^{-2} and stable cycling behavior. This power output is rare for ZABs and the cycling behavior of $MnCo_2O_4$/CF-Hydrogel-30-mM was the same or better than the batteries (with GPEs) reported by Roy et al. [225], Tang et al. [235], Miao et al. [224], Chen et al. [223], Ramakrishnan et al. [27], Muthurasu et al. [32] and Chen et al. [37], even though those studies used lower current densities and/or shorter cycling durations for battery cycle testing. For example, the batteries reported by He et al. [236] and Tran et al. [237], using PAA as the GPE, have relatively high maximum power densities of 158 and 146 mW cm^{-2}, respectively. The battery reported by He et al. [48] had a high initial efficiency of ~69% at 10 mA cm^{-2}; however, the battery was only cycled 16 times (6 h). The best performing ZAB cell in the work by Tran et al. failed after 160 cycles (80 h), although their cell was cycled at a current density of 20 mA cm^{-2}.

Table 6.4. Comparison of ZAB cycling, efficiency and power density performance

Electrocatalyst	**Electrolyte**	**Current density (mA cm^{-2})**	**Number of cycles-total cycling duration**	**Initial/final efficiency (%)**	**Power density (mW cm^{-2})**	**Ref.**
$MnCo_2O_4$/CF ($MnCo_2O_4$/CF-Hydrogel-30-mM)	PAA-KOH	10	200 cycles - 100 h	62.6/56.1	240	This work
$(Co,Fe)_3O_4$/N-CNT	PAA-KOH	20	160 cycles - 80 h	60.8/failed	146	[237]
CoPS	PAA-KOH	5	150 cycles – 25 h	60/~54	N/A	[225]
FeCo-NC	PAA-KOH	10	16 cycles – 6 h	~69/~69	158	[236]
N, S-C-Co_9S_8	PAA-Fe^{3+}-CS/NH_4Cl	5	360 cycles - 120 h	32.8/31.6	55.4	[235]
$LaMnO_3$	PAA-KOH	5	100 cycles – 17 h	64/57.5	52.9	[224]
Co_3O_4	PVA–OH–MXene	2	320 cycles - 160 h	~45/~40	70	[223]
CS-NFO@PNC	PVA-KOH	5	240 cycles - 40 h	~57/~54	51	[27]
N-CNTs@MOF-FeCo	PVA-KOH	5	60 cycles - 10 h	~75/~53	70	[32]
CoMn1.5Ni0.5O4	PAMC	5	190 cycles – 32 h	~63/~42	~86	[37]
Fe_3C/Co(Fe)O_x@ NCNT	Aqueous KOH	10	150 cycles – 25 h	~57/~55	231	[234]
$MnCo_2O_4$/CF	Aqueous KOH	10	200 cycles - 100 h	63.7/58.9	127	[12]
FeCoMoS	Aqueous KOH	2	420 cycles - 70 h	60/56	118	[28]

6.4 Conclusions

The pursuit of high power and efficient Zn-air batteries (ZABs) with gel polymer electrolyte with stable cycling performance was the starting point of this work. Cubic spinel type $MnCo_2O_4$ coated carbon fibers ($MnCo_2O_4$/CF) were used to prepare well-engineered air electrodes for ZABs. PAA-KOH based gel polymer electrolytes (GPEs) were synthesized; the best performing composition for the GPEs was 6.5 M KOH, 0.5 M PAA, 0.2 M ZnO, 30 mM MBAA and 1.5 mM KPS (Hydrogel-30-mM). The ZAB cell made with Hydrogel-30-mM and $MnCo_2O_4$/CF ($MnCo_2O_4$/CF-Hydrogel-30-mM) had an initial roundtrip efficiency of 62.6% at 10 mA cm^{-2} which degraded by only 6.5% after 100 h (200 cycles, 30 min/cycle). This performance was superior to that of the cell made with the benchmark electrocatalyst, consisting of Pt and RuO_2 mixed with carbon black (Pt-Ru), and Hydrogel-30-mM, which had an initial roundtrip efficiency of 61.3% but failed after ~110 cycles. The maximum power output for $MnCo_2O_4$/CF-Hydrogel-30-mM was 240 mW cm^{-2}, which is far superior to other ZABs with GPEs in the literature. The superior performance is attributed to the air electrode, consisting of micron-scale carbon fibers, which provide high macro-porosity to increase the air/electrocatalyst/electrolyte three phase boundary area leading to better oxygen reduction reaction (ORR) and oxygen evolution reaction (OER) kinetics.

Chapter 7: Efficient Low Temperature Performance of All Solid-State Zinc-air Batteries with $MnCo_2O_4$/Carbon Fiber Bifunctional Electrocatalyst and Poly(acrylic Acid) (PAA) Gel Polymer Electrolyte

A version of this chapter has been submitted for publication in the journal Batteries and Supercaps:

Z. Abedi, J. Cui, W. Cehn and D.G. Ivey, "Efficient Low Temperature Performance of All Solid-State Zinc-air Batteries with $MnCo_2O_4$/Carbon Fiber Bifunctional Electrocatalyst and Poly(acrylic Acid) (PAA) Polymer Electrolyte" *Batteries and Supercaps.*, 2022.

7.1 Introduction

Development of new and sustainable energy storage devices has become crucial as the world moves towards clean and sustainable energy. Rechargeable (secondary), zinc-air batteries (ZABs) have shown promising battery performance for use as alternative energy storage devices to traditional batteries like Li-ion batteries. [1] Furthermore, ZABs are cost effective devices that benefit from safe operation and high energy density. [2] The main components of a ZAB cell are a metallic Zn electrode, an alkaline electrolyte, a separator, and an air electrode; the air electrode is often carbon based and contains electrocatalysts. [3,4] The name air electrode is taken from the air reactions that take place at this electrode. The oxygen reduction reaction (ORR) and oxygen evolution reaction (OER) occur at the air electrode during discharge and charge, respectively. [5] These reactions suffer from poor kinetics which results in problems like low battery voltage efficiency and poor cycling behavior. [6] This necessitates the use of effective electrocatalysts to improve the battery performance. [7]

Many effective electrocatalysts for use in ZABs have been developed. Transition metal oxides (TMOs), carbonaceous materials like graphite and carbon nanotubes, and precious metals like Pt, Ir and Ru are the most important materials that have shown promising catalytic behavior towards ORR and/or OER. [8–14] The cost, scarcity, and instability (in terms of battery cycling performance) of precious metals have made their widespread use in ZABs impractical. [15] Although TMOs have proven to be active towards ORR/OER, their insulating nature is an issue for energy storage devices. Carbon-based materials are used as conductive substrates for TMOs to improve charge transfer and conductivity issues. [5,10,14,16–18]

Carbon fibers have been shown to be excellent candidates for use in energy storage devices; they can be used as the conductive substrate for TMOs. Carbon fibers can be synthesized from various precursors like food scraps, polyaniline (PANI), and asphaltene. Asphaltene is viscous and high carbon content by-product of the oil sands industry with significantly more supply than demand. Melt-spinning can be employed to prepare micron-scale carbon fibers from asphaltene. [5,17,19–21]

In previous work by some of the authors, low-cost micron-scale carbon fibers were used as the air electrode material/electrocatalyst in ZABs with aqueous electrolytes. Spinel type MnCo2O4 coated on asphaltene derived carbon fibers (MnCo2O4/CF) was synthesized and homemade air electrodes were prepared using MnCo2O4/CF. The performance of the synthesized MnCo2O4/CF as the air electrode material in aqueous ZABs at room temperature was quite good in terms of battery efficiency and cycling stability. [5]

The design of the air electrode and the electrolyte are important parameters in addition to the electrocatalyst used, affecting the battery performance. [5,22] The air electrode has to be porous and the electrocatalyst needs to be well dispersed throughout the air electrode to allow for

efficient oxygen penetration and adsorption during discharge. If the electrocatalyst used is not bifunctional (active towards both ORR and OER), two different electrocatalysts or two separate air electrodes could be used. [23] Aqueous and gel polymer electrolytes are often used in ZABs. Cell leakage, evaporation, and flooding are the main issues when using aqueous electrolytes. [24–26] Hydrogels are a category of gel polymer electrolytes that are capable of absorbing a significant amount of water without dissolving. Previous work has shown that when all the other components are the same, the use of a hydrogel electrolyte can lead to higher power densities and better battery performance. This was attributed to the higher viscosity of the hydrogel electrolyte compared with aqueous electrolytes, which resulted in less clogging of porosity and larger electrocatalyst/air/electrolyte contact area. [27]

The purpose of this work is to study the all solid state battery performance, at sub-zero temperatures, of ZABs made with $MnCo_2O_4$/CF as the air electrode material and alkaline poly(acrylic acid) hydrogel electrolyte.

7.2 Experimental

7.2.1 Bifunctional Electrocatalyst Synthesis

Asphaltene based carbon fibers were synthesized via the procedure reported in the recent literature. [171,175] The fibers were then coated with $MnCo_2O_4$ ($MnCo_2O_4$/CF) using a previously developed process and the coated fibers were used as the air electrode material in this work. [12] In summary, asphaltene derived fibers were carbonized at 1500 ^oC and then soaked in ~20 ml of 28 wt% NH_4OH for 10 min followed by a 5 h sonication step to coat the fibers with $MnCo_2O_4$. The sonication solution contained 30 ml of reagent alcohol, 100 mg of NaOH, 166.67 mg of Mn(II) acetate ($Mn(Ac)_2$ or $C_4H_6MnO_4$), and 333.33 mg of Co(II) acetate ($Co(Ac)_2$ or $C_4H_6CoO_4$). $MnCo_2O_4$/CF was dried in a vacuum oven at 60 ^oC for 12 h after the sonication step.

The homemade air electrodes were prepared by pasting a mixture of 90 wt% $MnCo_2O_4$/CF, 5 wt% polytetrafluoroethylene (PTFE), and 5 wt% carbon black onto hydrophobic carbon paper (Fuel Cell Store: Toray Paper 060-TGP-H-060). The purpose of using the commercial carbon paper was to provide structural support for the electrocatalyst layer. The mass loading of $MnCo_2O_4$/CF on the carbon paper was ~10 mg cm^{-2}.

A mixture of 30 wt% Pt and 15 wt% RuO_2 combined with carbon black, purchased from Alfa Aesar, was used to prepare electrodes with the ORR/OER benchmark electrocatalyst (Pt/RuO_2) for electrochemical performance comparison with $MnCo_2O_4$/CF. A spray coating suspension, containing 50 mg of Pt-RuO_2 powder, 2 ml of deionized water, 0.1 ml of Nafion 5 wt%, and 1 ml of ethanol was prepared by sonicating the suspension for 30 min. The suspension was then spray coated on the same carbon paper with a mass loading of ~1 mg cm^{-2}.

A 30 min annealing step at 350 ^oC in a Lindberg/Blue M™ Moldatherm™ box furnace was employed for all prepared electrodes.

7.2.2 Electrolyte Synthesis

Poly(acrylic acid) (PAA) was used as the host polymer for the solid state electrolyte. To prepare the alkaline hydrogel electrolytes, 6.5 M KOH, 0.5 M acrylic acid, 0.2 M ZnO, 30 mM N,N'-methylenebis(acrylamide) (MBAA), and 1.5 mM potassium persulfate ($K_2S_2O_8$ (KPS)) were mixed using a vortex mixer. MBAA and KPS were used as the crosslinker and the polymerization reaction thermoinitiator, respectively. The polymer precursor solution was kept at 60 ^oC in a vacuum oven for 1 h to allow the polymerization reaction to complete. The final hydrogel electrolyte was then cooled to room temperature overnight. KOH and ZnO were purchased from Fisher Scientific and acrylic acid, MBAA, and KPS were purchased from Sigma-Aldrich.

7.2.3 Battery Testing Configuration

Half-cell tests were conducted and the results published in a previous study dealing with the catalytic behavior of the electrocatalyst. [5] Zinc-air battery full cell testing was done by using the prepared air electrode as the working electrode and a 1 cm x 3 cm Zn sheet as the counter electrode. The synthesized PAA-KOH hydrogel was used as the electrolyte. A Ligfreezer Lo-Temp Equipment DW-60W28 mini freezer was used for the low temperature battery tests. A thermometer was used to calibrate the temperature of the freezer; at any temperature, the temperature fluctuation was ±3 oC. Batteries were tested at room temperature (21 oC), 0 oC, -10 oC, -25 oC and -45 oC. The discharge/charge performance, battery efficiency, battery voltage, cycling behavior, and power values were investigated using the full cell set-up.

7.2.4 Electrochemical Measurements

A Biologic VSP potentiostat was used to conduct the battery tests. Galvanostatic cycling with potential limitation (GCPL) tests were employed to measure the battery charge/discharge voltage at current densities of $\pm$2, $\pm$5, $\pm$10, and $\pm$20 mA cm^{-2}. The cut-off voltage for charge and discharge was 3.0 and 0.5 V vs Zn/ZnO, respectively. Modular galvano (MG) tests with a current density (j) range of $-400 < j < 0$ mA cm^{-2} were used to measure the power output and the cell voltage and to study the maximum reachable current density without failure. The charge and discharge cut-off values were chosen as 3.0 and 0.5 V vs. Zn/ZnO, respectively. Battery failure was defined as either the charge voltage exceeding the upper cut-off voltage or the discharge voltage falling below the lower cut-off voltage. Electrochemical impedance spectroscopy (EIS) was utilized to measure the electrolyte resistance to investigate the battery performance in terms of diffusion of the charge carrier species. EIS tests for all samples were performed over a frequency range from 500 kHz to 50 mHz with an alternating potential amplitude of 5 mV.

7.2.5 Materials Characterization

Field emission scanning electron microscopy (FE-SEM) coupled with energy dispersive X-ray (EDX) spectroscopy was used to study the microstructures and compositions of the pristine and cycled electrodes (ZEISS Sigma 300 VP-FE-SEM).

7.3 Results and Discussion

Full cell battery charge/discharge tests at different current densities and temperatures for both Pt/RuO_2 and $MnCo_2O_4$/CF were conducted (Figure 7.1). It should be noted that the battery performance of $MnCo_2O_4$/CF at 21 ^oC and 0 ^oC completely overlap; i.e., there is no degradation in performance when the temperature is decreased to 0 ˚C. For cells prepared with either Pt/RuO_2 or $MnCo_2O_4$/CF, the performance of the battery degrades at all current densities as the temperature is decreased (except for $MnCo_2O_4$/CF at 0 ^oC). The charge voltage increases and the discharge voltage decreases, decreasing the battery efficiency. This is likely due to the reduced mobility of the charge carriers and increased viscosity of the hydrogel electrolyte. [238,239] Reduced mobility of the charge carriers, such as ions, leads to inefficient and reduced charge transfer and battery performance. The increase in the viscosity of the hydrogel electrolyte also negatively affects charge transfer efficiency and rate, which degrade the battery performance. As the electrolyte becomes more viscous, charge transfer becomes more difficult. Charge carrier mobility is further reduced as the electrolyte becomes more viscous. For example, the ZAB efficiency for Pt/RuO_2 and $MnCo_2O_4$/CF at 10 mA cm^{-2} at 0 ^oC are 56.2% and 55.8%, respectively, and at -25 ^oC are 44.4% and 34.4%, respectively. Reduced electrochemical reaction kinetics due to decreased mobility of charge transfer species and increased viscosity of the electrolyte at subzero temperatures are the main reasons for performance degradation. As the

mobility of the charge carrier species decreases, collisions between the molecules decrease as well, leading to reduced reaction rates. [238]

Figure 7.1 also shows that the ZAB performance of $MnCo_2O_4$/CF at all temperatures and current densities is superior to that of Pt/RuO_2. As mentioned in the previous paragraph, the battery voltages for $MnCo_2O_4$/CF at 21 ^oC and 0 ^oC (curves in bright yellow and green in Figure 7.1(b)) completely overlap. $MnCo_2O_4$/CF is capable of charging/discharging without failure even at current densities as high as 20 mA cm^{-2} at all temperatures with the exception of -45 ^oC at 20 mA cm^{-2}. At -45 ^oC, $MnCo_2O_4$/CF can only perform at current densities $\leq$ 10 mA cm^{-2}. The lowest

temperature at which Pt/RuO_2 can fully charge/discharge is -10 ^oC. At -45 ^oC, Pt/RuO_2 can only be operated at current densities $\leq$ 5 mA cm^{-2}. At -25 ^oC ,the battery fabricated with Pt/RuO_2 can

be discharged at all current densities, but the battery failed during the charging process at 20 mA cm^{-2}. It can be concluded that the superior catalytic behavior of $MnCo_2O_4$/CF to Pt/RuO_2 in aqueous electrolytes and at room temperature, that has been reported previously, is retained in gel polymer electrolytes and even at low temperatures. [12] Table 7.1 summarizes the charge and discharge voltages (E) shown in Figure 7.1 and Table 7.2 shows the efficiency and voltage gaps at current densities of 10 and 20 mA cm^{-2}.

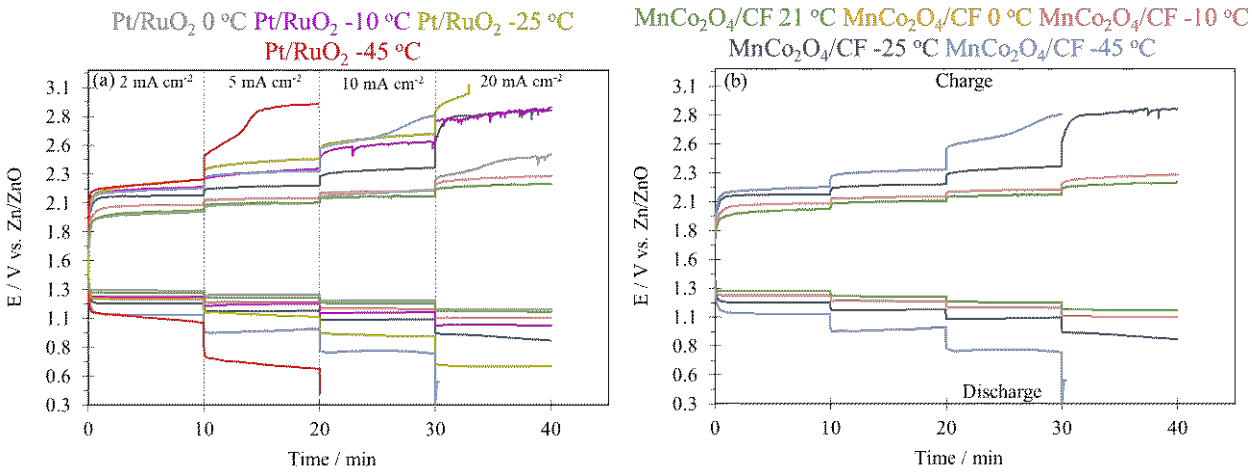

Figure 7.1. (a) Full cell charge/discharge battery test results at a range of current densities and temperatures and (b) expanded view of full-cell test results for $MnCo_2O_4$/CF.

Table 7.1. Battery full cell charge and discharge voltages for $MnCo_2O_4$/CF and Pt/RuO_2 at current densities of 10 and 20 mA cm^{-2}

Sample	**$MnCo_2O_4$/CF**				**Pt/RuO_2**			
Temperature	j = 10 mA cm^{-2}		j = 20 mA cm^{-2}		j = 10 mA cm^{-2}		j = 20 mA cm^{-2}	
	Charge E (V)	Discharge E (V)	Charge E (V)	Discharge E (V)	Charge E (V)	Discharge E (V)	Charge E (V)	Discharge E (V)
Room T	1.98	1.25	2.03	1.21	2.04	1.25	2.15	1.18
0 °C	2.10	1.18	2.20	1.11	2.15	1.20	2.38	1.13
-10 °C	2.15	1.14	2.23	1.06	2.57	1.10	2.83	0.99
-25 °C	2.34	1.04	2.81	0.92	2.62	0.90	Exceeded cut-off	0.63
-45 °C	2.67	0.77	Exceeded cut-off	Exceeded cut-off	Exceeded cut-off	Exceeded cut-off	Exceeded cut-off	Exceeded cut-off

Table 7.2. Battery full cell efficiencies and voltage gaps for $MnCo_2O_4$/CF and Pt/RuO_2 at current densities of 10 and 20 mA cm^{-2}

Sample	**$MnCo_2O_4$/CF**				**Pt/RuO_2**			
Temperature	j = 10 mA cm^{-2}		j = 20 mA cm^{-2}		j = 10 mA cm^{-2}		j = 20 mA cm^{-2}	
	Voltage gap (V)	Efficiency (%)	Voltage gap (V)	Efficiency (%)	Voltage gap (V)	Efficiency (%)	Voltage gap (V)	Efficiency (%)
Room T	0.73	63.1	0.82	59.6	0.79	61.3	0.97	54.9
0 ^{o}C	0.92	56.2	1.09	50.5	0.95	55.8	1.25	47.5
-10 ^{o}C	1.01	53.0	1.17	47.5	1.47	42.8	1.84	35.0
-25 ^{o}C	1.3	44.4	1.89	32.7	1.72	34.4	Failed	Failed
-45 ^{o}C	1.9	28.8	Failed	Failed	Failed	Failed	Failed	Failed

Nyquist plots obtained from the solid state batteries made with $MnCo_2O_4$/CF and the PAA-KOH hydrogel electrolyte are presented in Figure 7.2. Figure 7.2(a) represents the EIS test results at all temperatures, while Figure 7.2(b) and 2(c) show expanded EIS plots at 21 ^{o}C and -45 ^{o}C, respectively. The solution resistance (R_s), which is determined from the first intercept of the plot with the x axis, increases as the temperature decreases. For example, R_s for $MnCo_2O_4$/CF at 21 ^{o}C is 1 **Ω** and at -45 ^{o}C is 12 **Ω**. The increase in solution resistance is due to the increase in viscosity of the gel polymer electrolyte as the temperature decreases. Diffusion of charge carrier species becomes less efficient as the viscosity of the electrolyte increases; this can negatively affect the battery performance and efficiency. The charge transfer resistance (R_{ct}) at the surface of the air electrode also increases due the higher viscosity and lower temperature. The battery

tested at ~21 ºC has a typical EIS plot with a semicircle in the high frequency region which enters the Warburg region (linear 45˚ line) as the frequency decreases. On the other hand, the battery tested at -45 ºC does not enter the Warburg region until very low frequencies. Furthermore, the fact that the EIS plots move towards higher real portion values of the impedance (Re (Z)) as the temperature decreases indicates that diffusion is a limiting factor that degrades battery performance.

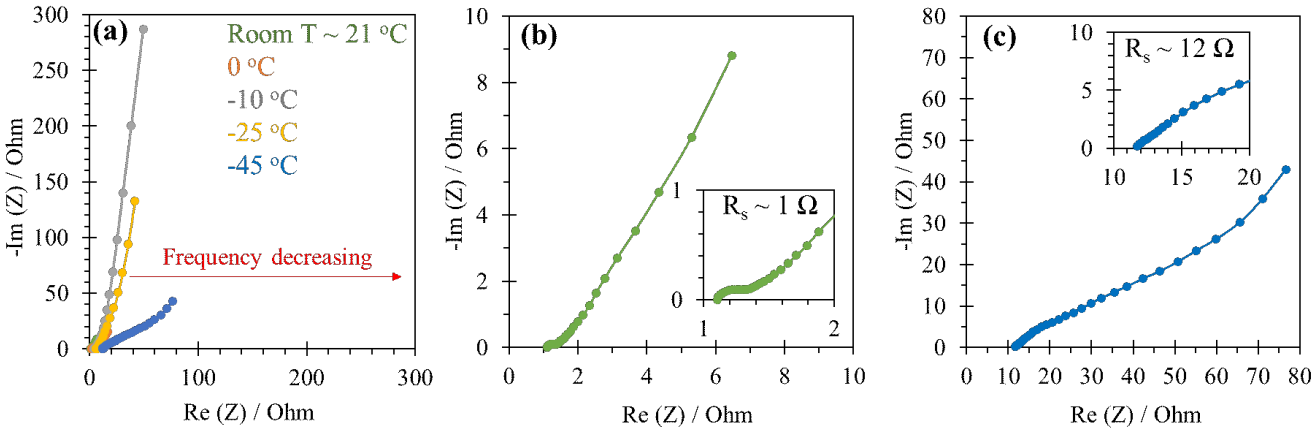

Figure 7.2. EIS test results for $MnCo_2O_4$/CF in PAA-KOH hydrogel electrolyte at (a) different temperatures, (b) at room temperature, and (c) at -45 ºC.

The battery charge/discharge cycling behavior for $MnCo_2O_4$/CF and Pt/RuO_2 at room temperature and lower temperatures are presented in Figure 7.3 and Figure 7.4, respectively. Cycling tests at room temperature were conducted at a current density of 10 mA cm^{-2}, while 2 mA cm^{-2} was used for cycling tests at lower temperatures. For all temperatures, a cycling test included 10 min of discharge, 5 min of rest, and 10 min of charge followed by another 5 min of rest. Each cycling test had a duration of 100 h which is equal to 200 cycles.

At room temperature (Figure 7.3), $MnCo_2O_4$/CF in the PAA-KOH hydrogel electrolyte battery has stable charge/discharge cycling behavior, while Pt/RuO_2 in the PAA-KOH hydrogel

electrolyte battery is unstable. The initial charge and discharge voltages for $MnCo_2O_4$/CF are 2.01 and 1.22 V vs. Zn/ZnO, respectively, which degrade to 2.16 and 1.12 V vs. Zn/ZnO, respectively, after 200 cycles. The initial and final battery efficiencies for this cell are 60.7% and 51.8%. The initial battery efficiency of the cell made with Pt/RuO_2 is 55.8% with 2.06 and 1.15 V vs. Zn/ZnO as the initial charge and discharge voltages, respectively. However, the discharge voltage of this battery reaches the cut-off voltage after ~70 cycles which causes cell failure. Due to poor battery performance of Pt/RuO_2 at room temperature, the cycling behavior of this cell was not investigated at lower temperatures.

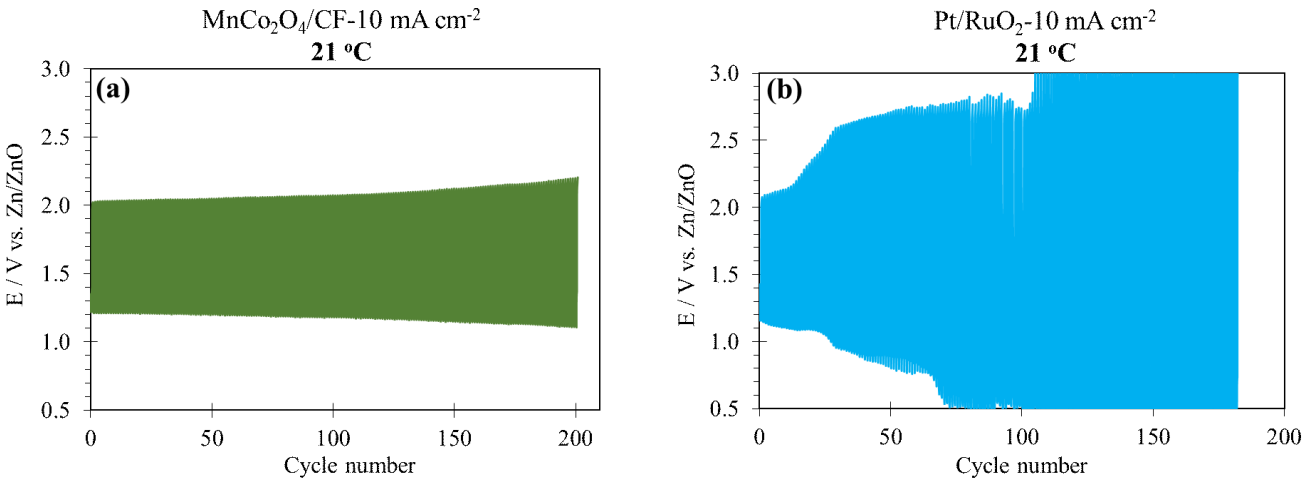

Figure 7.3. Cycling behavior of (a) $MnCo_2O_4$/CF and (b) Pt/RuO_2 in PAA-KOH hydrogel electrolyte at room temperature at 10 mA cm^{-2}.

For low temperature cycling (Figure 7.4), 2 mA cm^{-2} was chosen as the cycling current density in order to compare the results with the recent literature. Table 7.3 summarizes the voltage and efficiency values obtained from the cycling tests. Figure 7.4 and Table 7.3 indicate that battery performance degrades and battery efficiency is reduced as the temperature is decreased. For example, the initial battery efficiencies at 0, -10, -25 and -45 °C are 64.3%, 59.3%, 53.3%, and

45.2%, respectively. The performance degradation with decreasing temperature is a result of the reduced diffusion rate and reaction rate (due to reduced collisions between molecules) of the charge carrier species which lead to reduced electrochemical reaction kinetics and the increase in the viscosity of the electrolyte at subzero temperatures, as discussed previously. Even though lower temperatures negatively affect battery performance, the solid state battery made with $MnCo_2O_4$/CF in the PAA-KOH hydrogel electrolyte successfully completed 200 cycles even at -45 ^oC. The battery cycling performance is quite stable at temperatures as low as -25 ^oC, where the initial and final efficiencies are 53.3% and 49.1%, respectively. The periodic fluctuations in the charge and discharge voltages that are most pronounced at -45 ^oC are due to the temperature fluctuations (± 3 ^oC) inside the freezer that were explained in section 7.2.3.

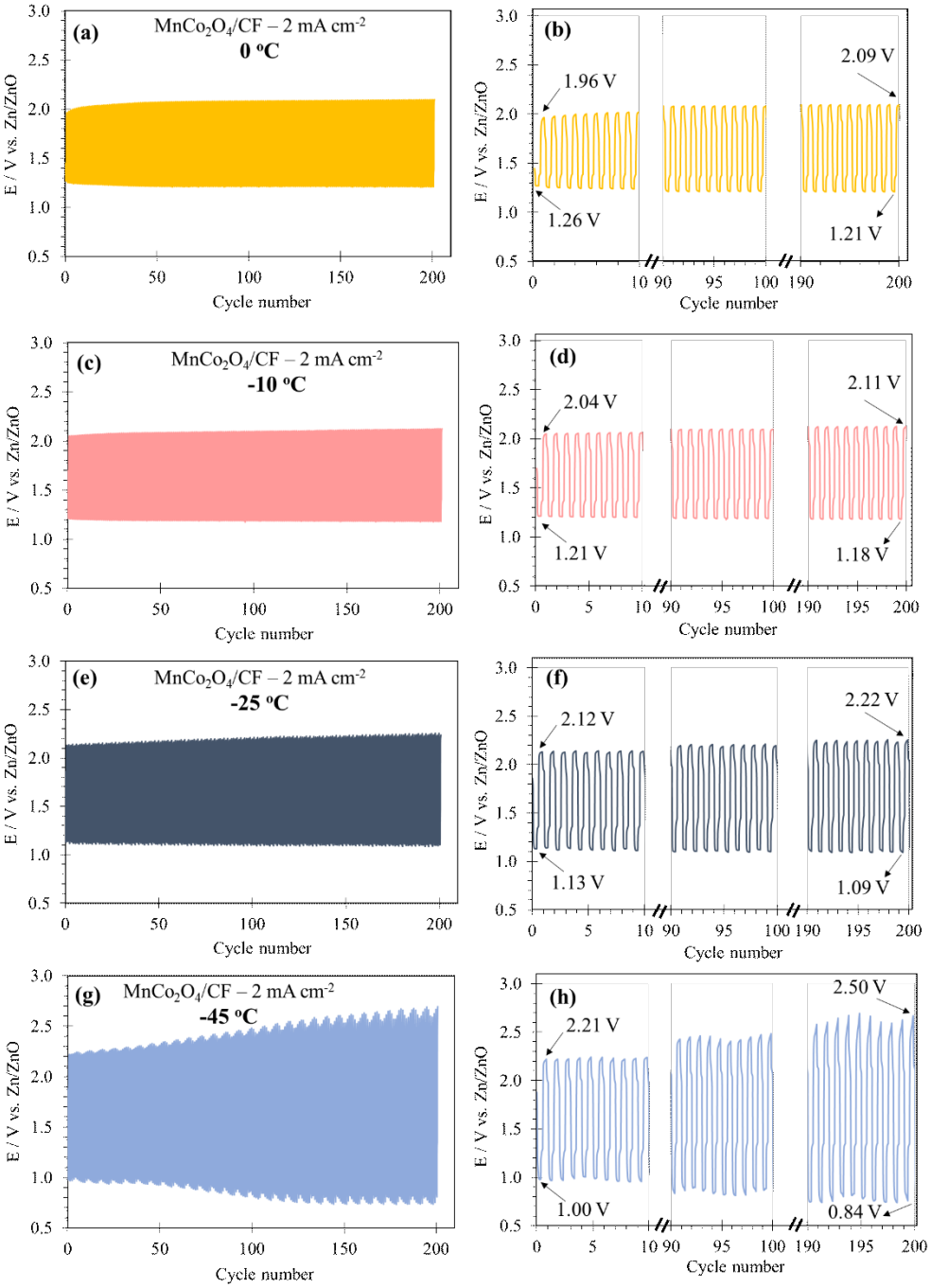

Figure 7.4. Cycling test results for $MnCo_2O_4$/CF in PAA-KOH hydrogel electrolyte at (a) and (b) 0 ºC, (c) and (d) -10 ºC, (e) and (f) -25 ºC, and (g) and (h) -45 ºC.

Table 7.3. Initial and final battery voltages and efficiencies obtained from the cycling tests at low temperatures

	Initial			**Final**		
Temperature	Charge E (V)	Discharge E (V)	Efficiency (%)	Charge E (V)	Discharge E (V)	Efficiency (%)
0 ^{o}C	1.96	1.26	64.3	2.09	1.21	57.9
-10 ^{o}C	2.04	1.21	59.3	2.11	1.18	55.9
-25 ^{o}C	2.12	1.13	53.3	2.22	1.09	49.1
-45 ^{o}C	2.21	1.00	45.2	2.50	0.84	33.6

The power density and polarization curves for the battery prepared with $MnCo_2O_4$/CF in the PAA-KOH hydrogel electrolyte are presented in Figure 7.5. The maximum power output at room temperature is ~240 mW cm^{-2} (Figure 7.5(a)). This value decreases to ~ 75 mW cm^{-2} at 0 ^{o}C.

At first glance, these results appear to contradict the rate test results shown in Figure 7.1(b), where the curves overlap for tests at both 21 ^{o}C and 0 ^{o}C. However, it should be noted that rate testing was only done at current densities up to 20 mA cm^{-2}. If the power densities for the 21 ^{o}C and 0 ^{o}C tests are compared for current densities less than 20 mA cm^{-2}, it is clear that the results overlap. The power density curves diverge at current densities exceeding 20 mA cm^{-2}. At higher current densities, the effect of viscosity becomes more apparent.

As the viscosity of the GPE increases, the reduced ion (OH^- and Zn^{2+}) or dissolved gas (O_2) diffusion rate negatively affects battery performance. Recent work showed that the effect of diffusion on battery performance is not significant at low current densities (e.g., j < 5 mA cm^{-2}),

since the charge/discharge rates are slow enough to provide enough time for the diffusing species to move either towards or away from the air electrode. The effect of ion species diffusion becomes more significant at higher current densities (e.g., 50 mA cm^{-2}) as the diffusion rates are not fast enough to respond to the higher ORR/OER rates. As such battery performance degrades at 0 ^{o}C at current densities greater than ~20 mA cm^{-2}. [240,241] At 0 ˚C, the maximum current density applicable to the cell without causing failure is ~180 mA cm^{-2} while at room temperature the battery does fail even at 350 mA cm^{-2} (Figure 7.5(a) and (b)). Furthermore, the battery voltage drops more rapidly with increasing current density as the temperature decreases. For example, the minimum battery voltage at room temperature is ~0.67 V vs. Zn/ZnO (at 350 mA cm^{-2}), while at 0 ^{o}C this voltage drops to ~0.28 V vs. Zn/ZnO (at 180 mA cm^{-2}, just before failure) (Figure 7.5(b)). The degradation in power density and cell voltage as the temperature is decreased is attributed to the increase in viscosity of the electrolyte which also reduces the mobility of charge carriers as discussed previously. Table 7.4 summarizes the maximum power densities and current densities. Even though the power density, maximum current density and cell voltage decrease as the temperature is reduced, the battery performance is still superior to the work reported in the recent literature (Table 7.5).

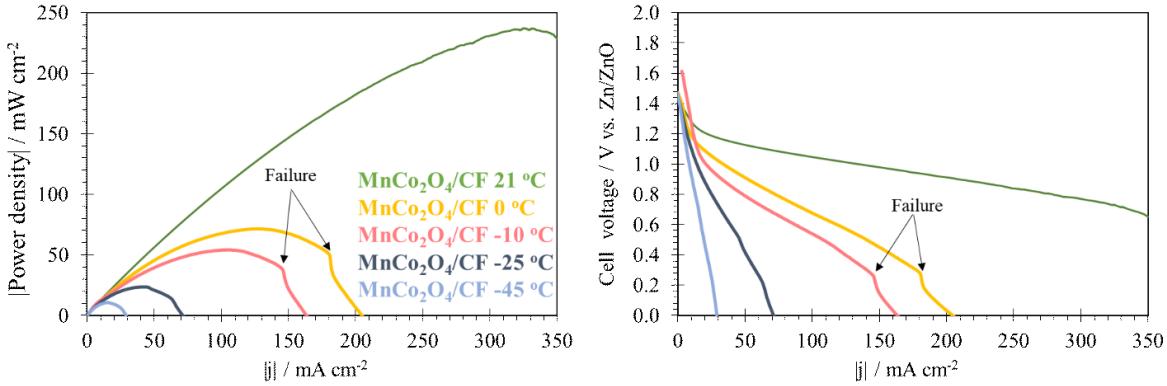

Figure 7.5. (a) Power output and (b) discharge polarization curves for $MnCo_2O_4$/CF in the PAA-KOH hydrogel electrolyte at different temperatures.

Table 7.4. Cell voltage, current density and power density values for $MnCo_2O_4$/CF in the PAA-KOH hydrogel electrolyte at different temperatures

Temperature	**Max j (mA cm^{-2})**	**Max power density (mW cm^{-2})**
Room T	350	240
0 °C	180	75
-10 °C	150	50
-25 °C	70	25
-45 °C	30	12

Chen et al. employed a PAA-KOH based gel electrolyte and Pt/C and RuO_2 as the air electrode. [30] The current density used for the cycling tests was 1 mA cm^{-2} at 25 °C and -20 °C. The cells were tested for 100 cycles and the initial and final efficiencies of the cells were 79% and 52%, respectively, at 25 °C and 60% and 36%, respectively, at -20 °C. Furthermore, the maximum power density of the cells at 25 °C and -20 °C were reported as 10 and 8 mW cm^{-2}, respectively.

[242] In the recent work reported by Zhang et al., all solid state ZAB cells were prepared with Pt/C-RuO_2 as the air electrode material and sodium polyacrylate-KOH as the electrolyte. The cells were tested at different temperatures of 25 ºC and -20 ºC. At 25 ºC, the battery completed 86 cycles (29 h) at 1 mA cm^{-2} with initial and final efficiencies of 65% and 63%, respectively. The maximum power density at 25 ºC was ~68 mW cm^{-2}. Reducing the temperature to -20 ºC negatively affected the maximum power density (20 mW cm^{-2}) and efficiency; however, the battery was able to complete 133 cycles (44 h). [243] Jiang et al. assembled all solid state ZAB cells with Co_3O_4/RuO_2 and poly(2-acrylamido-2-methylpropanesulfonic acid)/polyacrylamide (PAMPS/PAAm) as the electrocatalyst and the electrolyte, respectively. [32] This battery was able to complete 177 cycles (60 h) at 25 ºC at a current density of 1 mA cm^{-2}. The maximum power densities at 0 ºC and 25 ºC were 43 mW cm^{-2} and 57 mW cm^{-2}, respectively. [244] The work by An et al. introduced an effective all solid state ZAB cell with $NiCo_2O_4$ as the electrocatalyst and a PVA-KOH based gel electrolyte. The cell was successfully cycled for 33 h at 25 ºC and 15 h at -10 ºC at 1 mA cm^{-2}. The power output of the battery at 25 ºC was 151 mW cm^{-2}; no power density at -10 ºC was reported. [245] It is noteworthy that the zinc-air batteries in this work yielded superior results compared with those reported in the recent literature even though harsher testing conditions were used in this work. Current densities used in this work for full-cell and cycling tests are larger and the cycling durations are longer than most relevant recent works (Table 7.5) while providing stable battery performance with high power densities.

Table 7.5. Comparison of low temperature zinc-air battery performance from this work with the recent literature

Electrocatalyst	**Temperature Electrolyte**	**Current density (mA cm^{-2})**	**Number of cycles-total cycling duration**	**Initial/final efficiency (%)**	**Maximum Power density (mW cm^{-2})**	**Ref.**
$MnCo_2O_4$/CF	21 ºC PAA-KOH	10	200 cycles - 100 h	63/56	240	This work
$MnCo_2O_4$/CF	0 ºC PAA-KOH	2	200 cycles - 100 h	64/58	75	This work
$MnCo_2O_4$/CF	-25 ºC PAA-KOH	2	200 cycles - 100 h	53/49	25	This work
Pt/C and RuO_2	-20 ºC PAA-KOH	1	100 cycles – not provided	60/36	8	[242]
Pt/C and RuO_2	25 ºC PAA-KOH	1	100 cycles – not provided	79/52	10	[242]
Pt/C and RuO_2	-20 ºC Sodium polyacrylate-KOH	1	133 cycles – 44 h	61/50	20	[243]
Pt/C and RuO_2	25 ºC Sodium polyacrylate-KOH	1	86 cycles - 29 h	65/63	68	[243]
Co_3O_4/RuO_2	0 ºC PAMPS-KOH	1	5 cycles – 1 h	51/50	43	[244]
Co_3O_4/RuO_2	25 ºC PAMPS-KOH	1	177 cycles – ~ 60 h	76/57	57	[244]

$NiCo_2O_4$	-10 ºC PVA-KOH	1	15 h	55/50	Not provided	[245]
$NiCo_2O_4$	25 ºC PVA-KOH	1	33 h	55/47	151	[245]

In summary, superior performing, all solid state ZABs, relative to the recent literature, were prepared with $MnCo_2O_4$/CF as the air electrode and a PAA-KOH based hydrogel electrolyte. The better performance is attributed to the following: 1) The use of micron-scale carbon fibers in the fabrication of the air electrode which provided porosity and voids that enhance the redox reactions at the air electrode at all temperatures; 2) the use of cost effective carbon fibers as a conductive substrate for $MnCo_2O_4$ which improved charge transfer at the air electrode; and 3) the optimized hydrogel electrolyte chemistry. [241]

Pristine and cycled air electrodes were characterized using a FE-SEM (Figure 7.6). Carbon fibers in the pristine material are completely coated with $MnCo_2O_4$ particles. The EDX maps for Mn and Co overlap completely which confirms mixed Mn-Co oxide formation (Figure 7.6(a)-(d)). This behavior was established in a previous study. [12] SEM/EDX analysis shows that after 200 cycles (100 h) of testing at both 0 ºC and -45 ºC, $MnCo_2O_4$ particles still coat the CFs in the electrodes (Figure 7.6(e)-(l)). Figure 7.6(m) shows EDX spectra for the pristine and cycled electrodes at -45 ºC, taken from the entire image shown in Figure 7.6(a) and 6(i),. The presence of K and Zn peaks for the cycled electrode is due to the zincate species and KOH in the electrolyte, precipitated as ZnO and KOH, on the surface of the electrodes. However, Mn and Co peaks are still visible after cycling at -45 ºC for 100 h.

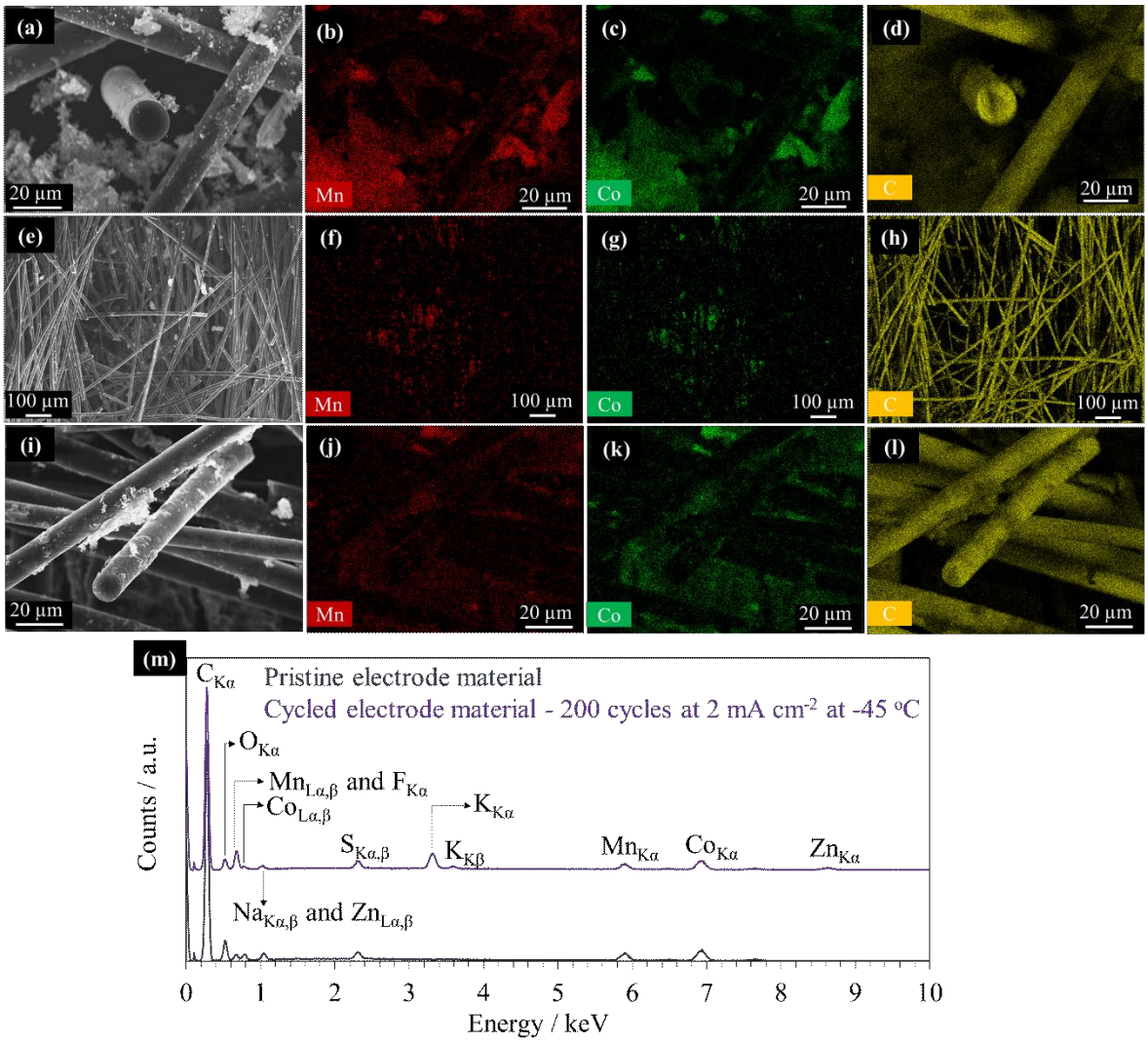

Figure 7.6. SEM/EDX analysis of $MnCo_2O_4$/CF electrodes. (a)-(d) pristine, (e)-(h) cycled at 0 °C, (i)-(l) cycled at -45 °C, and (m) EDX spectra from the electrodes.

7.4 Conclusions

All solid state zinc-air battery (ZAB) cells were prepared using an efficient $MnCo_2O_4$/carbon fiber electrocatalyst and an alkaline poly(acrylic acid) (PAA) hydrogel electrolyte. The low temperature battery performance was evaluated in terms of charge/discharge voltages and efficiency, long term cycling stability, and power density. Battery tests were performed at room temperature, 0 °C, -10 °C, -25 °C, and -45 °C, with voltage efficiencies of ~63%, 53% and 30%

(10 mA cm^{-2}) at room temperature, 0 ºC and -45 ºC, respectively. The performance was also superior to cells using Pt/RuO_2 as the air electrode catalyst. Long term cycling behavior was evaluated at 2 mA cm^{-2} at all test temperatures. The cells with $MnCo_2O_4$/carbon fiber air electrodes successfully completed 200 cycles (100 h) at all temperatures, while batteries prepared with Pt/RuO_2 failed after 70 cycles (35 h) at room temperature. The room and low temperature battery performance of batteries with $MnCo_2O_4$/carbon fiber electrocatalysts was superior to that reported in the recent literature in terms of the cycling life, efficiency, and power output (~240 and 75 mW cm^{-2} at room temperature and 0 ºC, respectively), even though higher current densities and lower temperatures were used in this work compared with the most recent work. This study shows that the high performance of the prepared ZABs is due to the unique design of the air electrode, which utilize micron-scale $MnCo_2O_4$ coated carbon fibers that provide voids and macroporosity for efficient air electrode reactions.

Chapter 8: Conclusions and Future Work

8.1 Conclusions

In Summary, this work has reported the development of high performance electrode materials and electrodes from asphaltene derived carbon fibers for use in energy storage devices. Electrochemical double layer supercapacitors, pseudocapacitors and Zn-air batteries are the devices that were investigated. The results have shown that asphaltene, as a by-product of oil sands production, can be used for the electrode/electrocatalyst material in high performance energy storage devices. Asphaltene derived activated carbon fibers were used as the electrode material in electrochemical double layer supercapacitors with maximum specific capacitances of 310 F g^{-1} and 210 F g^{-1} at 40 mA g^{-1} in aqueous and ionic liquid electrolytes, respectively. These activated carbon fibers were then used as a conductive substrate for birnessite type MnO_2 as the active material for pseudocapacitors, with stable performance that reached 328 F g^{-1} at 40 mA g^{-1}. Asphaltene derived carbon fibers were also used as the electrode material and the conductive substrate for a $MnCo_2O_4$ electrocatalyst coating for use as the air electrode in zinc-air batteries. The battery performance was investigated in both aqueous and gel polymer electrolytes at room temperature. In addition, batteries made with gel polymer electrolyte were tested in the temperature range of 21 ^oC to -45 ^oC. This battery was able to successfully operate at all temperatures with an efficient performance that outperformed the benchmark Pt/RuO_2 electrocatalyst.

8.2 Future Work

- Due to the relatively large size of the carbon fibers, the porosity of the activated carbon fibers could not be imaged using transmission electron microscopy (TEM). Focused ion beam (FIB) techniques can be used to prepare thin activated carbon fiber samples for

TEM to image the porosity in the carbon fibers. This can provide information as to whether the porosity is only on the surface or evenly distributed throughout the fibers (cross section imaging) and either confirm or refute the N_2 physisorption test results.

- Investigation of Zn-oxygen batteries with the same efficient electrocatalyst is of interest as it may be able to shed light on the reactions that the electrode material may undergo during charge/discharge of Zn-air batteries. Replacement of air with oxygen can eliminate carbonate formation at the air electrode and increase the discharge potential. However, a new compatible battery cell needs to be developed for this application.
- Accurately measuring the oxidation state of Mn and Co in the $MnCO_2O_4$/CF electrocatalyst could give insight into the identity of the mixed oxide. This could be done using high intensity XPS spectra with sharp peaks and min background signal that can be acquired, using a synchrotron.
- In-situ X-ray characterization techniques like XPS and XRD, using a synchrotron, could be performed on the electrodes in Zn-air batteries and pseudocapacitors, prepared in this work, to further investigate the charge storage mechanism in pseudocapacitors and any transformation of the electrocatalyst material in Zn-air batteries.
- Perovskite oxides (e.g., $LaMnO_3$, $LaCoO_3$ and $LaNiO_3$) have great potential as highly active and stable bifunctional catalysts. The performance of the homemade Zn-air battery air electrode made with asphaltene derived carbon fibers and perovskite oxides can be investigated.
- Incorporation of one or more additional transition metals into the birnessite type MnO_2 could increase the specific capacitance, energy and power output for the pseudocapacitor developed in this work. Ternary and higher order oxides containing Mn, Fe, Co and Ni

have been demonstrated to enhance the pseudocapacitive performance. However, this incorporation may affect the crystal structure (phase) of the birnessite.

References

[1] Clark MP. Atomic Layer Deposition of Metal Oxides for the Preparation of High Performance Zn-Air Battery Electrodes 2020.

[2] McDougall A, Abedi Z, Ivey DG. Tri- and Tetra-Metallic Oxides Anchored to Heteroatom Doped Carbon Nanotubes as Bifunctional Electrocatalysts for Rechargeable Zinc-Air Batteries. J Appl Electrochem 2021:1. https://doi.org/10.1007/s10800-021-01643-0.

[3] Abedi Z, Leistenschneider D, Chen W, Ivey DG. Improved Capacitive Behavior of Birnessite Type Mn Oxide Coated on Activated Carbon Fibers. J Electrochem Soc 2022;169:010507. https://doi.org/10.1149/1945-7111/ac436d.

[4] Lewandowski A, Galinski M. Practical and theoretical limits for electrochemical double-layer capacitors. J Power Sources 2007;173:822–8. https://doi.org/10.1016/j.jpowsour.2007.05.062.

[5] Liu C, Li F, Lai-Peng M, Cheng HM. Advanced materials for energy storage. Adv Mater 2010;22:28–62. https://doi.org/10.1002/adma.200903328.

[6] Liu J, Wang J, Xu C, Jiang H, Li C, Zhang L, et al. Advanced Energy Storage Devices: Basic Principles, Analytical Methods, and Rational Materials Design. Adv Sci 2018;5. https://doi.org/10.1002/advs.201700322.

[7] Béguin F, Presser V, Balducci A, Frackowiak E. Carbons and electrolytes for advanced supercapacitors. Adv Mater 2014;26:2219–51. https://doi.org/10.1002/adma.201304137.

[8] ST53 n.d. https://www.aer.ca/providing-information/data-and-reports/statistical-

reports/st53.html (accessed April 2, 2020).

[9] Abedi Z, Leistenschneider D, Chen W, G. Ivey D. Superior performance of electrochemical double layer supercapacitor made with asphaltene derived activated carbon fibres. Energy Technol 2020;2000588:1–11. https://doi.org/10.1002/ente.202000588.

[10] Yao ZC, Tang T, Hu JS, Wan LJ. Recent Advances on Nonprecious-Metal-Based Bifunctional Oxygen Electrocatalysts for Zinc-Air Batteries. Energy and Fuels 2021;35:6380–401. https://doi.org/10.1021/acs.energyfuels.1c00275.

[11] Sun L, Wang X, Wang Y, Zhang Q. Roles of carbon nanotubes in novel energy storage devices. Carbon 2017;122:462–74. https://doi.org/10.1016/j.carbon.2017.07.006.

[12] Abedi Z, Leistenschneider D, Chen W, Ivey DG. Spinel Type Mn−Co Oxide Coated Carbon Fibers as Efficient Bifunctional Electrocatalysts for Zinc-Air Batteries. Batter Supercaps 2022;5. https://doi.org/10.1002/batt.202100339.

[13] Li Y, Lu J. Metal-Air Batteries: Will They Be the Future Electrochemical Energy Storage Device of Choice? ACS Energy Lett 2017;2:1370–7. https://doi.org/10.1021/acsenergylett.7b00119.

[14] Borchardt L, Oschatz M, Kaskel S. Tailoring porosity in carbon materials for supercapacitor applications. Mater Horizons 2014;1:157–68. https://doi.org/10.1039/c3mh00112a.

[15] Horn M, Gupta B, MacLeod J, Liu J, Motta N. Graphene-based supercapacitor electrodes: Addressing challenges in mechanisms and materials. Curr Opin Green Sustain Chem

2019;17:42–8. https://doi.org/10.1016/j.cogsc.2019.03.004.

[16] Clark MP, Qu W, Ivey DG. Nanostructured manganese oxide and manganese oxide/polyethylenedioxythiophene rods electrodeposited onto nickel foam for supercapacitor applications. J Appl Electrochem 2017;47:39–49. https://doi.org/10.1007/s10800-016-1015-4.

[17] Meng C, Gall OZ, Irazoqui PP. A flexible super-capacitive solid-state power supply for miniature implantable medical devices. Biomed Microdevices 2013;15:973–83. https://doi.org/10.1007/s10544-013-9789-1.

[18] Lee JS, Kim ST, Cao R, Choi NS, Liu M, Lee KT, et al. Metal-air batteries with high energy density: Li-air versus Zn-air. Adv Energy Mater 2011;1:34–50. https://doi.org/10.1002/aenm.201000010.

[19] Cheng F, Chen J. Metal–air batteries: From oxygen reduction electrochemistry to cathode catalysts. Chem Soc Rev 2012;41:2172–92. https://doi.org/10.1039/c1cs15228a.

[20] Mainar AR, Iruin E, Colmenares LC, Kvasha A, de Meatza I, Bengoechea M, et al. An overview of progress in electrolytes for secondary zinc-air batteries and other storage systems based on zinc. J Energy Storage 2018;15:304–28. https://doi.org/10.1016/j.est.2017.12.004.

[21] Song Z, Ding J, Liu B, Shen Y, Liu J, Han X, et al. Investigation of failure mechanism of rechargeable zinc–air batteries with poly(acrylic acid) alkaline gel electrolyte during discharge–charge cycles at different current densities. Chem Eng J 2022;429:132331. https://doi.org/10.1016/j.cej.2021.132331.

[22] Borchers N, Clark S, Horstmann B, Jayasayee K, Juel M, Stevens P. Innovative zinc-based batteries. J Power Sources 2021;484:229309. https://doi.org/10.1016/j.jpowsour.2020.229309.

[23] Abedi Z, Leistenschneider D, Chen W, Ivey DG. ECS Meeting Stable Electrodes Fabricated from Carbon Fibers for Electrochemical Double Layer Supercapacitors, Pseudocapacitors and Zn-air Batteries. Meet Abstr 2021;MA2021-02:1917.

[24] __Clark_Michael_P_201505_MSc.pdf n.d.

[25] Clark S, Mainar AR, Iruin E, Colmenares LC, Blázquez JA, Tolchard JR, et al. Towards rechargeable zinc-air batteries with aqueous chloride electrolytes. J Mater Chem A 2019;7:11387–99. https://doi.org/10.1039/c9ta01190k.

[26] Clark MP, Xiong M, Cadien K, Ivey DG. High Performance Oxygen Reduction/Evolution Electrodes for Zinc-Air Batteries Prepared by Atomic Layer Deposition of MnO_x. ACS Appl Energy Mater 2020;3:603–13. https://doi.org/10.1021/acsaem.9b01829.

[27] Ramakrishnan S, Velusamy DB, Sengodan S, Nagaraju G, Kim DH, Kim AR, et al. Rational design of multifunctional electrocatalyst: An approach towards efficient overall water splitting and rechargeable flexible solid-state zinc–air battery. Appl Catal B Environ 2022;300:120752. https://doi.org/10.1016/j.apcatb.2021.120752.

[28] Ramakrishnan S, Balamurugan J, Vinothkannan M, Kim AR, Sengodan S, Yoo DJ. Nitrogen-doped graphene encapsulated FeCoMoS nanoparticles as advanced trifunctional catalyst for water splitting devices and zinc–air batteries. Appl Catal B Environ 2020;279:119381. https://doi.org/10.1016/j.apcatb.2020.119381.

[29] Pan L, Chen D, Pei P, Huang S, Ren P, Song X. A novel structural design of air cathodes expanding three-phase reaction interfaces for zinc-air batteries. Appl Energy 2021;290:116777. https://doi.org/10.1016/j.apenergy.2021.116777.

[30] Gu P, Zheng M, Zhao Q, Xiao X, Xue H, Pang H. Rechargeable zinc-air batteries: A promising way to green energy. J Mater Chem A 2017;5:7651–66. https://doi.org/10.1039/c7ta01693j.

[31] Janani G, Chae Y, Surendran S, Sim Y, Park W, Kim JK, et al. applied sciences Rational Design of Spinel Oxide Nanocomposites with Tailored Electrochemical Oxygen Evolution and Reduction Reactions for ZincAir Batteries n.d.:1–21.

[32] Muthurasu A, Chae SH, Hoon Ko T, Chandra Lohani P, Yong Kim H. Highly ordered nanoarrays catalysts embedded in carbon nanotubes as highly efficient and robust air electrode for flexible solid-state rechargeable zinc-air batteries. J Colloid Interface Sci 2022;616:679–90. https://doi.org/10.1016/j.jcis.2022.02.097.

[33] Clark MP, Muneshwar T, Xiong M, Cadien K, Ivey DG. Saturation Behavior of Atomic Layer Deposition MnO_x from Bis(Ethylcyclopentadienyl) Manganese and Water: Saturation Effect on Coverage of Porous Oxygen Reduction Electrodes for Metal-Air Batteries. ACS Appl Nano Mater 2019;2:267–77. https://doi.org/10.1021/acsanm.8b01895.

[34] Qu L, Liu Y, Baek J, Liming D. Nitrogen-Doped Graphene as Efficient Metal-Free Electrocatalyst for Oxygen Reduction in Fuel Cells. ACS Nano 2010;4:1321–6. https://doi.org/10.1021/nn901850u.

[35] Xiong T, Zhu M, Zhang Y, Lee WSV, Yu ZG, Xue J. Interlayer Engineering of MnO_2

with High Charge Density Bi^{3+} for High Rate and Stable Aqueous Supercapacitor . Batter Supercaps 2020;3:519–26. https://doi.org/10.1002/batt.202000007.

[36] Guan C, Sumboja A, Wu H, Ren W, Liu X, Zhang H, et al. Hollow Co3O4 Nanosphere Embedded in Carbon Arrays for Stable and Flexible Solid-State Zinc–Air Batteries. Adv Mater 2017;29. https://doi.org/10.1002/adma.201704117.

[37] Chen B, Miao H, Yin M, Hu R, Xia L, Zhang C, et al. Mn-based spinels evolved from layered manganese dioxides at mild temperature for the robust flexible quasi-solid-state zinc-air batteries. Chem Eng J 2021;417:129179. https://doi.org/10.1016/j.cej.2021.129179.

[38] Tran TNT, Clark MP, Chung HJ, Ivey DG. Effects of Crosslinker Concentration in Poly(Acrylic Acid)-KOH Gel Electrolyte on Performance of Zinc-Air Batteries. Batter Supercaps 2020;3:409–16. https://doi.org/10.1002/batt.201900199.

[39] Leistenschneider D, Abedi Z, Chen W, Ivey DG. Coating of Low-Cost Asphaltenes-Derived Carbon Fibers with V2O5 for Supercapacitor Application. Energy and Fuels 2022. https://doi.org/10.7868/s0044453716010143.

[40] Wang G, Zhang L, Zhang J. A review of electrode materials for electrochemical supercapacitors. Chem Soc Rev 2012;41:797–828. https://doi.org/10.1039/c1cs15060j.

[41] Kotz R, Carlen M. Principles and applications of Caps. Electrochim Acta 2000;45:2483–98. https://doi.org/10.1016/S0013-4686(00)00354-6.

[42] Shukla AK, Sampath S, Vijayamohanan K. Electrochemical supercapacitors: Energy storage beyond batteries. Curr Sci 2000;79:1656–61.

[43] Huang J, Ridge O, Qiao R, Feng G. Chapter 5 . Modern Theories of Carbon-Based Electrochemical Capacitors 2013.

[44] Bard AJ, Faulkner LR. Electrochemical Methods - Fundamentals and Applns. vol. 2. 2012. https://doi.org/10.1016/B978-0-12-381373-2.00056-9.

[45] Astle MJ, Beyer WH, Wagner W, Bange K. The Limitations of Energy Densily for Electrochemical Capacitors 2000;144:2026–31.

[46] Wang LH, Toyoda M, Inagaki M. Dependence of electric double layer capacitance of activated carbons on the types of pores and their surface areas. Xinxing Tan Cailiao/ New Carbon Mater 2008;23:111–5. https://doi.org/10.1016/s1872-5805(08)60015-3.

[47] Cataldo E, Di A, Maccarrone F, Paffuti G. Measure of the capacitance coef fi cients of square electrodes using capacitance-to-digital converters. J Electrostat 2017;87:26–31. https://doi.org/10.1016/j.elstat.2017.03.002.

[48] Yoo J, Kim J, Kim YS. Liquid electrolyte-free cylindrical Al polymer capacitor review: Materials and characteristics. J Power Sources 2015;284:466–80. https://doi.org/10.1016/j.jpowsour.2015.03.023.

[49] Babakhani B, Ivey DG. Improved capacitive behavior of electrochemically synthesized Mn oxide / PEDOT electrodes utilized as electrochemical capacitors. Electrochim Acta 2010;55:4014–24. https://doi.org/10.1016/j.electacta.2010.02.030.

[50] Peng L, Liang Y, Dong H, Hu H, Zhao X, Cai Y, et al. Super-hierarchical porous carbons derived from mixed biomass wastes by a stepwise removal strategy for high-performance supercapacitors. J Power Sources 2018;377:151–60.

https://doi.org/10.1016/j.jpowsour.2017.12.012.

[51] Chmiola J, Yushin G, Gogotsi Y, Portet C, Taberna PL. Anomalous Increase in Carbon Capacitance at Pore Sizes Less Than 1 Nanometer 2006;7:1760–4.

[52] Village E. Interface Applications in Nanomaterials. vol. 18. 2011. https://doi.org/10.1016/B978-0-12-375049-5.00005-0.

[53] Kuphaldt TR. Lessons In Electric Circuits: DC. Open B Proj 2009;III:1–526.

[54] Murata K, Mitsuoka K, Hiral T, Walz T, Agre P, Heymann JB, et al. Structural determinants of water permeation through aquaporin-1. Nature 2000;407:599–605. https://doi.org/10.1038/35036519.

[55] Raza W, Ali F, Raza N, Luo Y, Kim K, Yang J. Nano Energy Recent advancements in supercapacitor technology. Nano Energy 2018;52:441–73. https://doi.org/10.1016/j.nanoen.2018.08.013.

[56] Bueno PR. Nanoscale origins of super-capacitance phenomena. J Power Sources 2019;414:420–34. https://doi.org/10.1016/j.jpowsour.2019.01.010.

[57] Cakici M, Raghava K, Alonso-marroquin F. Advanced electrochemical energy storage supercapacitors based on the flexible carbon fiber fabric-coated with uniform coral-like MnO_2 structured electrodes. Chem Eng J 2017;309:151–8. https://doi.org/10.1016/j.cej.2016.10.012.

[58] Fic K, Platek A, Piwek J, Frackowiak E. Sustainable materials for electrochemical capacitors. Mater Today 2018;21:437–54. https://doi.org/10.1016/j.mattod.2018.03.005.

[59] Wang Y, Shi Z, Huang Y, Ma Y, Wang C, Chen M, et al. Supercapacitor Devices Based

on Graphene Materials 2009:13103–7.

[60] You A, Be MAY, In I. Supercapacitor electrodes from multiwalled carbon nanotubes 2003;2421:1–4.

[61] Han X, Jiang H, Zhou Y, Hong W, Zhou Y, Gao P, et al. A high performance nitrogen-doped porous activated carbon for supercapacitor derived from pueraria. J Alloys Compd 2018;744:544–51.https://doi.org/10.1016/j.jallcom.2018.02.078.

[62] Xu B, Wu F, Chen R, Cao G, Chen S, Yang Y. Mesoporous activated carbon fiber as electrode material for high-performance electrochemical double layer capacitors with ionic liquid electrolyte. J Power Sources 2010;195:2118–24. https://doi.org/10.1016/j.jpowsour.2009.09.077.

[63] Babakhani B, Ivey DG. Anodic deposition of manganese oxide electrodes with rod-like structures for application as electrochemical capacitors. J Power Sources 2009;195:2110–7. https://doi.org/10.1016/j.jpowsour.2009.10.045.

[64] Conway BE, Birss V, Wojtowicz J. The role and utilization of pseudocapacitance for energy storage by supercapacitors. J Power Sources 1997;66:1–14. https://doi.org/10.1016/S0378-7753(96)02474-3.

[65] Kate RS, Khalate SA, Deokate RJ. Overview of nanostructured metal oxides and pure nickel oxide (NiO) electrodes for supercapacitors: A review. J Alloys Compd 2018;734:89–111. https://doi.org/10.1016/j.jallcom.2017.10.262.

[66] Messaoudi B, Joiret S, Keddam M, Takenouti H. Anodic behaviour of manganese in alkaline medium. Electrochim Acta 2001;46:2487–98. https://doi.org/10.1016/S0013-

4686(01)00449-2.

[67] Conway BE. Transition from “supercapacitor” to “battery” behavior in electrochemical energy storage. J Electrochem Soc 1991;138:1539–48. https://doi.org/10.1149/1.2085829.

[68] Ghodbane O, Pascal JL, Favier F. Microstructural effects on charge-storage properties in MnO_2-based electrochemical supercapacitors. ACS Appl Mater Interfaces 2009;1:1130–9. https://doi.org/10.1021/am900094e.

[69] Toupin M, Brousse T, Bélanger D. Charge storage mechanism of MnO_2 electrode used in aqueous electrochemical capacitor. Chem Mater 2004;16:3184–90. https://doi.org/10.1021/cm049649j.

[70] Sopčić S, Peter R, Petravić M, Mandić Z. New insights into the mechanism of pseudocapacitance deterioration in electrodeposited MnO_2 under negative potentials. J Power Sources 2013;240:252–7. https://doi.org/10.1016/j.jpowsour.2013.04.008.

[71] Ghodbane O, Ataherian F, Wu NL, Favier F. In situ crystallographic investigations of charge storage mechanisms in MnO_2-based electrochemical capacitors. J Power Sources 2012;206:454–62. https://doi.org/10.1016/j.jpowsour.2012.01.103.

[72] Kuo SL, Wu NL. Investigation of pseudocapacitive charge-storage reaction of MnO_2.n.H $_2$O supercapacitors in aqueous electrolytes. J Electrochem Soc 2006;153:1317–24. https://doi.org/10.1149/1.2197667.

[73] Pang SC, Anderson MA. Novel electrode materials for electrochemical capacitors: Part II. Material characterization of sol-gel-derived and electrodeposited manganese dioxide thin films. J Mater Res 2000;15:2096–106. https://doi.org/10.1557/JMR.2000.0302.

[74] Kundu M, Liu L. Direct growth of mesoporous MnO_2 nanosheet arrays on nickel foam current collectors for high-performance pseudocapacitors. J Power Sources 2013;243:676–81. https://doi.org/10.1016/j.jpowsour.2013.06.059.

[75] Yano M, Suzuki S, Miyayama M, Ohgaki M. Electrode properties and microstructures of MnO_2 nanosheet thin films as cathodes for electrochemical capacitors. Solid State Ionics 2013;233:32–7. https://doi.org/10.1016/j.ssi.2012.12.009.

[76] Xiao J, Yang S, Wan L, Xiao F, Wang S. Electrodeposition of manganese oxide nanosheets on a continuous three-dimensional nickel porous scaffold for high performance electrochemical capacitors. J Power Sources 2014;245:1027–34. https://doi.org/10.1016/j.jpowsour.2013.07.024.

[77] Liu H, Lu B, Wei S, Bao M, Wen Y, Wang F. Electrodeposited highly-ordered manganese oxide nanowire arrays for supercapacitors. Solid State Sci 2012;14:789–93. https://doi.org/10.1016/j.solidstatesciences.2012.04.003.

[78] Ho CL, Wu MS. Manganese oxide nanowires grown on ordered macroporous conductive nickel scaffold for high-performance supercapacitors. J Phys Chem C 2011;115:22068–74. https://doi.org/10.1021/jp2081337.

[79] Wang L, Deng D, Ng KYS. Facile one-step synthesis of MnO_2 nanowires on graphene under mild conditions for application in supercapacitors. J Mater Sci 2013;48:6410–7. https://doi.org/10.1007/s10853-013-7441-3.

[80] Yousefi T, Golikand AN, Hossein Mashhadizadeh M, Aghazadeh M. Facile synthesis of α-MnO_2 one-dimensional (1D) nanostructure and energy storage ability studies. J Solid State Chem 2012;190:202–7. https://doi.org/10.1016/j.jssc.2012.01.062.

[81] Santhanagopalan S, Balram A, Meng DD. Scalable high-power redox capacitors with aligned nanoforests of crystalline MnO_2 nanorods by high voltage electrophoretic deposition. ACS Nano 2013;7:2114–25. https://doi.org/10.1021/nn3044462.

[82] Hu CC, Chen WC, Chang KH. How to Achieve Maximum Utilization of Hydrous Ruthenium Oxide for Supercapacitors. J Electrochem Soc 2004;151. https://doi.org/10.1149/1.1639020.

[83] Jow TR, Zheng JP. Amorphous thin film ruthenium oxide as an electrode material for electrochemical capacitors. Mater Res Soc Symp - Proc 1995;393:433–8. https://doi.org/10.1557/proc-393-433.

[84] Baptista JM, Sagu JS, KG UW, Lobato K. State-of-the-art materials for high power and high energy supercapacitors: Performance metrics and obstacles for the transition from lab to industrial scale – A critical approach. Chem Eng J 2019;374:1153–79. https://doi.org/10.1016/j.cej.2019.05.207.

[85] Zhang LL, Zhao XS. Carbon-based materials as supercapacitor electrodes. Chem Soc Rev 2009;38:2520–31. https://doi.org/10.1039/b813846j.

[86] Snook GA, Kao P, Best AS. Conducting-polymer-based supercapacitor devices and electrodes. J Power Sources 2011;196:1–12. https://doi.org/10.1016/j.jpowsour.2010.06.084.

[87] Suematsu S, Oura Y, Tsujimoto H, Kanno H, Naoi K. Conducting polymer films of cross-linked structure and their QCM analysis 2000;45:3813–21.

[88] Deng L, Hao Z, Wang J, Zhu G, Kang L, Liu Z. Electrochimica Acta Preparation and

capacitance of graphene / multiwall carbon nanotubes / MnO_2 hybrid material for high-performance asymmetrical electrochemical capacitor. Electrochim Acta 2013;89:191–8. https://doi.org/10.1016/j.electacta.2012.10.106.

[89] Bahloul A, Nessark B, Briot E, Groult H, Mauger A, Zaghib K, et al. Polypyrrole-covered MnO_2 as electrode material for supercapacitor. J Power Sources 2013;240:267–72. https://doi.org/10.1016/j.jpowsour.2013.04.013.

[90] Sharma RK, Rastogi AC, Desu SB. Electrochimica Acta Manganese oxide embedded polypyrrole nanocomposites for electrochemical supercapacitor 2008;53:7690–5. https://doi.org/10.1016/j.electacta.2008.04.028.

[91] Yuan G, Li X, Dong Z, Westwood A, Rand B. The structure and properties of ribbon-shaped carbon fibers with high orientation. Carbon 2013;68:426–39. https://doi.org/10.1016/j.carbon.2013.11.019.

[92] Miller GC, Yu J, Joseph RM, Choudhury SR, Mecham SJ, Baird DG, et al. Melt-spinnable polyacrylonitrile copolymer precursors for carbon fi bers 2017;126:87–95. https://doi.org/10.1016/j.polymer.2017.08.023.

[93] Bautista-quijano R, Petra P. Strain sensing , electrical and mechanical properties of polycarbonate / multiwall carbon nanotube mono fi lament fi bers fabricated by melt spinning 2016;82:181–9. https://doi.org/10.1016/j.polymer.2015.11.030.

[94] Díez N, Álvarez P, Santamaría R, Blanco C, Menéndez R, Granda M. Optimisation of the melt-spinning of anthracene oil-based pitch for isotropic carbon fi bre preparation. Fuel Process Technol 2012;93:99–104. https://doi.org/10.1016/j.fuproc.2011.09.016.

[95] Kim BJ, Eom Y, Kato O, Miyawaki J, Kim BC, Mochida I, et al. Preparation of carbon fibers with excellent mechanical properties from isotropic pitches. Carbon 2014;77:747–55. https://doi.org/10.1016/j.carbon.2014.05.079.

[96] Hou R, Guo Z, Zheng X. Electrochimica Acta Functionalization of carbon fi ber electrode by high temperature oxidation and its electrocatalytic behaviors. Electrochim Acta 2020;329:135122. https://doi.org/10.1016/j.electacta.2019.135122.

[97] Faheem M, Ashraf M, Fazal H, Hafeez A, Shezad N, Hussain M. Journal of Analytical and Applied Pyrolysis Recent trends in activated carbon fibers production from various precursors and applications — A comparative review. J Anal Appl Pyrolysis 2019:104715. https://doi.org/10.1016/j.jaap.2019.104715.

[98] Yue Z, Economy J. Carbonization and activation for production of activated carbon fibers. 2017. https://doi.org/10.1016/B978-0-08-100660-3.00004-3.

[99] Huang Y, Ma E, Zhao G. Thermal and structure analysis on reaction mechanisms during the preparation of activated carbon fibers by KOH activation from liquefied wood-based fibers. Ind Crops Prod 2015;69:447–55. https://doi.org/10.1016/j.indcrop.2015.03.002.

[100] Pestana I, Ramiro C, Alexandre P, Mourão M. Environmental Nanotechnology , Monitoring & Management Pesticides abatement using activated carbon produced from a mixture of synthetic polymers by chemical activation with KOH and K_2CO_3. Environ Nanotechnology, Monit Manag 2019;12:100261. https://doi.org/10.1016/j.enmm.2019.100261.

[101] Oginni O, Singh K, Oporto G, Dawson-andoh B, Mcdonald L, Sabolsky E. Bioresource Technology Reports In fl uence of one-step and two-step KOH activation on activated

carbon characteristics. Bioresour Technol Reports 2019;7:100266. https://doi.org/10.1016/j.biteb.2019.100266.

[102] Singh J, Bhunia H, Basu S. Adsorption of CO 2 on KOH activated carbon adsorbents : E ff ect of di ff erent mass ratios 2019;250. https://doi.org/10.1016/j.jenvman.2019.109457.

[103] Zhang Y, Song X, Xu Y, Shen H, Kong X. Utilization of wheat bran for producing activated carbon with high specific surface area via NaOH activation using industrial furnace. J Clean Prod 2019;210:366–75. https://doi.org/10.1016/j.jclepro.2018.11.041.

[104] Norouzi S, Heidari M, Alipour V, Rahmanian O, Fazlzadeh M. Bioresource Technology Preparation, characterization and Cr (VI) adsorption evaluation of NaOH- activated carbon produced from Date Press Cake ; an agro-industrial waste. Bioresour Technol 2018;258:48–56. https://doi.org/10.1016/j.biortech.2018.02.106.

[105] Wang C, Liu T. Nori-based N , O , S , Cl co-doped carbon materials by chemical activation of $ZnCl_2$ for supercapacitor. J Alloys Compd 2017;696:42–50. https://doi.org/10.1016/j.jallcom.2016.11.206.

[106] Pis B, Ozgu K. ScienceDirect Chemical and structural optimization of ZnCl 2 activated carbons via high temperature CO_2 treatment for EDLC applications 2018;3:2–11. https://doi.org/10.1016/j.ijhydene.2018.03.222.

[107] Kumar A, Jena HM. Adsorption of Cr (VI) from aqueous phase by high surface area activated carbon prepared by chemical activation with $ZnCl_2$. Process Saf Environ Prot 2017;109:63–71. https://doi.org/10.1016/j.psep.2017.03.032.

[108] Mamaní A, Ramírez N, Deiana C, Giménez M. Journal of Environmental Chemical

Engineering Highly microporous sorbents from lignocellulosic biomass : Different activation routes and their application to dyes adsorption. J Environ Chem Eng 2019;7:103148. https://doi.org/10.1016/j.jece.2019.103148.

[109] Xiao Y, Long C, Zheng M, Dong H, Lei B, Zhang H, et al. High-capacity porous carbons prepared by KOH activation of activated carbon for supercapacitors. Chinese Chem Lett 2014;25:865–8. https://doi.org/10.1016/j.cclet.2014.05.004.

[110] Su XL, Chen JR, Zheng GP, Yang JH, Guan XX, Liu P, et al. Three-dimensional porous activated carbon derived from loofah sponge biomass for supercapacitor applications. Appl Surf Sci 2018;436:327–36. https://doi.org/10.1016/j.apsusc.2017.11.249.

[111] Gong C, Wang X, Ma D, Chen H, Zhang S, Liao Z. Electrochimica Acta Microporous carbon from a biological waste-stiff silkworm for capacitive energy storage. Electrochim Acta 2016;220:331–9. https://doi.org/10.1016/j.electacta.2016.10.120.

[112] Park SJ, Kim KD. Influence of activation temperature on adsorption characteristics of activated carbon fiber composites. Carbon 2001;39:1741–6. https://doi.org/10.1016/S0008-6223(00)00305-5.

[113] Thommes M, Kaneko K, Neimark A V., Olivier JP, Rodriguez-Reinoso F, Rouquerol J, et al. Physisorption of gases, with special reference to the evaluation of surface area and pore size distribution (IUPAC Technical Report). Pure Appl Chem 2015;87:1051–69. https://doi.org/10.1515/pac-2014-1117.

[114] Goldstein JI, Newbury DE, Michael JR, Ritchie NWM, Scott JHJ, Joy DC. Scanning electron microscopy and x-ray microanalysis. 2017. https://doi.org/10.1007/978-1-4939-6676-9.

[115] Kwiecińska B, Pusz S, Valentine BJ. Application of electron microscopy TEM and SEM for analysis of coals , organic-rich shales and carbonaceous matter. Int J Coal Geol 2019;211:103203. https://doi.org/10.1016/j.coal.2019.05.010.

[116] Inkson BJ. 2 - Scanning electron microscopy for materials characterization. Elsevier Ltd; 2016. https://doi.org/10.1016/B978-0-08-100040-3.00002-X.

[117] R.Sandler S, Karo W, Bonesteel J-A, Pearce EM. Experiment 21 - X-ray diffraction. Polym Synth Charact Acad Press 1998:173–84.

[118] Qin Z, Chen X, Ouyang N, Lan S, Jiang G, Zhang J, et al. Characterisation of hexagonal birnessite with a new and rapid synthesis method-Comparison with traditional synthesis. RSC Adv 2019;9:25951–6. https://doi.org/10.1039/c9ra03332g.

[119] Shard AG. X-ray photoelectron spectroscopy. Elsevier Inc.; 2020. https://doi.org/10.1016/B978-0-12-814182-3.00019-5.

[120] Nesbitt HW, Banerjee D. Interpretation of XPS Mn (2p) spectra of Mn oxyhydroxides and constraints on the mechanism of MnO_2 precipitation. Am Mineral 1998;83:305–15.

[121] Álvarez NDLS, Abedul MTF. Determination of ascorbic acid in dietary supplements by cyclic voltammetry. Elsevier Inc.; 2020. https://doi.org/10.1016/B978-0-12-815932-3.00002-4.

[122] Conder J, Fic K, Electrochemistry T. Supercapacitors (electrochemical capacitors) 10. 2019. https://doi.org/10.1016/B978-0-12-814893-8.00010-9.

[123] Laheäär A, Przygocki P, Abbas Q, Béguin F. Appropriate methods for evaluating the efficiency and capacitive behavior of different types of supercapacitors. Electrochem

Commun 2015;60:21–5. https://doi.org/10.1016/j.elecom.2015.07.022.

[124] Taberna PL, Simon P, Fauvarque JF. Electrochemical characteristics and impedance spectroscopy studies of carbon-carbon supercapacitors. J Electrochem Soc 2003;150:292–300. https://doi.org/10.1149/1.1543948.

[125] Loveday D, Peterson P, Rodgers B. Evaluation of organic coatings with electrochemical impedance spectroscopy: Part 1: Fundamentals of electrochemical impedance spectroscopy. CoatingsTech 2004;1:46–52.

[126] Loveday D, Peterspm P, Rodgers B. Evalution of organic coatings with electrochemical impedance spectroscopy part 2: Application of EIS to coatings. CoatingsTech 2004;1:88–93.

[127] Kasturi PR, Ramasamy H, Meyrick D, Sung Lee Y, Kalai Selvan R. Preparation of starch-based porous carbon electrode and biopolymer electrolyte for all solid-state electric double layer capacitor. J Colloid Interface Sci 2019;554:142–56. https://doi.org/10.1016/j.jcis.2019.06.081.

[128] Zardkhoshoui AM, Davarani SSH. Ultrahigh energy density supercapacitors based on facile synthesized Ni,CoOH-rGO/NF hybrid electrodes. J Alloys Compd 2018;769:922–31. https://doi.org/10.1016/j.jallcom.2018.07.321.

[129] Farah N, Ng HM, Numan A, Liew CW, Latip NAA, Ramesh K, et al. Solid polymer electrolytes based on poly(vinyl alcohol) incorporated with sodium salt and ionic liquid for electrical double layer capacitor. Mater Sci Eng B Solid-State Mater Adv Technol 2019;251. https://doi.org/10.1016/j.mseb.2019.114468.

[130] Schlee P, Hosseinaei O, Baker D, Landmér A, Tomani P, Mostazo-López MJ, et al. From Waste to Wealth: From Kraft Lignin to Free-standing Supercapacitors. Carbon 2019;145:470–80. https://doi.org/10.1016/j.carbon.2019.01.035.

[131] Sevilla M, Diez N, Ferrero GA, Fuertes AB. Sustainable supercapacitor electrodes produced by the activation of biomass with sodium thiosulfate. Energy Storage Mater 2019;18:356–65. https://doi.org/10.1016/j.ensm.2019.01.023.

[132] Fuertes AB, Sevilla M. High-surface area carbons from renewable sources with a bimodal micro-mesoporosity for high-performance ionic liquid-based supercapacitors. Carbon 2015;94:41–52. https://doi.org/10.1016/j.carbon.2015.06.028.

[133] Pandolfo AG, Hollenkamp AF. Carbon properties and their role in supercapacitors. J Power Sources 2006;157:11–27. https://doi.org/10.1016/j.jpowsour.2006.02.065.

[134] Alimohammadi S, Zendehboudi S, James L. Review article A comprehensive review of asphaltene deposition in petroleum reservoirs : Theory , challenges , and tips. Fuel 2019;252:753–91. https://doi.org/10.1016/j.fuel.2019.03.016.

[135] Keshmiri K, Huang H, Nazemifard N. Micro fl uidic platform to evaluate asphaltene deposition during solvent- based extraction of bitumen. Fuel 2019;239:841–51. https://doi.org/10.1016/j.fuel.2018.11.044.

[136] Akbarzadeh K, Hammami A, Kharrat A, Zhang D, Allenson S, Creek J, et al. Asphaltenes - problematic but rich in potential. Oilfield Rev 2007;19:22–43.

[137] Kiliç M, Apaydin-Varol E, Pütün AE. Preparation and surface characterization of activated carbons from Euphorbia rigida by chemical activation with $ZnCl_2$, K_2CO_3 ,

NaOH and H_3PO_4. Appl Surf Sci 2012;261:247–54. https://doi.org/10.1016/j.apsusc.2012.07.155.

[138] Jeong JH, Kim B. Journal of the Taiwan Institute of Chemical Engineers Electrospun porous carbon nanofibers with controllable pore sizes by boron trioxide for electrochemical capacitor electrodes. J Taiwan Inst Chem Eng 2018;84:179–87. https://doi.org/10.1016/j.jtice.2018.01.003.

[139] Ma C, Song Y, Shi J, Zhang D, Zhai X, Zhong M, et al. Preparation and one-step activation of microporous carbon nanofibers for use as supercapacitor electrodes. Carbon 2013;51:290–300. https://doi.org/10.1016/j.carbon.2012.08.056.

[140] Wei L, Yushin G. Nanostructured activated carbons from natural precursors for electrical double layer capacitors. Nano Energy 2012;1:552–65. https://doi.org/10.1016/j.nanoen.2012.05.002.

[141] Lota G, Centeno TA, Frackowiak E, Stoeckli F. Improvement of the structural and chemical properties of a commercial activated carbon for its application in electrochemical capacitors 2009;53:2210–6. https://doi.org/10.1016/j.electacta.2007.09.028.

[142] Azadian F, Rastogi AC. Electrochimica Acta Energy storage performance of thin fi lm nanocrystalline vanadium oxide with fl uorinated tin oxide current carrier electrode for solid- state transparent supercapacitors based on ionic liquid gel electrolyte. Electrochim Acta 2020;330:135339. https://doi.org/10.1016/j.electacta.2019.135339.

[143] Gunday ST, Cevik E, Yusuf A, Bozkurt A. Synthesis, characterization and supercapacitor application of ionic liquid incorporated nanocomposites based on SPSU/Silicon dioxide. J

Phys Chem Solids 2020;137:109209. https://doi.org/10.1016/j.jpcs.2019.109209.

[144] Ni G, Qin F, Guo Z, Wang J, Shen W. Electrochimica Acta Nitrogen-doped asphaltene-based porous carbon fi bers as supercapacitor electrode material with high speci fi c capacitance. Electrochim Acta 2020;330:135270. https://doi.org/10.1016/j.electacta.2019.135270.

[145] Gilliam RJ, Graydon JW, Kirk DW, Thorpe SJ. A review of specific conductivities of potassium hydroxide solutions for various concentrations and temperatures. Int J Hydrogen Energy 2007;32:359–64. https://doi.org/10.1016/j.ijhydene.2006.10.062.

[146] Zhang H, Zhang X, Ma Y. Electrochimica Acta Enhanced capacitance supercapacitor electrodes from porous carbons with high mesoporous volume. Electrochim Acta 2015;184:347–55. https://doi.org/10.1016/j.electacta.2015.10.089.

[147] Miao L, Duan H, Wang Z, Lv Y, Xiong W, Zhu D, et al. Improving the pore-ion size compatibility between poly (ionic liquid) - derived carbons and high-voltage electrolytes for high energy-power supercapacitors. Chem Eng J 2020;382:122945. https://doi.org/10.1016/j.cej.2019.122945.

[148] Li Y, Zhang D, Zhang Y, He J, Wang Y, Wang K, et al. Biomass-derived microporous carbon with large micropore size for high-performance supercapacitors. J Power Sources 2020;448:227396. https://doi.org/10.1016/j.jpowsour.2019.227396.

[149] Banda H, Aradilla D, Benayad A, Chenavier Y, Daffos B, Dubois L, et al. One-step synthesis of highly reduced graphene hydrogels for high power supercapacitor applications. J Power Sources 2017;360:538–47. https://doi.org/10.1016/j.jpowsour.2017.06.033.

[150] Wei W, Cui X, Chen W, Ivey DG. Manganese oxide-based materials as electrochemical supercapacitor electrodes. Chem Soc Rev 2011;40:1697–721. https://doi.org/10.1039/c0cs00127a.

[151] Zhang X, Yu P, Zhang H, Zhang D, Sun X, Ma Y. Rapid hydrothermal synthesis of hierarchical nanostructures assembled from ultrathin birnessite-type MnO_2 nanosheets for supercapacitor applications. Electrochim Acta 2013;89:523–9. https://doi.org/10.1016/j.electacta.2012.11.089.

[152] Raj B, Padhy AK, Basu S. Review, Futuristic Direction for R & D Challenges to Develop 2D Advanced Materials Based Supercapacitors. J Electrochem Soc 2020;167:136501. https://doi.org/10.1149/1945-7111/abb40d.

[153] P. L. Taberna, P. S, Fauvarque JF. Electrochemical Characteristics and Impedance Spectroscopy Studies of Carbon-Carbon Supercapacitors. J Electrochem Soc 2003;150:A292–300. https://doi.org/10.1149/1.1543948.

[154] Zhu X, Xia Q, Liu X, Zhang Q, Xu J, Lin B, et al. Retarded layered-to-spinel phase transition in structure reinforced birnessite with high Li content. Sci Bull 2021;66:219–24. https://doi.org/10.1016/j.scib.2020.09.032.

[155] Zhao Y, Fang Q, Zhu X, Xue L, Ni M, Qiu C, et al. Structure reinforced birnessite with an extended potential window for supercapacitors. J Mater Chem A 2020;8:8969–78. https://doi.org/10.1039/d0ta01480j.

[156] Jabeen N, Hussain A, Xia Q, Sun S, Zhu J, Xia H. High-Performance 2.6 V Aqueous Asymmetric Supercapacitors based on In Situ Formed $Na_{0.5}MnO_2$ Nanosheet Assembled Nanowall Arrays. Adv Mater 2017;29. https://doi.org/10.1002/adma.201700804.

[157] Sadak O, Wang W, Guan J, Sundramoorthy AK, Gunasekaran S. MnO_2 Nanoflowers Deposited on Graphene Paper as Electrode Materials for Supercapacitors. ACS Appl Nano Mater 2019;2:4386–94. https://doi.org/10.1021/acsanm.9b00797.

[158] Sun L, Song G, Sun Y, Fu Q, Pan C. One-step construction of 3D N/P-codoped hierarchically porous carbon framework in-situ armored Mn_3O_4 nanoparticles for high-performance flexible supercapacitors. Electrochim Acta 2020;333:135496. https://doi.org/10.1016/j.electacta.2019.135496.

[159] Verma S, Khosla A, Arya S. Performance of Electrochemically Synthesized Nickel-Zinc and Nickel-Iron (Ni–Zn//Ni–Fe) Nanowires as Battery Type Supercapacitor. J Electrochem Soc 2020;167:120527. https://doi.org/10.1149/1945-7111/abaf72.

[160] Xun Z, Liu Y, Gu J, Liu L, Huo P. A Biomass-Based Redox Gel Polymer Electrolyte for Improving Energy Density of Flexible Supercapacitor. J Electrochem Soc 2019;166:A2300–12. https://doi.org/10.1149/2.1571910jes.

[161] Khomenko V, Raymundo-Piñero E, Frackowiak E, Béguin F. High-voltage asymmetric supercapacitors operating in aqueous electrolyte. Appl Phys A Mater Sci Process 2006;82:567–73. https://doi.org/10.1007/s00339-005-3397-8.

[162] Gupta SP, Gosavi SW, Late DJ, Qiao Q, Walke PS. Temperature driven high-performance pseudocapacitor of carbon nano-onions supported urchin like structures of α-MnO_2 nanorods. Electrochim Acta 2020;354:136626. https://doi.org/10.1016/j.electacta.2020.136626.

[163] Wang L, Ouyang Y, Jiao X, Xia X, Lei W, Hao Q. Polyaniline-assisted growth of MnO_2 ultrathin nanosheets on graphene and porous graphene for asymmetric supercapacitor with

enhanced energy density. Chem Eng J 2018;334:1–9. https://doi.org/10.1016/j.cej.2017.10.005.

[164] Wu P, Gao M, Yu S, Feng M, Liu S, Fu J. MnO2 nanosheets grown on N and P co-doped hollow carbon microspheres for high performance asymmetric supercapacitor. Electrochim Acta 2020;354:136681. https://doi.org/10.1016/j.electacta.2020.136681.

[165] M. RIPERT , J. PANNETIER YC& CP. Manganese dioxides: structural model and in-situ neutron powder diffraction investigation of thermal annealing and electrochemical reduction. Mat Res Soc Symp Proc 1991;210:359–65.

[166] Zhu S, Huo W, Liu X, Zhang Y. Birnessite based nanostructures for supercapacitors: Challenges, strategies and prospects. Nanoscale Adv 2020;2:37–54. https://doi.org/10.1039/c9na00547a.

[167] Labbe M, Clark MP, Abedi Z, He A, Cadien K, Ivey DG. Atomic layer deposition of iron oxide on a porous carbon substrate via ethylferrocene and an oxygen plasma. Surf Coatings Technol 2021;421:127390. https://doi.org/10.1016/j.surfcoat.2021.127390.

[168] Nakayama M, Osae S, Kaneshige K, Komine K, Abe H. Direct Growth of Birnessite-Type MnO 2 on Treated Carbon Cloth for a Flexible Asymmetric Supercapacitor with Excellent Cycling Stability . J Electrochem Soc 2016;163:A2340–8. https://doi.org/10.1149/2.1031610jes.

[169] Zhu Y, Xu H, Tang J, Jiang X, Bao Y, Chen Y. Synthesis of γ-MnO_2 /PANI Composites for Supercapacitor Application in Acidic Electrolyte . J Electrochem Soc 2021;168:030542. https://doi.org/10.1149/1945-7111/abef82.

[170] Hu H, Wu M. Heavy oil-derived carbon for energy storage applications. J Mater Chem A 2020;8:7066–82. https://doi.org/10.1039/d0ta00095g.

[171] Leistenschneider D, Zuo P, Kim Y, Abedi Z, Ivey DG, de Klerk A, et al. A mechanism study of acid-assisted oxidative stabilization of asphaltene-derived carbon fibers. Carbon Trends 2021;5:10 0 090 Contents. https://doi.org/10.1016/j.cartre.2021.100090.

[172] Li C, Zhang X, Lv Z, Wang K, Sun X, Chen X, et al. Scalable combustion synthesis of graphene-welded activated carbon for high-performance supercapacitors. Chem Eng J 2021;414:128781. https://doi.org/10.1016/j.cej.2021.128781.

[173] Li C, Zhang X, Wang K, Su F, Chen CM, Liu F, et al. Recent advances in carbon nanostructures prepared from carbon dioxide for high-performance supercapacitors. J Energy Chem 2021;54:352–67. https://doi.org/10.1016/j.jechem.2020.05.058.

[174] Zhou Q, Tang G, Chen X, Su F. Flexible Supercapacitors Based on CNT/MnO_2 -BP Composite Yarn Synthesized by In Situ Reduction . J Electrochem Soc 2021;168:080524. https://doi.org/10.1149/1945-7111/ac1cff.

[175] Zuo P, Leistenschneider D, Kim Y, Abedi Z, Ivey DG, Zhang X, et al. Asphaltene thermal treatment and optimization of oxidation conditions of low-cost asphaltene-derived carbon fibers. J Ind Eng Chem 2021;104:427–36. https://doi.org/10.1016/j.jiec.2021.08.039.

[176] Demarconnay L, Raymundo-Piñero E, Béguin F. Adjustment of electrodes potential window in an asymmetric carbon/MnO_2 supercapacitor. J Power Sources 2011;196:580–6. https://doi.org/10.1016/j.jpowsour.2010.06.013.

[177] Ma Z, Shao G, Fan Y, Wang G, Song J, Shen D. Construction of Hierarchical α-MnO_2

Nanowires@Ultrathin δ-MnO_2 Nanosheets Core-Shell Nanostructure with Excellent Cycling Stability for High-Power Asymmetric Supercapacitor Electrodes. ACS Appl Mater Interfaces 2016;8:9050–8. https://doi.org/10.1021/acsami.5b11300.

[178] Ilton ES, Post JE, Heaney PJ, Ling FT, Kerisit SN. Applied Surface Science XPS determination of Mn oxidation states in Mn (hydr) oxides. Appl Surf Sci 2016;366:475–85. https://doi.org/10.1016/j.apsusc.2015.12.159.

[179] Gorlin Y, Jaramillo TF. A Bifunctional Nonprecious Metal Catalyst for Oxygen Reduction and Water Oxidation. J Am Chem Soc 2010:13612–4. https://doi.org/10.1021/ja104587v.

[180] Liu J, Yang L, Song Z, Xu C. Microstructures and capacitance performance of MnO 2 films fabricated by ultrasonic-assisted electrodeposition. Appl Surf Sci 2019;478:94–102. https://doi.org/10.1016/j.apsusc.2019.01.205.

[181] Biesinger MC, Payne BP, Grosvenor AP, Lau LWM, Gerson AR, Smart RSC. Applied Surface Science Resolving surface chemical states in XPS analysis of first row transition metals , oxides and hydroxides : Cr , Mn , Fe , Co and Ni. Appl Surf Sci 2011;257:2717–30. https://doi.org/10.1016/j.apsusc.2010.10.051.

[182] Deng X, Bai X, Cai Z, Huang M, Chen X, Huang B, et al. Renewable carbon foam / ı - MnO_2 composites with well-defined hierarchical microstructure as supercapacitor electrodes. Integr Med Res 2020;9:8544–55. https://doi.org/10.1016/j.jmrt.2020.05.130.

[183] Ma Z, Jing F, Fan Y, Hou L, Su L, Fan L. High-Stability MnO_x Nanowires @ C @ MnO_x Nanosheet Core – Shell Heterostructure Pseudocapacitance Electrode Based on Reversible Phase Transition Mechanism. Small 2019;1900862:1–11.

https://doi.org/10.1002/smll.201900862.

[184] Chen H, Zeng S, Chen M, Zhang Y, Zheng L, Li Q. Oxygen Evolution Assisted Fabrication of Highly Loaded Carbon Nanotube/MnO_2 Hybrid Films for High-Performance Flexible Pseudosupercapacitors. Small 2016;12:2035–45. https://doi.org/10.1002/smll.201503623.

[185] Sun Y, Huang N, Sun X, Wang D, Zhang J, Qiao S, et al. An improvement on capacitive properties of clew-like MnO_2 by thermal treatment under nitrogen. Int J Hydrogen Energy 2017;42:20016–25. https://doi.org/10.1016/j.ijhydene.2017.05.234.

[186] Wang D, Kong L, Liu M, Zhang W, Luo Y. Amorphous Ni e P materials for high performance pseudocapacitors. J Power Sources 2015;274:1107–13. https://doi.org/10.1016/j.jpowsour.2014.10.179.

[187] Li HB, Yu MH, Lu XH, Liu P, Liang Y, Xiao J, et al. Amorphous Cobalt Hydroxide with Superior Pseudocapacitive Performance. ACS Appl Mater Interfaces 2014;6:745–9. https://doi.org/10.1021/am404769z.

[188] Li HB, Yu MH, Wang FX, Liu P, Liang Y, Xiao J, et al. Amorphous nickel hydroxide nanospheres with ultrahigh capacitance and energy density as electrochemical pseudocapacitor materialsas. Nat Commun 2013:1–7. https://doi.org/10.1038/ncomms2932.

[189] Pei P, Wang K, Ma Z. Technologies for extending zinc-air battery's cyclelife: A review. Appl Energy 2014;128:315–24. https://doi.org/10.1016/j.apenergy.2014.04.095.

[190] Park J, Park M, Nam G, Lee JS, Cho J. All-solid-state cable-type flexible zinc-air battery.

Adv Mater 2015;27:1396–401. https://doi.org/10.1002/adma.201404639.

[191] Pan J, Tian XL, Zaman S, Dong Z, Liu H, Park HS, et al. Recent Progress on Transition Metal Oxides as Bifunctional Catalysts for Lithium-Air and Zinc-Air Batteries. Batter Supercaps 2019;2:336–47. https://doi.org/10.1002/batt.201800082.

[192] Müller S, Holzer F, Haas O. Optimized zinc electrode for the rechargeable zinc-air battery. J Appl Electrochem 1998;28:895–8. https://doi.org/10.1023/A:1003464011815.

[193] Wang L, Wang Y, Wu M, Wei Z, Cui C, Mao M. Nitrogen , Fluorine , and Boron Ternary Doped Carbon Fibers as Cathode Electrocatalysts for Zinc – Air Batteries. Small 2018;1800737:1–7. https://doi.org/10.1002/smll.201800737.

[194] Suntivich J, Gasteiger HA, Yabuuchi N, Nakanishi H, Goodenough JB, Shao-Horn Y. Design principles for oxygen-reduction activity on perovskite oxide catalysts for fuel cells and metal-air batteries. Nat Chem 2011;3:546–50. https://doi.org/10.1038/nchem.1069.

[195] Yang S, Cheng Y, Xiao X, Pang H. Development and application of carbon fiber in batteries. Chem Eng J 2020;384:123294. https://doi.org/10.1016/j.cej.2019.123294.

[196] Wu M, Wang Y, Wei Z, Wang L, Zhuo M, Zhang J, et al. Ternary doped porous carbon nano fi bers with excellent ORR and OER performance for zinc – air. J Mater Chem A 2018:10918–25. https://doi.org/10.1039/c8ta02416b.

[197] Xiong M, Ivey DG. Electrodeposited Co-Fe as an oxygen evolution catalyst for rechargeable zinc-air batteries. Electrochem Commun 2017;75:73–7. https://doi.org/10.1016/j.elecom.2016.12.018.

[198] Costa JM, Clark MP, de Almeida Neto AF, Ivey DG. In-situ transformation of

electrodeposited W–Co oxide to $ZnCo_2O_4$ nanoparticles as an effective bifunctional catalysts in Zn-air batteries. Int J Hydrogen Energy 2020;45:16122–32. https://doi.org/10.1016/j.ijhydene.2020.04.052.

[199] Li L, Yang J, Yang H, Zhang L, Shao J, Huang W, et al. Anchoring Mn_3O_4 Nanoparticles on Oxygen Functionalized Carbon Nanotubes as Bifunctional Catalyst for Rechargeable Zinc-Air Battery. ACS Appl Energy Mater 2018;1:963–9. https://doi.org/10.1021/acsaem.8b00009.

[200] Sayah A, Habelhames F, Bahloul A, Nessark B. Electrochemical synthesis of polyaniline-exfoliated graphene composite films and their capacitance properties Electrochemical synthesis of polyaniline-exfoliated graphene composite fi lms and their capacitance properties. J Electroanal Chem 2018;818:26–34. https://doi.org/10.1016/j.jelechem.2018.04.016.

[201] Liu BN, Luo F, Wu H, Liu Y, Zhang C, Chen J. One-Step Ionic-Liquid-Assisted Electrochemical Synthesis of Ionic-Liquid-Functionalized Graphene Sheets Directly from Graphite. Adv Funct Mater 2008;18:1518–25. https://doi.org/10.1002/adfm.200700797.

[202] Fromm O, Heckmann A, Rodehorst UC, Frerichs J, Becker D, Winter M, et al. Carbons from biomass precursors as anode materials for lithium ion batteries : New insights into carbonization and graphitization behavior and into their correlation to electrochemical performance. Carbon 2018;128:147–63. https://doi.org/10.1016/j.carbon.2017.11.065.

[203] Ross PN, Sattle M. The Corrosion of Carbon Black Anodes in Alkaline Electrolyte. J Electrochem Soc 1988;135:1464. https://doi.org/10.1149/1.2096029.

[204] Zhang HW, Lu YX, Li B, Huang GF, Zeng F, Li YY, et al. Acid-induced topological

morphology modulation of graphitic carbon nitride homojunctions as advanced metal-free catalysts for OER and pollutant degradation. J Mater Sci Technol 2021;86:210–8. https://doi.org/10.1016/j.jmst.2021.01.030.

[205] Worku AK, Ayele DW, Habtu NG, Teshager MA, Workineh ZG. Recent progress in MnO_2-based oxygen electrocatalysts for rechargeable zinc-air batteries. Mater Today Sustain 2021;13:100072. https://doi.org/10.1016/j.mtsust.2021.100072.

[206] Wang W, Kuai L, Cao W, Huttula M, Ollikkala S, Ahopelto T, et al. Mass-Production of Mesoporous MnCo2O4 Spinels with Manganese(IV)- and Cobalt(II)-Rich Surfaces for Superior Bifunctional Oxygen Electrocatalysis. Angew Chemie - Int Ed 2017;56:14977–81. https://doi.org/10.1002/anie.201708765.

[207] Wang Q, Xue Y, Sun S, Yan S, Miao H, Liu Z. Facile synthesis of ternary spinel Co – Mn – Ni nanorods as efficient bi-functional oxygen catalysts for rechargeable zinc-air batteries. J Power Sources 2019;435:226761. https://doi.org/10.1016/j.jpowsour.2019.226761.

[208] Su H, Wang X-T, Hu J-X, Ouyang T, Xiao, Kang; Liu Z-Q. Co–Mn spinel supported self-catalysis induced N- doped carbon nanotubes with high efficiency electron transport channels for zinc–air batteries. J Mater Chem A 2019;7:22307–22313. https://doi.org/10.1039/c9ta08064c.

[209] Li K, Zhang R, Gao R, Shen G, Pan L, Yao Y. Applied Catalysis B : Environmental Metal-defected spinel $Mn_xCo_{3-x}O_4$ with octahedral Mn-enriched surface for highly efficient oxygen reduction reaction 2019;244:536–45. https://doi.org/10.1016/j.apcatb.2018.11.072.

[210] Wei C, Feng Z, Scherer GG, Barber J, Shao-Horn Y, Xu ZJ. Cations in Octahedral Sites: A Descriptor for Oxygen Electrocatalysis on Transition-Metal Spinels. Adv Mater 2017;29:1–8. https://doi.org/10.1002/adma.201606800.

[211] Cheng F, Zhang T, Zhang Y, Du J, Han X, Chen J. Enhancing Electrocatalytic Oxygen Reduction on MnO_2 with Vacancies. Angew Chemie - Int Ed 2013:2474–7. https://doi.org/10.1002/anie.201208582.

[212] Yongfu Sun, Gao S, Lei F, Liu J, Liang L, Xie Y. Atomically-thin non-layered cobalt oxide porous sheets for highly efficient oxygen-evolving electrocatalysts. Chem Sci 2014;5:3976–82. https://doi.org/10.1039/c4sc00565a.

[213] Aasen D, Clark MP, Ivey DG. $(Co,Fe)_3O_4$ Decorated Nitrogen-Doped Carbon Nanotubes in Nano-Composite Gas Diffusion Layers as Highly Stable Bifunctional Catalysts for Rechargeable Zinc-Air Batteries . Batter Supercaps 2020;3:174–84. https://doi.org/10.1002/batt.201900168.

[214] Cano ZP, Park MG, Lee DU, Fu J, Liu H, Fowler M, et al. New Interpretation of the Performance of Nickel-Based Air Electrodes for Rechargeable Zinc–Air Batteries. J Phys Chem C 2018;122:20153–66. https://doi.org/10.1021/acs.jpcc.8b06243.

[215] Wang K, Pei P, Wang Y, Liao C, Wang W, Huang S. Advanced rechargeable zinc-air battery with parameter optimization. Appl Energy 2018;225:848–56. https://doi.org/10.1016/j.apenergy.2018.05.071.

[216] Xu N, Zhang Y, Wang Y, Wang M, Su T, Coco CA, et al. Hierarchical bifunctional catalysts with tailored catalytic activity for high-energy rechargeable Zn-air batteries. Appl Energy 2020;279:115876. https://doi.org/10.1016/j.apenergy.2020.115876.

[217] Pan L, Chen D, Pei P, Huang S, Ren P. A novel structural design of air cathodes expanding three-phase reaction interfaces for zinc-air batteries. Appl Energy 2021;290:116777. https://doi.org/10.1016/j.apenergy.2021.116777.

[218] Yan Y, Liang S, Wang X, Zhang M, Hao SM, Cui X, et al. Robust wrinkled MoS2/N-C bifunctional electrocatalysts interfaced with single Fe atoms for wearable zinc-air batteries. Proc Natl Acad Sci U S A 2021;118. https://doi.org/10.1073/pnas.2110036118.

[219] Zhou T, Xu W, Zhang N, Du Z, Zhong C, Yan W, et al. Ultrathin Cobalt Oxide Layers as Electrocatalysts for High-Performance Flexible Zn–Air Batteries. Adv Mater 2019;31:1–8. https://doi.org/10.1002/adma.201807468.

[220] Fan X, Liu J, Ding J, Deng Y, Han X, Hu W, et al. Investigation of the Environmental Stability of Poly(vinyl alcohol)–KOH Polymer Electrolytes for Flexible Zinc–Air Batteries. Front Chem 2019;7:1–8. https://doi.org/10.3389/fchem.2019.00678.

[221] Fu J, Lee DU, Hassan FM, Bai Z, Park MG, Chen Z. Flexible High-Energy Polymer-Electrolyte-Based Rechargeable Zinc-Air Batteries. Adv Mater 2015;27:5617–22. https://doi.org/10.1002/adma.201502853.

[222] Xu Y, Zhang Y, Guo Z, Ren J, Wang Y, Peng H. Flexible, Stretchable, and Rechargeable Fiber-Shaped Zinc-Air Battery Based on Cross-Stacked Carbon Nanotube Sheets. Angew Chemie - Int Ed 2015;54:15390–4. https://doi.org/10.1002/anie.201508848.

[223] Chen Z, Li W, Yang X, Ke C, Chen H, Li Q, et al. Gel polymer electrolyte with MXene to extend cycle lifespan of flexible and rechargeable Zinc–Air batteries. J Power Sources 2022;523:231020. https://doi.org/10.1016/j.jpowsour.2022.231020.

[224] Miao H, Wu X, Chen B, Wang Q, Wang F, Wang J, et al. A-site deficient/excessive effects of LaMnO3 perovskite as bifunctional oxygen catalyst for zinc-air batteries. Electrochim Acta 2020;333:135566. https://doi.org/10.1016/j.electacta.2019.135566.

[225] Roy B, Shebin KJ, Sampath S. Pyrite-type cobalt phosphosulphide bifunctional catalyst for aqueous and gel-based rechargeable zinc-air batteries. J Power Sources 2020;450:227661. https://doi.org/10.1016/j.jpowsour.2019.227661.

[226] Amaral MM, Venâncio R, Peterlevitz AC, Zanin H. Recent advances on quasi-solid-state electrolytes for supercapacitors. J Energy Chem 2022;67:697–717. https://doi.org/10.1016/j.jechem.2021.11.010.

[227] Alipoori S, Mazinani S, Aboutalebi SH, Sharif F. Review of PVA-based gel polymer electrolytes in flexible solid-state supercapacitors: Opportunities and challenges. J Energy Storage 2020;27:101072. https://doi.org/10.1016/j.est.2019.101072.

[228] Moura MJ, Figueiredo MM, Gil MH. Rheological study of genipin cross-linked chitosan hydrogels. Biomacromolecules 2007;8:3823–9. https://doi.org/10.1021/bm700762w.

[229] Arnolds O, Buggisch H, Sachsenheimer D, Willenbacher N. Capillary breakup extensional rheometry (CaBER) on semi-dilute and concentrated polyethyleneoxide (PEO) solutions. Rheol Acta 2010;49:1207–17. https://doi.org/10.1007/s00397-010-0500-7.

[230] Simon BA, Gayon-Lombardo A, Pino-Muñoz CA, Wood CE, Tenny KM, Greco K V., et al. Combining electrochemical and imaging analyses to understand the effect of electrode microstructure and electrolyte properties on redox flow batteries. Appl Energy 2022;306. https://doi.org/10.1016/j.apenergy.2021.117678.

[231] Xu Q, Zhao TS, Zhang C. Effects of SOC-dependent electrolyte viscosity on performance of vanadium redox flow batteries. Appl Energy 2014;130:139–47. https://doi.org/10.1016/j.apenergy.2014.05.034.

[232] Saito M, Kawaharasaki S, Ito K, Yamada S, Hayamizu K, Seki S. Strategies for fast ion transport in electrochemical capacitor electrolytes from diffusion coefficients, ionic conductivity, viscosity, density and interaction energies based on HSAB theory. RSC Adv 2017;7:14528–35. https://doi.org/10.1039/c7ra00455a.

[233] Bohnke O, Frand G, Rezrazi M, Rousselot C, Truche C. Fast ion transport in new lithium electrolytes gelled with PMMA. 2. Influence of lithium salt concentration. Solid State Ionics 1993;66:105–12. https://doi.org/10.1016/0167-2738(93)90033-Y.

[234] Wang M, Qian T, Liu S, Zhou J, Yan C. Unprecedented Activity of Bifunctional Electrocatalyst for High Power Density Aqueous Zinc-Air Batteries. ACS Appl Mater Interfaces 2017;9:21216–24. https://doi.org/10.1021/acsami.7b02346.

[235] Tang K, Fu J, Wu M, Hua T, Liu J, Song L, et al. Synergetic Chemistry and Interface Engineering of Hydrogel Electrolyte to Strengthen Durability of Solid-State Zn–Air Batteries. Small Methods 2022;6:1–11. https://doi.org/10.1002/smtd.202101276.

[236] He Y, Yang X, Li Y, Liu L, Guo S, Shu C, et al. Atomically Dispersed Fe–Co Dual Metal Sites as Bifunctional Oxygen Electrocatalysts for Rechargeable and Flexible Zn–Air Batteries. ACS Catal 2022;12:1216–27. https://doi.org/10.1021/acscatal.1c04550.

[237] Tran TNT, Aasen D, Zhalmuratova D, Labbe M, Chung HJ, Ivey DG. Compositional Effects of Gel Polymer Electrolyte and Battery Design for Zinc-Air Batteries. Batter Supercaps 2020;3:917–27. https://doi.org/10.1002/batt.202000054.

[238] Karpas Z, Berant Z, Shahal O. Effect of Temperature on the Mobility of Ions. J Am Chem Soc 1989;111:6015–8. https://doi.org/10.1021/ja00198a007.

[239] Guttman A, Horváth J, Cooke N. Influence of Temperature on the Sieving Effect of Different Polymer Matrices in Capillary SDS Gel Electrophoresis of Proteins. Anal Chem 1993;65:199–203. https://doi.org/10.1021/ac00051a002.

[240] Gennero De Chialvo MR, Chialvo AC. The polarisation resistance, exchange current density and stoichiometric number for the hydrogen evolution reaction: Theoretical aspects. J Electroanal Chem 1996;415:97–106. https://doi.org/10.1016/S0022-0728(96)04713-4.

[241] Abedi Z, Cui J, Chen W, Ivey DG. Zinc–Air Batteries with an Efficient and Stable $MnCo_2O_4$ /Carbon Fiber Bifunctional Electrocatalyst and a Poly(acrylic Acid)-Based Gel Electrolyte. ACS Appl Energy Mater 2022;5:14164–74. https://doi.org/10.1021/acsaem.2c02699.

[242] Chen R, Xu X, Peng S, Chen J, Yu D, Xiao C, et al. A Flexible and Safe Aqueous Zinc-Air Battery with a Wide Operating Temperature Range from -20 to 70 °C. ACS Sustain Chem Eng 2020;8:11501–11. https://doi.org/10.1021/acssuschemeng.0c01111.

[243] Zhang Y, Chen Y, Alfred M, Huang F, Liao S, Chen D, et al. Alkaline sodium polyacrylate-starch hydrogels with tolerance to cold conditions for stretchable zinc-air batteries. Compos Part B Eng 2021;224:109228. https://doi.org/10.1016/j.compositesb.2021.109228.

[244] Jiang D, Wang H, Wu S, Sun X, Li J. Flexible Zinc–Air Battery with High Energy Efficiency and Freezing Tolerance Enabled by DMSO-Based Organohydrogel Electrolyte.

Small Methods 2022;6:1–9. https://doi.org/10.1002/smtd.202101043.

[245] An L, Huang B, Zhang Y, Wang R, Zhang N, Dai T, et al. Interfacial Defect Engineering for Improved Portable Zinc–Air Batteries with a Broad Working Temperature. Angew Chemie 2019;131:9559–63. https://doi.org/10.1002/ange.201903879.